

Smart Opto-mechanical actuators for tactile applications

Núria Torras Andrés

Microelectronics and Electronic Systems Department

Universitat Autònoma de Barcelona

A thesis submitted for the degree of
Philosophiæ Doctor (PhD) in Engineering

September 2014



El Prof. Jaume Esteve Tintó, professor d'investigació de l'Institut de Microelectrònica de Barcelona, IMB-CNM (CSIC), i el Dr. Jordi Roig de Zárate, titular d'universitat de la Universitat Autònoma de Barcelona,

CERTIFIQUEN:

que la memòria de la present tesi doctoral titulada "**Smart Opto-mechanical actuators for tactile applications**" presentada per Núria Torras Andrés per a optar al grau de Doctora en Enginyeria per la Universitat Autònoma de Barcelona ha estat realitzada sota la seva direcció i tutela dins del programa de doctorat en Microelectrònica i Sistemes electrònics de la Universitat Autònoma de Barcelona.

Bellaterra,
Setembre 2014

La autora:

Núria Torras Andrés

Directors de Tesi:

Prof. Jaume Esteve Tinó

Dr. Jordi Roig de Zárate.

Resum

La discapacitat visual és una greu amenaça que limita la capacitat de les persones per comunicar-se. Amb els anys, s'han explorat diverses propostes tecnològiques basades tan en estímuls auditius com tàctils per aportar solucions reals a la gent que pateix aquest tipus de discapacitat. Entre les més rellevants destaquen les tècniques d'audiodescripció i els dispositius Braille basats en actuació piezoelèctrica, que són els que actualment es troben al mercat.

A dia d'avui, al vell mig de la cursa tecnològica, hi ha una demanda creixent de comunicació rica i fluida mitjançant el tacte. Tan és així que la majoria d'interruptors, botons i tecles de gran part dels dispositius electrònics del nostre entorn estan essent substituïts per pantalles tàctils, afegint barreres físiques i augmentant les dificultats de comunicació de les persones cegues.

Noves generacions de materials, principalment els polímers, han despertat un gran interès en els darrers anys gràcies a les seves atractives propietats, que poden adaptar-se a la carta en funció de les necessitats. De tots ells, els elastòmers de cristalls líquids, LCE, en són un clar exemple. Els LCE tenen la capacitat intrínseca d'auto-organitzar-se a nivell molecular, desencadenant canvis controlats i totalment reversibles en les seves dimensions a escala macroscòpica, en resposta a diversos tipus d'estímuls externs; canvis que poden adaptar-se per desenvolupar actuadors capaços de produir tan esforços mecànics de tracció com d'empenta.

La recerca presentada en aquesta tesi descriu les principals característiques dels LCE des del punt de vista de l'enginyeria i discuteix les seves possibles aplicacions com a actuadors, amb el principal objectiu d'aportar solucions innovadores als actuals sistemes tàctils, a partir del disseny, fabricació i caracterització de diferents actuadors basats en aquests materials i la seva foto-actuació a partir de llum visible. Propostes que combinen tècniques de processament de materials i tecnologia de microsisemes per aportar solucions tecnològiques innovadores cap a una nova generació d'actuadors intel·ligents.

Abstract

Visual disability is a serious threat that limits the persons' ability to communicate. Over the years several attempts for the development of technologies based on audio and tactile stimuli have been explored to provide real solutions to individuals with this disability. Among them, audio description techniques and Braille devices based on piezoelectric actuation are the most relevant solutions on the market.

Nowadays, with all the technological improvements, there is a growing demand for rich communication through touch. Thus switches, buttons and keyboards of most commonly used electrical devices are being replaced by tactile displays, adding new physical barriers and increasing communications difficulties of blind people.

New generation of materials, especially soft polymer composites, have been of increased interest in the last few years due to their many attractive properties, which can be tailored on demand to achieve a broad range of requirements. Liquid-crystalline elastomers, LCE, are a clear example. Such materials possess the intrinsic ability to self-organize at molecular level resulting in a controllable and fully reversible change on their dimensions at macroscale in response to applied external stimuli, which can be easily adapted to make actuators producing pulling or pushing forces.

The research presented in this thesis describes the main characteristics of LCE materials from engineering point of view and discusses their potential applications as actuators with the main objective to provide innovative solutions towards current tactile available systems, through the design, fabrication and characterization of different actuator approaches based on these interesting elastomeric materials and their photo-induced actuation using visible light. Novel approaches combining material processing techniques and microsystems technology to provide original solutions towards a new generation of smart actuators.

A la meva família

Agraïments

Amb aquestes senzilles paraules m'agradaria donar les gràcies a totes aquelles persones que han fet possible aquesta tesi.

Primerament voldria donar les gràcies als meus directors de tesi, al Prof. Jaume Esteve i al Dr. Jordi Roig. Gràcies Jaume per haver confiat en mi des de l'inici d'aquest camí i haver-me donat la oportunitat d'iniciar-me al món de la recerca en el camp de la micro i la nanotecnologia al CNM. Gràcies per haver-me donat la llibertat i les facilitats necessàries per poder formar-me en diferents àrees i poder ampliar els meus coneixements més enllà del projecte. Gràcies Jordi per al teu suport i per haver-me donat la oportunitat de compartir l'experiència de la docència amb el teu equip.

També voldria donar les gràcies al diferents membres del projecte europeu NOMS en el qual s'enmarca el gruix d'aquesta tesi. Per la seva feina i dedicació al projecte i per les seves contribucions, que han ajudat a fer possibles molts dels resultats aquí presentats. I al Dr. Antoni Sánchez-Ferrer, de la ETH de Zürich, pel seu suport i estreta col·laboració, de la qual han sorgit treballs i propostes molt interessants. I espero que segueixin endavant i poder ampliar la llista ben aviat!

Gràcies també a l'Associació/Col·legi d'Enginyers Industrials de Catalunya que, amb el suport de l'Agrupació Sòcio-Cultural dels Enginyers Industrials de Catalunya, han premiat el meu esforç i dedicació en aquest treball concedint-me una beca per finalitzar amb èxit els meus estudis de doctorat.

Gràcies a tots els companys del Grup de Micro & NanoTools: José Antonio, Marta, Rodrigo, Sara, Carlos, Gonzalo, Carolina, amb els que m'he sentit molt còmoda treballant i dels que he après moltíssimes coses, no només relacionades amb la recerca, i que han fet tan fàcil el treball del dia a dia. Molt especialment els comentaris i consells d'en José Antonio i la oportunitat que m'ha donat de participar als projectes MINAHE3 i 4 (y espero també el 5!!) i les seves lliçons d'ANSYS. Ahora a por las plataformas! I també el suport, la paciència, el dinamisme i bon humor de la Marta. Per la seva experiència i coneixements en microsisitemes i per donar-me un cop

de mà amb els Runs! Gràcies a tots dos per compartir amb mi els esmorzars i ajudar-me a comenar amb alegria i bon humor un nou dia de feina.

No podria acabar de parlar de la gent del grup sense dedicar unes paraules a en Kirill. Amb ell vam compartir els inicis d'aquest treball i d'ell vaig aprendre moltes coses que han fet possible bona part dels resultats d'aquesta tesi. Gracias Kirill por tratar de inculcarme precisión y rigurosidad en el trabajo, por tus comentarios críticos y por tu paciencia en el laboratorio.

Gràcies també a en Jordi, la Neus, en Xavi, la Marta, en Carlos, la Núria (la Torres amb "e"), l'Alberto, l'Ana: la colla del "tupper". Per acollir-me al grup i fer l'hora de dinar tan divertida. Pels pastissos, els flams de turró i les pastes! Gràcies per fer-me riure amb els vostres acudits i fer-me sentir una més des del primer dia.

Als companys de despatx: en Sergi, la Daniela, la Sara, la Carolina, en Maxim, pel bon ambient de treball i les converses disteses, i molt especialment a la Diana i a la Consuelo: per les sessions al Verdi, els sopars internacionals i les fanstàstiques converses.

Gràcies també a la gent de l'IMB-CNM que, durant aquests anys m'han ofert la seva ajuda i que amb la seva feina, han fet possible que tot segueixi endavant.

Finalment la meva família. Gràcies als meus pares pel seu suport, per fer-me costat en aquest camí que he escollit i fer l'esforç d'entendre les meves explicacions: nanotubs, cristalls líquids,... A la meva mare pels seus consells i el menjar casolà que tan bé m'ha anat per agafar forces en llargs dies de feina. I al meu pare, per la seva paciència i sàvies paraules, i pels seus missatges de bon dia tan positius. Si us plau, no deixis mai d'enviar-los! Al meu germà, el Mr. Photoshop, per les vegades que m'ha donat un cop de mà amb els dissenys de les portades. Realment la de la tesi t'ha quedat genial! I a la resta de la meva curta però molt ben avinguda família, per creure en mi.

I no podia acabar aquest escrit sense dedicar unes paraules al Dani; el meu company en aquest intrèpid i bonic viatge que és la vida. Moltes gràcies per fer més lleus les meves angoixes i per ajudar-me a no defallir en els moments de més nervis. Per animar-me i fer-me riure quan estic trista. Gràcies per ser aquí. —

Contents

1	Introduction	1
1.1	A bit of history	3
1.2	Braille devices on the market	4
1.3	Non-commercial alternative solutions	8
1.4	Tactile dynamic Braille displays	9
1.5	New materials for Braille actuators	11
1.6	Summary	14
1.7	Framework	17
I	LIQUID CRYSTALLINE ELASTOMERS: Smart & soft materials	19
2	Introduction to LCE	21
2.1	General Overview	22
2.2	Synthesis and preparation	25
2.2.1	LCE alignment	26
2.2.2	LCE properties and applications	28
2.2.3	LCE integration in MEMS/NEMS	29
2.3	Actuation Mechanisms	32
2.3.1	Thermal actuation: direct heating	32
2.3.2	Photo-induced actuation	35
2.4	LCE nanocomposites	37
2.4.1	LCE-CNT composites	38
2.4.1.1	LCE-CNT preparation	40
2.5	Discussion and summary	43

CONTENTS

3	LCE-CNT films characterization	45
3.1	Material conformation characterization	46
3.1.1	Microscopy analysis	46
3.1.1.1	SEM characterization: CNT identification at surface level	46
3.1.1.2	TEM characterization: CNT identification at inner level	48
3.1.2	X-ray diffraction analysis	50
3.1.3	Differential Scanning Calorimetry analysis	51
3.2	Material actuation	52
3.2.1	Thermoelastic characterization	53
3.2.2	Photo-induced actuation: opto-thermomechanical experiments .	56
3.2.2.1	“In-situ” observation of photo-actuation	56
3.2.2.2	Bending dynamics	60
3.2.2.3	Light absorption	65
3.2.2.4	Mechanical strength measurements	68
3.2.2.5	Photo-induced stress measurements	71
3.3	Material modeling	74
3.3.1	Model description	76
3.3.1.1	CNTs behavior	77
3.3.1.2	Light propagation	77
3.3.1.3	Light source radiation	78
3.3.1.4	LCE-CNT material characteristics and shape	79
3.3.2	Final considerations	79
3.4	Discussion and summary	82
II	Design and fabrication of a tactile device	85
4	“U-shaped” actuators for tactile applications: NOMS device for visually im- paired	87
4.1	Concept and working principle of the actuator	90
4.2	Characterization of the “U-shape” actuator	93
4.2.1	Setup configuration for testing	93
4.2.2	Photomechanical actuation	94
4.2.2.1	Influence of distance	94

4.2.2.2	Force measurements	96
4.3	Optimization of the "U-shape" actuator	97
4.3.1	Contact between the finger and the pin. Transmitted force and required energy	97
4.3.2	Intensity of light applied	100
4.3.2.1	Dynamic testing	100
4.3.2.2	Cyclic testing	103
4.3.3	Light source efficiency	104
4.4	Final "U-shape" actuator design	106
4.4.1	Ribbon of nematic LCE-CNT material	106
4.4.2	The pins: elements in contact with human finger	107
4.4.3	Support layers	107
4.4.4	Light source selection	108
4.4.5	Optical micro-lenses	110
4.5	Optimization of the final "U-shape" actuator	111
4.6	Actuator integration on a tactile device	113
4.6.1	Actuators layer	113
4.6.2	LED board	115
4.6.3	Hardware and control	115
4.6.4	Communication interface	116
4.7	Characterization of the device	118
4.7.1	Force and time measurements	118
4.7.2	Dynamic actuation	121
4.8	Real testing	123
4.9	Discussion and summary	124
III	Research on alternative photo-sensitive materials	129
5	Alternative material strategies	131
5.1	Dye-doped LCE material conformation	133
5.1.1	Selection of dyes	133
5.1.1.1	IR dye	134
5.1.1.2	Visible dyes	135

CONTENTS

5.2	Dye-doped LCE nanocomposites preparation	138
5.3	Dye-doped LCE nanocomposites actuation	139
5.3.1	Thermoelastic characterization	139
5.3.2	Photo-induced actuation	140
5.3.2.1	IR measurements	141
5.3.2.2	Visible light measurements	142
5.4	Dye-doped LCE actuators	146
5.5	EVA-CNT conformation	149
5.6	EVA-CNT nanocomposites preparation	150
5.7	EVA-CNT nanocomposites actuation	151
5.7.1	Mechanical strength measurements	151
5.7.2	Photomechanical actuation	152
5.7.3	Photo-induced actuation	153
5.8	EVA-CNT actuators	156
5.9	Discussion and summary	158
IV	Novel technologies for the fabrication of actuators in an array	161
6	Punch and die molded actuators	163
6.1	Concept	164
6.2	Molds design and fabrication	166
6.3	Fabrication and optimization of actuators	168
6.3.1	Actuators fabrication: stamping process	168
6.3.2	Actuators optimization: mechanical response limit	170
6.4	Characterization	172
6.4.1	Setup configuration	172
6.4.2	Photomechanical actuation	174
6.5	Discussion and summary	177
7	Gas-pressure molded actuators	179
7.1	Concept	180
7.2	Molds design and fabrication	181
7.3	Fabrication and optimization of the actuators	186

7.3.1	Optimization of the molding process	186
7.3.2	Actuators fabrication: gas-pressure molding-based process	188
7.4	Characterization	191
7.4.1	Material conformation: microscopy analysis	191
7.4.2	Thermal actuation	192
7.4.3	Photomechanical actuation	193
7.5	Discussion and summary	196
8	Micropillar array	199
8.1	Concept and processing principles	201
8.2	Molds design and fabrication	202
8.3	Fabrication of actuators	204
8.3.1	Synthesis of nematic side-chain LCE	204
8.3.2	LCE Micropillar array preparation	205
8.4	Characterization	207
8.4.1	Material conformation characterization	208
8.4.1.1	DSC measurements	208
8.4.1.2	Swelling measurements	209
8.4.1.3	X-ray Analysis	210
8.4.1.4	Polarized light analysis	212
8.4.2	Micropillar actuators characterization	213
8.4.2.1	Thermoelastic experiments	213
8.4.2.2	Thermomechanical experiments	214
8.5	Discussion and summary	217
9	Micropillar array actuators: integration on a device	219
9.1	Concept and working principle of the device	220
9.2	Design and Fabrication of the device	221
9.2.1	Thermoresistors	222
9.2.1.1	Design	222
9.2.1.2	Fabrication	224
9.2.2	Circuitry	226
9.2.2.1	Design and selection of the main components	226
9.2.2.2	Fabrication	227

CONTENTS

9.3	Micropillar array actuators fabrication	229
9.4	Thermoelectrical micropillars characterization	230
9.4.1	Thermoelastic experiments	230
9.4.2	Thermomechanical experiments	232
9.5	System optimization	234
9.6	Discussion and summary	236
	Conclusions and Future work	239
	Appendixes	245
A	Tactile perception and Braille system	245
A.1	Basic tactile perception mechanisms	245
A.1.1	Mechanoreceptors	245
A.1.2	Haptic perception	246
A.2	Braille Standards	247
B	Protection layer	251
	References	253
	Scientific contributions	261
	List of abbreviations	267

1

Introduction

Visual impairment is known as a serious threat that limits and affects the communication, education and socialization of human beings causing them serious integration problems in the society. Thus, blind people depend on tactile and auditory perceptions to sense the world around them; two possible channels to receive information.

According to the World Health Organization, WHO, there are approximately 30 million of visually impaired people in Europe, number which represents around 10% of the people with visual disabilities worldwide [1]. These incredible statistics justify the need for investment in new technologies to provide real solutions to individuals with this disability.

In this sense, several types of solutions have been developed, although only a few of them have been marketed, with the main purpose of improving the quality of the daily life of blind people, helping them in communication tasks through these two senses. This is the main objective of Tiflotechnology. Thus, different solutions ranging from simple typewriters and printer machines [2, 3] to computer adapted keyboards and assisted devices with voice synthesizers [4, 5] can be found, as well as complex portable equipment for object recognition [6, 7, 8, 9, 10] which usually combines both tactile and audio stimuli.

From the systems based on audio stimulus, audio description, AD, (which would be the equivalent to sign language used by deaf people) is the most commonly used. Firstly proposed by Gregory T. Frazier in 1974, this system consists in an audio track in which "a describer inserts spoken words to provide representations of

1. INTRODUCTION

information contained in the visual field of the production” [10]. Current examples of the application of AD include life description in TV and conferences, audio tours (mainly at public places and museums) and audio books, among others. A relatively simple solution that has allowed increasing the accessibility to conventional electronic devices, such as computers and mobile phones, via specific text-to-speech software (e.g., TextTALK, Emacspeak, Screader), and free access applications. A recent example of that is “On-The-Bus”, an accessible guiding application for public transportation usage in cities based on Android operating system developed by MASS Factory, a Spin-off of the Biomedical Applications and Technologies for Personal Autonomy Group, GABiTAP, from Universitat Autònoma de Barcelona [11] (see Figure 1.1).



Figure 1.1: On-the-Bus application for an accessible guiding in public transportation in cities. Image courtesy of MASS Factory [11].

On the other hand, there are the systems based on tactile perception. Unlike the previous ones, such systems are more challenging, not only from the technology point of view but also from the end users, who need developing the skill to read and decode the data received through touch by means of Braille system; tactile patterns resulting in combinations of raised or absent dots [12, 13]. Very basic Braille notions can be found in appendix A.2 together with its main characteristics to better understand the difficulties involving Braille-based systems and therefore part of the work developed within this thesis.

1.1 A bit of history

Since Louis Braille perfected and standardized a tactile codification system in 1821, Braille code has been the most used system for blind and visually impaired people to receive and give written information through touch. In 1829, with the publication of the first Braille book titled "Method of writing words, music and plain song by means of dots, for use by the blind and arranged by them", Louis Braille triggered a strong interest to develop Braille-based methods and technologies to produce tactile-readable text worldwide [14]. Thus, before the ends of nineteenth century, various Braille-based personal typewriter machines were presented, such as Perkins (United States, 1851), and Frank H. Hall (Jacksonville, Illinois, USA, 1892), as well as some adaptations of Braille code for specific purposes, such as the representation of mathematic symbols and music notation (Abreu system, Spain, 1855) among others. Was in early twentieth century, when the first printer machines appeared and beside them the first Braille books. Figure 1.2 depicts some examples of the above mentioned machines.



Figure 1.2: Braille machines from 19th century. German electromagnetic printer machine from 1938 [3] -left- and Frank H. Hall Braille personal typewriter machine [14] -right-.

The Optacon (Optical-to-Tactile Converter) was probably the first device to put electronic technology at the service of blind people [5, 15]. Delevoped in 1963 at Standford University, California, by Prof. John Linvill, Optacon was composed of a 24-by-6 array of piezoceramic vibrating pins (around 230 Hz of fixed frequency) equipped with a camera to allow the real-time conversion of printed characters into an equivalent vibrotactile pattern on a pad under the user's index fingertip [16]. It was at

1. INTRODUCTION

this time when the concept of transitory Braille (i.e., dynamic Braille) emerged leaving static Braille (paper books and charts) behind.

Few years later, Optacon II was upgraded by a computer interface and by the function enabling the tactile vibrating display of inkprint shapes of letters from the computer screen which were coded as ASCII characters, switching from 6 to 8 dot Braille system and thus allowing up to 256 combinations (previous system was limited to 64 characters) (see Figure 1.3 -left-). Although its great intrinsic value as a tool enabling blind people to read printed text directly, however, this device had a very short life mainly due to its poor performance [5].



Figure 1.3: Commercially available Braille devices from 20th century: Optacon and Optacon II [5, 17].

However, it was not until mid-seventies, in coincidence with the arrival of computers when the interest of the scientific community on blindness increased considerably, giving rise to the idea of computerized Braille. Since then, some research groups started to collaborate with blind associations to apply the new technologies for the creation of novel communication interfaces. As result, together with the increase in public awareness of the need for improving the lifestyles of human beings, different technologies have been developed to produce tactile-readable text.

1.2 Braille devices on the market

The most prevalent commercially available solution for transitory Braille devices involves systems based on the reversible piezoelectric effect in some crystalline materials which are able to produce electrical charges resulting from an applied mechanical force [18]. A modular technology which consist of arrays of 20, 27, 40,

80, or 2 x 80 modules in parallel, known as Braille lines, where each module represents a Braille cell (i.e., a single Braille character) [19]. A detailed image in Figure 1.4 -top- shows a standard Braille cell module in "L" configuration with its corresponding electronics. Notice that the dimensions of the entire module are very big compared to the active tactile area around the dots.

This type of actuation system allows the fabrication of sturdy actuators that can be rapidly switched between 'on' and 'off' states [20, 21], suitable for representing a few Braille characters and providing a complete range of Braille access products, from large desktop computer Braille systems up to small, portable devices (see pictures in Figure 1.4 -bottom-).

One of the first examples of commercially available Braille-based solutions in Spain (still on the market) was Eco Plus [22]. Supplied by the Spanish national organization of blind Individuals, ONCE, Eco Plus is a Windows and Linux compatible computer peripheral based on piezoceramic components which can be coupled to a standard QWERTY keyboard to combine both text typing and reading [23]. Its large dimensions (62 cm x 26 cm x 4 cm) and its high weight (4.5 Kg), however, limit its portability, proving to be a good choice for working in the office or at home but impractical as portable device as shown in Figure 1.4 -bottom left-.

Following the same operation principle various device versions from different companies have been emerged with improvements in the aesthetics (materials and colors), the autonomy of the batteries (> 20 hours of non-stop usage), and especially in the weight (≤ 1 kilo) for providing more compact and portable solutions. An example of these improvements is depicted in bottom right image in Figure 1.4: the Active Braille 40 from ARC technology [24]. Such systems are compatible with all major screen reader software for Windows and Linux based on AD and allow the convenience of entering text in Braille with the intuitive functionality of a PC keyboard, even the possibility of directly typing in Braille by means of the inclusion of keys for this purpose (keys on top of the Active 40 Braille line in Figure 1.4 -bottom right-).

Among all the advantages, piezoelectric Braille devices offer sturdiness and low power consumption, as well as enough forces and displacements to guarantee a correct tactile perception (see appendix A for more information about tactile perception mechanisms in human fingertips), which make them the best solution since decades [12, 25, 26].

1. INTRODUCTION



Figure 1.4: Current transitory Braille devices based on piezoelectric technology. "L"-shape Braille cell module with its corresponding electronics -top- with two examples of Braille devices on the market using such technology: Eco Plus-ONCE Braille keyboard [23] -bottom left-, and Active Braille 40 from ARC technology [24] -bottom right-.

However, they present some disadvantages. The most common issues reported are:

- Large dimensions of the actuator (i.e., Braille cell) with a complex structure which difficult its assembly and scalability, and restrict its packaging to a finite number of modules arranged in line or in a few rows. Large number of cells complicates the portability and increases complexity and costs,
- Expensive technology, with prices ranging from €3,500 up to €9,000 even more, as function of the number of Braille cells and the device functionalities (storage capacity, external batteries, Bluetooth and USB connections, etc.); prices which have remained unchanged the last 10 to 20 years [26],
- Abrupt change between on-off states (raising and lowering the Braille dots) together with too rigid contact elements (i.e., Braille dots),
- Noise. In spite the improvements, they still do not operate completely in silence, thus making them inconvenient for use as Braille-reading devices in public areas such as libraries, schools and offices,

1.2 Braille devices on the market

- Poor spatial resolution that limits this technology to only represent text and few symbols. Graphical information cannot be displayed due to packaging restrictions,
- Expensive maintenance. If a single pin breaks (frequently due to high lateral forces produced by the fingers when reading characters) it is necessary to replace the whole module. Moreover, the lifetime of piezo-driven modules is short,
- Moderate reading speed due to the limitation in the amount of characters displayed per line and the text refreshing rate,
- Rereading text is not allowed. If necessary, the user should go back and reload the previous lines (one by one).

Although full-page (6000 to 8000) dots Braille cell functional devices have not been attained so far [27, 28], a first approach was presented in 2011 by Metec AG company: the HyperBraille device [29] (see Figure 1.5). Thanks to a novel upright design of the piezo-driven Braille cells ("I" configuration), it allows higher integration density resulting in array of 120 x 60 dots. However lower spatial resolution, large dimensions and high weight (around 5.5 Kg), as well as a very high price (€45,000 to €50,000) make such option unattractive.



Figure 1.5: Novel piezo-driven technology for the fabrication of high density Braille device: Hyperbraille [29].

All of these above described current available solutions allow for reading and writing text as well as simple mathematics and music Braille notation. However, they do not allow the representation of more complex graphical information due to their physical limitations for a high density of integration.

1.3 Non-commercial alternative solutions

Over the years, various technologies have been explored to introduce novel actuators and mechanisms as alternatives to piezoelectric systems trying to overcome some of the issues they present. Thus, different actuator technologies have been employed, leading to pneumatic valves [30], Peltier elements [31], electrodes and motors [32, 33] among others. From the different materials used for the fabrication of actuators, shape memory alloys, SMA, [34] and electro- and magneto-rheological, MR, fluids [12, 27, 35, 36, 37], are of special interest due to its intrinsic characteristics since offer high deformations (i.e., displacements) and reversibility.

Although these developments deserve attention, most of them commonly suffer from low actuation speed due to complex mechanisms [13], limiting its expansion to few characters [38]. Furthermore, low efficiency, poor resolution, complexity, non-portability and high manufacturing costs besides constant maintenance (short lifetime) make them impractical for the fabrication of real devices which require repetitive performance, thus limiting most of them to lab-scale prototypes.

Alternatively, large refreshable Braille devices have been attempted by means of microtechnology to improve integration and lower cost. As well-known techniques, silicon microtechnologies offer scalability, batch production of identical elements as well as integration of multiple modules to achieve large scale devices [39]. Moreover, micro- and nano-electromechanical systems, MEMS and NEMS, enable integrated electronic circuitry, thus offering a reduced package to fit Braille requirements. Attempts to produce tactile devices through MEMS technology have been introduced so far resulting in a wide range of operation stimuli, e.g., photoelectric [40], electromagnetic [25, 41, 42] thermoelectric and thermopneumatic [43, 44, 45, 46], among others. However, none of these prototypes have been commercialized, so far, presumably due to high cost or low reliability. Figure 1.6 depicts two examples of different lab-scale proposed alternatives: an electromagnetic vibrotactile display (Figure 1.6a) and a MR fluid-based system (Figure 1.6b), both of them using MEMS technology.

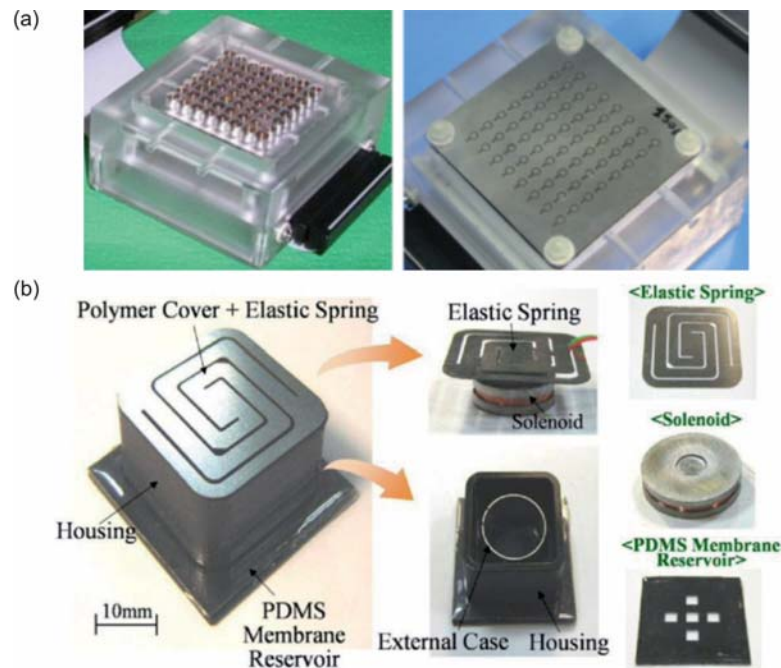


Figure 1.6: Examples of non-commercial alternative solutions for the fabrication of Braille devices. a) Vibrotactile electromagnetic display arranged in an 8 x 8 dots matrix. Reprinted with permission from Ref. [37]. Copyright 2010, Elsevier. b) MR fluid system combining polymer and microfabrication. Reprinted with permission from Ref. [41]. Copyright 2007, Elsevier.

1.4 Tactile dynamic Braille displays

Nowadays, in the middle of the technology race, there is a growing demand for communication through touch because of the increased number of opportunities in a wide range of areas such as entertainment (e.g., smartphones, tablets), medical technologies (e.g., virtual surgery training, sensory substitution), research (e.g., study of perception), and many more [25, 47]. Recent improvements in consumer electronics have included the replacement of buttons, switches and keyboards by touch-screens, giving rise to what is known as tactile displays, which have become one of the most important communication devices today. One can find tactile displays in ATMs, in public information offices and stands, in smartphones and tablets, even in a great number of household electric appliances. While this technology has considerable advantages for the average consumer, visually impaired people are unable to use such equipment [48].

1. INTRODUCTION

The adaptation of Braille to haptic systems and refreshable screens to produce rich tactile communication has become a social need, and numerous research groups have been attempted to provide useful solutions. However, it is not a straightforward task and presents considerable technological challenges: dynamic performance of actuators is required with lower latency and reduced response times. In addition, all of the systems developed for this purpose should meet some required specifications for Braille characters representation, especially geometric restrictions (i.e., dot dimensions and height, pitch between consecutive dots, etc.), as well as produce optimal forces and minimum displacements to assure their correct tactile perception [49, 50]. Ideally, such devices should also be light, portable, and have a reasonable battery life [48].

Throughout the last decade, different public and private funding organisms together with blind associations and research groups worldwide have tackled the problem of building useful and cost-effective tactile displays that allow for rich tactile communication [12]. Thus several research projects dedicated to the development of novel technologies for the fabrication of Braille-based devices have been granted by different institutions to encourage both the scientific community and the companies to push up the research around this field.

A close example is the European Union who has funded and still funds through different programs several challenging projects to this purpose, such as Touch-Hapsys (IST-2001-38040, 2002-2005) [51], NOMS Project (FP7-228916, 2009-2012) [28], ARGUS (FP7-28841, 2011-2014) [52], ADLAB (517992-LLP-1, 2011-2014) [53] and more recently BLINDPAD (FP7-ICT-2013-10, 2014-2016) [54] among others; most of them emerged in parallel to the development of this thesis.

However, the challenge is not trivial and most of the technologies prototyped have been stopped at lab-sale (non-commercial solutions) since none of the proposed designs seems to be at all satisfying due to the multiple stringent requirements.

Similarly, different ICT multinational companies such as Microsoft ® Apple ® Samsung ® LG ® and others, have licensed numerous patents about Braille displays and touchscreens in the last few years [55, 56], but none of them has been already materialized. The concept of Braille and tactile displays has also come to industrial designers' attentions, who have proposed very attractive and innovative designs that have them deserved numerous awards (e.g., IDEA and TED) but as in a similar way to

the patents, everything is remaining on ideas. Pictures in Figure 1.7 show some recent examples of Braille system approaches, most of them smartphones.



Figure 1.7: Recent proposals for the integration of Braille into new technologies: a) Touch Messenger Braille mobile phone from Samsung Electronics, 2006 [57]; b) Tactility Toshiba mobile phone designed by Siwei Liu, 2009 [58]; c) Squibble Portable Braille Interface designed by Andrew Mitchell, 2009[59]; d) Touchscreen Braille phone, designed by Sumit Dagar, 2011 [60]; e) Omnifer case designed by J. D’Alessandro from Auburn University [61]; and f) DrawBraille Mobile Phone designed by Shikun Sun from Sheffield Hallam University, 2012 [62].

For a deeper understanding of the problem, exhaustive studies of the perception mechanisms as well as the development of revolutionary technologies are still needed to improve the life of visually impaired people, which is still a hot topic in society today.

1.5 New materials for Braille actuators

New generation of materials, especially soft polymer composites, have been of increasing interest in the last few years due to their many attractive and varied characteristics. In addition to their low cost, they are generally lightweight, fracture-tolerant and pliable, and can be molded into almost any conceivable shape [48].

Research into shape-memory and shape-changing polymers (also known as

1. INTRODUCTION

actively moving polymers) [63] has created several materials with the ability to reversibly change their shape and size under the application of a wide range of external stimuli, e.g., heat, light, electric and magnetic fields [64]. This engaging nature, together with the above mentioned characteristics allow going a step further and make polymers to have considerable potential for a new generation of highly integrated actuators; more efficient technologies able to provide tactile responses in similarity with the conventional piezoelectric systems.

So far, preliminary prototypes of Braille devices based on polymeric actuators have been reported; most of them feature the exploitation of polymers with electroactive, EA, properties which produce deformation under the application of external electric and electromagnetic fields [65, 66]. The most common examples of such field-activated materials are conducting polymers [67, 68], dielectric and ferroelectric elastomers [50, 69, 70, 71], ionic polymer-metal composites, IPMC, [44, 49, 72] and polyvinylidene fluorides, PVDF, [73], among others.

The first refreshable Braille system based on EAP technology was conceived by Yoseph Bar-Cohen in 1998 [65, 74]. Since then, other researchers have reported the development of different types of EAP-based actuators for Braille displays, some of them described in the following lines (see pictures Figure 1.8).

Heydt and Chhokar [75] investigated in 2003 the use of dielectric EAP to create a diaphragm-like actuator which contracted along its thickness and expanded laterally under the application of voltages (from 2 to 6) kV pushing attached pins (Figure 1.8a). The very thin diaphragm film (thickness in the range of 30-100 μm) with compliant electrodes on both sides was supported by an outer circle frame where air pressure provide the required prestrain for actuation [75, 76].

Kato and co-workers [49] introduced in 2007 a large-area, flexible and lightweight sheet-type Braille display by means of electrically activated IPMC with high-quality organic field effect transistors, FETs, resulting in a prototype containing 6-by-4 array of actuators (see Figure 1.8b). Such actuation mechanism revolved around irreversible thermal actuation in which the thermal action of a powerful light source induces dilation of soft polymeric materials at specific sites. However, reversibility requires a cooling cycle that resulted slow and inefficient, imposing restrictions in the duty factor of the prototype.

Lately in 2009, researchers from Sungkyunkwan University in South Korea proposed a tactile Braille display using thin, cylinder-shaped polymer membranes coated with carbon electrodes with a thickness of about $50\ \mu\text{m}$ [13]. A bubble-shaped arrangement was developed, where the actuation of the elastomer produced an out-of-plane deformation that pushed a pin in the vertical direction. Similar to Heydt and Chhokar approach, the elastomer was pre-stretched to provide the required “spring” action. A great degree of miniaturization was achieved in the fabrication of the prototype (see Figure 1.8c) due to a multilayer design resulting in a height of the fully assembled device of approximately 9 mm [76].

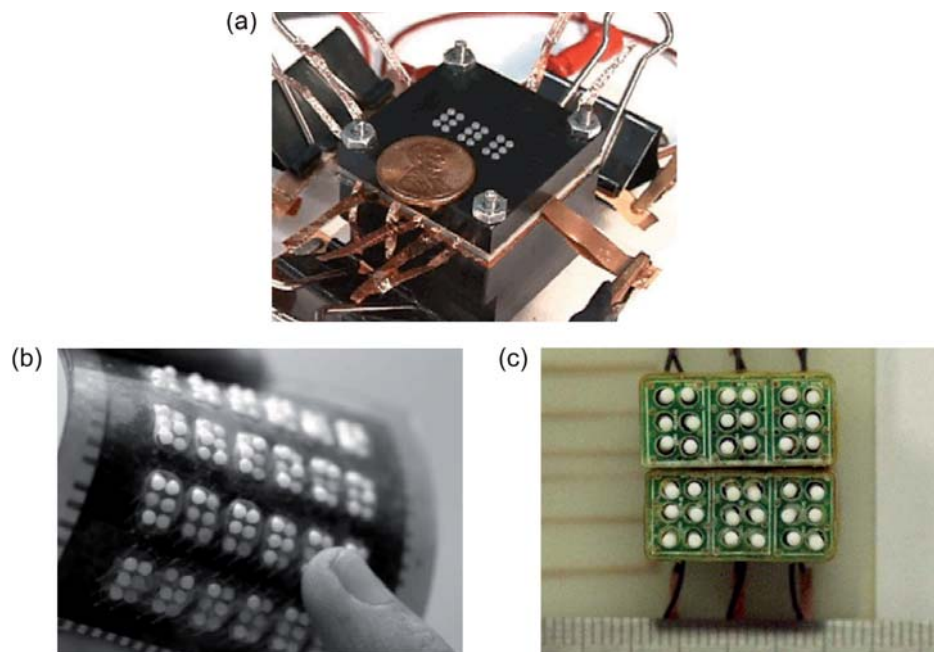


Figure 1.8: Examples of different prototypes of novel Braille systems devices based on EAP. a) Dielectric elastomer diaphragm-like actuator. Reprinted with permission from Ref. [75]. Copyright 2003, Society for Information Display; b) IPMC flexible film with organic FET. Reprinted with permission from Ref. [49]. Copyright 2007, IEEE; and c) Tactile Braille display based on cylinder-shaped membranes. Reprinted with permission from Ref. [13]. Copyright 2009, John Wiley & Sons.

Although they are emerging technologies and there are still numerous challenges to devising low-cost mechanisms, materials, and processing techniques for compact refreshable Braille displays, advances in polymers and especially in EAP technology may make those capabilities feasible in the not-too-distant future [38].

1. INTRODUCTION

Recently, another type of actuating polymeric materials with very attractive properties have been emerged as powerful alternative towards piezoelectrics and EAPs [77]: the so-called liquid crystalline elastomers, LCE [64, 78]. Such materials possess the intrinsic ability to self-organize at molecular level resulting in a controllable and fully reversible change on their dimensions at macroscale in response to applied stimuli, which can be easily adapted to make actuators producing pulling or pushing forces on demand [48]. Further details of LCE material conformation, actuation and characteristics are given in the next chapter, Chapter 2.

Originally proposed for the development of artificial muscles in robotics [79, 80], the interest in LCEs has increased in the last years and their use has extended to other fields ranging from basic science research (i.e., studies about their soft elasticity, properties and actuation dynamics [81, 82]) to applied science and technology (i.e., fabrication of optical components and displays [83, 84]).

Actuation in LCEs typically occurs under heating since a thermal gradient is required in order to induce the change in dimensions and thus movement [85]. However, the use of electric and magnetic fields, even light has also been explored to reach actuation with successful results [86]. Among them, photo-induced actuation is in particular attractive because it can be triggered by an external "remote" (i.e., wireless) stimulus allowing electro-mechanical decoupling and simplifying the arrangement, thus reducing the packaging and improving the miniaturization capabilities of the system. Moreover, provides low noise and the speed and periodicity of the stimulus can be finely controlled [69].

All these advantages of photo-actuation together with the incredible characteristics of LCE materials make the conjunct great potential candidates for the design and fabrication of a new generation of smart actuators able to provide alternative Braille-based solutions to such major need.

1.6 Summary

This thesis presents novel developments and technological contributions to the liquid-crystalline elastomer, LCE, applications field performed at both IMB-CNM (CSIC) and UAB. Particularly, this work is dedicated to the design, fabrication and characterization of smart opto-mechanical actuators based on this type of elastomeric materials to be

integrated within tactile devices and future Braille systems combining material science and microtechnology.

The work is organized in 9 chapters: the current introductory chapter and 8 experimental chapters that have been divided in four sections.

The first section (Chapters 2 and 3) is devoted to the general understanding of the fundamental properties involving LCE materials and its actuation mechanisms previous to the development of the actuators. Thus, different strategies regarding the improvement of the mechanical response of the material upon illumination have been investigated taking advantage of the incorporation of light-absorbing elements into the polymeric matrix as a way to create LCE composites. This is the case of carbon nanotubes, CNTs, which reduce the response times of the material and improve its actuation mechanisms under uniform illumination since their main advantage lies in their capability to absorb light over a wide range of wavelengths and to convert it directly into local heat.

The second section of the current thesis presents the first actuator approach regarding the integration of LCE-CNT materials into a real tactile device: the "U-shape" actuator, which is based on the stress gradient generated on an LCE-CNT film under illumination to exert a vertical force on a movable component forming the Braille dot. The design, characterization and later optimization of the actuator is presented with the ultimate goal to develop a fully functional prototype containing an array of 10 by 10 actuators; the first refreshable haptic display able to represent Braille characters and simplified graphical information based on such materials: the NOMS device. An accurate description of the whole system and its different parts and components is presented in Chapter 4 together with the operation of the device and testing.

With the main purpose of improving the actuation performance of the system and thus reducing some of the issues concerning the integration of individual LCE-CNT actuators into the device, two different strategies are followed: (i) improve the material and (ii) improve the actuators conformation.

A research on alternative photo-sensitive materials is presented in section three, with the main purpose to create novel LCE nanocomposites with similar characteristics to LCE-CNT films which allow simplifying the fabrication process of the samples and thus improving their mechanical response. To that end, two different alternatives are investigated in Chapter 5. The first approach is based on replacing CNTs by

1. INTRODUCTION

other photo-active component capable to thermally triggering the phase change in the liquid-crystalline matrix while maintaining its structure. Visible and infra-red photo-sensitive dye molecules were selected to that end. On contrary, the second approach makes use of commercially-available polymers as alternative matrices for the fabrication of CNT-based photo-active composites, in this case replacing LCEs. In this sense, ethylene-vinyl acetate copolymer, EVA, was selected for its suitable characteristics. In both cases, the first experimental results are presented as well as a comparison between them and LCE-CNT samples.

In the last section, section fourth, different fabrication strategies are explored in parallel with the work presented in previous section to obtain different actuators conformations taking advantage of the use of different molding techniques as a way to simultaneously shape and align the material in one single step. In this manner, it is possible to obtain arrays of identical actuators with a customized mechanical deformation. The first approach described in Chapter 6 lies in the combination of punch and die molding technique and the application of mechanical stretching. This method is considered as the first approach in LCE actuators development that allows obtaining shaped polydomain regions (i.e., single actuators) within a unique monodomain (i.e., in the same sample), able to be individually actuated. A second approach, presented in Chapter 7, makes use of the application of controlled gas-pressure to shape and align LCE-CNT material also using molding techniques, resulting in an improvement of the previous approach in terms of material deformation and displacement. Finally, Chapter 8 describes an alternative procedure to fabricate arrays of individual micropillars again combining mechanical pressure and molding in two steps. With this processing variation, a different orientation of the liquid crystal units is reached for the first time, allowing an expansion of the material in the preferred direction in contrast with the previous presented approaches. In this manner, pushing actuators are obtained with an increase of height under actuation. Taking advantage of the good results obtained with this last approach and the possibility to obtain directly pushing forces with large deformations, an alternative tactile device concept based on such actuators is introduced in Chapter 9, where detailed information around the concept and the first experimental results are presented.

Finally, general conclusions of this work are presented together with the ongoing work and some remarks about the future prospects.

1.7 Framework

The present work has been partially carried out within the framework of a FP7 European research Project (FP7-NMP-228916), *NOMS: Nano-Opto Mechanical Systems*. This project is very brief presented below.

The Nano-Opto-Mechanical Systems, NOMS, project (September 2009 - August 2012) had as goal to develop a refreshable tactile tablet for visually impaired people, able to represent Braille characters and simplified graphical information in a simple and faster way. The project proposed combining material science and technology to offer an unexplored solution in visual-aid technology: a tactile device based on the light-induced mechanical actuation of nanotube-enriched elastomeric materials.

The majority of the work developed in this thesis was conducted within the framework of this project and parts of the experimental results were obtained thanks to the collaborative work between the different partners; mainly the composites synthesis, the hardware and electronics development as well as the fabrication of the different actuator's components. A detailed list at the end of each chapter states the different contributions to the work. However, most part of the characterization of the materials, all the actuator designs proposed, their modeling and their experimental validation were carried out mainly at IMB-CNM facilities, since Micro & Nano tools group was the project coordinator of this research project.

A detailed list of the partners of NOMS project is presented below:

- Prof. J. Esteve, K.E. Zinoviev, C.J. Camargo, H. Campanella and E.M.Campo from Instituto de Microelectrónica de Barcelona, IMB-CNM (CSIC).
- Prof. E. M. Terentjev and Dr. J. E. Marshall from Cavendish Laboratory, University of Cambridge, UK.
- M. Vallribera, R. Malet, S. Zuffanelli, Dr. V. Soler and Dr. J. Roig from Microelectronics and Electronic Systems Department of Universitat Autònoma de Barcelona.
- F. Vossen and F.M.H. Cromptvoets from Philips Research in Eindhoven, Netherlands.
- Dr. N. Walker from Microsharp Corporation Ltd., Oxfordshire, Uk.

1. INTRODUCTION

- Prof. B. Röder and Dr. P. Bruns from the Biological Psychology and Neuropsychology Department of University of Hamburg, Germany.
- B. Mamojka and P. Teplický from Unia Nevidiacich a Slaborzrakych Slovenska (UNSS), the slovak National union of Blinds, Slovakia.
- M. Omastová and I. Krupa from Polymer Institute of the Slovak Academy of Science in Bratislava, Slovakia.
- D. Wenn from iXscient Lt., Uxbridge, Uk.

In parallel to NOMS project, collaborations with other researchers have been established to develop part of the work herein presented. Similarly, at the end of each chapter, a list of the collaborators with their contributions is detailed.

Part I

**LIQUID CRYSTALLINE
ELASTOMERS: Smart & soft
materials**

2

Introduction to LCE

This first chapter of the present thesis introduces the reader to liquid crystalline materials world: how they are organized at microscale and behave, to better understand all the later work developed for the design, fabrication and characterization of the different types of actuators proposed in this thesis. Thus, a brief summary of their main characteristics is presented without going in depth into chemical aspects, for a general understanding of the main difficulties involving the work with such interesting materials.

In the first section of the chapter, a general overview of liquid crystalline elastomers is given from their early days with few details of their internal structure and the possible configurations together with a description of their actuation concept. The second section is divided in two parts. In the first one, a brief introduction to the material preparation is given, with special emphasis on the alignment process, which is the key-step to getting the so desired mechanical response. The main LCE properties, which are in an intimate relation with the composition and the preparation process, are also described, together with some examples of the main LCE-based actuators reported until today. The actuation mechanisms, mainly the thermal actuation by direct heating of the material and the photo-induced actuation under UV light irradiation, are introduced in the second part of this section. Finally in the third section, some investigations on LCE nanocomposites are described, which allow the possibility to tailor the material characteristics to make it act under the application of wide variety of external stimulus rather than UV light or heat. From the different possibilities, LCE with embedded carbon nanotubes, LCE-CNT, are of special interest since, thanks to the

2. INTRODUCTION TO LCE

optical properties of CNTs, it is possible to obtain a photo-thermomechanical response of the material under visible light irradiation. Such composites are those that have mostly been used throughout this thesis.

All the LCE samples used to perform all the work in this thesis have been synthesized and prepared at Cavendish Laboratory facilities at University of Cambridge, UK, under the supervision of Prof. Eugene M. Terentjev, a well-known expert in this field, following the processes outlined in this chapter. The changes made to the samples preparation process to adapt the material to the fabrication of actuators will be introduced in the corresponding chapters.

2.1 General Overview

Liquid crystalline elastomers, LCE, are a relatively new class of materials that combine properties of polymers (entropy elasticity) with the self-organization nature of liquid crystals, LC, [87], which merge order (similar to a crystal) and mobility (like a viscous liquid). Since their first observation by Friedrich Reinitzer and Otto Lehmann in 1888 [88, 89] liquid crystals have been widely studied due to their varied and widespread properties attracting the attention of many chemists and physicists worldwide. However was not until the mid-70s when the Nobel Prize laureate in physics Pierre-Gilles de Gennes reported his theoretical studies about the order phenomena in LC, when these materials became hot topic within studies of soft matter [90, 91, 92].

Since then, LC have experienced an explosive growth because of their successful application in a wide variety of areas [93, 94, 95], mainly in science and engineering, playing an important role in modern technology due to their presence in most common devices, especially the information displays [96].

Among others, the most interesting property of LCE is the ability to self-organize at the molecular level into so-called mesophases; resulting in a controllable and fully reversible change of their dimensions at macroscale (shape and size) during phase transitions in response to an applied external stimuli [64]. In this manner it is possible to use the stress generated into the material to produce movement.

From material point of view LCE are such complex systems which have weakly cross-linked polymer networks containing rigid anisotropic units (so-called mesogens)

incorporated to the polymer backbone [64]. These mesogens can be organized on different configurations and mesophases throughout the polymer backbone due to the presence of various chemical spices, such as spacers and crosslinker units [97] which strongly condition the dynamics of the material [98].

A schematic representation of a typical LCE structure is depicted in Figure 2.1 where the main components can be identified. In this manner, mesogens can be connected either head-to-tail, forming polymer main-chain LCEs, MCLCEs, attached as side-chain groups to the main polymer backbone via flexible spacers, which results in side-chain LCEs, SCLCEs, or by combining both types of configurations [78, 99, 100].

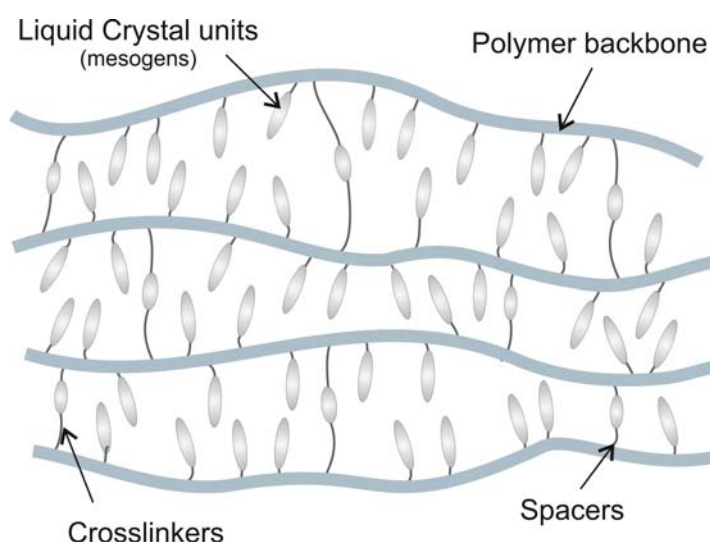


Figure 2.1: Schematic structure of a liquid crystalline elastomer with its main components.

Traditionally, there are several classifying criterion of liquid crystalline polymeric systems. Thus, they can be grouped by (i) the location of mesogenic groups along the polymer backbone (i.e., LC architecture), (ii) the types of mesophases (i.e., positional order of the mesogens) and (iii) the mesogens conformation (i.e., shape) among others. Figure 2.2 summarizes the most relevant examples of LC.

From the existing LC mesophases, the simplest one is referred to as the nematic phase. In this state, the rigid LC structures have a preferred orientation with little translational freedom, but no positional order (see Figure 2.2). Is the less ordered existing phase and, therefore, the less viscous [100]. Consequently, the mesogens alignment can be more easily manipulated than in the more ordered phases. If a LCE

2. INTRODUCTION TO LCE

contains LC units capable of adopting a nematic phase, then as long as all of such units have the same preferred orientation, parallel to a director n (i.e., the material forms a monodomain), then the transition between the nematic phase and the high temperature isotropic phase (in which the orientation of the LC units has no preferred direction -see Figure 2.2-) will cause a change in the overall dimensions of the material. Heat and the resulting thermal gradient acts by promoting entropic disorder into the LCE matrix (i.e., mesogens' misalignment), leading to a material contraction. This effect is the so-called thermo-mechanical effect.




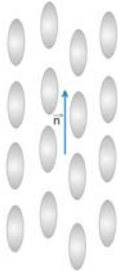
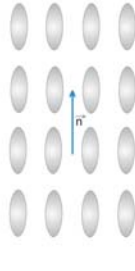
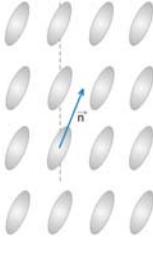





Location of mesogenic groups	Side-chain LCP (SCLCP)	Main-chain LCP (MCLCP)	SCLCP/MCLCP (combination)	
				
Mesophases	Nematic	Smectic-A	Smectic-C	Isotropic
				
Mesogens conformation	Calamitic	Discotic	Sandic	Bent-core
				

Figure 2.2: Main classification criteria of LCP. Adapted from [87, 101].

Figure 2.3 schematically represents such material transformation due to the phase change from nematic (crystal phase) to isotropic (liquid phase) state; a fully reversible process which induces an anisotropic contraction of the material; a phenomenon produced at microscale and visible at macroscale which can be exploited for the fabrication of new generations of stimuli-responsive actuators.

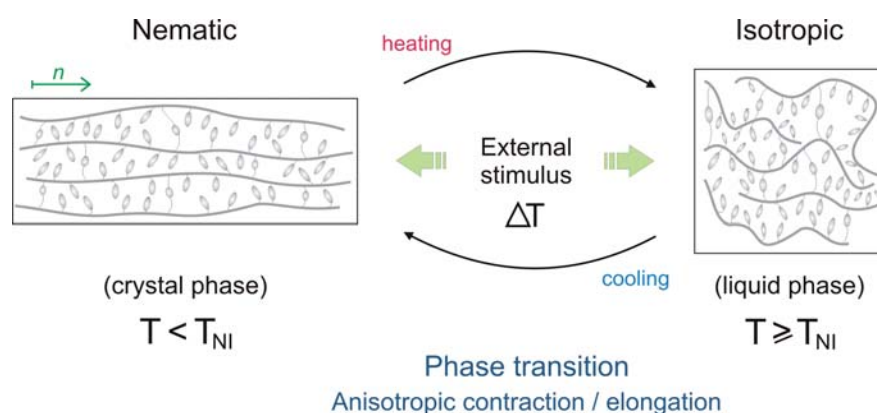


Figure 2.3: Schematic representation of the concept of actuation in liquid crystalline elastomers induced by changes on the molecular arrangement of the material at different temperatures. Adapted from [102].

2.2 Synthesis and preparation

Prior to the synthesis and preparation of the LCE, it is very important to consider the expected final characteristics of the material. Similar to mesogens, the main polymer chain (i.e., polymer backbone) can also vary, leading to different types of LCE structures with distinct characteristics and behavior, specially the temperature's working range which is defined by the glass transition, T_g , and the phase-transition, T_{NI} , temperatures, and the flexibility of the polymer backbone. LCE based on acrylates [103, 104, 105], epoxy resins [106, 107, 108] and silicones [85, 109, 110] are some reported examples.

Silicone-based polymeric matrices, of which polydimethylsiloxane ($-Si(CH_3)_2O-$) is an example, are doubtlessly one of the most commonly used polymer backbones for preparing LCEs since they have very low T_g (around $-123^\circ C$) and T_{NI} ranging from $55^\circ C$ to $90^\circ C$, leading to a large operating temperature range (from $-100^\circ C$ to $250^\circ C$) with good thermal stability and constancy of properties [100]. In addition, thanks to the silicones' flexibility, they allow to obtain deformations of the whole sample (contraction and expansion movements) with relatively high actuation forces and present photo-actuation even at room temperature; very suitable and valuable characteristics for the fabrication of actuators. For these reasons, siloxane-based LCEs were chosen to perform the work in this thesis.

Figure 2.4 illustrates as example one of the chemical compositions for a polysiloxane SCLCE system used within this work. In this case, the polymer backbone consists of

2. INTRODUCTION TO LCE

polymethylhydrosiloxane, PMHS; a flexible siloxane chain containing reacting Si-H units. Rigid rod-like LC mesogens (MBB) and cross-linking units (11UB) were added in 1:9 ratio respectively to form the final LCE material.

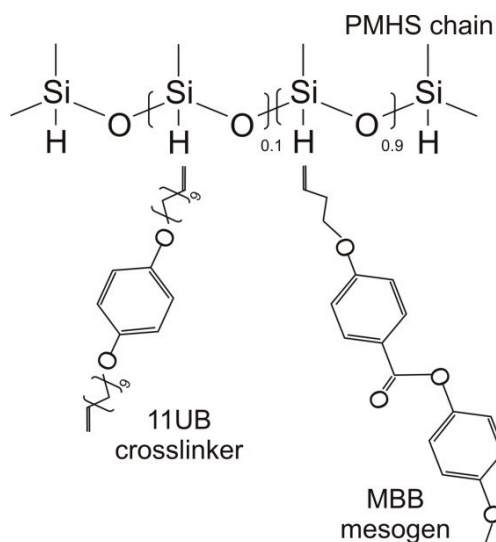


Figure 2.4: Scheme of the typical molecular structure of a polysiloxane SCLCE system used within this thesis.

2.2.1 LCE alignment

Although liquid crystals self-assemble at the molecular level into nematic or smectic phases (see Figure 2.2), their director does not align uniformly throughout the sample in a spontaneous way. Hence, the mesogens are randomly distributed in the elastomer network forming a so called polydomain [111]. In order to produce actuation (i.e., contraction or expansion movement) under the application of an external stimulus, however, it is strictly necessary for the system (the mesogens and thus the polymer chains) to be macroscopically aligned along one preferred direction forming a monodomain. To achieve an overall orientation therefore such process must be undertaken before the material is crosslinked (i.e., completely cured) by means of the application of external alignment forces. This is the key-step in preparing LCE-based actuators.

Several techniques have been reported so far for this purpose. Hence, soft-molding techniques [112], ink-jet-printing [113], microfluidics [114, 115] and electrospinning

processes [116], even the application of surface forces and both electric and magnetic external fields in certain direction have successfully been introduced for the manipulation of mesogens at molecular level. However in practice it is synthetically challenging to create well-aligned monodomain LCE films with the dimensions required for their use as actuators.

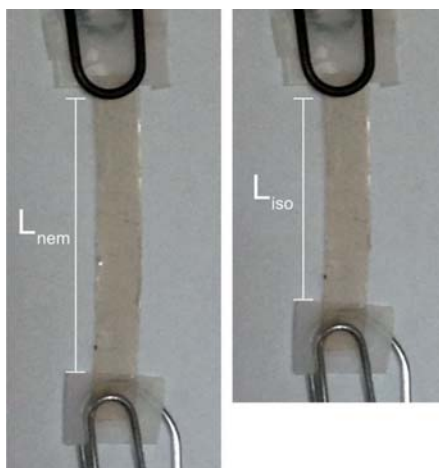


Figure 2.5: Example of the contraction phenomenon on a stretched LCE film under heating where a clear change in length can be observed.

The most popular and effective method for the preparation of monodomain polysiloxane based LCE samples results to be the two-steps synthetic methodology outlined by Küpfer and Finkelmann in 1991, which is based on the application of unidirectional mechanical stretching to produce alignment [85]. Such widely-used method starts with a polymer mixture containing LC units which is first prepared and lightly cross-linked to form a gel of a certain length, L_{nem} . This gel should be consistent enough to be mechanically stretched in one direction but not too rigid, to ensure enough mobility of the polymer chains and thus create alignment of the LC units inside the elastomer without breaking. The stretching force should be progressively applied to avoid cracks in the material, resulting in an increase in the length of the sample and its corresponding reduction in width. With the material held in a stretched state, a second crosslinking step is then carried out to fix the topology of the polymer chains and the length of the sample. After this second crosslinking stage is completed, the material is completely cured and capable of recovering its initial length, L_{iso} , (producing a contraction movement in the direction of stretching) when heated through T_{NI} , leading

2. INTRODUCTION TO LCE

to actuation proportional to the elongation applied. Contraction values ranging from 15% to 50% even higher have been reported using such procedure; values which are strongly related to the composition of the LCE material, the alignment process and the stretching force, and the actuation type [117].

An example of such unidirectional contraction is depicted in Figure 2.5 where a free-standing SCLCE film obtained by the above described stretching method was heated from nematic state at room temperature to the isotropization temperature (in this case, $T_{NI} = 85\text{ }^{\circ}\text{C}$), resulting in a reversibly contraction of 26.43 %.

Most part of the LCE material used within this thesis, especially all the film-like samples employed for the characterization of the material and the study of its main properties, have been prepared and aligned following this stretching method.

2.2.2 LCE properties and applications

As polymer-based materials LCE have many advantages compared with other types of smart materials since combine properties of the anisotropic liquid crystalline systems with typical properties of polymers. Thus, softness, flexibility, durability and light-weight are some of their characteristics [64]. Moreover, they are relatively inexpensive, easy manufacturable and implementable, fracture tolerant, pliable and biocompatible [103].

From the physico-chemical point of view, other distinguishing features of LCE systems are [98]:

- very high strength and high elastic modulus, particularly in the direction of orientation,
- relatively low viscosity,
- high chemical and fire resistance, due to their ordered and compact structure,
- low solubility and resistance to solvents,
- high temperature of vitrification/melting,
- low thermal expansion coefficient, resulting in high stability of shape and dimensional precision (processability).

Similar to the LCE ability to change in length, all these properties are closely related to the synthesis and the crosslinking procedures during the material preparation [118, 119]. Thus, aspects as the length of the spacers and its location within the polymer chains, the structure of the starting reagents, the type of mesogens, the density of crosslinking, even the curing temperature, affect the final behavior of the LCE and strongly determine their mechanical properties [97, 98, 120, 121]. Moreover, such properties can be easily modulated by applying external perturbations such as light, temperature, electro-magnetic fields, changes of solvent or pH, and so on, which also induce changes in the molecular and supramolecular organization of such systems. This feature is the basis of all their further applications [122, 123].

Because of these special properties, liquid crystal technology has a major effect on many areas of science and engineering, as well as device technology offering an alternative towards piezoelectrics, hydrogels, and many other polymeric systems [77]. The most common and successful application of LC technology is LC displays, LCD, [83, 124] that can be found in most of TV, computers and electronic equipment and which have cast plasma technology aside due to its excellent optical characteristics. Other elements such as polarizers [125] and optical fibers [84] for integrated optics are also being proposed.

However, from the actuators' design point of view, the most interesting properties are the ones involving the mechanical actuation (i.e., contraction phenomenon), which are gaining interests in the last few years. A proof of that is the fact that many reviews have been appeared so far that state from different perspectives the increasing efforts for the fabrication of mechanical LCE actuators based on strain [87, 103, 111, 126]. One of the first applications proposed by de Gennes in the early seventies was the use of LCE films as artificial muscles in robotics [79, 80], which later has been extended to the fabrication of actuators for manipulating micro-objects [127].

2.2.3 LCE integration in MEMS/NEMS

From the different existing possibilities, the most attractive from the engineering point of view is the integration of LCE materials into the well-known silicon-based technologies, and thus fabricate hybrid micro- and nano-electromechanical systems, MEMS and NEMS, with novel and interesting properties, able to use the reversible

2. INTRODUCTION TO LCE

and well-controlled contraction movement of LCE under the application of different types of external stimulus to induce work without needing any electric connections and complex setups.

In the last five years, some efforts have been performed in this direction and some examples of such integration can be found in the literature, which include microvalves for microfluidics [128, 129], tweezers and grippers [130] even motors [131] (see Figure 2.6); most of them based on the integration of the LCE material into the device once both elements (the device and the elastomer material) have already been fabricated; fact that limits the shape and the type of movement achieved.

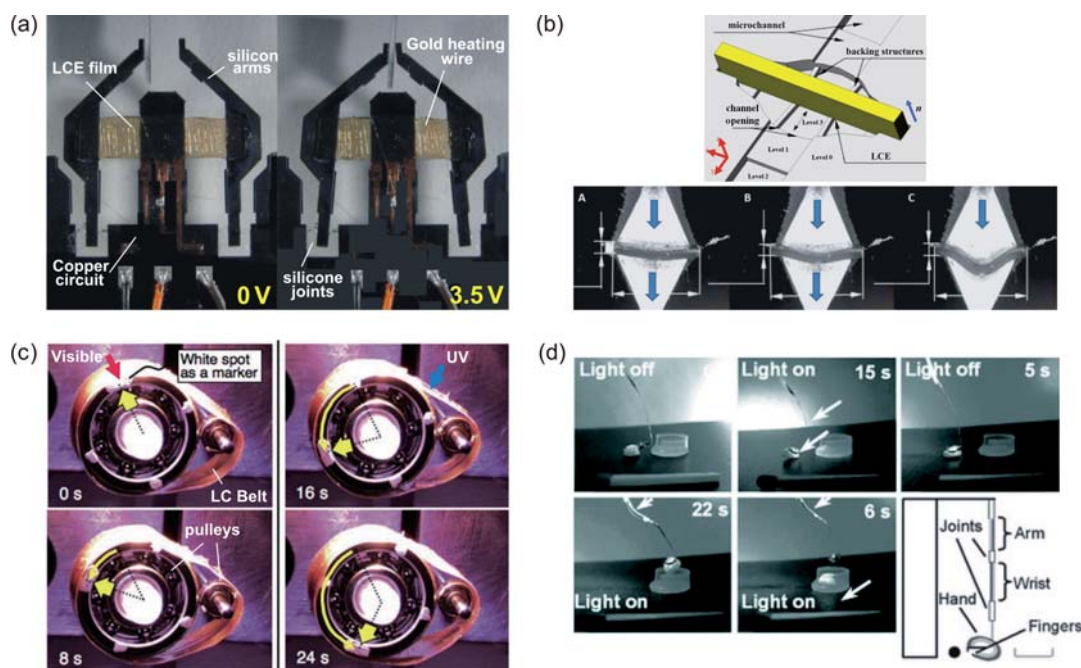


Figure 2.6: LCE actuators. (a) A microgripper closes its arms under the application of a controlled thermal actuation induced by electrical power. Reprinted with permission from Ref. [130]. Copyright 2009, Wiley-VCH. (b) A flow-regulating microvalve which seals and opens the chamber of the microfluidic chip under the application of temperature gradients. Reprinted with permission from Ref. [128]. Copyright 2011, Wiley-VCH. (c) A plastic motor propelled by bending and unbending movement produced by simultaneous irradiation with UV and visible light. Reprinted and adapted with permission from Ref. [131]. Copyright 2008, Wiley-VCH. (d) A robotic arm able to pick, lift, move and place an object using visible light. Reprinted with permission from Ref. [127]. Copyright 2010, The Royal Society of Chemistry.

The “in-situ” integration of LCE materials into MEMS devices (prior to the fabrication of the microsystem) is still a challenge for several aspects. On one hand, most of the silicon processing techniques used for the fabrication of MEMS, such as etching and patterning techniques, deposition and growth of layers, etc. [132, 133] require high working temperatures (hundreds of degrees) with different atmospheric conditions and the use of aggressive chemical agents, such as potassium hydroxide, KOH, tetramethylammonium hydroxide, TMAH, and hydrofluoric acid, HF, which can damage LCE material. On the other hand, the preparation of LCE samples, which require the formation of a monodomain (mesogens alignment and orientation in a preferred direction) in order to produce actuation; processes that should be realized prior to the final crosslinking of the material and which simultaneously fix the final shape of the samples.

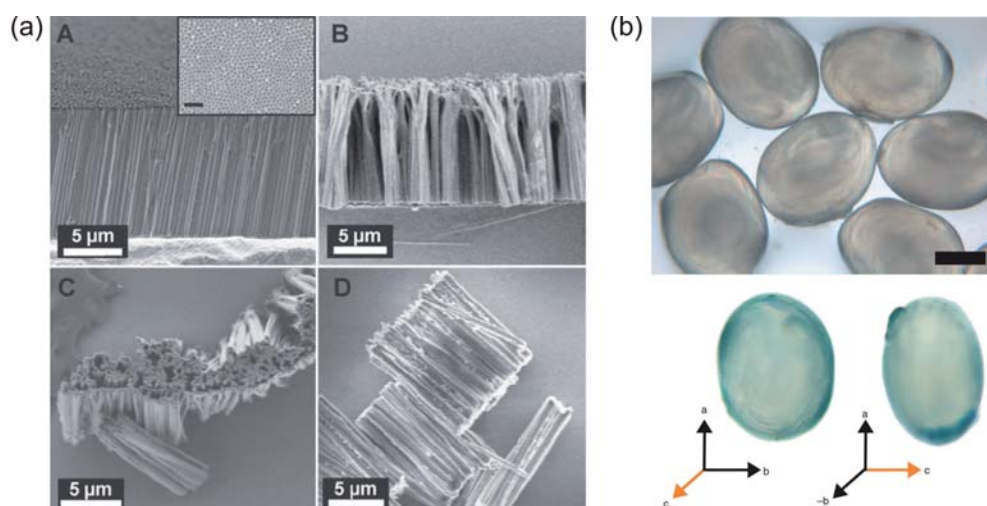


Figure 2.7: LCE and nanotechnology. (a) Aligned LCE nanowires obtained by the use of anodized aluminum oxide as a template. Reprinted with permission from Ref. [134]. Copyright 2011, Wiley-VCH. (b) Ellipsoidal-shaped core-shell LCE microparticles obtained using microfluidics. Scale bar = 200 μm . Reprinted with permission from Ref. [135]. Copyright 2012, Nature Publishing Group.

These requisites strongly affect the integration of the LCEs in microsystems. However, the first attempts in this direction have recently been reported [136, 137, 138].

Some groups have gone a step further and have already reported few original methods of producing aligned LCE, thus moving the actuation phenomenon to the nanoscale. Various types of particles [115, 135, 139] and nanowires [140, 141] using

2. INTRODUCTION TO LCE

both microfluidic systems and molding techniques are examples. Figure 2.7 depicts two of them.

With the main purpose of the fabrication of opto-mechanical actuators for tactile applications and using the knowledge acquired on microfabrication and processing, four innovative methods for integrating LCE materials with microtechnology based on different techniques are successfully developed and presented in this dissertation (see last section, Chapters 6 to 9), which have significantly contributed to enlarge this list.

2.3 Actuation Mechanisms

2.3.1 Thermal actuation: direct heating

As already mentioned, to promote the phase change between nematic and isotropic states and thus induce changes in sample's topology, an increase of temperature should be applied to ensure reaching T_{NI} [85]. In this sense, thermal actuation by direct heating is the simplest way to produce such effect [64, 110, 118, 142, 143].

A common thermoelastic experiment consists in the measurement of the length variation in a free-standing LCE sample as function of temperature on reaching the thermal equilibrium [82, 85] (see example of LCE contraction depicted in Figure 2.5). From the dimensions of the sample at each temperature, one can evaluate its changes in length or, in other words, the uniaxial thermal expansion (cooling) or uniaxial thermal contraction (heating) coefficient of the material, which is defined as:

$$\lambda = \frac{L}{L_{iso}} = 1 + \frac{\Delta L}{L_{iso}}$$

where L denotes the current length of the sample and L_{iso} its length when completely contracted. Such values can be, then, plotted to evaluate the evolution of the uniaxial thermal expansion rate of the material as function of temperature. An example is depicted in Figure 2.8, where a polysiloxane nematic SCLCE film was used.

As shown, on increasing temperature from nematic phase, the sample contracts progressively. However, when temperature is close to T_{NI} (approximately 5 to 10 °C below), an abrupt change in the slope of the curve is produced (inflexion point), reaching quickly the thermal equilibrium at isotropic phase [97]. At this moment, the

sample movement stops. This concept of losing anisotropy can be correlated with the increase of disorder in the LCE structure. Thus, both spontaneous deformation and order parameter variation can simultaneously be measured, demonstrating their close relationship [64, 110].

Normally this change of dimensions is measured along the alignment direction of the material (the longitudinal direction in the case of the samples used in this thesis), where the biggest change occurs. However, changes in the other two directions of the sample (width and thickness) are also produced to a lesser extent, due to the nature of the material, which is considered nearly incompressible (details of such behavior can be found in the next chapter, Chapter 3). Changes in length and width of the material can be observed in the insets of Figure 2.8.

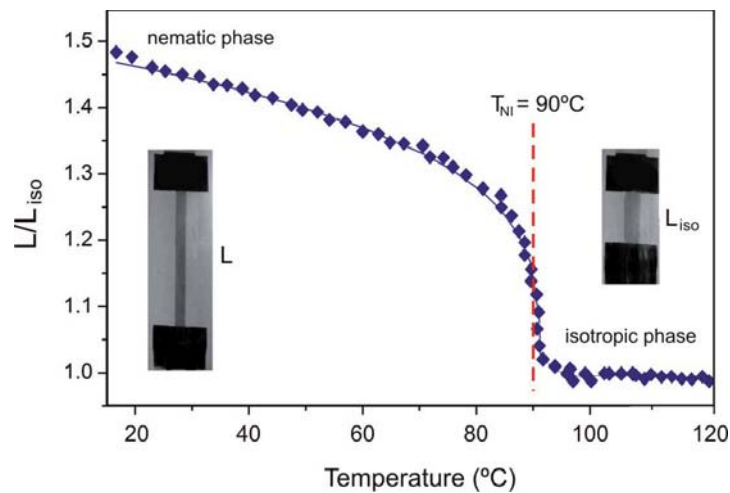


Figure 2.8: Thermoelastic experiment. Evolution of the uniaxial thermal expansion, λ , as function of temperature for a nematic SCLCE. The isotropization temperature was identified around 90 °C.

Thermomechanical experiments can also be performed through which is possible to measure the force response of LCE films and subsequently convert it to stress *via* division by the cross-sectional area of the film, which is considered almost constant along the sample. In this manner, one can get approximately the stress generated inside the LCE due to the increase of disorder upon heating with time, and thus relate such stress gradient with temperature [64]. A typical thermomechanical experiment for the same LCE film in Figure 2.8 is plotted in Figure 2.9, where the evolution of the induced

2. INTRODUCTION TO LCE

stress during one heating-cooling cycle is depicted as function of temperature and time. Similar to the previous experiment, on increasing the temperature the internal stress created in the elastomer grows until the thermal equilibrium is reached. In that point, the curve describes a plateau which corresponds to the maximum thermomechanical response produced by the film (isotropic state). When the thermal actuation is ceased, then the process is reverted leading to a passive relaxation of the film; the stress starts to diminish with time until the initial stress value and thus the length of the film are recovered.

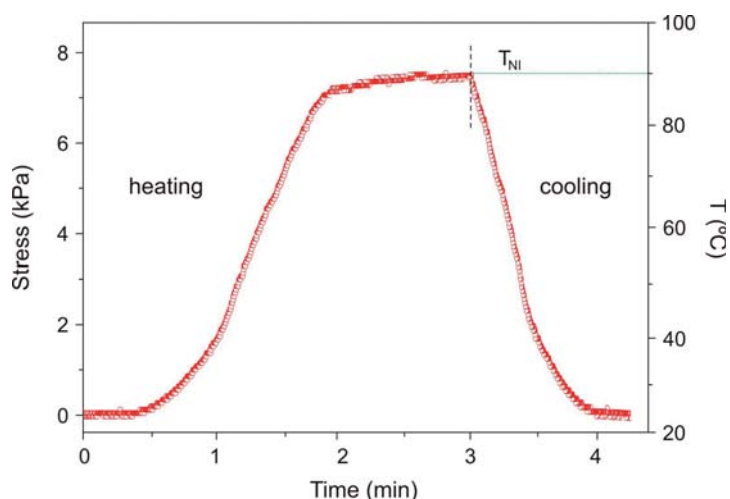


Figure 2.9: Stress evolution inside a nematic SCLCE film as function of temperature and time for one heating-cooling cycle.

It is worth noting that the actuation time, which is the time to reach the maximum contraction (i.e., the maximum stress), is quite high (in the order of minutes). Although thermal actuation is a robust mechanism and the most-common stimulus exploited to date to trigger these shape changes in LCE films, is not ideal for applications in which this material is to be used as an actuator, since its response in time is too slow. Moreover, it is difficult to create a localized and homogeneous thermal stimulus in the whole sample that can be applied remotely and rapidly tuned. For these reasons, different alternatives have been reported to induce actuation through a wide variety of external stimulus other than heat: e.g., light [144, 145], magnetic and electric fields, [146, 147, 148] even % of humidity of the surrounding air and the polarity of a solvent [149]. Among all of them, photo-induced actuation is of particular interest.

2.3.2 Photo-induced actuation

Photo-induced actuation in LCE is probably the most attractive actuation type since it allows for direct, remote and punctual wireless manipulation of the material, with well controllable speed and actuation energy. Moreover, it is a clean, cheap and an environmentally friendly energy source. It was first established by Finkelmann *et al.* in 2001 [150] and it has been deeply investigated during the last decade from both the theoretical and the experimental points of view. Photo-induced actuation of LCE is based on some, or all of the mesogenic groups having the ability to photo-isomerize (i.e., to change their arrangement). Several chromophores are known in photochemistry: spiropyranes, diarylethenes, fulgides, stilbenes, viologens, etc. [100]. However, the most widely-studied example of this behavior is that of azobenzene derivatives, which change their structure from the rod-like (trans) isomer (which forms LC phases) to the 'bent' (cis) isomer (which does not show LC behavior) upon the absorption of a photon [151, 152, 153]. The switch between trans and cis isomers, which is also reversible, has demonstrated to also trigger a phase change in LC materials and a resulting overall change in their bulk dimensions [154, 155, 156, 157]; a change in much the same way that a temperature change does, by disrupting the macroscopic orientational order in the material [81, 158].

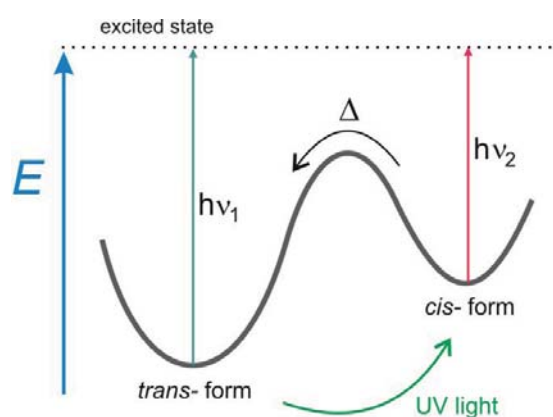


Figure 2.10: Photochromism of azobenzene and energetic profile for its trans-to-cis and cis-to-trans isomerization processes. Adapted from [100].

However, such change is produced only when the system is irradiated with light of particular wavelengths: UV light ($h\nu_1$), for the trans-to-cis conversion, and visible light ($h\nu_2$), for the cis-to-trans isomerization [159] are the most common ones. A schematic

2. INTRODUCTION TO LCE

representation of both trans and cis forms and the energy necessary for its conversion is depicted in Figure 2.10.

Similar to direct heating, photomechanical experiments (equally named optomechanical) can also be performed to measure the stress generated inside the LCE film as function of time upon irradiation. Figure 2.11 shows a typical actuation curve corresponding to one "on-off" actuation cycle, where the stress evolution in time can be observed. On turning the light on, in this case UV light, the internal stress in the elastomer grows until reaching the equilibrium in the isotropic phase (cis form), point where the curve describes again a plateau. When switching off the light, the thermal back cis-to-trans isomerization of the azo-molecule occurs and the stress starts to decrease until reaching again the initial value.

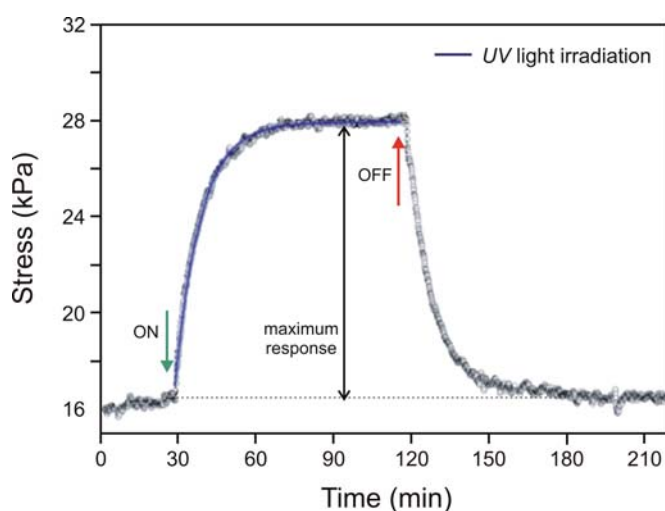


Figure 2.11: Stress evolution inside a LCE film upon UV light irradiation.

Compared to the thermomechanical experiments above described, the shape of the actuation curves are pretty similar. However, in this case the actuation times are higher; samples take several minutes, even hours to reach the maximum contraction depending on the characteristics of the light source and the chemistry used. Such increase on the actuation time can be explained by the mechanism itself to induce the phase change upon irradiation, since the mesogens start rearranging their topology to the 'bent' cis forms one at a time and gradually propagate such effect to the neighboring molecules, similar to the domino effect. A uniform and homogeneously distributed illumination along the sample can help to accelerate this process.

Although during last decades many efforts have been dedicated to improve both preparation and properties modulation to enhance the mechanical efficiency and optimize the response time of such systems, they are still not ideal for practical applications [81]. Moreover, it is known that a prolonged exposition to UV light may cause material degradation and therefore a reduction in its utility life.

In the context of this thesis in which a very specific tactile application is defined, several considerations of safety from end-users' point of view should be taken into account for the selection of the material and its characteristics. In this sense, UV photoactuation was dismissed to be a wavelength (usually between 300 to 400 nm) out of the safety range of the human eye, which is defined by the visible spectrum. However, aspects such as portability, lightness and wireless control, make photo-induced actuation the most suitable one for the purpose of this thesis. Thus, with the main purpose of improving the actuation parameters while maintaining the contraction movement, innovative solutions should be adopted.

2.4 LCE nanocomposites

A great advantage from polymers and elastomers is that they can be arranged into almost any conceivable configuration and their properties can be tailored to achieve a broad range of requirements [65]. Their high adaptability and their 'tunability' allow a wide variety of combinations (with other polymers as well as other types of materials) to create custom-made nanocomposites that can be tailored to the applications for which they are intended. Hence it is possible to improve the actuation parameters of LCE and thus be able to produce movement in response of different types of stimuli rather than heat or UV light. In this sense, several types of LCE composites have been reported up to now as efficient mechanisms to induce actuation [160]. For instance, LCE composites with embedded electrically and magnetically active nanoparticles such as MoO_{3-x} nanowires [161] and superparamagnetic iron oxide particles [148, 162, 163, 164] have been proposed, as well as carbon particles [81, 165] and azobenzene-based dye molecules [151] among others.

From the point of view of final actuators and leaving aside the material characteristics, there are two key parameters standing out above the others. Those are the maximum mechanical response they are able to generate as well as the time

2. INTRODUCTION TO LCE

required to produce it, and the time to recover the initial state. In this sense, LCE with embedded ferromagnetic nanoparticles resulted attractive, since they have a robust mechanical response and relatively short actuation times [147, 148]. However they require higher levels of energy to generate movement. Thus, to obtain similar actuation times and forces than direct heating, voltages from 1.5 MV/m to 25 MV/m and frequencies in the range of 240 kHz to 3 MHz are often used, since a magnetic field with higher strength provides more energy and therefore a larger temperature increase. These actions, however, involve complex setup configurations and higher power consumptions, nowadays resulting in a low efficient mechanism impractical for the fabrication of portable devices.

Again, photoactuation turns out to be the most attractive option.

2.4.1 LCE-CNT composites

To improve the actuation parameters together with make the LCE material responsive to the broad-spectrum light (visible to infra-red, IR), a light-absorbing component must be incorporated into the material. A clear example of that are the carbon nanotubes, CNTs, which have the ability to absorb photons over a wide range of wavelengths and convert it directly into heat [166]. Thus, a fast local way of heating LCE matrix was proposed to induce movement [81, 167, 168]. CNTs also have high thermal conductivity along their main axis, which can also help with heat transport through the material, decreasing the response time and potentially improving the material properties of the composite [169], that retains the structure of the LC matrix and acquires a mechanical response under illumination [170, 171]. Thus, actuation times can be reduced and the material can be actuated in the visible range (safety for the human eye). Because of the characteristics of CNTs, the LCE-CNT composites can actuate well below T_{NI} transition temperature, fact that make CNTs even more attractive than other types of nanoparticles for applications where high temperatures are undesirable. This is the case of tactile devices.

In spite of their previous appearance in different scientific reports, it was not until 1991 when Sumio Iijima brought CNTs into the awareness of the scientific community as a whole [172] publishing its studies about their elastic response to visible light, one of the earliest reports on photomechanical actuation on CNTs [173]. Since then,

CNTs have attracted much interest due to their interesting characteristics and are being applied in research fields as diverse as biology, medicine and microelectronics among others. In the last years, several studies have been carried out to better understand the chemistry around LCEs and physics involved in their photo-induced actuation [170, 174, 175], as well as the dynamic effects due to the incorporation of CNTs inside the elastomeric matrix [81], obtaining encouraging results for this revolutionary new phenomenon.

Table 2.1 summarizes the main characteristics involving LCE-CNT composites actuation in comparison with both thermal and photo-induced actuation mechanisms above described. As reflecting the publication dates of the related works, the development of LCE nanocomposites (in this particular case, LCE-CNT) and the study of their properties as actuating materials have been contemporary of the elaboration of this thesis and are still ongoing, leading to a wide leeway for improvement.

The inclusion of CNTs is, however, a critical challenge in the preparation of monodomain samples: CNTs cannot be well-dispersed within the polymeric matrix by simple mixing because as nanostructured solid elements, they tend to form aggregates. Thus, the proper CNTs dispersion is one of the most common issues reported. A non-appropriate mixture will form an inhomogeneous material (i.e., a non-continue matrix) which will have a strong effect on the properties of the final composite, resulting in bad actuation [168] even damage. A poor dispersion of CNTs and, in general, nanoparticles within the elastomeric matrix can result in inferior mechanical response and a deficient actuation performance since can disrupt the underlying LC order [160]. Moreover, parameters such as LCEs' chemical composition, the preparation procedures, the alignment quality and so on, can also affect the photoactuation achieved by CNT-LCE composites [160]. For this reason it is very important to develop an accurate procedure for the composite preparation. Methods such as shear-mixing and ultrasonication have been successfully employed to break apart CNTs clusters [176, 177, 178] and different types of dispersing agents have recently been added to prevent the CNTs form re-aggregates once mixed [179, 180].

2. INTRODUCTION TO LCE

Table 2.1: Comparison of the main actuation characteristics between LCE-CNT composites and both thermal and photo-induced mechanisms.

LCE material	Actuation type	Main characteristics	References
Pure LCE	Thermal actuation	Changes in the whole LCE's backbone structure (entropy variations) due to direct heating.	Küpfer <i>et al.</i> 1991 [85]
		Bulk phenomenon.	Finkelmann <i>et al.</i> 2001 [82]
		- ↑↑ contraction ratio	Thomsen <i>et al.</i> 2001 [143]
		- ↑↑ stress (actuation force)	Tajbakhsh <i>et al.</i> 2001 [110]
		- ↑ efficiency	
		- ↑↑ actuation times (minutes)	
LCE + photochromic molecules	Photo-induced actuation (optomechanical response)	Direct conversion of light into mechanical energy (molecular rearrangement) due to photochemical phase transition of the material.	Finkelmann <i>et al.</i> 2001 [150]
		Surface level phenomenon (limited to thin films due to the rigidity of the polymer chains).	Hogan <i>et al.</i> 2002 [167]
			Yu <i>et al.</i> 2003 [152]
		- ↑ contraction ratio	Camacho <i>et al.</i> 2004[144]
		- ↑ stress (actuation force)	van Oosten <i>et al.</i> 2008 [157]
		- ↓ efficiency	Yager <i>et al.</i> 2009 [155]
		- ↑ actuation times (seconds to several minutes)	
LCE-CNT nanocomposites	Opto-thermomechanical actuation	Conversion of absorbed light into local heat due to CNTs presence.	
		Deeper actuation in the material but not as in bulk.	Torras <i>et al.</i> 2011 [171]
		- ↑↑ contraction ratio	Torras <i>et al.</i> 2011 [170]
		- ↑↑ stress (actuation force)	Marshall <i>et al.</i> 2012 [81]
		- ↑ efficiency (better than photo-induced actuation but still low)	Li <i>et al.</i> 2012 [168]
		- ↓↓ actuation times (few seconds to a minute)	

2.4.1.1 LCE-CNT preparation

The monodomain LCE-CNT samples used in most parts of this thesis were prepared at Cavendish laboratory facilities at University of Cambridge using the above described

mechanical stretching procedure (see section 2.2.1) outlined by Küpfer and Finkelmann in 1991 [85] since it has been demonstrated that anisotropic particles embedded in such rubbery elastic medium experience a similar alignment effect during stretching, choosing the same preferred orientation than the LCE mesogens [97]. Hence, the same PMHS SCLCE matrix containing MBB mesogens (90 %) and 11UB crosslinker (10 %) described in Figure 2.4 can still be used. However, a new step should be added before the first crosslinking for the preparation of LCE-CNT samples.

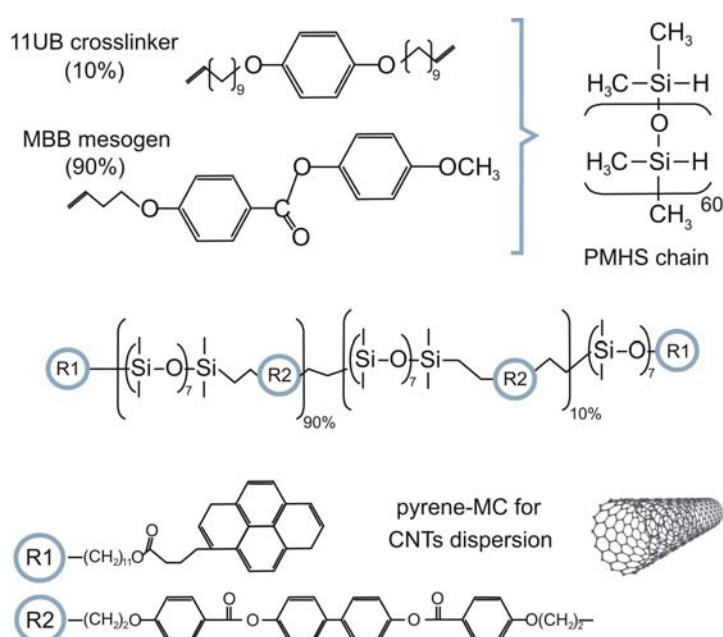


Figure 2.12: Scheme showing the components used to create LCE-CNT samples. MBB reacting mesogens (90 %) together with 11UB crosslinker (10 %) were attached to the PMHS chain. CNTs/pyrene-MC suspension dissolved in toluene was added to the mixture to create the final composite.

In order to facilitate the dispersion of CNTs within the elastomeric matrix and thus avoid the formation of aggregates while maintaining the mechanical and elastic properties of the material, a combination of ultrasonication and dispersing agents was chosen. Once the initial LCE mixture is ready (PMHS matrix together with the correspondent crosslinker and the MBB mesogens content), certain weight fraction of CNTs dispersed in toluene is added to a second polymer (which is compatible with the previous mentioned matrix) consisting of a main-chain LC polymer with an end-capping pyrene group (PyMC), and later to the rest of the components in

2. INTRODUCTION TO LCE

a centrifuge. Such PyMC polymer was synthesized at home using the procedure described elsewhere [179]. A schematic representation in Figure 2.12 depicts the main chemicals used.

Finally, the mixture is ultrasonicated to obtain a homogeneous material [181] until reaching the consistency of a weakly cross-linked gel (first crosslinking). Once at this stage, the process can continue with the alignment of the material by stretching, where the final shape and size of the samples is fixed (second crosslinking). In this moment the samples are ready to be actuated. Figure 2.13 show a scheme of such process. Details of the synthetic procedure and the sample's processing can be found in [179].

Concerning to weight fraction of CNTs embedded into the LCE samples, there is no an established value in literature since it depends on several factors as the type of CNTs, the dispersion method employed, the chemicals used, etc. However concentrations from 1.0 wt.% can induce stiffening of the structure thus reducing the overall L/L_{iso} ratio [179].

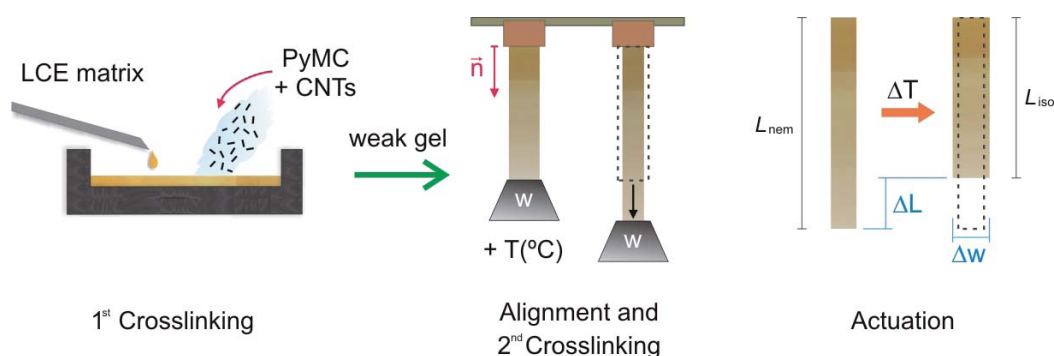


Figure 2.13: Schematic representation of the samples fabrication process.

The CNTs content of the LCE samples used in this thesis was variable, as function of the samples' utility. Thus, to check the material conformation (dispersion and alignment of CNTs within the LCE matrix), samples with higher content of CNTs were chosen to ensure ease observation by means of electron microscopy techniques, whereas for the optomechanical characterization and the measurement of the main material properties, samples with lower content of CNTs were used (below 0.5 wt.%). In all cases, multiwalled CNTs (MWCNTs) of diameters ranging between 30 nm to 50 nm were used.

2.5 Discussion and summary

In this first chapter, a general overview to liquid crystalline elastomers has been presented with the main objective to introduce the reader the main characteristics involving the actuation phenomenon of such interesting materials, to better understand how they behave and the so important relationship between the process for samples preparation and their subsequent mechanical response under the application of heat. Thanks to this attractive behavior, LCE have been proposed from their early stages for the fabrication of actuators, especially as artificial muscles in robotics.

Because of their nature, which combine the entropic elasticity from of polymers with the self-organization of liquid crystal structures, LCE have a wide variety of properties, which can be tuned on demand to create novel custom-made composites able to respond to various external stimuli. This is the case of the LCE-CNT materials outlined in this chapter; novel composites capable of producing mechanical actuation under the application of light within the broad-band visible-IR without producing changes in the overall actuation mechanisms of the elastomeric matrix, thanks to the particular optical properties of CNTs. Thus, such attractive characteristics together with relatively high contractions and lower actuation times compared to other LCE types make LCE-CNT to be pushed as candidates for the fabrication of smart opto-mechanical actuators.

In the following chapter, Chapter 3, LCE-CNT composites are characterized and analyzed in depth to better comprehend their behavior and actuation mechanism prior to the design, fabrication and characterization of the different actuators reported in this thesis. Only a deep understanding of the material can help to achieve its successful integration into different technological processes. Later, the main results of a parallel research on alternative photo-sensitive composites are presented, with the main objective to improve the LCE-CNT material performance.

2. INTRODUCTION TO LCE

3

LCE-CNT films characterization

This chapter summarizes the main characterization results obtained for LCE-CNT composites containing different CNT concentrations with the purpose of general understanding the fundamentals involving their contraction phenomenon and thus, their mechanical actuation when illuminated, with the final objective to facilitate the design of future photo-actuators based on such materials. To that end, different characterization techniques ranging from conventional optical microscopy to X-ray diffraction have been explored combined with innovative setups for an "in-situ" observation and recording of the contraction phenomena.

Thus, the following chapter is divided in three sections. In the first one, a fundamental study using scanning and transmission electron microscopies is presented to check the quality of the CNTs dispersion within the LCE matrix and to evaluate their alignment. X-ray and calorimetry analyses are also performed to complete the characterization of the material conformation and to determine the effects on the elastomeric matrix behavior due to the presence of CNTs. In the second section, the main parameters involving LCE-CNT composites actuation are evaluated. Thanks to the "in-situ" observation of the photo-actuation through different setup configurations, parameters such as Young and Poisson's coefficients, the optical absorption spectra and stress induced by contraction of the material, among others can be analyzed. Finally, in the last section, some finite element modeling investigations are presented with the main purpose to build a first empirical 3D model describing the material deformation under actuation which will serve as a bridge between basic

3. LCE-CNT FILMS CHARACTERIZATION

elastomeric physics and device engineering and design, taking advantage of the previous experimental results obtained.

3.1 Material conformation characterization

Before starting with the photo-actuation characterization of the samples, some studies were performed to evaluate the internal conformation of the LCE-CNT material mainly to i) check the quality of the CNTs dispersion within the polymer matrix (evaluation of their alignment), and ii) to determine the effects on the elastomeric matrix behavior due to the presence of CNTs. Scanning and transmission electron microscopies, SEM and TEM, as well as X-ray diffraction and calorimetry tests were the selected techniques.

3.1.1 Microscopy analysis

With the main objective to check the quality of the CNTs dispersion within the LCE matrix and evaluate their alignment, both SEM and TEM microscopies were used to be very common characterization techniques in materials science to see small objects in finer detail allowing high contrast and resolution [182]. Thus combining these two inspection methods, a complete mapping at both surface and inner levels of the samples was obtained.

Electron microscopy of polymer nanocomposites, however, comes with difficulties in determining both imaging and sample preparation conditions that preserve the integrity of the matrix while offering enough contrast from the nanoelements in it, since polymers are known to degrade under electron beam irradiation due to both charging and thermal effects [183]. For this reason, different strategies were followed.

Both SEM and TEM microscopes used in this section are located at microscopy service facilities of Universitat Autònoma de Barcelona, UAB.

3.1.1.1 SEM characterization: CNT identification at surface level

Firstly, the examination of different LCE-CNT composites was carried out using SEM to examine the surface of the samples searching for CNT presence (surface inspection), since this type of microscopy technique is very useful to obtain valuable information about morphology, surface topology and composition of the inspected samples.

3.1 Material conformation characterization

In preliminary measurements using conventional SEM equipment [184] some LCE-CNT composites were inspected with a carbon coating to reduce undesired effects due to electron beam interaction. A through-the-lens detector was used to capture mostly secondary electrons, SE, emissions. In spite of micrographs obtained revealed a significantly different contrast from their uncoated counterparts, a remarkable absence of surface-laying CNTs was observed mainly because of the coating. To solve these problems, a different type of SEM was chosen: a MERLIN Field Emission SEM microscope from Zeiss (Germany). This type of microscope is equipped with a fine jet nitrogen flow system for charge compensation which was specially designed for high-resolution imaging of non-conductive samples. In this manner, better micrographs were obtained without previous sample preparation reducing high contrast zones due to an elevated electron interaction.

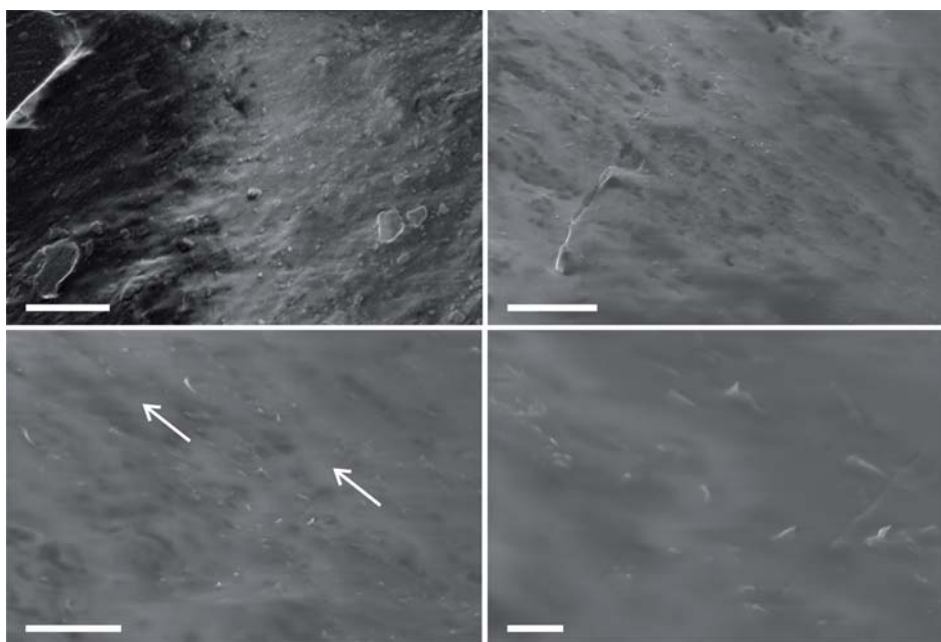


Figure 3.1: SEM micrographs of different CNT-LCE samples containing 2 wt.% of MWCNT. Scale bars are from top left to bottom right 200 μm , 10 μm , 5 μm and 1 μm respectively.

In spite it was demonstrated that concentrations below 1 wt.% do not significantly affect the actuation mechanisms of the elastomeric matrix [179], samples containing 2.0 wt.% of CNT were selected for inspection to guarantee an easy identification of

3. LCE-CNT FILMS CHARACTERIZATION

CNTs. Samples containing 0.1 wt.% and 0.3 wt.% of nanotubes were also inspected.

Figure 3.1 show some of the micrographs obtained where it is possible to distinguish the presence of CNT (high contrast elements) at different magnifications. From the images it can be guessed that CNT tend to be aligned in one preferred direction (see white arrows in Figure 3.1) as expected, disclosing good dispersion despite the large CNT load of the sample. However, further analysis with high magnification was necessary to confirm that trend.

Despite some charging artifacts, high contrast was observed from the LCE-CNT interfaces-collected by the detector resulting in significantly crisper and contrasty images and thus, proving the suitability of using this "in-situ" charge compensation system with this type elastomeric composites.

3.1.1.2 TEM characterization: CNT identification at inner level

Once demonstrated the possibility to distinguish the presence of CNT on the surface of the samples, deeper analysis was carried out by means of TEM with the main objective to distinguish the alignment patterns of the embedded CNT within the polymer matrix and thus check the alignment efficiency of the stretching process during the preparation of samples.

As it is known, TEM is a microscopy technique which enables the user to examine fine detail ultra-thin samples thanks to their interaction with the transmitted electron beam which passes through them. Hence, sample regions even as small as a single column of atoms can be observed.

Therefore, in contrast with previous SEM inspections, quite complex methods are required for preparing few nanometers-thick samples. To that end, two different well-known approaches were investigated. In both cases, monodomain SCLCE samples with 0.1 wt.% of CNT content were used. First, Focused Ion Beam, FIB, milling was used to micromachine a lamella (i.e., ultra-thin sample for TEM examination) on a 1560 XB SEM/FIB microscope from Zeiss (Germany) at clean room facilities of IMB-CNM (CSIC). The thinning protocol used were described in detail elsewhere [185], starting by depositing a platinum layer to protect the top surface of the composite from prolonged exposure to milling ions. After plucking and soldering a piece of sample to a copper grid, a combination of medium (50 pA and 30 keV) and fine milling (50 pA and 5

3.1 Material conformation characterization

keV) was applied to produce the desired lamella. Figure 3.2 shows SEM images of the sample before -left- and after the ion milling process -right-. As depicted, the thinned lamella showed heavy irradiation damage, suggesting excessive irradiation dose. Some areas in the far right edge suggested transparency and are absent of curtain effects. However, it is worth emphasizing that during milling, no apparent contrast was observed from CNTs, either from electron or ion imaging, suggesting that this lamella's preparation technique is not the most suitable one for elastomeric samples. It was then for that reason that an alternative method was used leading to more successful results for the preparation of TEM samples based on microtomy. An EM UC7 ultramicrotome from LEICA (Germany) was employed for the preparation of different lamellas with thicknesses between 60 nm and 70 nm which were cut under cryo-conditions using a diamond blade to avoid polymer matrix degradation.

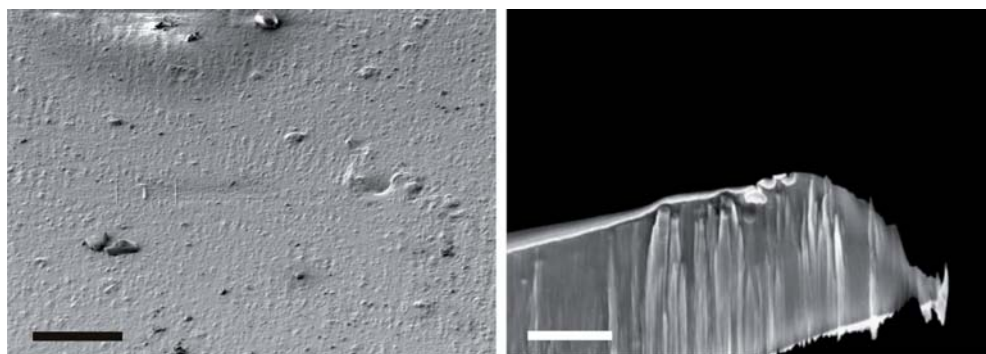


Figure 3.2: FIB milling sample preparation for TEM inspection. SEM images of the sample before -left- and after -right- the ion milling process.

Figure 3.3 shows a few TEM micrographs obtained by JEM-1400 Plus TEM from JEOL (USA) from both types of lamellas. Images in Figure 3.3a correspond to the ion milling lamella whereas images in Figure 3.3b to the one obtained by the microtome. As expected, a complex contrast was observed in the first case adding difficulties for the CNT identification. Moreover, some platinum aggregates were formed on the borders of the sample probably produced by the elastomer melting due to excess of energy. On the contrary, CNTs could be easily observed on the other type of lamellas prepared reinforcing the suitability of this protocol for TEM samples preparation. Images in Figure 3.3b also confirm the tendency of the CNTs to be oriented on the direction of alignment (see black arrow on the left image) and verifies that they were quite

3. LCE-CNT FILMS CHARACTERIZATION

well dispersed in the LCE matrix during the synthesis although small agglomerations scattered throughout the sample can be distinguished (no higher than $1\ \mu\text{m}$).

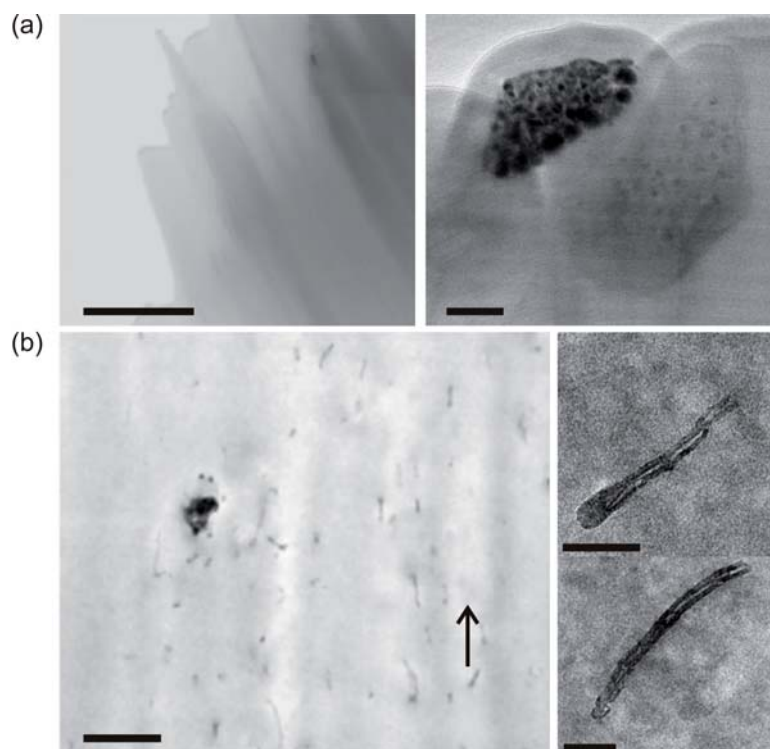


Figure 3.3: TEM micrographs of the two types of lamella: (a) FIB lamella. Scale bars: 500 nm and 50 nm. (b) Microtome lamella. General TEM micrograph -left- where the tendency of CNTs to be aligned in one direction -arrow- can be observed. Scale bar: $1\ \mu\text{m}$. Detailed TEM views of the aligned CNTs -right-. Scale bars: 100 nm.

3.1.2 X-ray diffraction analysis

Series of LCE-CNT materials were fabricated and mechanically stretched to create mono-domain films with varying the concentration of CNTs. 0.01 wt.%, 0.05 wt.% and 0.10 wt.% of content were chosen to evaluate in depth the degree of order of the CNTs embedded into the LCE matrix. In order to quantify the degree of nematic order present in the films, wide-angle X-ray diffraction measurements were carried out on a PW1830 wide-angle X-ray generator from Phillips, using $\text{Cu K}\alpha 1$ radiation ($1.54\ \text{\AA}$) at microscopy facilities of University of Cambridge, UCAM (UK).

Figure 3.4 -left- shows the correspondent 2D X-ray diffraction pattern obtained for

3.1 Material conformation characterization

the above mentioned measured samples. Two characteristic areas of high intensity can be observed in the parallel, which indicates the LC ordering in the material. It should be noted that the concentration of CNTs in these samples was too low for X-ray analysis to be affected by ordering of the CNTs; thus this characteristic intensity pattern was due entirely to the ordering of the LC mesogens in the material. 1D X-ray pattern in Figure 3.4 -right- demonstrates the change in intensity with azimuthal angle where both brighter regions of the diffraction pattern can be clearly distinguished, showing the maxima at 0°C and 180°C . These intensity changes proved to be similar for each of the different samples studied, indicating that the degree of nematic ordering was consistent across each of these samples, ensuring reproducible actuation in response to heat.

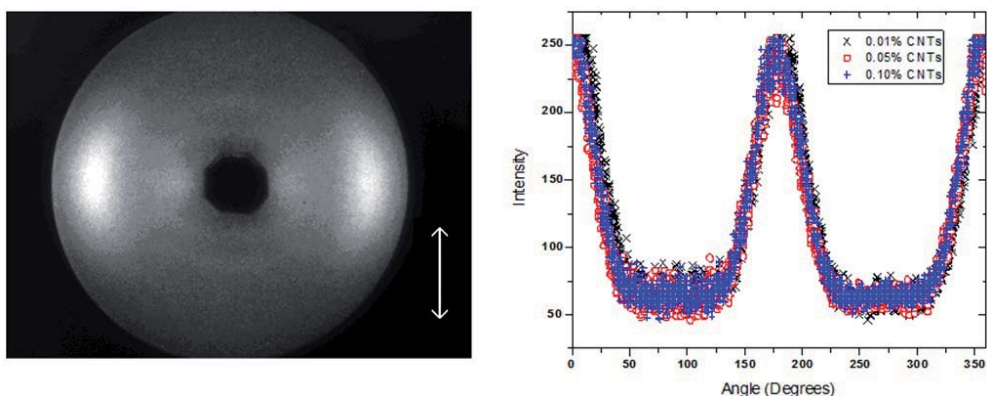


Figure 3.4: X-ray diffraction analysis. Diffraction pattern of a sample a 0.1 wt.% CNTs, where the characteristic of nematic liquid crystal ordering within the material can be observed -left-. The white arrow indicates the orientation of the LC director. The variation of X-ray intensity as function of the azimuthal angle -right- indicates good reproducibility of the liquid crystal ordering.

3.1.3 Differential Scanning Calorimetry analysis

Finally, the phase transformation behavior and the thermal characteristics of two different LCE samples (a pure LCE sample and one containing 0.3 wt.% of CNTs) were evaluated by Differential Scanning Calorimetry, DSC, measurements performed at UCAM facilities. Hence, a DSC-7 Perkin Elmer differential scanning calorimeter was used laying down a heating/cooling rate of $dT/dt = 10\text{Kmin}^{-1}$. The graph in Figure 3.5 show the main results obtained.

3. LCE-CNT FILMS CHARACTERIZATION

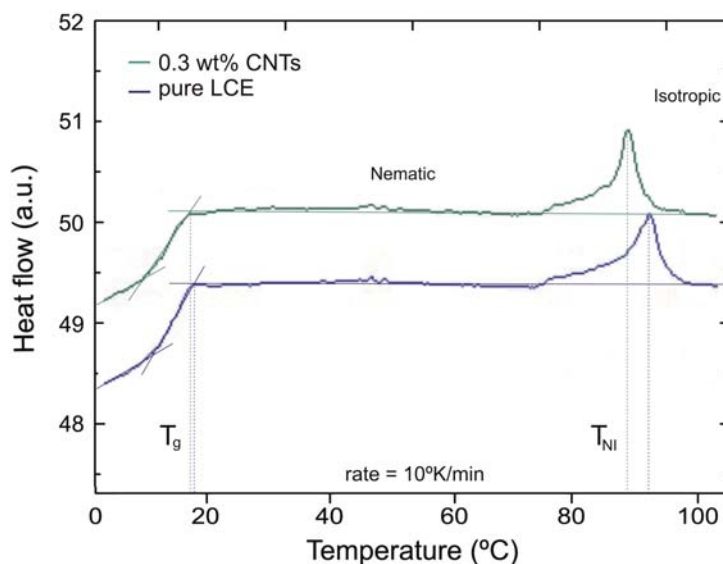


Figure 3.5: DSC data for two samples containing 0 wt.% (pure LCE) and 0.3 wt.% of CNTs. The operating range of this actuator is between the glass transition, T_g , at approximately 15 °C, and the isotropic phase, T_{NI} , which can be identified at 90 °C.

The DSC traces indicate that the T_g for both of these materials is similar, at approximately 15 °C, and that the T_{NI} can be identified at approximately 90 °C. These materials therefore have similar operating temperature ranges; however, a small decrease in the clearing temperature can be observed. The presence of highly anisotropic CNT segments along the LCE matrix introduced some disorder into the LCE matrix, as it was previously demonstrated by Marshall et. al [81].

3.2 Material actuation

After the first studies about the material conformation, the following characterization tests were focused to obtain the basic macroscale properties of the LCE-CNT elastomers under photo-actuation, starting from some of the previously published studies for the characterization of pure LCE samples [64, 109, 110, 143, 150, 186] which are an example. Thus, parameters such as the material contraction rate, the Young's modulus, the amount of energy required for actuation and the forces produced as well as the dynamics of the contraction, were analyzed with the main purpose to understand the behavior and actuation mechanisms of those composites and thus, be able to design

different approaches for the fabrication of actuators.

To that purpose, custom-made setups were designed for testing and different techniques such as stress-strain assays and "in-situ" photo-actuation observation using SEM and an IR camera were used. The main results obtained were grouped in two different sections as function of the type of characterization used.

3.2.1 Thermoelastic characterization

In accordance with the main characteristics involving LCE elastomers described in Chapter 2, these elastomers contract in the direction of orientation of the mesogens (LC units) and CNTs with increasing the temperature. It has been demonstrated that LCE-CNT composite contraction can be realized using either direct heating or illumination, in which case the energy of light is converted into the local heat [166], and strongly depends on the type of polymer which forms the elastomeric backbone.

In case of polysiloxane backbones, which is the type used within this work, the transition temperature between nematic and isotropic phase, T_{NI} , is usually in the range of 60 °C to 90 °C. Such variations in T_{NI} may be caused by the type of chemicals used during the synthesis (mainly the crosslinker type and its concentration).

The change of natural length of monodomain LCE elastomers with temperature (i.e., its contraction movement) typically follows the same behavior, resulting in slow variation in the samples length at lower temperatures (from room temperature to approximately 15 to 20 °C below T_{NI}) in nematic state, and faster close to T_{NI} , when maximum contraction is reached (optimal mechanical contraction rate), leading to the uniaxial thermal contraction ratio, $\lambda = L/L_{iso}$; parameter which is used to compare the degree of deformation achieved for different samples (see Chapter 2 for details). However, as already mentioned, such value of maximum contraction is strongly subject to the orientation degree (i.e., order) of the LC units fixed during sample preparation.

Usually to perform such thermoelastic measurements, a conventional oven is used where the samples (without an applied load) were freely suspended inside in a vertical position. This procedure works well for characterization of large samples, however results impractical for small ones.

With the main purpose of characterize small samples, a self-constructed apparatus was designed. In this manner, it was possible to i) guarantee a uniform heating of

3. LCE-CNT FILMS CHARACTERIZATION

the whole sample, and ii) reduce the influence of the environment on the experiment, since this materials resulted to be very sensitive to small deviations of temperature produced by air convection. Figure 3.6 shows a scheme of its main parts.

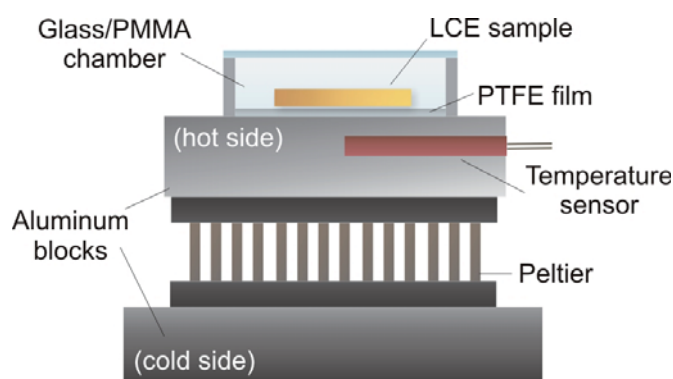


Figure 3.6: Setup designed for thermoelastic measurements of small LCE samples.

Similar to a small oven, this apparatus mainly consist of two parts:

- an atmospheric chamber where the sample is laid. It was made by a combination of glass and poly(methyl methacrylate), PMMA, to allow sample control and inspection at any time during the experiment. In this manner, the measurement of the length and width variations of the samples can be monitored using a CCD camera attached to a conventional optical microscope.
- a self-constructed miniaturized hotplate which supplies and controls the temperature delivered to the sample. This mechanism consists of a peltier (TEC 1.4-6, Thorlabs) and a temperature sensor coupled to a power controller (ITC 510, Thorlabs). Two aluminum plates were attached to both sides of the peltier to in order to stabilize and homogenize the temperature increasing the thermal inertia of the system.

The miniaturized oven was heated at an average rate of $0.4^{\circ}\text{C}\cdot\text{s}^{-1}$ to assure uniform heating. In that case, the samples were horizontally leaned on top. To avoid sticking problems and to reduce the contact area between the sample and the oven surface, a strip of Polytetrafluoroethylene, PTFE, commercially known as Teflon [®], was added. The resulting images were then manually processed.

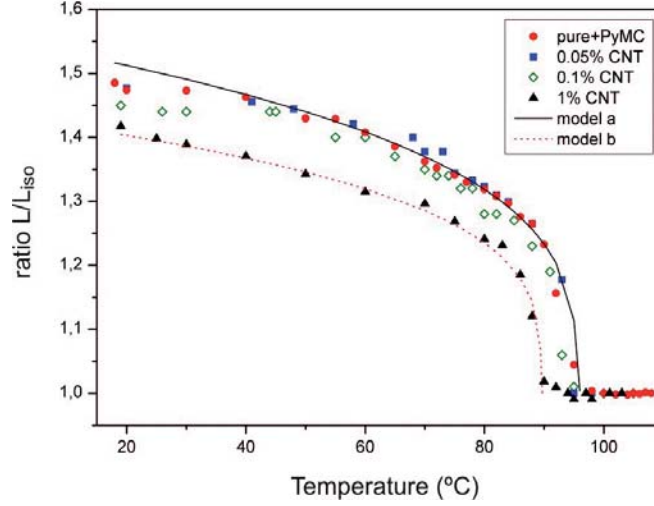


Figure 3.7: Contraction measurements obtained as function of temperature, for samples containing four different concentrations of CNTs (depicted as symbols); solid and dash lines depict the expression below, as function of temperature, T , and illustrate a reduction of the contraction rate of the samples at high CNTs concentrations.

The measured variation in the sample length, $\lambda = L/L_{iso}$, with temperature was fitted to a function given by the expression

$$\lambda = \frac{L}{L_0} = \left[1 + \alpha \left(1 - \frac{T}{T_{NI}} \right)^\beta \right]^{-1}$$

where L is the length of the samples in the isotropic state, i.e., when they are fully contracted and L_0 their length at room temperature (nematic state), and both α and β are fitting coefficients from the curve. Samples containing different concentrations of CNTs were measured as well as a neat one (exactly with the same synthetic characteristics) to check if variations on the contraction behavior between them were produced due to the inclusion of CNTs. The contraction curves of the samples as function of temperature are presented in Figure 3.7.

As expected, no significant differences were found at lower CNTs concentrations [81]. This is because using this type of samples excitation (the phenomenon is purely thermal) CNTs really do not have a strong influence on the contraction movement, and all the samples contract following the same pattern (Figure 3.7, model a), where the values of α and β coefficients resulted to be 0.37 and 0.22 respectively. However, a reduction of contraction was observed at high CNT concentrations (Figure 3.7, model

3. LCE-CNT FILMS CHARACTERIZATION

b). This is because an increased concentration of CNTs, which while increases the ability of the material to absorb light, also has the effect of disrupting the nematic order in the composite, resulting in a stiffer and less homogeneous material.

3.2.2 Photo-induced actuation: opto-thermomechanical experiments

After first thermoelastic experiments, different photo-actuation experiments were designed in order to obtain detailed information about the LCE-CNT composites and their main actuation parameters.

3.2.2.1 "In-situ" observation of photo-actuation

A cantilever is probably the most versatile mechanical structure able to give a lot of information about the material that it is made of. Using this approach, different experiments can be carried out to study the actuation mechanisms of a LCE cantilever exposed to heat [174] and thus, get the most important material parameters for designing actuators based on these materials [144, 153, 175]. For these reasons, such structure was used on several occasions during the experimental characterization of LCE-CNT materials.

Prior to the quantification of the photo-thermomechanical actuation of LCE-CNT, a qualitative experiment for the "in-situ" observation of the material contraction at the microscale was designed with the main purpose to better understand this phenomenon. A highly advantageous approach since stimulus, in that case, light can be provided "in-situ" and no additional manipulation is required on the composite, preserving the inherent mechanisms behind actuation. To that end, a quite complex setup was designed using the vacuum chamber of a dual beam SEM/FIB microscope (1560 XB, Zeiss) located at clean room facilities of IMB-CNM (CSIC), equipped with three micromanipulator probes. First, small LCE-CNT sample with of $300\mu\text{m}$ thickness containing 0.1 wt.% concentration of CNTs was cut in rectangular shape (1200×300) μm^2 in order to ensure uniform illumination and consequently, a more uniform heat distribution too, and placed in a specially designed support as a free-standing cantilever inside of the vacuum chamber. Underneath, a 660 nm of wavelength laser diode, LD, was added as excitation light source at approximately 1 mm. Pictures in

Figure 3.8 show the SEM/FIB equipment used as well as a detailed view of the interior of the SEM/FIB vacuum chamber where the main setup components can be identified.

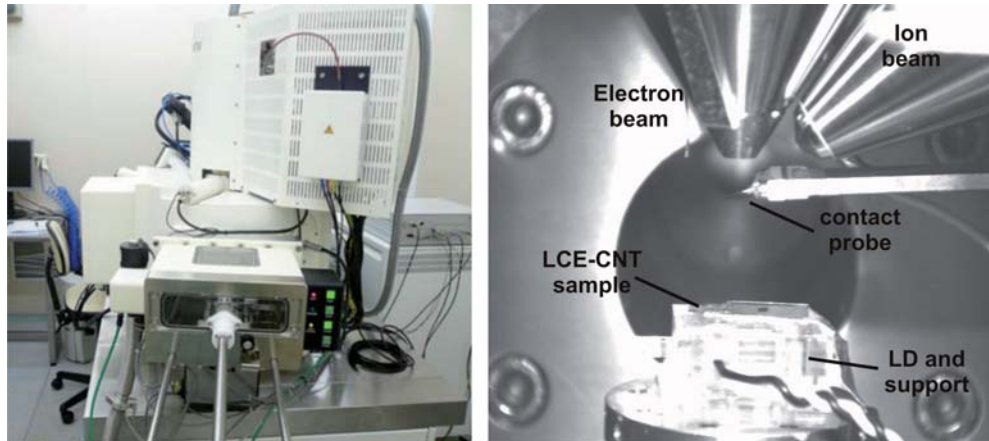


Figure 3.8: Setup for the "in-situ" observation of the LCE-CNT photo-actuation. FIB/SEM equipment at clean room facilities of IMB-CNM (CSIC) -left-. Detailed view of the interior of the vacuum chamber with the main setup components -right-.

Initially, mobile electrical contacts were devised by means of two tungsten tips coupled to the micromanipulator probes. In this way, the LD could be directly contacted and switched on and off from inside the vacuum chamber while the current controller was placed outside. However, due to the setup dimensions and the spatial distribution of the LD electrical contacts, certain displacement in z direction as well as some sample rotation was required, fact that would produce a mismatch between both electron and ion beams (loose of the coincidental point) and thus, imaging recording problems. Hence, the setup was modified welding directly the opposite LD ends to the Tungsten tips in order to fix the electrical contacts allowing a correct "in-situ" observation. In this manner, the LD could still be contacted from the inside of the chamber while maintaining the current controls outside. Before starting with the tests, an ultra-thin gold coating was deposited on the top surface of the structure to avoid any interaction between them and the electron beam (undesired charging effects due to the elastomeric nature of the sample).

Figure 3.9 shows a SEM sequence of images captured from an "in-situ" actuation movie before, during and after light irradiation, to illustrate the shape changes of the cantilever during the contraction and recovery movements. In that case, the sample

3. LCE-CNT FILMS CHARACTERIZATION

was uniformly illuminated at $1.6 \text{ W}\cdot\text{cm}^{-2}$ of power density. Same movies were recorded at different power densities (from 0.4 to $1.6 \text{ W}\cdot\text{cm}^{-2}$) to check its behavior and determine the first actuation parameters.

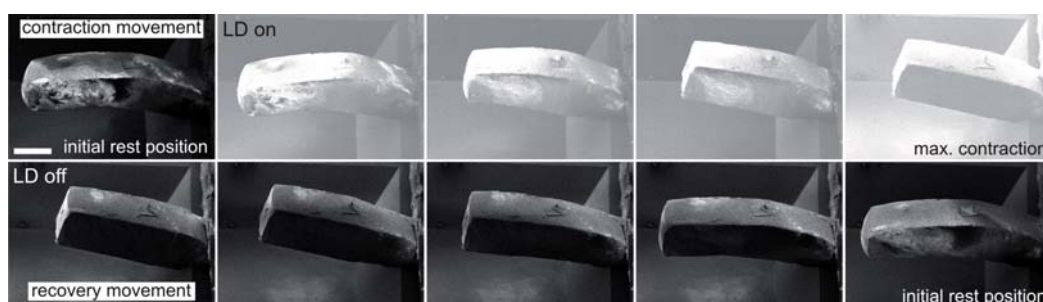


Figure 3.9: Image sequence showing the contraction and recovery movements of a free-standing cantilever-shaped composite captured during "in-situ" actuation. The scale bar represents $200 \mu\text{m}$.

In spite of the gold coating, the SEM image of the cantilever in the initial rest position (LD off) shows further evidence of local charging being developed within the bulk (first image of the sequence), in agreement with the previous microscopy experiments. Upon light irradiation (LD on), the cantilever responded with a contraction about 20 % in the parallel direction of sample's alignment whereas an expansion of about 6 % was observed in the other two directions, orthogonal to the alignment. After actuation, again an increased brighter contrast on the surface of the sample was observed (last image of the sequence, also referring to the initial rest position), most likely connected to local e-beam charging, which may be due to either the dynamics of internal electric fields or to the changes on the orientation of the cantilever with respect to the e-beam upon actuation.

Figure 3.10 depicts the contraction and recovery times obtained at different powers of incident light. Each power level was enough to obtain full contraction. The only parameter changing with power was the excitation time. As expected, it took less time for the samples to contract when more power was applied. Relaxation time did not change significantly, although it is obvious that the temperature to which the sample was heated, also increased with the power. The relaxation process is due to radiative heat loss by the sample (this must be the case in this situation because the experiment was conducted in a high vacuum, disallowing convective heat exchange

[187]). Theoretically, the cooling process should have taken little more time after the sample was irradiated at high powers, but as the irradiation rate is temperature dependent, it was difficult to distinguish among the relaxation time constants for various powers.

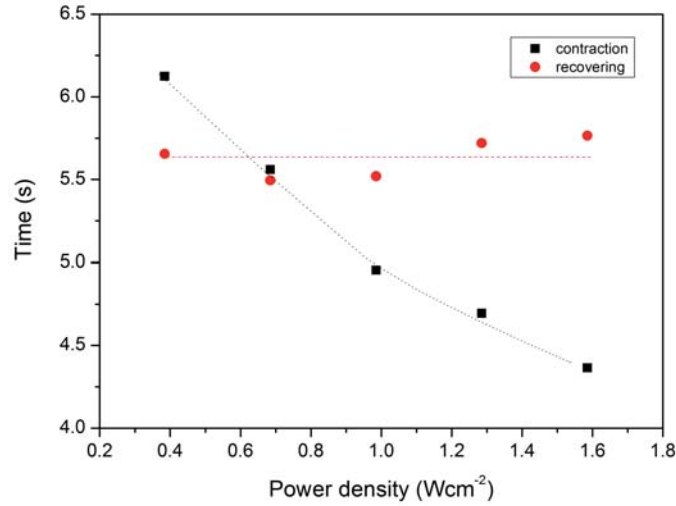


Figure 3.10: Contraction and recovery times of the LCE-CNT cantilever illuminated at different power densities.

As SEM allows 3D imaging another important parameter for the characterization of the material, the Poisson's ratio, could be obtained. As is well-known, the value of this parameter ranges between -1.0 and 0.5 for stable and isotropic materials along their elastic regions [64, 188] depending on their behavior under an applied stress (Young's and Shear modulus values). Usually, polymers are considered as nearly perfect incompressible materials (no changes in volume occur during deformation), for which the typical Poisson's ratio value ($\nu = 0.5$) can be numerically calculated following the next expression, which, at the same time, can be related to the strain variations on the sample [189],

$$\nu \cong - \left[\frac{\Delta L'}{\Delta L} \right] \cong - \left[\frac{\Delta L''}{\Delta L} \right]$$

$$\nu \cong - \frac{\epsilon_{lateral}}{\epsilon_{longitudinal}}$$

3. LCE-CNT FILMS CHARACTERIZATION

where ΔL is the length variation in the main direction of the contraction (longitudinal axis of the sample) and $\Delta L'$ and $\Delta L''$ correspond to the variations in length in the other two directions (lateral directions). For an incompressible material, $\Delta L' = \Delta L''$, so that $\nu = \nu' = 0.5$.

These expressions, however, are only valid when the material undergoes small contractions (within the elastic region). Recent studies have been demonstrated that with increasing strains such the Poisson's ratio varies, descending up to 0.2 as function of the type of LCE and their stretching conditions [190, 191].

By comparing the lateral movements of the samples recorded during the experiment with the contraction produced in the main movement direction, it was possible to obtain, as first approximation, a value for this parameter, resulting in a experimental Poisson's ratio of about 0.507 ± 0.005 .

3.2.2.2 Bending dynamics

As demonstrated in previous section, the "in-situ" photo-actuation phenomenon can be observed and the light absorption and the heat propagation dynamics can be quantitatively described on a cantilever illuminated from one side. With the main purpose to understand the main phenomenological aspects of heat propagation through the sample, a cantilever bending experiment was designed. In this manner, direct measurements of temperature evolution inside the cantilever were carried out to relate its kinetics to the applied irradiation power studied in the case where heat is not being provided by direct heat source but by the light-irradiated CNTs embedded in the polymer. Other aspects such as the time constants and the uniformity of the material could also be observed.

A cantilever made of LCE-CNT exposed to light demonstrates dynamic bending due to inhomogeneous strain distribution caused by exponential heat generation across the cantilever width which, at the same time, is related to the linear absorption of photons by the CNTs that, in contrast with the heat generation, attenuates with distance (Figure 3.11). A schematic representation of the experiment is depicted in Figure 3.11a. In that case, a LCE-CNT sample containing 0.1 wt.% of CNTs was cut into a rectangular strip of 3.9 mm x 1.2 mm at room temperature and fixed from one end to form a cantilever beam. Then the cantilever was placed in a plastic box to avoid

cooling due to air convection. A calibrated LD coupled to a current controller (Thorlabs ITC510) provided irradiation at wavelength of 660 nm, allowing instantaneous on-off switching. The LD emitted light with Gaussian intensity distribution and width a divergence of 30 and 10 degrees, in the vertical (Y axis) and horizontal (X axis) directions respectively, which correspond to 0.9 mm and 2.7 mm full width at half maximum, FWHM, of the spot on the plane of the cantilever front surface. The face exposed to the irradiation was located 5 mm from the LD and aligned symmetrically with respect to the center of the spot.

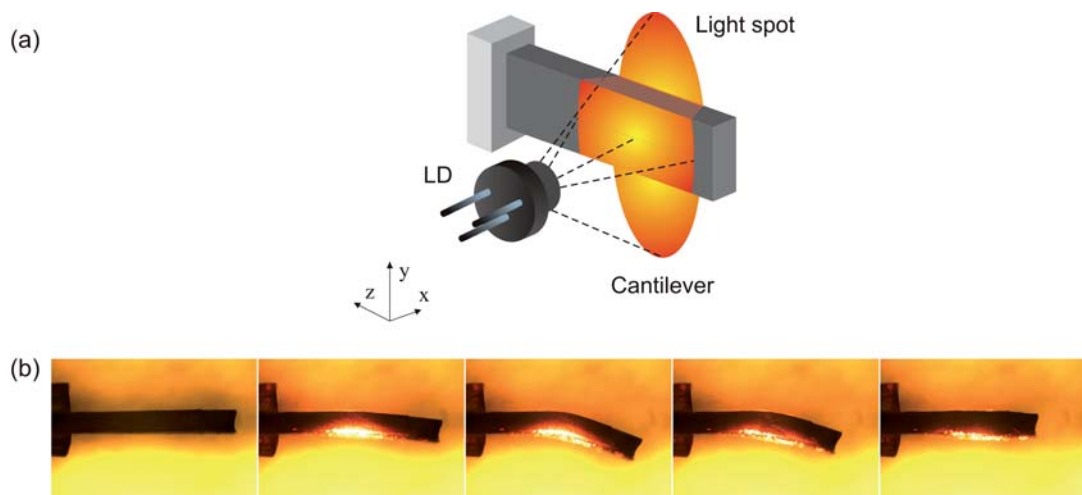


Figure 3.11: Cantilever bending dynamics. (a) Schematics of the experiment; (b) top view images of the cantilever. The images were obtained at 0 s, 2 s, 4 s, 8 s, and 14 s after the LD was switched on, with D_p fixed at $2.25 \text{ W} \cdot \text{cm}^{-2}$. The cantilever on the photos was 3.9 mm long, 1.2 mm wide and 0.45 mm thick. After irradiation, it is 3.15 mm long -contraction 1.24- and 0.5 mm thick -expansion 1.2-.

Movies of the cantilever bending motion were recorded by a conventional optical microscope camera and then manually analyzed. The temperature distribution over the cantilever top face was measured twice per second by a FLIR SC 5000-series IR camera located at IMB-CNM facilities, provided with ALTAIR software with 30 μm of resolution per pixel. In this manner, a real-time mapping of the heat propagation in the composite was obtained. A sequence of images in Figure 3.12 shows an example of the "in-situ" measurements of heat propagation and thus, the temperature distribution along the composite under uniform illumination. The emissivity of the sample was assumed to be 0.7 from prior experience. This value was adjusted to fit the temperature

3. LCE-CNT FILMS CHARACTERIZATION

of contraction of the material obtained in previous experiments with thermal actuation (see Thermoelastic characterization section above) to the temperature of contraction measured by the IR camera. When exposed to the irradiation at a constant power the cantilever starts bending and after some time comes to a steady state (Figure 3.11b) which is a function of the applied power.

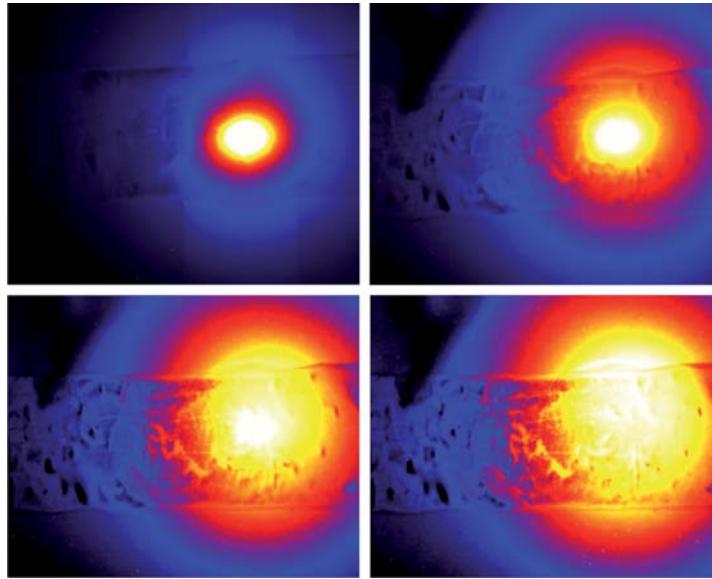


Figure 3.12: Thermal images obtained by the IR camera under uniform sample irradiation.

There could be distinguished three different modes reflecting the cantilever bending dynamics characterized by the cantilever curvature in steady state as function of the power density, D_p , in the center of the spot, in agreement with the sequence of images in Figure 3.11:

- Mode (a): The cantilever curvature increases with time immediately after the experiment starts when irradiating at constant power. This mode disappears when the isotherm T_{NI} crosses both the front and the back surfaces of the cantilever, while $D_p < 1.16 \cdot Wcm^{-2}$.
- Mode (b): In this mode, when the cantilever is illuminated at constant power, there is an initial increase of curvature with time, which decreases together with the length of the sample (material contraction) until reaching a steady state value ($1.16 < D_p < 2.10$) $W \cdot cm^{-2}$. When the isotherm T_{NI} crosses the sample from

the front to the back, a portion of the cantilever has zero stress gradient and therefore zero curvature. Further power increase just amplifies this segment of fully contracted material.

- Mode (c): The cantilever curvature decreases with time and then drops down to zero ($D_p > 2.10$) $W \cdot cm^{-2}$. No stress gradient can be found in the cross sections where the temperature is more than T_{NI} . The isotherms of temperatures below T_{NI} become symmetrical in cross section and no bending is produced.

The evolution of the upper apex position of the cantilever in the XY plane recorded during the experiment as function of different irradiation powers is depicted in Figure 3.13, where the three modes described can also be distinguished. A schematic representation of the measurements was also included for better understanding.

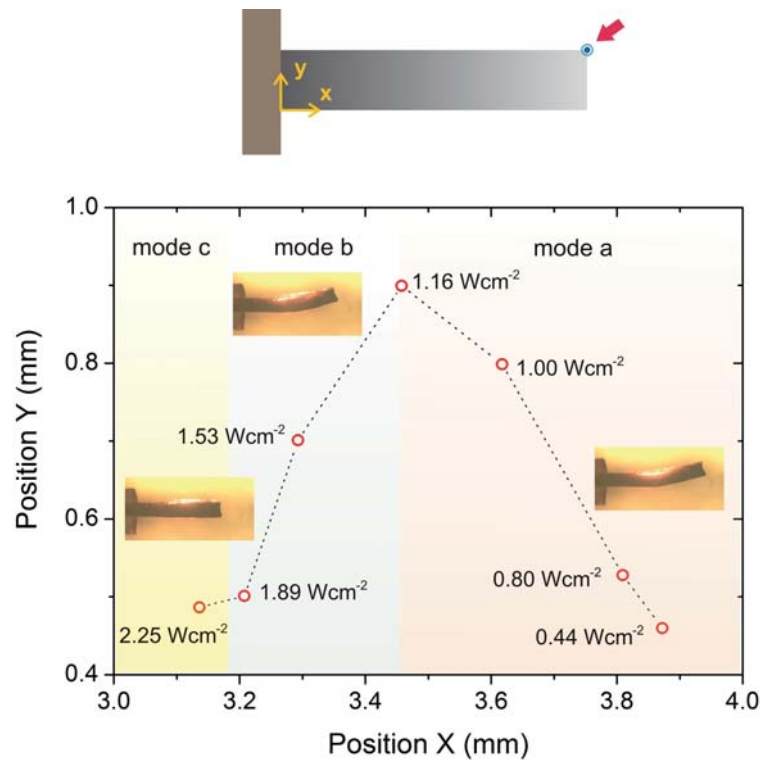


Figure 3.13: Cantilever upper apex position coordinates in steady state at different irradiation powers, where the three bending modes can be identified.

It is worth noting that the relaxation of the cantilever does not follow the same kinetics. The elongation of a fully contracted cantilever is not accompanied by bending

3. LCE-CNT FILMS CHARACTERIZATION

at all, because when the light is switched off the temperature gradient inside the cantilever quickly disappears.

During the experiment, as D_p increases, there comes a point where an interface exists between an area of the surface where temperatures are above T_{NI} and an area where the temperatures are below T_{NI} ; at this stage, the cantilever thickness experiences a quick change. The thickness increases by nearly 20 % in the segment with the higher temperature. A typical temperature distribution over a cantilever illuminated with a power density of $2.25 \text{ W} \cdot \text{cm}^{-2}$ is shown in figure 3.14 -left-. The temperature distribution is highly asymmetrical across the cantilever in the plane of the spot center, at $x = x_0$, becoming more uniform away from x_0 . Experimentally measured temperature evolution in two points located on the front and reverse sides of the cantilever at $x = x_0$ is demonstrated in Figure 3.14 -right-. In the steady state (starting from second 12) the difference in temperature between both sides is about 10 degrees. There is a significant delay of about 1 s before the temperature on the reverse side starts to increase at the same rate as the temperature in front.

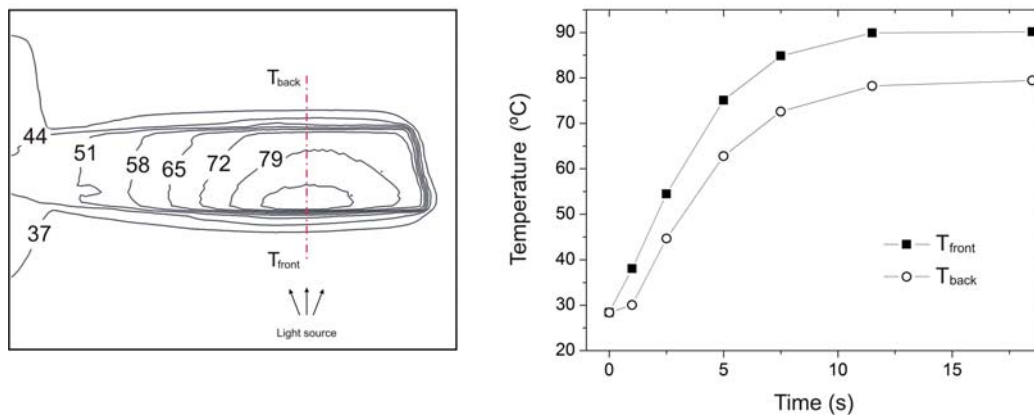


Figure 3.14: Heat propagation measurements. Two dimensional stationary temperature distribution over the cantilever -left- and temperature evolution -right- measured by IR camera. Squares represent temperature on the front illuminated side; circles depict temperature evolution on the back side of the cantilever. The LD power was fixed at $2.25 \text{ W} \cdot \text{cm}^{-2}$.

The temperature evolution inside the cantilever is governed by the heat equation (see equation below) whose dimensionality can be reduced if the inhomogeneous light distribution in one direction is neglected. Light incident on the cantilever is considered

uniform along the Y axis, while having a Gaussian distribution with mean value x_0 and variance μ in X direction. As the divergence of light exiting the LD is high (nearly 30°) in the vertical direction, it can be assumed (to a first approximation) that the cantilever is homogeneously illuminated from top to bottom, resulting in the relation:

$$C_v \frac{\delta T}{\delta t} - k_f \left(\frac{\delta^2 T}{\delta z^2} + \frac{\delta^2 T}{\delta x^2} \right) = \theta_0 \exp\left(-\frac{z}{\alpha}\right) \exp\left(-\left(\frac{x-x_0}{\mu}\right)^2\right)$$

where $\theta_0 = P_0/\alpha$ ($W \cdot m^{-3}$) stands for heat density on the front side.

It is difficult to solve this equation analytically, so numerical analysis was performed using commercially available software taking into account the three different modes above distinguished and assuming P_0 ($W \cdot m^{-2}$) to be the power flux density of light incident on the cantilever in the center of the spot. First results indicate that the contraction due to light irradiation is the same as that which occurs on heating the sample.

3.2.2.3 Light absorption

Absorption of UV light by elastomers with azobenzene groups leads to the reduction of mesogenic power of its component material because of the change in molecular shape [104]. In this case, the reduction of nematic order parameter (which leads to the phase change) is due to enthalpic (potential energy) effects. However, the absorption of visible-IR light by LCE with embedded CNTs causes a different effect: CNTs rapidly release heat into their surrounding and the resulting reduction of the nematic order is of entropic nature. The absorption coefficient, α , is an important parameter that gives information about the distribution of heat generated by light inside the film. Quantification of light absorption can be done on materials with known thickness and CNT concentration, in which α can be calculated by the Lambert-Beer formula (see equation below) from the film thickness, d , and the transmittance (the ratio of transmitted to incident power P_{out}/P_{in}) which in this case was measured experimentally.

$$\alpha = \frac{\ln(P_{out}/P_{in})}{d}$$

3. LCE-CNT FILMS CHARACTERIZATION

Absorption of three different samples was measured using a 670 nm wavelength LD as light source at different polarizations with respect to the LCE monodomain orientation, pumped by an LD current driver (Thorlabs ITC510). It was assumed that during samples preparation, nanotubes were aligned in the same direction than the mesogens in the polymeric matrix under stretching. The orientation of nanotubes leads to polarization-sensitive light absorption of the material, the property later used in polarization control using CNTs. Visually a polymer film approximately 0.4 mm thick containing more than 0.1 wt.% of CNTs appears black, i.e., only a small portion of light can be transmitted through. Using a lock-in amplification technique, the transmission coefficient was accurately registered to later calculate both the extinction coefficient and the sample's absorbance. Figure 3.15 shows a diagram of the experimental setup used to perform such measurements and table 3.1 summarizes the results obtained as function of polarization, material thickness and material composition (CNTs concentration).

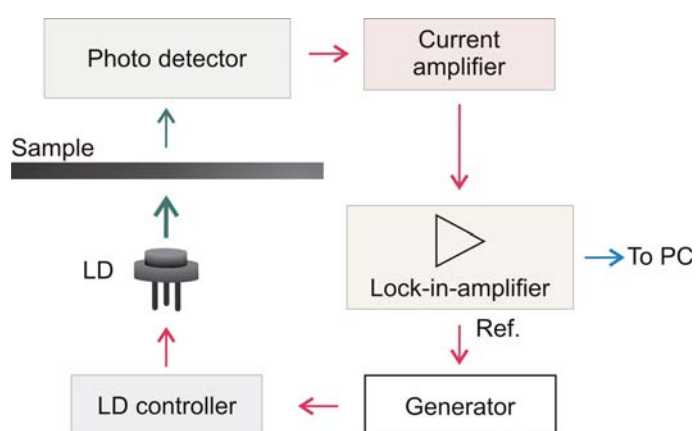


Figure 3.15: Sketch of the experiment used for measuring the transmission coefficients.

In parallel, measurements of the absorption of three samples with different content on CNTs were carried out in the range from Ultra violet, UV, to IR spectra to check if the presence of CNTs modify the material response to light. To that end, a neat LCE sample named control was measured too under the same conditions. Figure 3.16 shows the absorption spectra obtained, where a clearly dependence on the CNT content is observed. The noisy spectra at higher CNT concentration is simply an indication that all light was essentially absorbed and converted into local heat to stimulate the core

photo-actuation.

All of that leads to the conclusion that increasing the CNT content enhances the conversion of light into local heat. Thus, higher the CNT content more efficient the photo-actuation response of the composites. However, this conclusion contradicts the thermoelastic results obtained in previous section 3.2.1. From contraction point of view, the LCE matrix must remain fully elastic, with mobile polymer chains and the LC units unrestricted to change their phase order. Too many CNT segments would change the intrinsic property of LCE to reversibly change its shape on switching between the nematic and the isotropic phases, so an optimal balance between these two factors should be found. In this sense, measurements in terms of actuation force and power were required.

Table 3.1: Transmission measurements at 670 nm.

Sample	Thickness [mm]	CNTs wt. %	A Transmittance*	B Transmittance*	Extinction A/B [mm^{-1}]
Sample 1	0.4	0.3	$0.27 \cdot 10^{-3}$	$2.20 \cdot 10^{-3}$	20.6 / 15.3
Sample 2	0.5	0.1	$0.20 \cdot 10^{-3}$	$0.23 \cdot 10^{-3}$	16.4 / 16.1
Sample 3	0.2	0.1	$2.60 \cdot 10^{-2}$	$4.50 \cdot 10^{-2}$	18.3 / 15.5

* A and B denote correspondingly: the orientation of CNTs is parallel or perpendicular to vector E of the electromagnetic field of light.

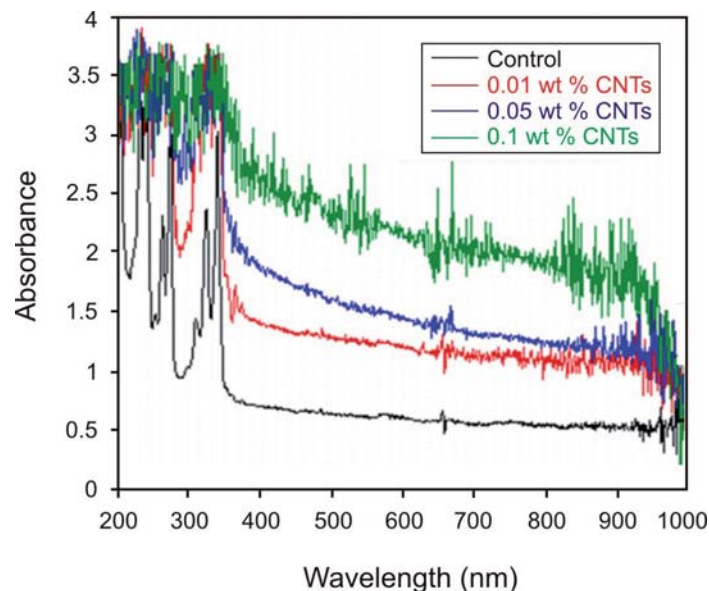


Figure 3.16: Absorption spectra for LCEs doped with increasing concentration of multi-walled CNTs.

3. LCE-CNT FILMS CHARACTERIZATION

3.2.2.4 Mechanical strength measurements

It has been demonstrated that the mechanical properties of LCE materials do not keep constant during both the curing process and the later actuation since they undergo to different phase changes, e.g., from gel to solid and from solid to liquid crystal, producing a significant variation of their main properties. The Young modulus is an example.

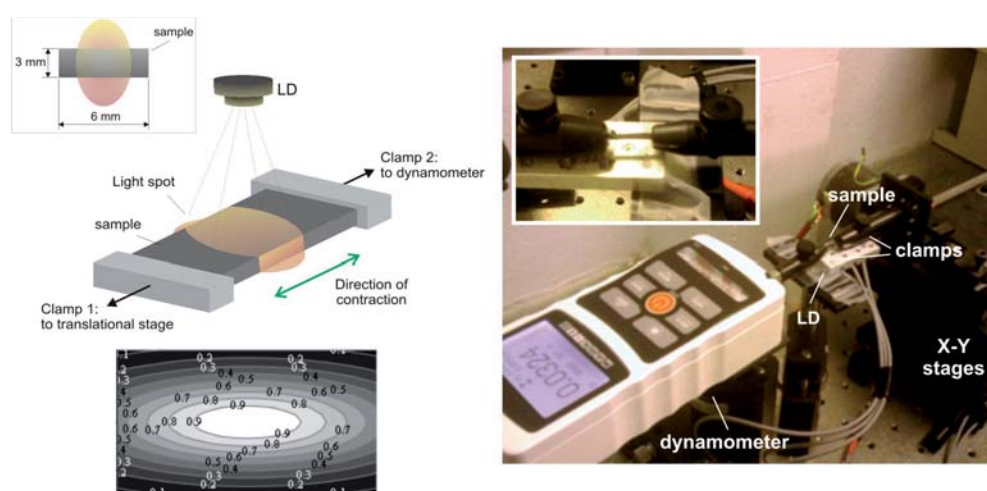


Figure 3.17: Setup for the force measurement experiments. Sketch of the experiment with all the components -left- where both the geometry of illumination and the normalized distribution of the LD's energy over the surface of the sample are depicted. A detail of the measuring zone is shown in the inset -right-.

With the ultimate goal to design and fabricate nematic photo-actuators, different types of force measurements were performed using two different ways of inducing stress in the samples: i) directly applying a tensile force (any external stimulus is applied neither light nor heat) or ii) using a light source to induce certain stress (testing directly under illumination). In this manner, a more complete understanding of the material behavior under actuation from the mechanical point of view can be provided, which results very useful for the future development of simulation models prior to the fabrication of the actuators. Thus, Young Modulus measurements were performed in both cases by means of the experimental setup depicted in Figure 3.17.

First, the different LCE-CNT films with thickness ranging between 0.3 mm to 0.4 mm were cut into rectangular shape strips of about 6 mm x 3 mm (length x width)

3. LCE-CNT FILMS CHARACTERIZATION

$$E = \frac{FS^{-1}}{\Delta LL^{-1}}$$

where S is the sample cross section, L is the sample length, ΔL represents the sample elongation.

When the strain was applied the samples experienced a strong increment of stress which was partially absorbed by the polymer chains resulting in an exponential relaxation of that stress taking about 10 s. This periodic process has a linear behavior, if approximated by the points corresponding to the relaxed state taken from each cycle. Thus the different samples tested demonstrated linear elastic behavior with stretching for low CNT content. Figure 3.19 shows the stretching results obtained in dark for samples containing different wt.% of CNTs, resulting in Young modulus in the range of 0.35 MPa to 0.5 MPa if calculated using these points; values which are in the range of the measurements reported in literature for neat LCE materials.

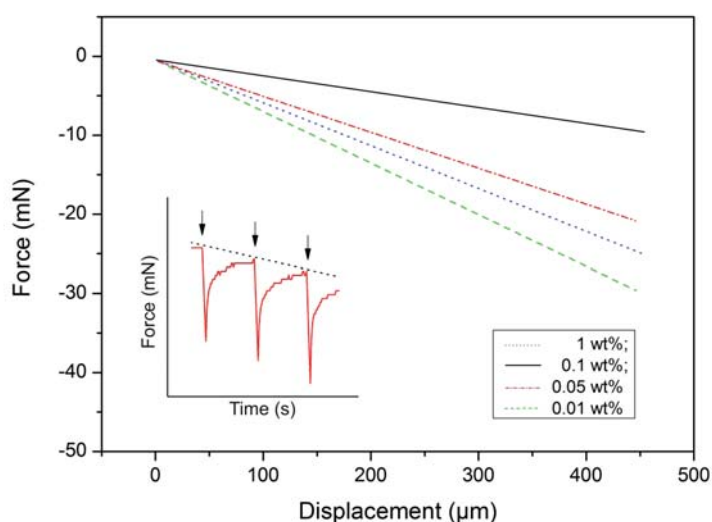


Figure 3.19: Results of stretching tests in dark for different samples containing 0.01 wt.%, 0.05 wt.%, 0.1 wt.% and 1 wt.% of CNTs. Schematics in the inset illustrate the displacement of the stage at each step.

It is worth noting that for high CNT content (1 wt.%), the measured modulus decreases significantly disrupting such linear behavior and thus evidencing an increase of the composite rigidity. Such behavior was previously observed in similar way in

the thermoelastic experiments, where a decrease in the L/L_{iso} ratio was obtained for the same CNT content (see Figure 3.7).

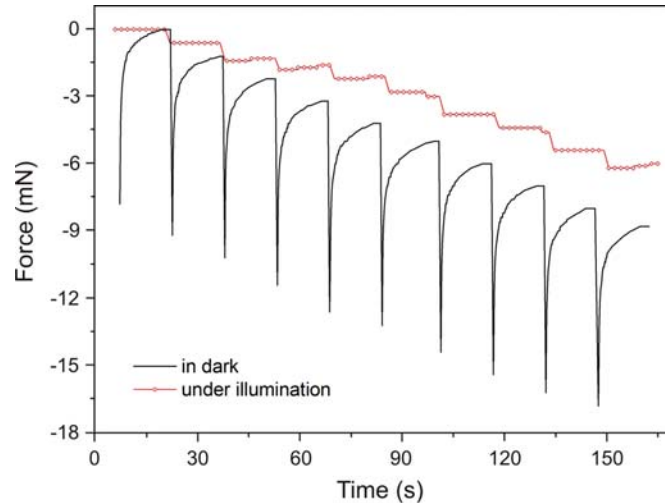


Figure 3.20: Time diagram comparison of the mechanically induced stress on a sample containing 0.1 wt.% of CNTs both in dark and under illumination.

On contrary, when samples were illuminated the mechanically induced stress did not show peaks or relaxation, resulting in a Young modulus drop. An example of that is depicted in Figure 3.20 where the force vs. time diagrams of the mechanically induced stress on a sample containing 0.1 wt.% of CNTs using both of the above mentioned methods are compared. In this case, the Young modulus measured in dark was 0.5 MPa; value which dropped down to 0.35 MPa when the sample was illuminated (i.e., the material became softer). At the same time, the photo induced stress was released by reducing the distance between the dynamometer and the clamp by 400 μm , resulting in the same behavior. No pronounced peaks were observed when the material was pre-stressed due to illumination. The Young modulus in this case was 0.38 MPa.

3.2.2.5 Photo-induced stress measurements

It is understood that the actuation of the LCE-CNT is due to the heating of the material, rather than a true photo-actuation, hence the slow response time. The results of the previous experiments in section 3.2.2.2 are in agreement with that, resulting the contraction due to irradiation by light the same as that occurs on heating the sample. The energy required for the actuation is dependent on thermal equilibrium conditions

3. LCE-CNT FILMS CHARACTERIZATION

in the system. Temperature change dynamics is a function of the power of light source, since temperature distribution over the sample is subject to change depending on the energy absorption rate, leading to a contraction which is independent of the irradiation wavelength [81]. To verify that, a sample with dimensions of 10 mm x 3 mm x 0.4 mm (length, width, thickness) was measured using the same setup depicted in Figure 3.17 at three different wavelengths resulting in no spectral dependence. Discounting the segments in the clamps the final length of the sample was 6 mm. The sample was illuminated sequentially by three different LDs, each projecting a total power of approximately 15 mW on the sample, resulting in stress values of 2.0 kPa, 2.3 kPa, and 1.9 kPa when the sample was illuminated correspondingly at wavelengths of 670 nm, 785 nm and 980 nm. The small differences between the stress values obtained are attributed to intensity deviations estimated by data taken from diodes' specifications.

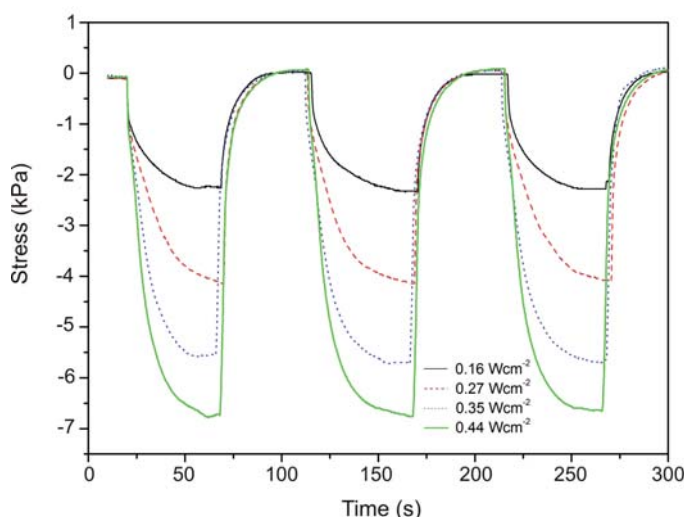


Figure 3.21: Stress periodically induced in the LCE sample with 1 wt.% CNTs by illumination at 785 nm as function of time.

Once stabilized, the material can be repeatedly irradiated as many times as needed showing repeatability in response. Figure 3.21 depicts three consecutive consecutive on-off actuation cycles (sample with CNT content of 0.3 wt.%) performed at different powers using a LD operating at wavelength of 785 nm and illuminating the sample with Gaussian intensity distribution, proving that the stress induced by illumination is a function of light power, which can be adjusted on demand to get specific material response. The power densities measured in the center of the spot are presented in

the legend to the graph, expressed in ($W \cdot cm^{-2}$), which were calculated as the power incident inside an area of a square centimeter. The actuation times are slightly different for different powers; this is the result of power dependent temperature dynamics in the sample.

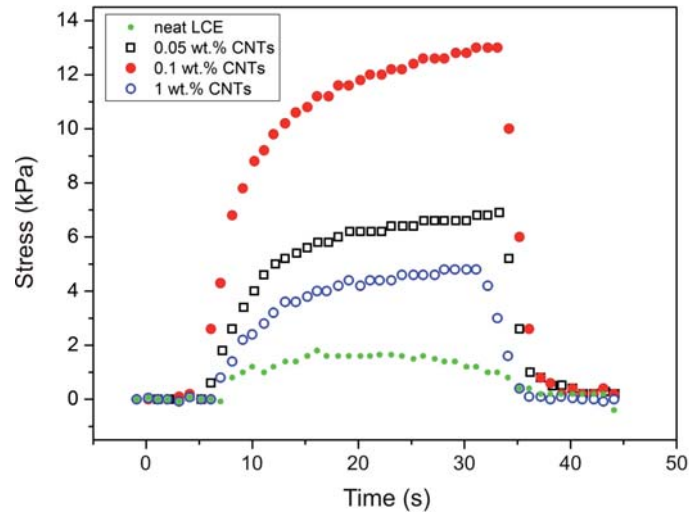


Figure 3.22: Photo-induced stress of LCE samples with different content of CNTs measured under the same conditions using a 670 nm wavelength LD at 110 mA.

Figure 3.22 shows a comparison between the photo-induced stresses obtained for samples with different CNT content measured under the same conditions. In this particular case, a 670 nm wavelength LD was used as a light source, illuminating at 110 mA. As expected, the results indicated that the actuation strength increases while increasing the CNT content for low concentrations. However, again a decrease of such response was observed for CNT concentrations from 1 wt.%, in agreement with the previous results obtained during the Young's modulus measurements and [81].

Photo-induced stress finally depends on the applied energy which is a product of time and the power of the light source. This energy would also depend on ambient conditions, because heat dissipation can vary with, for example, room temperature. Stress is subject to saturation due to the heat dissipation in the steady state and due to the nature of the material contraction, which is saturated when the sample is in the isotropic state, at local temperatures of above 80 °C. However, the achievable stress is still a function of power. That is partially due to non-uniform Gaussian distribution of light intensity over the sample, and extending the area, where the elastomer is in

3. LCE-CNT FILMS CHARACTERIZATION

the isotropic state. Basically, increasing the power of light, the overall temperature of the sample increases and this increase depends on the rate of energy supplied to the sample. Figure 3.23 shows the stress induced by irradiation of a sample containing 0.1 wt.% of CNTs as a function of applied energy. As can be observed, the response of the material remains stable when the light source is maintained illuminating at the same power (the material remains contracted), similar to the observed in the cantilever bending experiment. Thus, applying a power variation with time during actuation, it is possible to exert a dynamic manipulation of the material. Such concept will be later used to analyze and optimize the performance of the LCE-CNT actuators proposed.

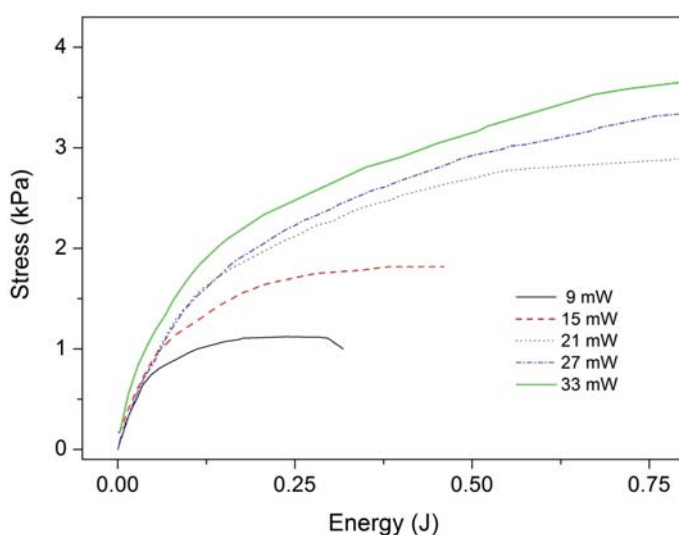


Figure 3.23: Stress induced by irradiation of the sample as a function of applied energy. The experiment was performed on a sample (1wt.% of CNT content and a cross section of 0.4 mm x 3 mm) irradiated by a LD emitting at 785 nm.

3.3 Material modeling

A computer-based model of the different LCE composite samples together with some numerical calculations was developed with the purpose of better understanding the material behavior under actuation. Thus, a more accurate prediction of the actuators performance could be done. In this sense the model represents a powerful tool for the optimization of the future actuators designed adjusting the different configurations tested to improve the actuation results.

The modeling of liquid crystal elastomers has received considerable attention almost since its appearance [192, 193, 194, 195, 196]. However, in the last decade it has suffered an increasing interest especially due to the development of novel LCE composites. At molecular level, it has been mentioned that LCE combines the entropy-induced elasticity with the liquid crystalline properties entailing a pure thermo-mechanical behavior. However, in case of photoresponsive materials, a new coupled phenomenon should be considered, capable of converting absorbed light into local heat, adding certain degree of complexity to the modeling process. This is the case of LCE-CNT composites.

Up to now, few works have been directed to the modeling of polymer-carbon nanotubes composites. Cantournet, *et al.* presented a constitutive model for the large strain deformation behavior of MWCNT-elastomer composites [169]. In that case, CNTs effect within the polymer was modeled by tracking the stretching and rotation of a distribution of wavy CNT. From experimental results they conclude that the strain energy density of the composite can be decomposed into i) a contribution from the elastomer and ii) a contribution from the nanotubes, resulting in a simple relation between the volume fractions of both components in the mixture expressed as:

$$U_c = f \cdot U_{MWCNT} + (1 - f)U_e$$

where U_c , U_e and U_{MWCNT} are the strain energy densities of the composite, the elastomer and the carbon nanotubes respectively, and f is the volume fraction of the carbon nanotubes. This model, however, is restricted to the mechanical behavior and it does not consider the dynamics of the material when it is external stimulated.

On the other hand, Ahir and Terentjev reported for the first time the photo-induced mechanical actuation in a polymer-nanotube composite when exposed to IR radiation [197]. They introduced a model of the opto-mechanical behavior of the material as a function of the orientational ordering of nanotubes induced by their uniaxial extension in which both the alignment and the concentration of CNTs inside the host matrix were the main variables. In this case, their material does not contain LC-mesogens which undoubtedly aggregates new variables to the dynamics of the composite.

Although many impressive experimental results have been obtained by studying the dynamic response of LCE-CNT composites to external stimuli, their dynamics is

3. LCE-CNT FILMS CHARACTERIZATION

yet not fully understood.

The implementation of a more complex empirical model describing the material deformation is thus required for an accurate prediction of its mechanical response of future actuators designed.

3.3.1 Model description

A transient three-dimensional model of a LCE-CNT composite cantilever used in this work was built using the software ANSYS ® Multiphysics software (ANSYS Inc., Canonsburg, PA, USA). This software uses finite element analysis, FEA, to solve the system equations and allows visualizing the resulted data in both graphical and numerical ways. The coupled-field elements PLANE13 and SOLID5 were employed for transduction from opto-thermal to mechanical field. These element types are suitable for modeling deformations in nearly incompressible elastoplastic materials as well as fully incompressible hyperelastic materials like LCE-CNT composites. Preliminary 2D model consisted in 1,600 nodes, but up to 32,000 nodes were used for the final 3D model.

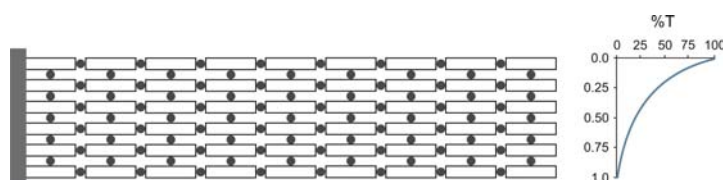


Figure 3.24: Schematic representation of the internal structure of the material in which the CNTs are homogeneously distributed along the whole sample's section.

Such model was varied throughout this thesis to adapt it to the different experimental result obtained. First the behavior of the material once cured was modeled to study the dynamics of a film under photoactuation, to better understand the experimental results obtained (see section 3.2.2.2 in this chapter). In this section the main model generalities and the as well as the main considerations adopted are described focused on the cantilever's bending study. Later on, the different processes proposed for shaping the composite in more complex geometries and in array for the fabrication of different actuator approaches were also modeled. In this manner, it was possible to individually optimize some of the parameters involving each

fabrication process (e.g., size, loads, pressure applied, etc.), thus reducing the number of experimental trials. Such model variations are later described and discussed in the corresponding chapters (see part IV).

In order to simplify the model, some assumptions were made which are briefly described in the following points:

3.3.1.1 CNTs behavior

In order to build a practical but realistic model for the light-activated LCE-CNT composite, the physical events in a typical opto-mechanical scenario common in this kind of materials were considered. Previous studies regarding LCE assert that there is a thermo-mechanical effect due to the phase transition when the nematic LCE is heated above its transition temperature, T_{NI} . This thermo-mechanical effect becomes in an opto-mechanical reaction when the LC units contain photo-isomerizable azobenzene groups, which undergo trans-cis isomerization on absorption of UV photons [150, 167]. It also happens for CNT-doped elastomers, which respond to IR light [198]. However, in the case of LCE-CNT composites, a mechanical contraction is also produced upon visible light irradiation. This phenomenon is due to the efficient light absorption of the CNTs over a range of wavelengths. CNTs convert this light into local heat very fast [166].

The experimental results in previous sections revealed that in contrast to the polymer-CNT composite presented by Ahir and co-workers [198], the effect of CNT on the liquid crystalline matrix is that mainly they act as transducers which convert the optical signal into thermal field, reaching similar thermal gradients using both types of excitation as experimentally proved. Thus, the basis of the model is the consideration of CNTs as local heaters embedded into the elastomeric matrix.

3.3.1.2 Light propagation

As observed experimentally during LCE-CNT characterization (see section 3.2 above in this chapter), the heat generation capacity of the CNTs is directly related to the incident optical power. In order to determine how much power receives a CNT located at certain depth is necessary to consider the optical absorption of the composite and model the light propagation through it. The main objective was determining the intensity field

3. LCE-CNT FILMS CHARACTERIZATION

in each point throughout the sample. To that end, it was assumed the material was structurally and chemically homogeneous and the CNTs were uniformly distributed without internal boundaries (see Figure 3.24). Therefore, scattering was not considered inside the composite.

Taking into account the experimental absorption results (see section 3.2.2.3 above) and the Beer-Lambert law, the light intensity can be expressed as function of the length of the sample, L ,

$$I(L) = I_0 \exp(\alpha L)$$

It is known that at large deformation, the optical properties of a polymer system may be affected by the state of deformation; specifically the refractive index of polymer [199]. This opto-mechanical coupling effect, however, was not considered for the modeling.

3.3.1.3 Light source radiation

Laser diodes, commonly used as light sources in a wide range of applications, were considered as the most suitable light source to build the model. From the mathematical point of view they have a well-known radiation pattern which can be easily described as a Gaussian beam simplifying the equations. From the applications point of view, it is possible to find LD with wavelengths ranging from UV to IR and they have a friendly and simple electronics not requiring the use of complex equipment. Moreover, their reduced dimensions enable their use in small actuators.

Thus, the intensity of light received for the sample can be expressed as:

$$I(r, z) = I_0 \left[\frac{w_0}{w(z)} \right]^2 \exp \left[\frac{-2r^2}{w^2(z)} \right]$$

where r is the radial distance from the center axis of the beam, z is the axial distance from the beam's narrowest point (the waist), $I_0 = I(0, 0)$ is the intensity at the center of the beam at its waist. $w(z)$ is the radius at which the intensity drops respectively to $1/e$ and $1/e^2$ of their axial values, and w_0 is the waist size.

For calculations of the heat generated by CNTs (given in $W \cdot m^{-3}$), a 660 nm wavelength LD (HL6512 from Thorlabs) was considered as light source.

3.3.1.4 LCE-CNT material characteristics and shape

Considering the aspects above mentioned and the results obtained from the experimental characterization, Table 3.2 summarizes the material constants employed to build the empirical model. 1 mm long and 0.6 mm wide cantilever with 0.4 mm of thickness containing 0.1 wt.% of CNTs was selected as modeling structure for its simplicity in shape as well as to be a type of structure previously studied (see section 3.2.2.2) with available experimental data.

Table 3.2: Numerical constants used to simulate the dynamic behavior of a cantilever made from a LCE-CNT film.

Material constants		Other constants	
Young modulus	0.3 MPa	Optical power	60 mW
Poisson ratio	0.5	Beam divergence θ_{\perp}	8.5 °C
Thermal conductivity	0.4 W/mK	Beam divergence θ_{\parallel}	21.0 °C
Density	1300 kg/m ³	Light wavelength	658 nm
Specific heat	200 J/kgK	Laser-sample distance	1.0 cm
Absorption coefficient	16 mm ⁻¹		

3.3.2 Final considerations

The heat generation capacity was attributed to single nodes (considering them similar to CNT units), assuming 20 internal layers across the thickness of the composite (they do not imply boundary conditions). Then, taking into account the Beer-Lambert law and the Gaussian distribution of the light simultaneously, the magnitude of the heat generation H can be reformulated as following:

$$H(r, z) = P_0 \left[1 - \exp\left(\frac{-2r^2}{w^2(z)}\right) \right] \exp(-\alpha z)$$

Two ANSYS® plots in Figure 3.25 depict the model during its building process. The first one, Figure 3.25 -top- reflects the heat generation rate as contour enforced whereas the external loads applied to the model before the simulation, such as the displacement restrictions, the radiation surfaces and the heat generation rate are shown in the bottom plot.

3. LCE-CNT FILMS CHARACTERIZATION

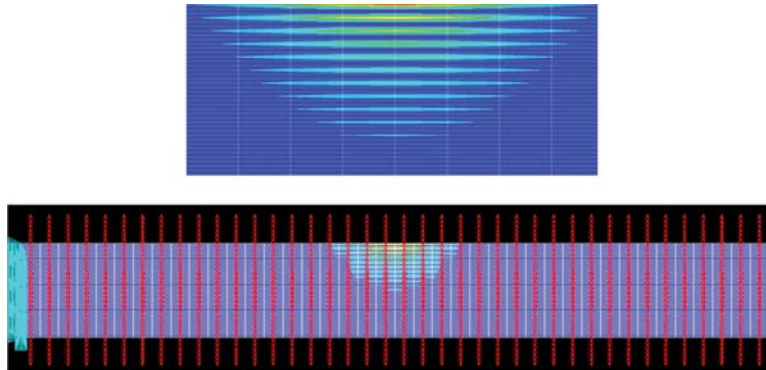


Figure 3.25: Plots of the building process of the FE model showing the heat generation rate as contour -top- and the external loads applied before simulation -bottom-.

Preliminary results extracted from this model were in agreement with the first experiments performed in which the transient response of a cantilever upon light-irradiation was analyzed (see section 3.2.2.2 above and [170]). According to previous studies and models of this kind of structure, when a temperature gradient is applied across the width of a cantilever an inhomogeneous strain distribution leads to bending motion [174].

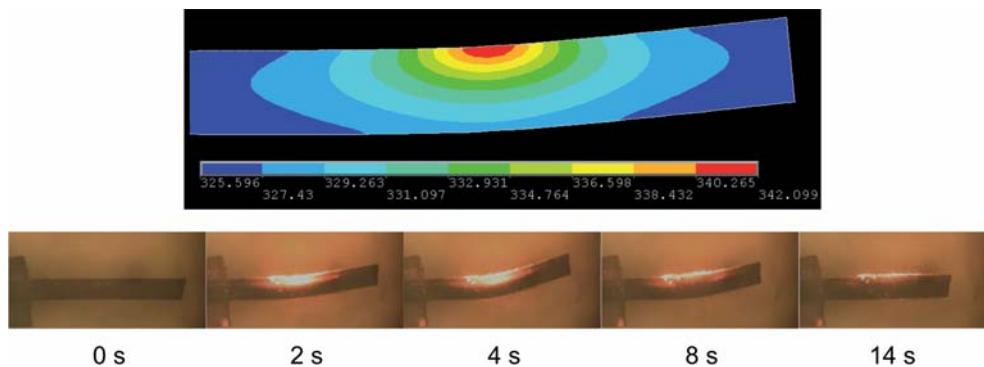


Figure 3.26: Thermal gradients distribution within a LD-irradiated LCE-CNT composite in an instant of its transient response. Deformation at $t = 4$ s evidenced a bending caused by an inhomogeneous strain distribution in agreement with previous experimental results.

Figure 3.26 shows the modeled thermal distribution at one instant of the transient response of the system where the Gaussian beam pattern of the thermal gradients can be appreciated. Similarly, the bending motion sequence of the film was obtained with results in agreement to the experimental data previously presented in the cantilever

experiments (section 3.2.2.2). In this case, the plot in the figure Figure 3.26 corresponds to that instant $t = 4$ s of the experiment.

The temperature across the film is maybe the most important parameter to be modeled, since it is, in fact, what provokes the mechanical reaction of the device. Experimentally it was not possible to measure the temperature deep inside the film; however the temperature distribution on both the top and bottom surfaces of the cantilever could be measured by using an IR camera, resulting in a thermal gradient of approximately $10\text{ }^{\circ}\text{C}$ between front and back surfaces (see Figure 3.14 in previous section). Thanks to these experimental measurements it was possible to adjust the thermal gradients obtained by the FE model, resulting in the possibility to predict temperature changes inside the material at any selected point. The temperature distribution results obtained by simulation are shown in Figure 3.27. As was expected, the thermal gradient has a linear behavior with the depth.

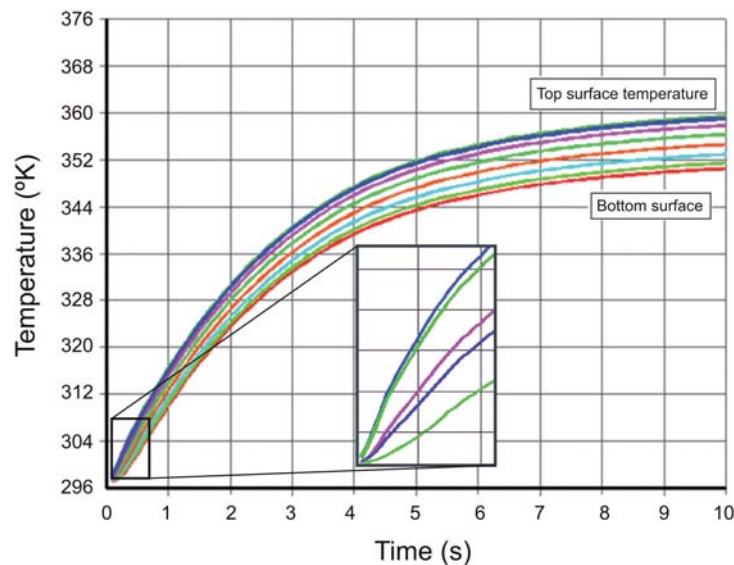


Figure 3.27: Transient thermal response of a modeled cantilever at different depths (light path length) of the composite.

Finally, once all the considerations previously described were taken into account and the transient thermal response adjusted in agreement with the experimental results, the FE model was completed. Thus, the bending motion of a LCE-CNT cantilever under illumination could be modeled.

3. LCE-CNT FILMS CHARACTERIZATION

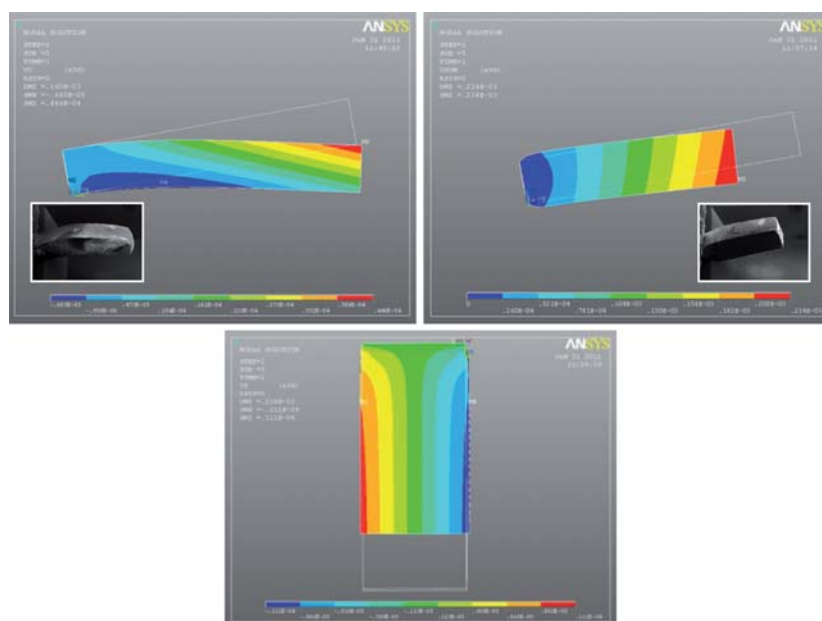


Figure 3.28: Modeling of the bending motion of a LCE-CNT cantilever under illumination where both the contraction and the total displacement of the different nodes are reflected.

Figure 3.28 shows some screenshots during simulations where the total displacement and the final contraction reached by the FE model can be observed. The images above illustrate the initial (rest position) and the final states of the cantilever (under illumination) evidenced by the changes in the sample's inclination; the first ones due to the gravity effect whereas the last, due to the induced contraction. The expansion of the material in the direction perpendicular to the movement is reflected in the image below.

3.4 Discussion and summary

In this chapter the main characterization results and modeling of different LCE-CNT composite samples have been presented with the purpose of general understanding the fundamentals of their mechanical actuation behavior when illuminated by visible light and with the final objective to facilitate the design of future photo-actuators based on LCE-CNTs.

In the first section, different techniques such as X-ray diffraction and DSC, as well as scanning and transmission electron microscopies have been used to analyze the

material conformation. In this manner, the quality of the CNTs dispersion together with their degree of alignment within the LCE matrix have been evaluated resulting in relatively homogeneous composites. No significant effects on the elastomeric matrix behavior have been detected due to the presence of CNTs in such concentrations.

An extensive performance characterization of the material under different conditions has been reported in the second section where the main parameters involving LCE-CNT composites actuation have been evaluated thanks to the "in-situ" observation of the photo-actuation phenomenon. Thus, parameters such as Young and Poisson's coefficients, and the optical absorption spectra were obtained. Both the mechanical strength and stress produced by the contraction of the material under excitation were also evaluated showing no significant difference between contraction induced by heat or by light. However, the concentration of CNTs affects both the mechanical and optical properties of the material, and it is very important for light absorption and subsequently for the parameters of the photo actuation of the material, the excitation speed and the achievable stress. No spectral dependence of the composites was observed, allowing their photo-actuation all over the range from UV to IR light.

Finally, after the characterization of the LCE-CNT samples, a 3D finite element model built for these composites was tuned using the knowledge acquired throughout testing and validated by comparing its prediction against the experimental results obtained during the analysis of the material's bending dynamics under irradiation. In this way, the model would allow predicting changes in the material performance (i.e., deformation achieved, mechanical force, etc.) when subjected to variations of different experimental parameters and represents a powerful tool for future design and optimization of LCE-CNT actuators.

Most part of the characterization work presented in this chapter has been carried out at IMB-CNM facilities as part of the NOMS project in collaboration with different people who helped in the preparation of the different setups used and in better understanding of the results obtained: microscopy analysis was performed in both IMB-CNM cleanroom and UAB microscopy service facilities with the assessment of Dr. Eva M. Campo, Carlos J. Camargo gave technical advice in FEA, and bending

3. LCE-CNT FILMS CHARACTERIZATION

dynamics analysis of the samples as well as optical measurements were guided by Dr. Kirill E. Zinoviev. The synthesis and preparation of the samples as well as both the X-ray and DCS analyses were performed by Dr. Jean E. Marshall and Prof. Eugene M. Terentjev at Cavendish Laboratory (University of Cambridge, UK). As result of such collaborative work, three conference proceedings and two indexed journal papers were successfully published (see publication list at the end of this thesis).

Part II

Design and fabrication of a tactile device

4

“U-shaped” actuators for tactile applications: NOMS device for visually impaired

Since in 1970's, when P. G. de Gennes proposed for the first time the possibility of using LCEs as artificial muscles [90, 118, 142], monodomains of LCE materials have been widely studied leading to a large number of scientific publications and studies, and they have been proposed for the fabrication of active devices [79, 87, 200] due to the big change in shape and length when disorder of LC units is induced by an external stimulus. However, LCE materials should be aligned (in a monodomain) and the mesogens properly oriented in a pre-defined direction. As described at the beginning of this work, the alignment of LCEs before or after the final fixation of the polymer chains in the macromolecule (i.e., final crosslinking) requires the use of external fields which simultaneously shape the material. This requisite strongly affects the use of the LCEs as actuators, and limits the integration into MEMS devices for the fabrication of real-world applications.

Examples for the design and fabrication of LCE actuators in literature can be classified in two different groups as function of the strategy followed for the integration of the LCE materials into the system to give rise to the final actuator: after or before the crosslinking [136]. The first group includes actuators based on the integration of LCE films which have been previously aligned and fully cross-linked. Thus, the shape and dimensions and their corresponding changes are limited to the degree of deformation

4. "U-SHAPED" ACTUATORS FOR TACTILE APPLICATIONS: NOMS DEVICE FOR VISUALLY IMPAIRED

imposed during the synthesis and preparation of such films. Usually, LCE films are obtained by 1D alignment - stretching of the sample before the final crosslinking - (e.g., LCE-CNT films obtained by the well-known stretching method outlined by Küpfer and Finkelmann in 1991, [85], long moving wires obtained by electrospinning [116], etc.) that produces a shortening in the direction of the deformation when the liquid-crystalline order is removed. A microgripper that opens and closes due to application of an electric field [130], a microvalve which pumps a fluid upon heating [128], a heliotropic solar cell [138], as well as a motor [131] are the most relevant reported examples of such type of actuators. The main advantage of these systems lies in that non-complex procedures are required for integration since once fabricated, LCE films can be cut and fixed, even glued on different surfaces to form the final actuator. Moreover, they allow the use of various well-known fabrication processes resulting on one side sufficiently oriented LCE films, and on the other side, the remainder parts of the actuators (i.e., supports, connections, etc.). However, the main limitations of this type of actuators reside in the size, the shape and the type of orientation achieved by the LCE films; factors that are strongly related to the final response of the material (deformation achieved and direction of movement), which are fixed during its preparation.

In contrast, the second group of actuators is based on the opposite concept that consists in the integration into the device of partially cross-linked LCE films which are then oriented and simultaneously cured "in-situ". In this manner it is possible to obtain LCE actuators in more complex shapes, far from the film-like ones, with various types of alignment (not limited to 1D). Thus, different movements (i.e., deformations) can be obtained leading to the fabrication of more elaborated actuators and devices. The main difficulties around these techniques, however, lie in the various procedures involving the LCE preparation, which require a very precise control of the whole device, and the difficulties in handling since, once LCE is weakly cured has the consistency of a gel. Thus, the system should be conceived and fabricated taking into account the shape changes produced on the material during both the alignment and crosslinking processes, which will strongly define the final type and degree of deformation achieved. Unlike the methods in the previous group, however, the main advantage of these techniques is that there is no limitation in shape and size of the actuators obtained neither with the types of orientation defined. Thus, with an accurate

design and the appropriate knowledge of the material, it is possible to design a custom-made fabrication process to reach the desired response for the material from the early beginning of the process.

Due to their complexity, such actuators are less common in literature; nevertheless there are some interesting examples. Keller and co-workers developed micron-sized thermo-responsive LCE actuators on a substrate by replica molding [112] whereas Jiang et al. reported an electro-thermally driven photonic crystal based on the combination of nematic materials, able to shift the Bragg-diffraction peak under actuation [201]. Both types of integration strategies identified are summarized in Table 4.1.

Table 4.1: Main characteristics of both types of integration strategies identified.

Integration strategy	Alignment	Shape & size	Deformation	References
After crosslinking	1D	thin films	already fixed	Yamada <i>et al.</i> 2008 [131]
			contraction	Sánchez-Ferrer <i>et al.</i> 2009 [130]
				Sánchez-Ferrer <i>et al.</i> 2011 [128]
				Li <i>et al.</i> 2012 [138]
Before crosslinking	3D	others	“in-situ” fixed	Buguin <i>et al.</i> 2006 [112]
			contraction/expansion	Jiang <i>et al.</i> 2009 [201]

From all the examples of LCE actuators reported in literature, however, none of them was conceived for tactile applications, probably due to the high number of restrictions limiting its design. To adapt LCE actuators to tactile applications, other and not less important aspects should be borne in mind. Together with short actuation times, relatively large displacements and reasonable forces, these actuators should fulfill other requirements among which the ones related to the tactile perception and safety play an important role: i) to have a surface gentle to the touch which reduces the actuator’s wear due to the friction with fingers; ii) to guarantee a reasonably-long useful lifetime due to a repeated actuation with several contraction and expansion cycles; iii) to have a design which bears finger forces against the movement of the actuator and maintains the deformation level of the material and its actuation ability; iv) to be safe for the end users in terms of over-heating and leakage currents, etc. The power consumption and energy efficiency are also important points to consider.

4. "U-SHAPED" ACTUATORS FOR TACTILE APPLICATIONS: NOMS DEVICE FOR VISUALLY IMPAIRED

The list of parameters to consider becomes larger and more restrictive when the actuators should be designed to reproduce Braille characters (see appendix A.2). In that case, restrictions on their geometry and their distribution in an array should be added to the previous list to allow the correct transmission of information through Braille code, resulting in a big challenge for the scientific community to develop new solutions to solve all these issues in only one device.

With the ultimate goal of developing a tactile device for Braille applications [48], a new actuator approach based on the integration of fully cross-linked LCE-CNT films was developed: a "U-shape" actuator. This chapter presents the design and characterization of the actuators and their integration on a fully-functional device. Due to its extension, the work in this chapter has been divided in two parts: a first part where the working principle, the main characteristics and the first characterization results of such new "U-shape" actuators are described, and a second part, where the operation principle of the device, a description of the developed system and its parts together with its operation performance are explored. The present work was developed within the frame of a European project named NOMS. At the end of the chapter, a detailed list of the partners and their corresponding contribution to this work is provided.

Design, fabrication and characterization of "U-shape" actuators

4.1 Concept and working principle of the actuator

During the LCE-CNT films characterization in previous chapter, Chapter 3, it was demonstrated that under an appropriate illumination, an LCE-CNT sample can produce a wide range of stresses with measured forces ranging from 10 mN to 65 mN, as function of the section and length of the sample, the power applied and especially to the preparation process (stretching and alignment), the key-step to obtain samples with good actuation characteristics. Taking into account the above mentioned requirements for the fabrication of tactile devices as well as Braille restrictions (see appendix A), and considering the different integration strategies, a novel approach for the fabrication of actuators was devised based on the use of a fully cross-linked LCE-CNT film in a "U-shape" configuration, illuminating from the underneath as

4.1 Concept and working principle of the actuator

shown in Figure 4.1 -left-. In this manner, it is possible to take advantage of the stress gradient generated in the film under illumination to induce movement on a movable component. Hence, when illuminated, the film contracts pushing an element, such as a ball or a piston, inserted in the cavity upward producing a vertical displacement, d , which can be at the same time used to exert a force. In that particular case, such vertical displacement (i.e., force) can be used to transmit tactile information in haptic and Braille systems where such pushing element will directly act as the moving Braille component.

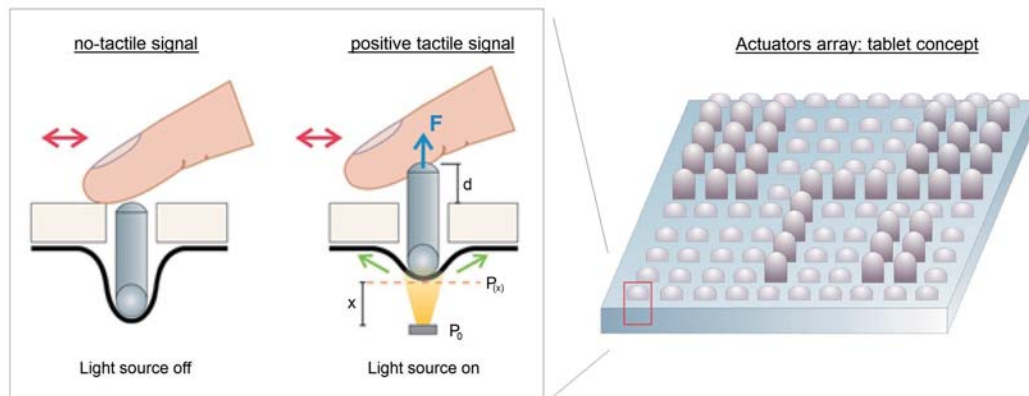


Figure 4.1: "U-shape" actuator concept. Under illumination, the stress gradient within the LCE-CNT film produces a vertical displacement d on a pushing element, resulting in a positive tactile signal -left-. An array of such actuators will lead the final tactile device -right-.

By using this actuator configuration, it is possible to arrange arrays of "U-shape" actuators leading to a compact and light tactile device (Figure 4.1 -right-) with resultant forces, F , under illumination which are large enough to produce the minimum displacement of the pin required to ensure correct tactile perception (see appendix A).

As proof of concept, a first non-optimized prototype of the "U-shape" actuator was developed to check its viability and to determine its main actuation parameters. A schematic representation of the actuator is depicted in Figure 4.2 where the actuator and all its components can be distinguished. A film of 2 mm long and 0.3 mm wide containing 0.3 wt.% of CNTs was cut and doubled to have a "U-shape" and its ends were fixed on a home-made PMMA support. The film curvature, ρ , was manually fixed during the assembly process approximately to 2.5 mm. Two PTFE tubes of 5 mm

4. "U-SHAPED" ACTUATORS FOR TACTILE APPLICATIONS: NOMS DEVICE FOR VISUALLY IMPAIRED

length and 1.6 mm of diameter were used as pushing elements allowing higher force transmission and at the same time, avoiding material damage. One of the tubes was introduced into the cavity formed by the foil in such a way that when illuminated, the foil flattens pushing it up. Conversely, the other tube was vertically placed just above the first tube inside a cavity previously micromachined on the PMMA support, ensuring a correct positioning of both elements. This last one named hereinafter pin, is the element which will provide the tactile signal.

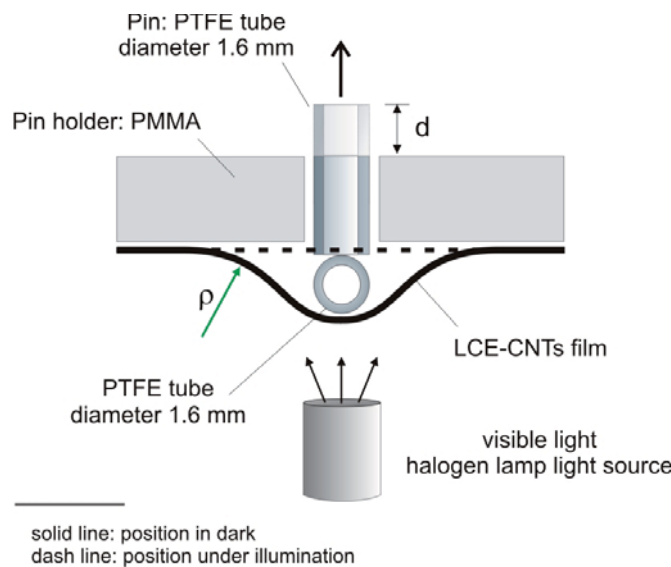


Figure 4.2: Schematic representation of the first version of the "U-shape" actuator.

PTFE was selected because of its lightness and bad adherence to ensure a correct transmission of forces and the desired displacement of the pin. In this way, the dead weight of the pins can be negligible compared to the shrinkage force of the film (less than 0.2% of its averaged value), thus preserving proper operation of the mechanism.

Figure 4.3 shows two images of the "U-shape" actuator captured before -left- and during -right- illumination; a visual proof of concept that illustrates the potential of such type of actuators. As a light source, a halogen lamp (visible light) equipped with a dual-arm fiber optic illuminator was chosen as light source to better direct the light to the surface of the sample. The end of the optical fiber was placed approximately 1 cm below the sample to ensure the illumination of the whole sample. Additionally, to reduce the amount of light captured by the camera and thus avoiding dazzle effects, a band-pass filter was added. To better appreciate the vertical displacement produced,

4.2 Characterization of the "U-shape" actuator

a glass slide of 15 mm × 15 mm × 0.15 mm was placed on top of the PMMA support directly in contact with the pin. A vertical displacement of about 2 mm was measured.



Figure 4.3: Images captured during the actuation of the first "U-shape" prototype as proof of concept.

As demonstrated during the characterization of the material in Chapter 3, the energy required for the actuation of LCE-CNT films is about several hundreds of mJ , calculated taking into account response time of the actuator and power of light flux. Considering the shape and curvature of the film, the force produced by the pin in this first prototype was estimated around 20 mN, value which resulted not bad considering that the actuator and the components were still not optimized. The redesign and optimization of the different components was later performed prior to the fabrication of the tactile device (second part of the present chapter).

4.2 Characterization of the "U-shape" actuator

4.2.1 Setup configuration for testing

Once verified the potential of this type of actuator, different testing measurements were carried out to study the performance of the "U-shape" actuator and thus obtain its main working parameters: mainly the vertical force exerted by the pin (for the moment, the PTFE tube) due to film shrinkage as function of the power applied as well as the actuation time and displacement.

For that purpose, an experimental setup similar to the one used for the force measurements on LCE-CNT films was used (see Figure 3.17 in Chapter 3). However, in this case the dynamometer was vertically positioned above the actuators, contacting its

4. "U-SHAPED" ACTUATORS FOR TACTILE APPLICATIONS: NOMS DEVICE FOR VISUALLY IMPAIRED

tip with the top surface of the pin. In this manner, a direct measurement of the exerted force was obtained. To assure a correct relative positioning between the dynamometer tip and the pins, three micro-translational stages were used, now manually controlled. The measured parameters were in real-time monitored by using the same LabVIEW data acquisition program previously developed. Images in Figure 4.4 show front and oblique views of the setup used.

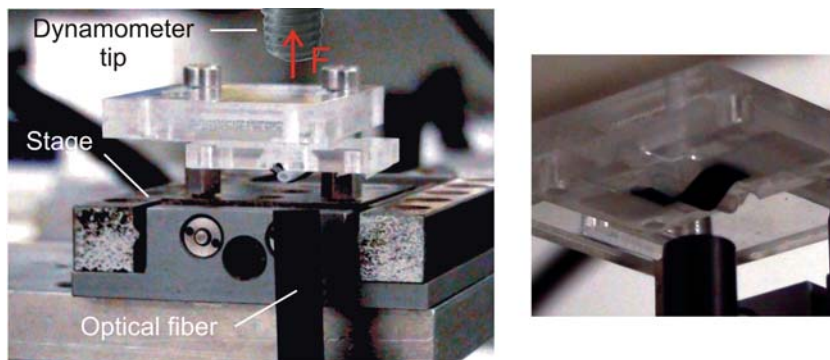


Figure 4.4: Setup used for "U-shape" actuator testing. Front and oblique views.

4.2.2 Photomechanical actuation

The photomechanical response of different "U-shape" actuators assembled under the same conditions was analyzed by measuring the forces exerted by the pins during the films contraction under illumination as function of the current intensity applied since, as demonstrated during the LCE-CNT films characterization, the response of such composites (mainly the stress) has an intimate relationship with the applied energy.

Before starting with the force measurements, however, some considerations should be taken into account, specially the ones related to the setup configuration since it has been demonstrated to have a strong influence on the results.

4.2.2.1 Influence of distance

First of all, the distance between the top surface of the pins and the dynamometer tip, set as d , was analyzed. Therefore, the same setup described above was used, fixing three different distances: $d= 0.0$ mm, 0.5 mm and 1.0 mm. In all cases, the distance between the light source (white light LED) and the bottom surface of the "U-shaped"

4.2 Characterization of the "U-shape" actuator

film was set at 2 mm. Figure 4.5 shows the time diagrams of the force produced by a pin at four different current intensities evidencing the influence of the distance d on the results obtained and thus, the need of an accurate setup since small variations in the positioning of the elements may produce important measurement errors.

As can be seen in the graphs, high current intensities were required for testing (from 200 to 350) mA in order to obtain at least 10 mN force for $d = 1.0$ mm (high distance). This fact is due to the wide angular intensity distribution of the light source which induces important reduction of the power density.

The influence of other parameters such as current intensity applied and the irradiation times on the actuator performance are discussed in the following sections.

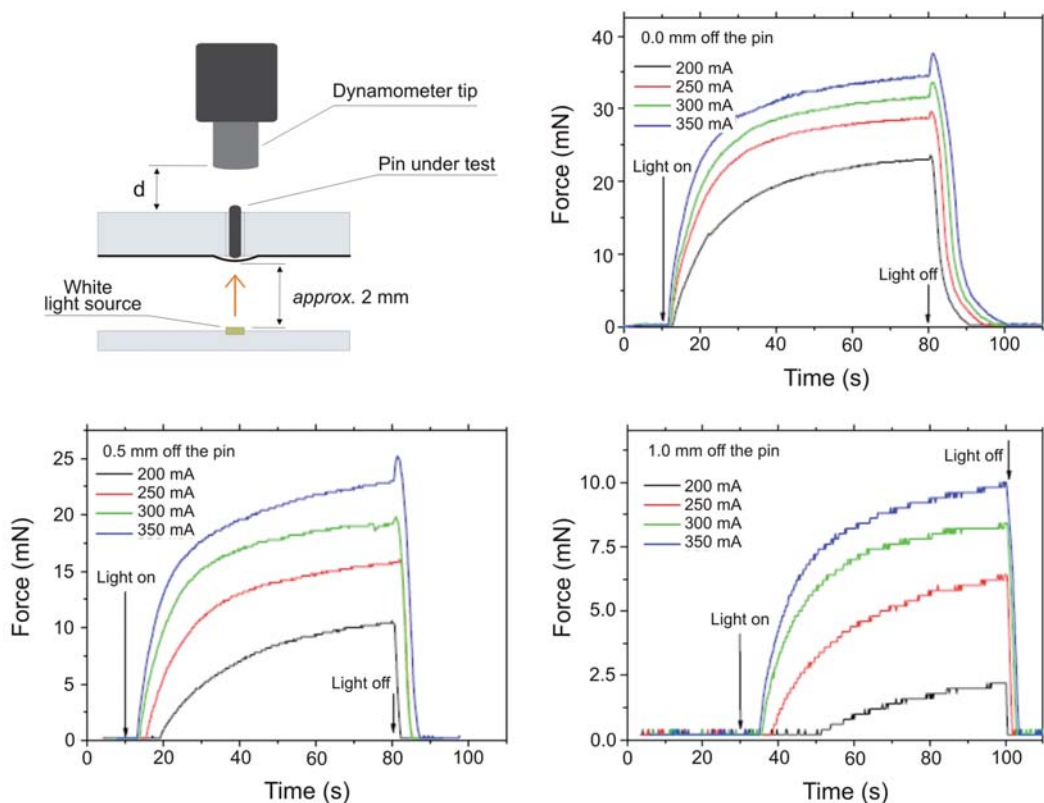


Figure 4.5: Sketch of the experimental setup for characterization of "U-shape" actuator stroke and force. Time diagrams of the force produced by a pin at four different current intensities. With the light source switched off, the tip of the dynamometer was 0 mm, 0.5 mm, and 1.0 mm off the pin.

4. "U-SHAPED" ACTUATORS FOR TACTILE APPLICATIONS: NOMS DEVICE FOR VISUALLY IMPAIRED

4.2.2.2 Force measurements

Taking into account the setup considerations above, force measurements of five different "U-shape" actuators were performed setting the distance $d = 0.0mm$. All the actuators were assembled using SCLCE films with 0.3 wt.% of CNT content and an averaged thickness of 0.2 mm. All the samples used were from the same batch, thus prepared under the same conditions to guarantee homogeneity on the material response while minimizing the differences in contraction (maximum force produced). In this case, the same 660 nm wavelength LD used for the bending dynamics study in Chapter 3 was used as light source to have a well-known Gaussian intensity distribution with low angular aperture, with working intensities ranging from 50 mA to 210 mA. Graph in Figure 4.6 plots the averaged force values from five "on-off" cycles as function of the current intensity applied for the five actuators measured, evidencing a clear dependence between these two parameters.

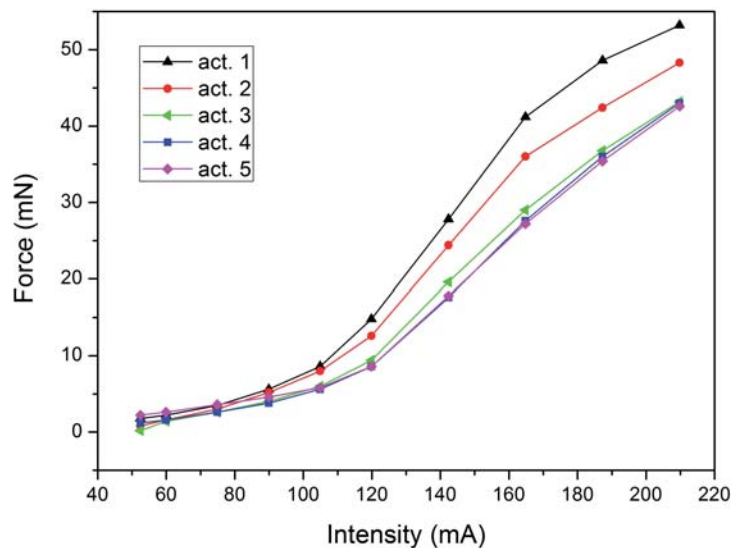


Figure 4.6: Time diagrams of the averaged actuation force measured as function of the current intensity applied for five different "U-shape" actuators. All LCE-CNT samples had 0.3 wt.% of CNTs.

It has to be noted that, even all the LCE-CNT samples came from the same preparation batch, a significant variation in the actuation force was obtained when comparing the measured values, resulting in 12 mN of variation. Differences in the individual assembly of the "U-shape" actuators which is completely manual process,

as well as some static and dynamic friction effects between the elastomeric films, the surface of the pins and the lateral walls of the support elements, can explain these variations.

However, the force values obtained were in all cases bigger than 15 mN, which is the minimum established value to guarantee a correct tactile perception (see appendix A). Later, the performance of the actuators was optimized by means of dynamic actuation. In this manner, a reduction of the power consumption during actuation was achieved while the minimum force maintained.

4.3 Optimization of the "U-shape" actuator

It has been demonstrated that the "U-shape" actuator proposed can be used as pushing actuator, since a good response in terms of actuation force is obtained, which results stable in time and gradually increases as function of the current intensity applied in similarity with previous measurements on LCE-CNT films. However, thinking about its future application in tactile devices, and especially for displaying Braille characters, the actuator should be optimized. In this sense, aspects such as the contact between the human finger and the pin, the transmitted forces, and the energy required for actuation have been evaluated. The dynamic performance and cyclic testing were also evaluated to complete the characterization of the actuator and thus improve its performance.

4.3.1 Contact between the finger and the pin. Transmitted force and required energy

One of the first aspects to take into account before starting with the optimization of the actuator is the transmission of forces, and specifically, the interaction produced between the pin and the fingertip.

The mechanical reaction of a fingertip to a normal contact with rigid planar surface has been widely studied and modeled [202, 203, 204]; however such models are usually valid only for one load distribution since they do not extend easily to other boundary conditions neither give any details about the stress distribution inside the tissues due to its highly complex structure [205]. A very brief introduction about tactile perception mechanisms on a fingertip and the main mechanoreceptors involving sense of touch can be found in appendix A to show the complexity of the human body.

4. "U-SHAPED" ACTUATORS FOR TACTILE APPLICATIONS: NOMS DEVICE FOR VISUALLY IMPAIRED

According to the literature, in order for a human being to sense with a fingertip a bump on a flat surface, the height of the bump should extend about $300 \mu\text{m}$ above that surface although differences of only few microns can be distinguished by comparing various surfaces, and at the same time, the pressure exerted by the finger on the bump should be at least 30 kPa to 40 kPa for its correct perception. This means that if one pushes down a pin with its fingertip which has a flat top area of 1 mm^2 and extends over $300 \mu\text{m}$ above a surface, then the pin should be able to withstand a force of about 30 mN. This is the force that should be provided from underneath the pin (i.e., force produced by the LCE-CNT film in this particular case) in order to support the pin itself under the finger pressure and keep it raised, as depicted in Figure 4.7a, value which is proportional to the stress induced by the film under illumination.

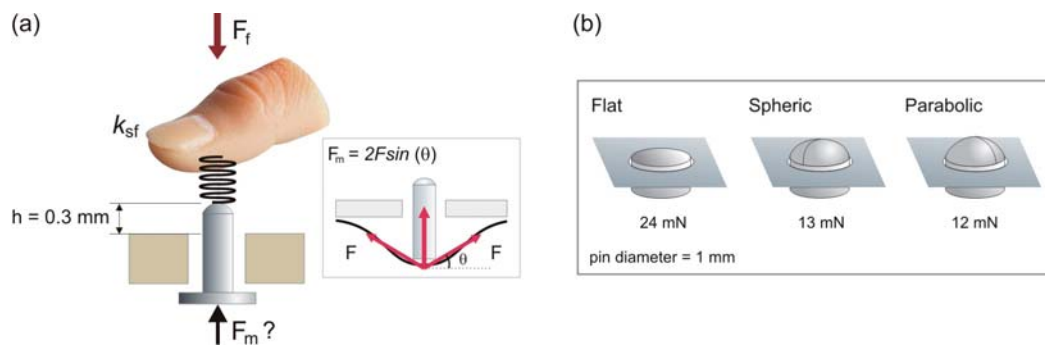


Figure 4.7: Contact between fingertip and the top surface of a pin. a) Schematics of the forces. b) The force required to maintain the pin in the active state as function of the shape of its top surface. For a rounded pin, the force is the half of the required for a flattened one.

The pressure produced by finger can be modeled as a pressure produced by a spring with a constant k_{sf} , which linearly increases with the force, resulting in an exponential form for the force-displacement curve when measured in quasi-static conditions:

$$k_{sf} = \frac{dF_m}{dh} = aF_m + b;$$

$$F_m = \frac{b}{a}(e^{(h-h_0)} - 1);$$

where h_0 is the initial position for which the force is null. Taking into account the values above mentioned, the spring constant of the finger tissue can be calculated to

be approximately $k_{sf} = 100N \cdot m^{-1}$. From the point of view of the curvature of the film, the projection of force is proportional to $\sin(\theta)$ term, then the most efficient geometry would be a design with vertical walls.

The force required to keep the pin actuated (i.e., in a raised position) depends, at the same time, on the shape of the top surface of the pin (see Figure 4.7b). However, the high deformability of the fingertip also facilitates establishing large contact areas between the skin and the object being touched even with low forces. The friction of the skin directly depends on the contact area in between, and at the same time, larger contact area enables easier control of the grip force. Thus, a rounded top surface of that contact element is always preferable as significantly reduces the force applied by the finger on it.

The deformability of the skin is also a key-factor in the large compliance of the fingertip. Measurements have shown that shearing the skin can lead to 100% of deformation without any damage, yet the Young's modulus remains relatively high $Y \approx 1$ MPa [206]. During lateral motion, a single bump on the surface can yield a skin stretch larger than 30% [207].

In order to bring the pin up to the "active" position (produce positive tactile signal) some energy is required. This energy can be calculated as a sum of the potential energy of the stressed spring (in this case, the finger skin) and the potential energy required in order to raise the pin of mass m by at least $300 \mu m$.

$$E_{min} = \frac{1}{2}k_{sf}h_0^2 + mgh_0P$$

That is the minimal mechanical energy required for operation of a single actuator in the ideal case, resulting in a value of about $7.5 \mu J$ if the pin weights 1 g. Thus, the energy required to maintain the mechanism under the pin in active position, E_0 , should be more than E_m , leading to the efficiency of the system as of E_m to E_0 .

All of that leads to the following conclusions:

- the geometry of the pin highly influences the transmission of forces. Thus, a pin with a rounded top surface helps reducing the minimum force required while ensuring good contact with the fingertip.
- the pin should be fabricated on a lightweight material in order to minimize its own weight (i.e., increase the vertical component of the force exerted by the

4. "U-SHAPED" ACTUATORS FOR TACTILE APPLICATIONS: NOMS DEVICE FOR VISUALLY IMPAIRED

material when contracted) and thus, reduce the total amount of energy required to raise it up.

- the pin should raise up a minimum height of 300 microns from the surface of the device to be correctly perceived. However, such value can be diminished in case of Braille reading, since the system is based on a comparison between raised and absent elements.

4.3.2 Intensity of light applied

4.3.2.1 Dynamic testing

Dynamic performance of "U-shape" actuators was proposed to adjust the actuation parameters and thus reduce the power consumption while maintaining the actuation forces. To that end, different power ramps were applied to shape the response curve of the actuators as desired. In this case, that means a boost of energy to quickly push the pin up followed by providing just sufficient energy to maintain it on a raised position (stable) allowing its correct reading. In this manner, it is possible to minimize the power consumption avoiding degradation of the material due to an over-exposure to light. Thus, parameters such as power, P_i , and time, t_i were evaluated to obtain an optimum power ramp.

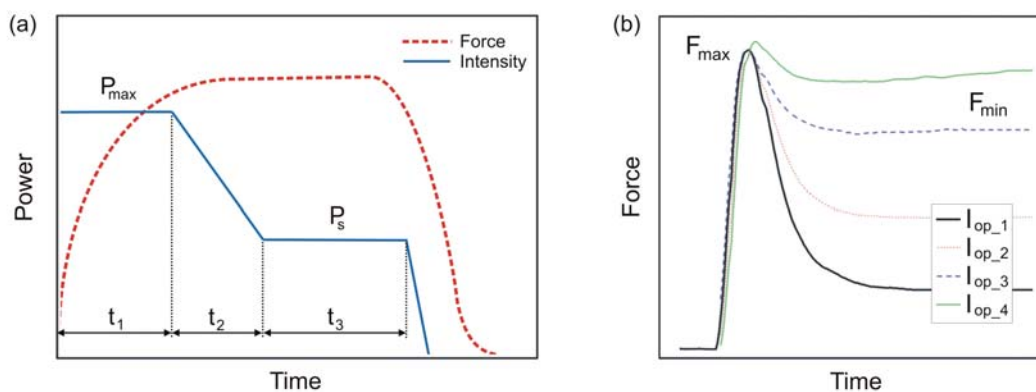


Figure 4.8: Schematic representation of one actuation cycle for the optimization of the actuator response, where the different testing parameters are depicted. (a) Example of the power ramps applied to guarantee a correct actuation of the pins, and (b) corresponding results showing the equivalent real force obtained.

4.3 Optimization of the "U-shape" actuator

Plot schemes in Figure 4.8 show one of the power ramps used for testing (Figure 4.8a) as well as the corresponding force responses obtained (Figure 4.8b) where the different testing parameters can be identified. High power P_{max} during t_1 seconds was applied first to quickly lift up the pin, movement producing a maximum force, F_{max} . Such energy boost was followed by a t_2 seconds of long descending ramp resulting in an operating current I_{op} (and its equivalence in power, P_s) providing for the pin to maintain certain force, F_{min} . This final intensity level, I_{op} , represents the amount of energy necessary to guarantee the raised position of the pin. The force produced by pins from different assembled "U-shape" actuators was measured using the setup schematically shown in Figure 4.5 above. However, in the present experiment the dynamometer tip was located slightly less than 0.1 mm above the pin to ensure a proper contact, and thus avoiding misreading values due to differences in the rest position of the different pins tested (manual assembly process).

Plots in Figure 4.9 depict the force dynamics obtained as function of I_{op} (i.e., P_s) values for different t_1 times) measured using 0.1 wt.% LCE-CNT samples. The measurements were carried out maintaining the same P_{max} value throughout the whole test (202.29 mA of equivalent current intensity), and thus ensuring $F_{max} = 22.8$ mN, value which remained constant throughout the whole experiment as can be seen in the graph in Figure 4.9 -left-. The different experimental values selected testing for the rest of parameters are shown in Table 4.2.

Table 4.2: Experimental values selected for dynamic testing.

Fixed parameters	Variable parameters
$t_2 = 3000$ ms	$t_1 = 2000$ ms, 3000 ms, 5000 ms, 7000 ms, 9000 ms
$t_3 = 5000$ ms	$I_{op} = 50$ mA, 75 mA, 100 mA, 125 mA, 150 mA

Finally, the measurements were repeated using different values of excitation energy, product of power P_{max} and time t_1 . As expected, the results showed a clear dependence between the actuation force and the operating current in a similar way than obtained during the LCE-CNT films characterization in Chapter 3, evidencing the need of adjusting the working parameters to reach the desired forces while reducing the power consumption.

4. "U-SHAPED" ACTUATORS FOR TACTILE APPLICATIONS: NOMS DEVICE FOR VISUALLY IMPAIRED

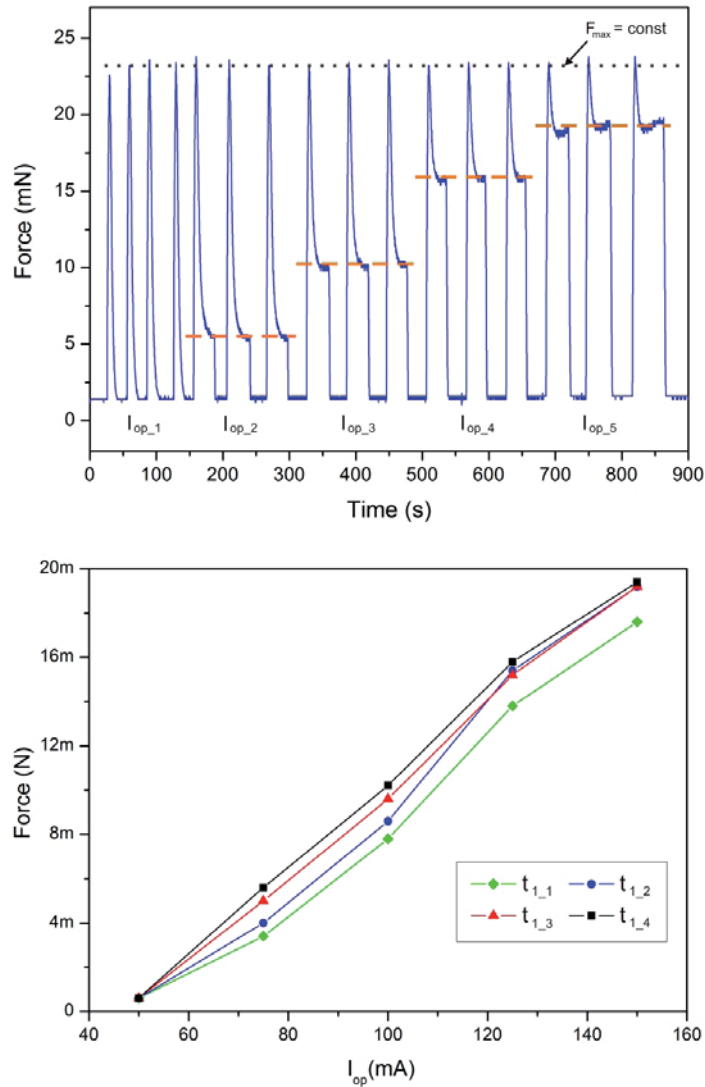


Figure 4.9: Dynamic testing for the same 0.1 wt.% LCE-CNT sample, where the influence of the different operating parameters can be observed.

In spite of that, however, using this first prototype, the minimum I_{op} value required to ensure a correct and stable raised position for the pin producing the minimum actuation force required (15 mN) resulted in the range between 125 mA to 150 mA, a relatively high value thinking on the fabrication of the tactile device, in which an array of several "U-shape" actuators will be working in parallel. In this sense, some efforts should be put on optimizing the overall design and the different components of the actuator.

4.3.2.2 Cyclic testing

To complete the measurements ensuring a good actuator performance over time (constant and stable pin behavior) and to check the material viability and repeatability of actuation, some fatigue tests were performed. As a first approach, tests of 100 cycles were established using lower power values for P_{max} and P_s , with corresponding current intensities of 172.32 mA and 74.92 mA, to avoid samples damage. The corresponding actuation times, t_1 , t_2 and t_3 , were fixed to 3000 ms, 5000 ms and 7000 ms respectively whereas a new parameter, $t_4 = 5000$ ms, was added to control the delay between consecutive cycles. During this time, the pin remained on a rest position without exerting any force. However, a minimum power was applied to avoid undesired peaks due to the continuous on-off switching.

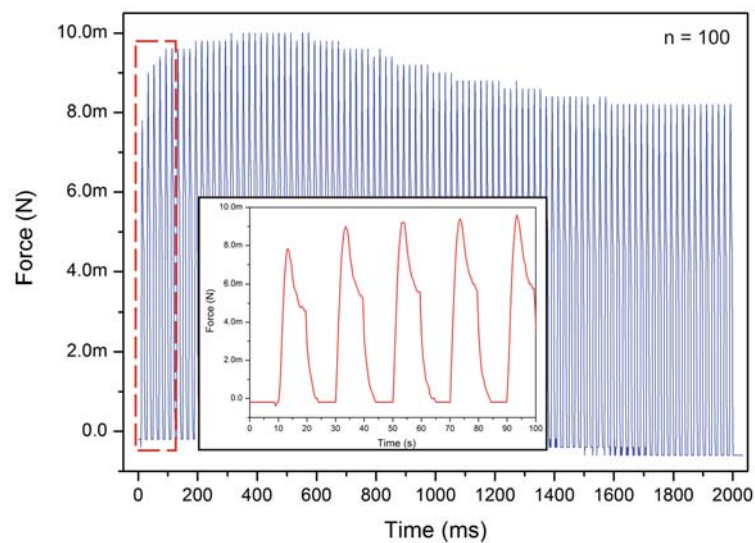


Figure 4.10: Cyclic actuation test of a "U-shape" actuator for $n = 100$ cycles. The inset depicts in detail the first five cycles run, where the different parts of the cycle (on-off switching) can be observed.

Figure 4.10 shows an example of the recorded pin behavior during cyclic tests (non-optimized power). As can be seen, the maximum force achieved in each cycle did not remain constant. After the first cycles, the force reached a maximum value of 9.8 mN, which decreased to 8.2 mN where remained constant until the end of the experiment. Such decrease represents a force variation of 16 %.

4. "U-SHAPED" ACTUATORS FOR TACTILE APPLICATIONS: NOMS DEVICE FOR VISUALLY IMPAIRED

Such decay was also observed after continuous strength and force measurements during the characterization of different LCE-CNT films in Chapter 3 and can be explained by the viscoelastic nature of the material. At early stage of the experiment, practically all the energy which is delivered to the sample is directly converted into heat and such heat in motion, reaching the maximum value just after a few cycles. However, as the experiment continues, some amount of energy was absorbed by the material. Notice that the minimum force value also experienced negative variation. Finally, after some cycles, the system reaches again the thermal equilibrium, keeping ΔF and ΔT constant.

In order to verify the actuators stability, same cyclic measurements were repeated in time at different days and weeks, even some months later. Neither actuation differences nor material damage was observed. However, few variations in force obtained were observed for the same actuator under same testing parameters (same power and times) due to the setup even always was calibrated before starting the measurements. Small variations in the relative position between the dynamometer tip and the top surface of the pin may produce noticeable differences.

4.3.3 Light source efficiency

It has to be mentioned that another important factor to take into account for the optimization of the actuator response is the light source. The selection of a good light source is very important since a uniform illumination of the film is necessary in order to reach a proper actuation response. Ideally, the LCE-CNT film should be illuminated from both sides, thus avoiding temperature gradients and in consequence, bending motion as in the case of cantilever studied in previous Chapter 3. Hence, the ideal design would be with two light sources mounted vertically on both sides of the actuator film. Their close location and illumination with minimal optical power loss would enhance the efficiency of the device and reduce the power consumption. However, by using this option, the actuator should be completely redesigned including a more complex vertical structure to allocate the light sources and their corresponding electronics, increasing the distance between two consecutive actuators in the array; fact which is not valid for Braille representation due to the restrictive spatial distribution

of the elements forming the different characters (see brief Braille notions in Appendix A.2).

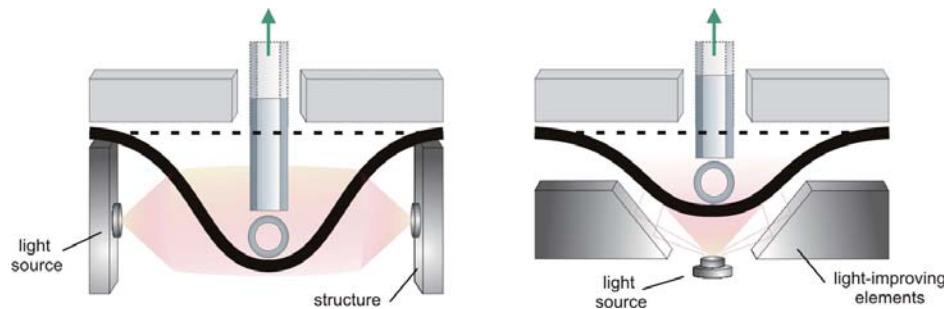


Figure 4.11: Strategies for the improvement of the "U-shape" actuator design with enhanced efficiency and reduced power consumption.

Another approach would be maintaining the actual design with only one light source but reducing its numerical aperture, thus increasing the power density delivered to the LCE-CNT film and diminishing the energy losses. In addition, special elements for light collection such as concentrators and diffractive structures can be used to improve the light path and focus it directly on the film. Both strategies are schematically depicted in Figure 4.11. The second approach purposed was selected for the fabrication of an optimized version of the "U-shape" actuator which is deeply discussed in the next part of the present chapter.

Actuator optimization and integration on a tactile device

From the first characterization results and after analyzing the influence of the different elements on the actuator performance, a new version of the "U-shape" actuator was conceived following the same concept and working principle but taking into account its later integration on a tactile device. Thus all the elements, such as the pin, the supports, as well as the light source, were optimized to reduce the power consumption of the system while maintaining or even improving the actuation force.

In this second part of the chapter, the final version of the actuator with all its components is presented together with the development of a tactile device for Braille application based on an array of such actuators: the NOMS device. The operation

4. "U-SHAPED" ACTUATORS FOR TACTILE APPLICATIONS: NOMS DEVICE FOR VISUALLY IMPAIRED

principle of the device, description of the developed system and its parts and its operation performance are explored.

4.4 Final "U-shape" actuator design

A detailed scheme of an assembled "U-shape" actuator with all its components is depicted in Figure 4.12. The other elements included: i) a ribbon of nematic LCE-CNT material, ii) the pin, iii) two different support layers: the top layer through which the pins move and the bottom layer enclosing the light source, iv) the light source, and v) arrays of micro-lenses casted on the surface of polyethylene terephthalate, PET, films.

The main characteristics of each component are described below. Figures 4.13 and 4.14 show pictures of these components.

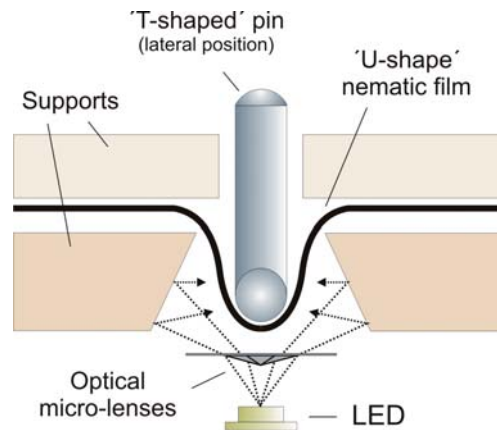


Figure 4.12: Detailed cross-section of the final version of "U-shape" actuator for its integration on a tactile device with all of its components.

4.4.1 Ribbon of nematic LCE-CNT material

For the fabrication of the final "U-shape" actuators, 1.2 mm wide LCE-CNT ribbons with thicknesses of between 0.3 mm and 0.4 mm were chosen. Similar to the preliminary "U-shape" actuator design, a batch containing several LCE-CNT films were first synthesized, aligned, and cross-linked at UCAM facilities following the previously described stretching method. According to the previous photoactuation measurements, the CNT content was set to 0.1 wt.% to be the most suitable concentration, in agreement with [81].

After completing the curing process, the resulting films were carefully cut using a blade to get the desired ribbons which were systematically characterized before the assembly of the actuators to ensure their correct operation. The mean values obtained of the basic LCE-CNT parameters measured for these samples are summarized in table 4.3. For details on the synthesis, preparation and characterization of the LCE films see chapters 2 and 3 in section I.

Table 4.3: Values of the basic LCE-CNT parameters measured.

Material properties	Values
Young's modulus	0.3 - 0.5 MPa
Poisson's ration	0.5
Heat capacity	$2.6 \times 10^5 Jm^{-3}K^{-1}$
Thermal conductivity	$0.4 Wm^{-1}K^{-1}$
Yield stress	100 kPa

4.4.2 The pins: elements in contact with human finger

'T-shaped' pins of 0.8 mm in diameter and 3.0 mm long with rounded edges were designed and fabricated via injection molding and placed inverted on top of the LCE-CNT ribbon to maximize the contact area and to allow higher force transmission. The mechanical contact between these two elements was carefully studied to avoid material damage. In this manner, polyoxymethylene, POM, was selected for the fabrication of the pins due to its lightness and lower roughness. Therefore, the dead weight of pins (in average 11.95 μg) can be neglected compared to the shrinkage force of the ribbon, thus preserving proper operation of the mechanism above described (first part of the present Chapter).

All the pin edges were rounded to avoid material damage. In agreement with the previous studies the top surface of the pin was also rounded to minimize the contact area and thus, reduce the force applied by the fingertip on the pin.

4.4.3 Support layers

To ensure vertical positioning of the pins and their permanent contact with the ribbon while protecting the material from dust, a PMMA support was added on top. In addition, another support made in aluminum with micro-machined reflecting facets

4. "U-SHAPED" ACTUATORS FOR TACTILE APPLICATIONS: NOMS DEVICE FOR VISUALLY IMPAIRED

was placed at the bottom to fix the LCE-CNT ribbons and at the same time, optimize the light path. All these elements were assembled layer by layer, forming the actuation board, where different actuators can be arranged in parallel, forming an array. In this way, damaged elements can be easily replaced.

From the design stage of the device, the possibility that end-users could damage the actuator during usage was taken into account. For that reason, the thickness of the top support layer was carefully adjusted to 2.5 mm to restrict the vertical displacement of the pin towards the LCE-CNT ribbon (negative vertical displacement) to a certain distance, limiting the amount of force the user can exert against it and, consequently, avoiding possible material damage. Therefore, end-users can only push the pin down until reaching the top surface of the device, which acts not only as a protection layer but also as a blocker.

4.4.4 Light source selection

The optical output of a light source varies significantly with its size, the power and the optical output beam shape. Thus, the selection of the light source should be based on the specific optical requirements of the LCE-CNT nanocomposite. Moreover, in this approach, the light source should also have a reduced packaging due to size restrictions for Braille characters representation.

An initial scan of the available light sources on the market was performed to choose the best option. Several Surface-Mount, SM, light source package sizes were identified that could realistically be used for the fabrication of the Braille device allowing a high integration rate. However, the optical output provided drops significantly when scaling down the size of the light sources. Thus, a compromise between the output power and the packaging size should be adopted.

Potential IR light emitting diodes, LED, (SFH 4235, OSRAM GmbH) were identified to offer enough optical performance to actuate the LCE-CNT ribbons (~ 630 mW). However, a quite large packaging (7.5 mm of pitch between consecutive light sources) together with the system overheating (high density of light sources per square centimeter) makes them not suitable for the current application.

VCSELs, Vertical Cavity Surface Emitting Laser, light sources were also considered as possible sources since allow achieving a better balance between resolution and

optical power than LEDs, offering small packages. However, they were dismissed due to reduced optical output per area as well as for their higher costs compared to LEDs, the prices of which are dropping rapidly due to their increased use for daily lighting applications.

According to the characterization results detailed in Chapter 3, LCE-CNT ribbons demonstrated actuation from ~ 100 mW of optical power, fact that permitted the selection of small light sources (smaller package close to Braille standard resolution) with lower optical powers, reducing overheating problems. Moreover, the incorporation of CNTs enables light absorption along all the visible spectra, leading to the selection of light sources safety for human eye.

As a result, a 2.04 mm x 1.64 mm x 0.70 mm cool-white LED (LUXEON-C, Philips) was chosen as light source. Its high compactness guarantees the required pitch for Braille characters representation (2.5 mm), as well as provides enough power to the material to obtain the desired forces (1 W of electrical input with nearly 0.3 W of optical output power).

Pictures in Figure 4.13 show the above detailed components of the actuators designed.

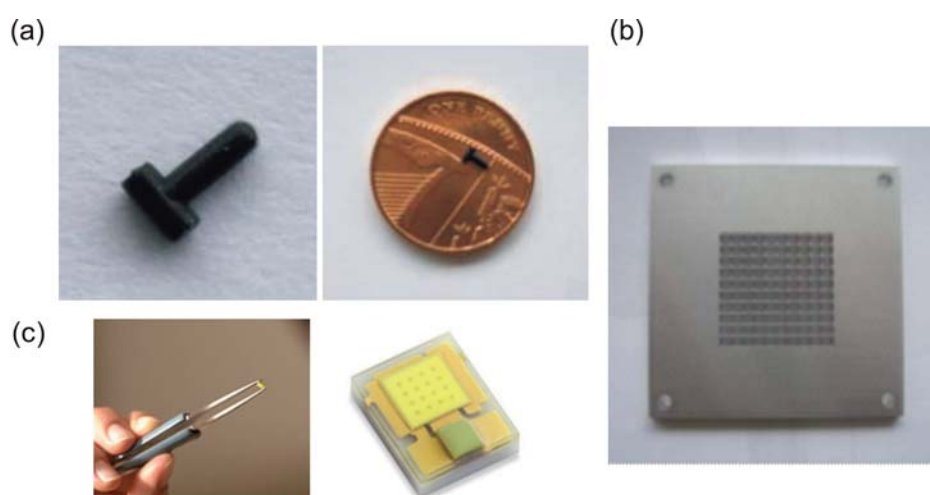


Figure 4.13: Different actuator components. (a) Molded POM pin -left- and same pin illustrated on a penny coin -right-, (b) refractive support, (c) LUXEON-C LED.

4. "U-SHAPED" ACTUATORS FOR TACTILE APPLICATIONS: NOMS DEVICE FOR VISUALLY IMPAIRED

4.4.5 Optical micro-lenses

According to the light source characteristics, the incorporation of other optical elements was required to concentrate and direct the light correctly to the "U-shaped" ribbon base and thus optimize the light efficiency of the system. For that purpose, a combination of collimating and focusing micro-lenses was designed and fabricated on PET by casting techniques. EZcom (Eldim) optical simulation software was used to adjust the design of the lenses and optimize their effect on the system, taking into account the specifications of both the light source and the material. A first foil containing collimating micro-lenses was mounted just above the LEDs facing downwards to vertically direct the light towards the LCE-CNT ribbon. For that reason, a combination of refractive and reflective symmetrical facets was used. In addition, a second foil containing focusing micro-lenses was mounted facing upwards, directly above the collimating lens, to correctly distribute the light to the center sides of the LCE-CNT ribbon and not to the ends. In that case, a combination of diverging and converging facets was used. Figure 4.14a shows a detail of the first rings of the Fresnel micro-lens as well as a picture of the fabricated foils containing the micro-lens array (Figure 4.14b).

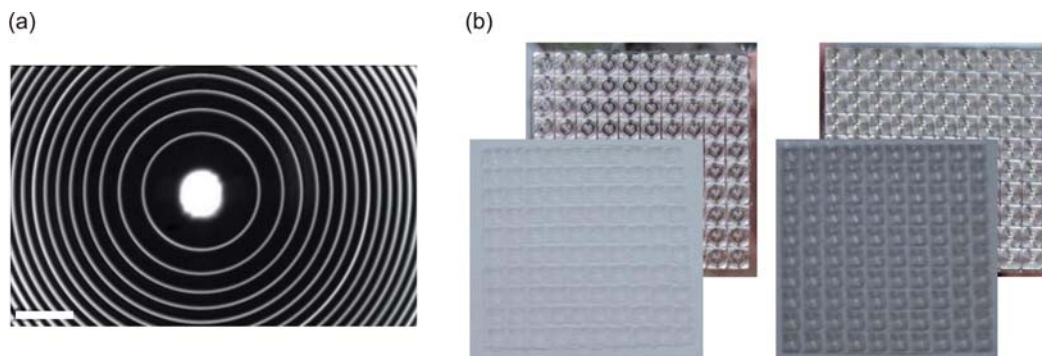


Figure 4.14: Micro-lenses foils. (a) Dark field optical microscope image with detailed first rings of the Fresnel micro-lenses. Scale bar = 200 μm ; (b) pictures of 10x10 array of both types of micro-lenses fabricated together with their shims.

The effect of the incorporation of the micro-lenses on the light beam shape and size is described below (4.5).

4.5 Optimization of the final "U-shape" actuator

Prior to experimental validation and optimization of the working parameters of the purposed device, it is important to individually characterize the actuators to adjust the positioning of elements (in that case, the distances between the light source, the micro-lenses and the material ribbon) to better understand the relationship between the LED output power and the amount of light absorbed by the LCE-CNT ribbon (directly related to its contraction) as well as the displacement of the pin.

In previous chapter, Chapter 3, the dynamic bending movement of a LCE-CNT cantilevers exposed to light were analyzed [170]. Due to the presence of CNTs, exponential heat generation is produced across the sample causing an inhomogeneous strain distribution, and at the same time, a non-uniform contraction movement of the structure. Therefore, a uniform and localized illumination should be applied to the elastomeric ribbons with well-established operational parameters. To help with this, some calculations were carried out considering the spatial distribution and the geometry of all the components, as well as the features of the light source.

The light absorption characteristics of the LCE-CNT ribbon were estimated experimentally by using collimated light of known intensity directed toward the sample and a conventional photodetector. Schematic representation of the setup used for these measurements is depicted in Figure 4.15. Considering the uniformity of the material and assuming that light decays exponentially in accordance with the Beer-Lambert law, nearly total light absorption by the material, 98 %, was obtained, with only 0.14 % of the light transmitted through the sample and 1.8 % reflected.

The working-power range of the actuator was determined by considering the input power of the LED (0.3 W) and its operational range of intensity of current (100 to 500) mA. Theoretically, the optical power incident to the LCE-CNT ribbon, $P(x)$, at a known distance, x , can be obtained by the following expression

$$P(x) = P_0[1 - e^{-kx}]$$

where the parameter k depends on the surface of the sample exposed to the light and the size and geometry of the spot at the transverse plane, where the interaction between the bottom side of the sample and the light path is produced (see scheme in Figure 4.1 -left-).

4. "U-SHAPED" ACTUATORS FOR TACTILE APPLICATIONS: NOMS DEVICE FOR VISUALLY IMPAIRED

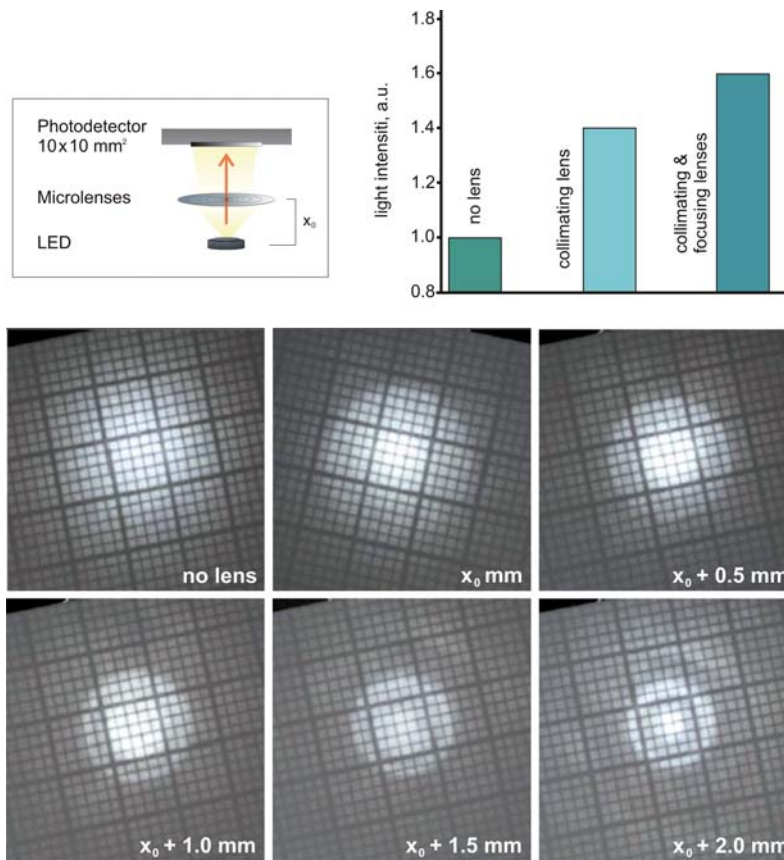


Figure 4.15: Micro-lenses characterization. Schematic of the experiment -top left- and the results -top right-. Images of the spot formed on the screen located 5 mm from the LED with no lens and with both collimating and focusing lenses -bottom-.

Initially, such distance was set to 0.5 mm ($x_0 = 0.5$) which is the shortest possible distance from the LED, to maximize the incident power. However, the inclusion of collimating and focusing Fresnel micro-lenses allowed increasing this distance up to 1.0 mm, while maintaining the power, and thus ensuring the correct illumination of the whole ribbon lower surface. Figure 4.15 depicts the effect of the inclusion of the micro-lenses on the system. The pictures showing the projection of the light collected by the lenses were taken on a screen at a distance of 5 mm from the LED.

Therefore, considering the low distance traveled by the light and the previous absorption measurements, losses were neglected resulting in $P(x)$ as the total amount of power used to obtain the experimental working parameters of the device.

Finally, the amount of energy required to achieve a tension of 15 mN, which is the

minimum value required for correct tactile perception was estimated. According to the previous calculations, the power-time product was in the range of 330 mJ - 420 mJ. Then, the average energy density, calculated by dividing the total power by the total illuminated area of the LCE-CNT ribbon, was in the range of 4 Jcm^{-2} to 5 Jcm^{-2} .

4.6 Actuator integration on a tactile device

Once the actuators and all its components were optimized, a fully functional prototype containing arrays of actuators was assembled following the multilayer concept, which was divided in three different units: a first one, named actuation layer, containing the actuators array and the micro-lenses, a second one with the LEDs and their corresponding electronics named LED board, and finally the control unit together with its corresponding communication interface. In this manner, a modular device was obtained which allowed for a straightforward rearrangement of different testing configurations and facilitated the replacement of damaged components.

Additionally, a protection layer was also designed to protect the top surface of the device and preserve the pins against the undesired effects due to the contact with fingers. In spite it was not added in the first version of the prototyped device, preliminary tests with different flexible materials available on the market were performed to qualitatively select the best option taking into account tactile perception criteria. The results of such research can be found in Appendix B.

4.6.1 Actuators layer

Figure 4.16 shows a schematic representation of the array of actuators proposed for the fabrication of the NOMS tactile device. In total, one hundred actuators were assembled and uniformly distributed in a 10×10 array, following the dimensions and distribution restrictions of Braille standards (see Appendix A.2).

First, the LCE-CNT ribbons were placed on top of the refractive support where each "U-shape" curvature was manually fixed and glued to avoid displacements during actuation. Then, the PMMA support containing the array of pins was added. To guarantee the vertical position of the pins and guide their movement during actuation, some apertures were added. In both cases, the size of the supports was $60 \text{ mm} \times 60 \text{ mm} \times 3.0 \text{ mm}$ and contain through holes in each corner to fix them to the LED board.

4. "U-SHAPED" ACTUATORS FOR TACTILE APPLICATIONS: NOMS DEVICE FOR VISUALLY IMPAIRED

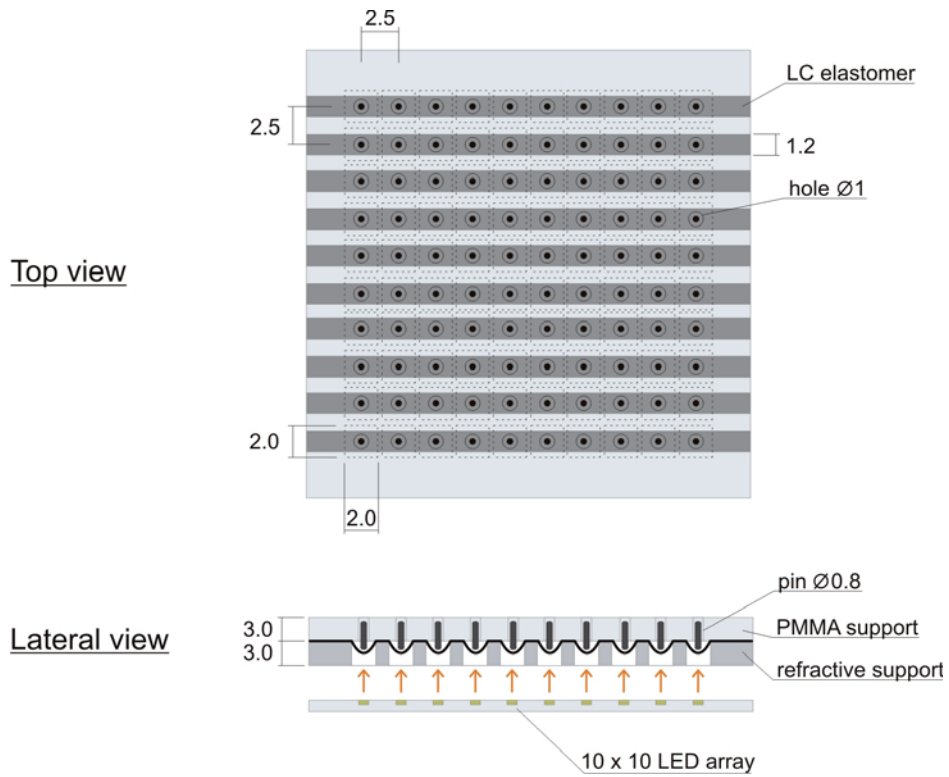


Figure 4.16: Schematic representation of the top and lateral views of the 10 x 10 array of actuators. All the dimensions are in millimeters.

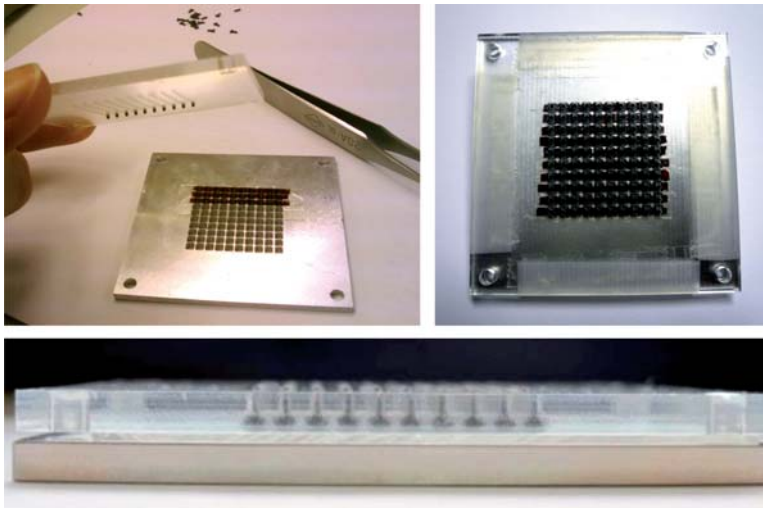


Figure 4.17: Integration of the components into actuators layer.

Finally, the PET foils containing both types of micro-lenses were added below the LCE-CNT ribbons. Between the lenses and the lower surface of the refractive support, some spacers were added to ensure the correct distance of the actuators to the light source. Images in Figure 4.17 show the actuator assembly process as well as a lateral view where a row of 10 completely assembled actuators can be observed.

4.6.2 LED board

For each actuator (i.e., Braille element) a light source is needed for actuation. Thus, the LED board contains the 10 x 10 array of LEDs mounted on a single layer in a 25 mm x 25 mm area. Due to the large number of LEDs in the prototype, a dedicated electronic architecture was required, leading to each LED being individually controlled by means of a specific LED driver (TLC5940 IC). In this manner, parameters such as the driving current and the illumination time can be adjusted to optimize the performance of the actuators. All of the drivers and connections were mounted on separate boards following again a multilayered model, and they were assembled together with the 10 x 10 LED-array in a single unit (see Figure 4.18).

To guarantee a correct heatsink for the LED board and prevent overheating, an air cooling system with two fans was added to provide the air flowing directed alongside both boards ensuring no damage to the material. For this reason, two slim line connectors were placed in line with the air flow to create a certain distance between the boards and, at the same time, to not obstruct the flow of air.

Finally, after integration of all these elements, a 60 mm x 75 mm x 30 mm compact package was obtained containing the array of 10 x 10 actuators. Four pins were added on corners to ensure the correct location of the actuators layer for testing (see details in Figure 4.18).

4.6.3 Hardware and control

Some hardware was required to operate the LED board. Therefore, a controller unit with all of the required circuitry and connections was developed (see Figure 4.18). The unit integrates the basic electronics to control the operation of the LEDs, as well as the communication ports with the computer and the power supplies for the LEDs

4. "U-SHAPED" ACTUATORS FOR TACTILE APPLICATIONS: NOMS DEVICE FOR VISUALLY IMPAIRED

(Tracopower TXL 050-05 S Module). A Bluetooth module (Roving Networks RN-42) was used for wireless communication between the controller and the computer. However, a USB connection and a parallel port were added to overcome interference problems, specially in places with many wireless signals. An on-chip programmable system (Cypress PSoC CY8C3866AXI-040) was chosen for hardware implementation to reduce the amount of logic control required allowing an easy updating of the device to accommodate new functionalities.

Pictures of the two separate packaging units resulting from system integration as well as the whole system are depicted in Figure 4.18. Some colored LEDs were included on the front-side package of the controller as visual indicators of the system status.

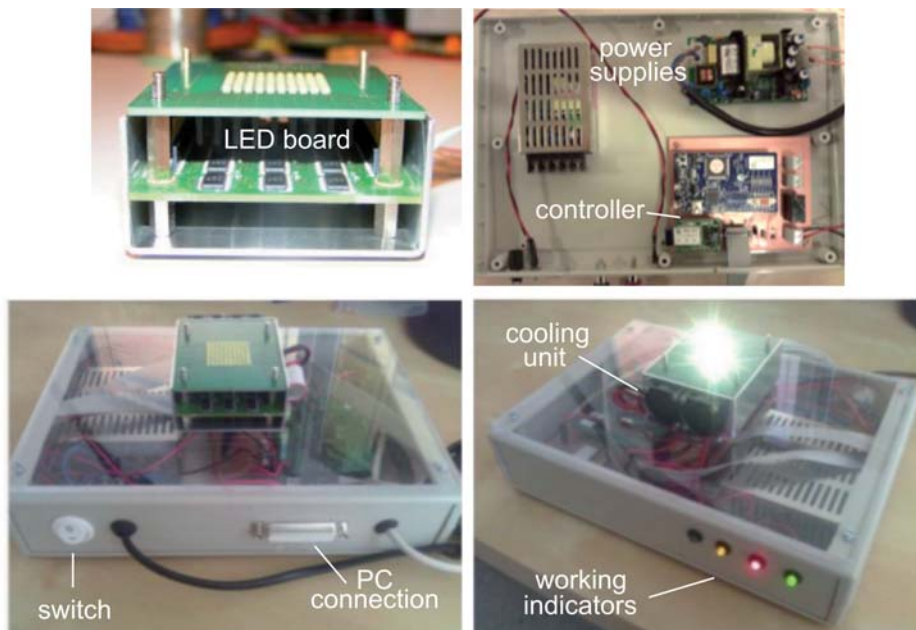


Figure 4.18: General views of the whole system assembled, including the LED board packaging and the controller.

4.6.4 Communication interface

Finally, image-transformation and communication software was developed to 'draw' the content to be shown on the tactile device and to control the working parameters of the system, such as the current intensity of the LEDs and the on-off switching times.

4.6 Actuator integration on a tactile device

The resulting user interface enables the drawing of simple shapes and the writing of Braille characters, as well as the possibility of individually control the working parameters of each LED in the array. Complex power ramps can be set to program cyclic testing with an accurate control over the driving currents and times. Moreover, the developed software permits saving and loading of previously stored information (up to ten different configurations for testing each time) which can be individually edited, drawn or erased. A sketch of the communication software function as well as its the user interface appearance are depicted in Figure 4.19.

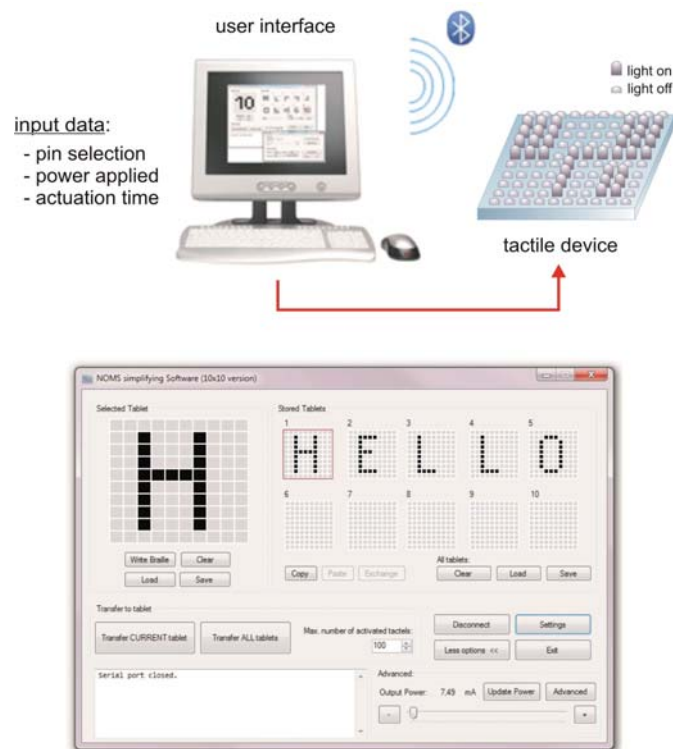


Figure 4.19: Communication software interface. Sketch of the communications function -top- and picture of the users' interface -bottom-.

This interface is also responsible for communications from the computer to the device using both Bluetooth and USB protocols, to send information to the tablet and to update the firmware of the device.

4.7 Characterization of the device

Different characterization procedures were used to check the performance characteristics and the feasibility of the proposed device. First of all, some tests were focused on the measurement of the pin's characteristics such as the pushing forces and the response times produced under actuation as function of the LEDs output power to define the actuation range of the device and check the dispersion on the measurements. Then, dynamic testing of the different actuators was performed to optimize their response in similar way than in the first and non-optimized "U-shape" prototype (first part of the chapter). In this manner, the main actuation parameters of the devices could be adjusted to minimize the energy consumption while maintaining the force level. Finally, the stability of the actuators' response was evaluated from the long-term actuation measurements through cyclic testing. The setup configuration and the measurements obtained, together with a discussion of the results are presented in the following sections.

4.7.1 Force and time measurements

First of all, some measurements were performed to study the performance of the new version of the "U-shape" actuators after the optimization of their components and thus, determine the main parameters involving the movement of the pins. For that purpose, the same experimental setup used for the characterization of the previous version of such actuators was used. However, in this case, the light source parameters such as the illumination times and the output intensity range were directly controlled by the communication software developed to that purpose. Both the dynamometer and device were coupled to a computer, which was used to control specially designed data acquisition software to record all the testing results. Pictures in Figure 4.20 show a general and a detailed view of the setup used.

First, measurements of the pins' displacements at maximum working conditions were carried out, resulting in a 1.3 mm maximum height. As depicted in the right image in Figure 4.20, a single pin can be distinguished from the top surface of the actuator array layer at a glance when the pin rises up. Therefore, it is easy to distinguish between two consecutive pins even if both of them are working simultaneously.

4.7 Characterization of the device

With the main purpose of avoiding possible internal damage or even rupture of the material due to excessive shrinkage stresses, a safety factor was applied to reduce the movement of the assembled pins. In this manner, the integrity of the LCE-CNT ribbons and their good operation can be preserved, increasing the utility life of the device. On average, the vertical displacement of the pins was measured to be 0.8 ± 0.2 mm. A certain dispersion in measurements was obtained, reflecting variability in height. Nevertheless, the displacement reached for the pins were in all cases at least double of the minimum value required for correct Braille characters representation. Differences in the assembly process of the "U-shape" ribbons (completely manual process), as well as some static and dynamic friction effects between the elastomer, the surface of the pins and the lateral walls of the support elements can explain these variations.

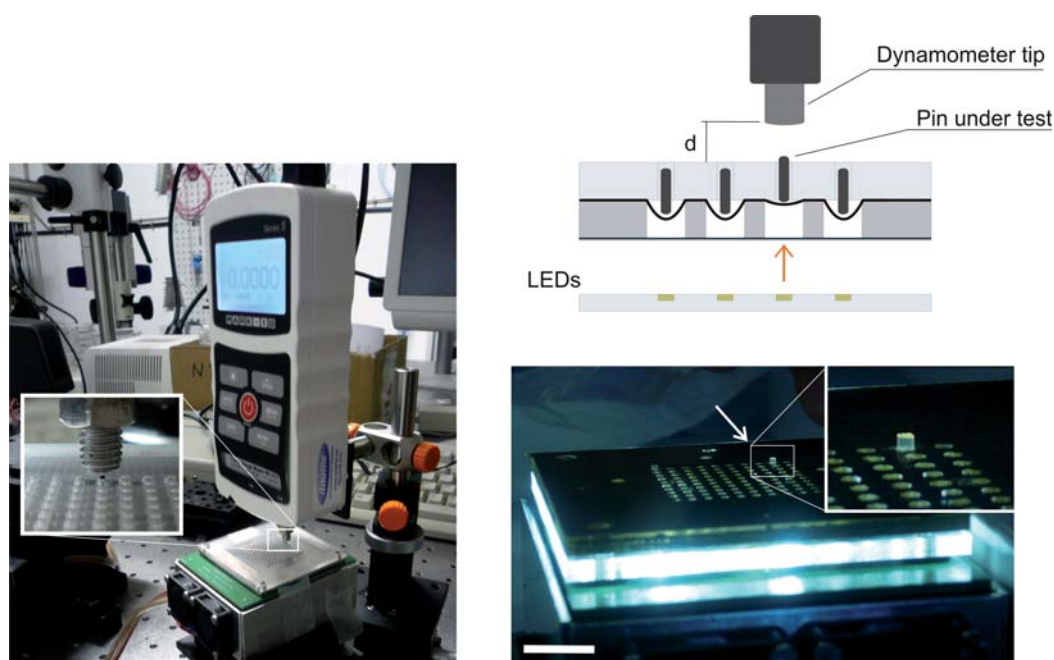


Figure 4.20: Experimental setup designed to measure the pins' characteristics. General and detail views of the setup where the contact between the dynamometer tip and a pin surface can be observed. A vertical displacement of 1.3 mm was measured under maximum working conditions for a single pin -white arrow-. Scale bar = 10 mm.

The characterization results of four different pins are presented in the graphs in Figure 4.21. The data plotted in the first graph correspond to the averaged maximum

4. "U-SHAPED" ACTUATORS FOR TACTILE APPLICATIONS: NOMS DEVICE FOR VISUALLY IMPAIRED

force values measured as a function of the applied intensity of light for different on-off actuation cycles. As expected, the force produced by the pins was strongly dependent on the intensity, allowing measurements of up to 40 mN (significantly higher than the 15 mN required) for higher intensity values, whereas the material response improves, reducing the actuation time by 200 % on average. Compared to the results obtained with the first design of the "U-shape" actuator using the same light source (see first graph in Figure 4.5 in the first part of this Chapter), an improvement of about 5 mN to 10 mN of the maximum force was reached with a reduction of 39.4 % of the current intensity applied; a very successful result.

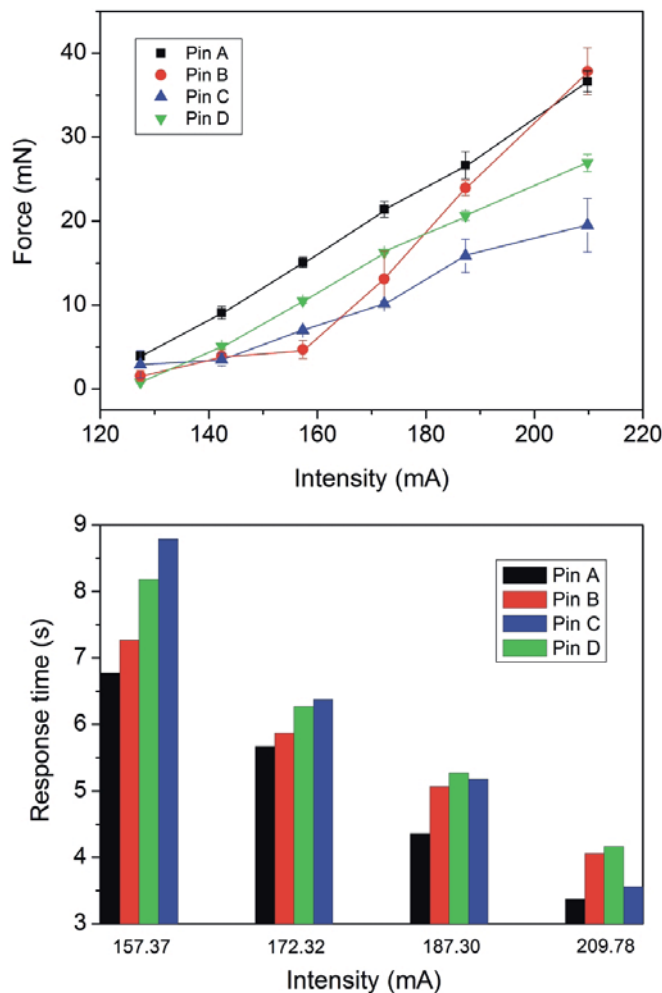


Figure 4.21: Characterization results from four tested pins. Actuation force -top- and response time -bottom- measurements as a function of the applied light intensity.

However, in spite of the accuracy during both the preparation of the different LCE-CNT samples used and the assembly process of the actuators, a significant variability between measured forces for different pins was still obtained under the same conditions. These variations ranged from 4.7 mN for low intensities to 25 mN for higher ones, increasing together with intensity, but losing linearity.

The main reason for these notable variations in measurements between pins is the assembly process of the actuators. As mentioned, this process is completely manual and every single actuator was individually assembled. Thus, small variations in the ribbon curvature to form the "U-shape" cause significant variations in the performance of the pins, reducing the linearity of the results. Moreover, the LCE-CNT ribbons used to obtain the present actuators were made from non-commercial materials, with most of their components synthesized at home, and were individually stretched using a manual process too, resulting in ribbons with variations in thickness and, consequently, in the force produced under illumination. An industrialized process for samples fabrication together with an automated assembly would help to obtain identical actuators, leading to a reduction of the variability for more accurate results. Another important aspect to consider is the interaction between the surface of the pins and LCE-CNT ribbons. As demonstrated during the material characterization (see section 3.2.2.5 in Chapter 3), the LCE-CNT material becomes softer and stickier under illumination, causing changes in their main properties, especially in the Young's modulus, that can induce difficulties on the mobility of the pins.

4.7.2 Dynamic actuation

From the device actuation point of view, higher forces and quick material response are required. These conditions, however, entail higher intensity values that may produce overheating of the material, its internal damage, and even its breakage due to the stress gradient generated when the ribbons are forced to experience faster contraction and expansion movements repeatedly. To avoid those undesired effects and to maximize the efficiency of the actuation mechanism, some actions were required. First, a well-controlled pre-stretching process was carried out during the sample fabrication to ensure forces of approximately 20 mN to 30 mN within a safety range, since for such specific application no longer forces are required. Second, in previous sections it has

4. "U-SHAPED" ACTUATORS FOR TACTILE APPLICATIONS: NOMS DEVICE FOR VISUALLY IMPAIRED

been proven that higher intensity values are only required initially to more quickly raise the pins up. Then, the working intensity can be reduced considerably to maintain the pin stability, allowing its correct reading (see Figures 4.8a-b).

Finally, to check the feasibility of the actuators and the whole system, some cyclic actuation tests were performed using dynamic manipulation of the actuator. Similar to the cyclic measurements previously performed with the non-optimized "U-shape" design, 100 on-off cycles were performed separately with different actuators.

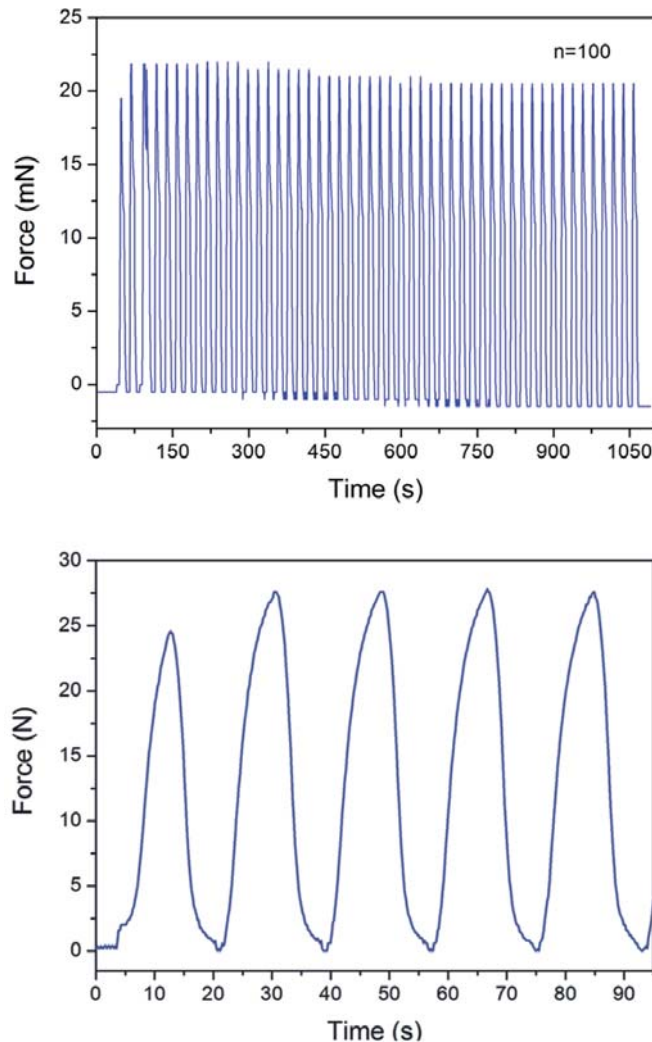


Figure 4.22: Cyclic actuation of a single pin. The response remains almost constant during the entire test for n=100 cycles -top-. Details of the shapes of the force peaks measured during cyclic testing -bottom-.

An example of those tests is illustrated in the force-time diagrams in Figure 4.22, resulting in an improvement on the measured force, 26.2 ± 0.2 mN, as a result of the previous optimization of all the components forming the actuator as well as its response under actuation. These results mean that less than 1 % variation occurred during the entire tests without material degradation, in contrast to the 16 % of variability previously obtained before the optimization of the actuators. This is a very low variation which is not perceptible by the user when touching. Later measurements in time demonstrated repeatability of actuation, where no behavior changes in terms of actuation force and time were observed. Longer tests ($n = 250$ cycles) were performed too with the same results.

4.8 Real testing

Finally, the capability of the proposed system to work as a real Braille device was evaluated by end users.

As part of the dissemination activities in the NOMS project, a workshop including hands-on sessions was organized in conjunction with the Slovak National Youth Computer Camp for Visually Impaired (Reset) for a real testing of the prototype of the device. A preliminary version containing an array of 2 by 2 actuators was provided to that end. The attendees including a total of 25 blind and partially sighted participants could test the prototype varying the actuation parameters and thus, evaluate its operation. Pictures from the workshop are shown in Figure 4.23.

The demonstration of the prototype was very successful. In general, the users were excited by the technology and appreciated the concept of the device as both a Braille display and a high resolution graphical display; although for the latter they would need to have a bigger array of actuators to check the haptic capability.

Other positive aspect they pointed out was the spring effect of the actuator when pushing against it which resulted to be much appreciated. When users push against a pin for reading, it first goes down but still pushing up due to contraction of the elastomer under illumination. Thus, once the users move their fingers, the pin immediately recovers its raised position allowing its correct tactile perception and a clear distinction between raised and absent pins.

4. "U-SHAPED" ACTUATORS FOR TACTILE APPLICATIONS: NOMS DEVICE FOR VISUALLY IMPAIRED



Figure 4.23: Pictures of the workshop during the testing of the device. Image courtesy of Slovak National Youth Computer Camp for Visually Impaired (Reset).

No cross-actuation between neighboring pins was detected in spite of the compact assembly due to Braille geometric restrictions. During the demonstration, the device was found to maintain an acceptable temperature for the users and did not overheat unacceptably thanks to the inclusion of the cooling unit, which was one of the initial worries from the end users. A very interesting feedback which provided novel perspectives for future improvement of the system and encouraged us to continue working in that direction.

4.9 Discussion and summary

In this chapter a novel opto-mechanical actuator approach based on the integration of fully cross-linked LCE-CNT films has been developed: a "U-shape" actuator which lies in the use of the stress gradient induced on a LCE-CNT film under illumination to exert a vertical displacement of a pin. Thanks to its particular geometry, the LCE-CNT

film is capable to vertically push the pin (previously inserted in the cavity upward) exerting a force while contracting. This approach has been conceived with the ultimate goal to create a tactile device based on the integration of such actuators in an array, able to represent Braille characters.

In the first part of the present chapter, the working principle and the main characteristics of this new type of actuator have been described and the first actuation measurements carried out, resulting in an averaged force of 40 mN obtained for the maximum intensity. Different aspects involving the contact between the finger and the pin, the geometry as well as the required energy for a correct operation of the actuator have been evaluated thinking on its use in future tactile applications.

Taking into account all these aspects and the preliminary characterization results, all the elements forming the actuator, such as the pin, the supports, as well as the light source, have been optimized leading to a new version of the "U-shape" actuators which have been integrated in a 10 × 10 array for the development of a complete tactile device for Braille applications, always following the Braille standards.

In the second part of the chapter, the final version of the actuator with all its components has been presented together with an accurate description of the whole tactile system and its different parts, and the operation performance of the device has been explored. Relevant parameters such as the actuation force and time have been assessed as a function of the current intensity of the light source in accordance with established tactile perception values.

Communication software and hardware have also been implemented to complete the layout of the device allowing the fabrication of a complete and fully functional prototype. Again, the performance of the actuators has been evaluated using dynamic actuation resulting in a reduction of 39.4 % of the current intensity applied (compared to the first "U-shape" design) while maintaining the same actuation force level. Finally, the capability of the proposed system to work as a real Braille device has successfully been evaluated by end users, encouraging continue this research. Noiseless and wireless, this type of actuation has great potential as an alternative to existing devices based on piezoelectric technology. Relatively compact and lightweight, the proposed device presents other advantages: the active material has no direct contact with the environment, thus avoiding material degradation caused by dust and skin secretions and increasing its service life.

4. "U-SHAPED" ACTUATORS FOR TACTILE APPLICATIONS: NOMS DEVICE FOR VISUALLY IMPAIRED

In spite of the results obtained and all the advantages, there are still some issues involving such approach that need to be improved.

The first one is related to the variability on the measured force between actuators, which can induce confusion when reading the tactile signal. Such variability is related to:

- Both the material preparation and the stretching processes. Although they have been widely used, both of them are still manual. In this way, even using the same chemical components and procedure each time, the degree of deformation achieved by the different films and therefore the maximum force produced is not the same.
- The inclusion of CNTs within the LCE matrix to create the photo-sensitive nanocomposite, which easily can form aggregates disrupting the natural behavior of the LCE films thus altering their mechanical response.
- The assembly process of the "U-shape" actuators. A very small variation in the ribbons curvature may produce noticeable differences in the displacement of the pins and, in consequence, in the maximum force perceived by the final users.

The second one refers to the power consumption of the system. In spite of its optimization, the energy required to photo-induce a mechanical response into LCE-CNT material is still high when thinking on a real tactile application in which, hundreds of actuators should be simultaneously working. In this case, a different solution for the light source should be adopted. Future work will be focused on improvement of such points.

As previously mentioned, the work described in this chapter has been developed within the frame of a European project named NOMS in collaboration with the different partners. A detailed list of the partners and their corresponding contribution to this work is provided below:

- Prof. J. Esteve, E.M.Campo, K.E. Zinoviev and C.J. Camargo from IMB-CNM (CSIC) were the project coordination team. They were in charge of the design, characterization and optimization of the "U-shape" actuators as well as the assembly and testing of the tactile device.

- Prof. E. M. Terentjev and Dr. J. E. Marshall working at Cavendish Laboratory of the University of Cambridge were in charge of material synthesis and samples preparation.
- M. Vallribera, R. Malet, S. Zuffanelli, Dr. V. Soler and Dr. J. Roig from Microelectronics and Electronic Systems Department of Universitat Autònoma de Barcelona were in charge of hardware and software design and implementation.
- F. Vossen and F.M.H. Cromptvoets from Philips Research electronic division in Netherlands were in charge of the light source and the circuitry, and developed the LED board.
- Dr. N. Walker from Microsharp Corporation Ltd. was in charge of the design and fabrication of the Fresnel micro-lenses and the refractive supports for the optimization of the light path.
- Prof. B. Röder and Dr. P. Bruns from the Biological Psychology and Neuropsychology Department of the University of Hamburg gave their advice in tactile perception mechanisms.
- B. Mamojka and P. Teplický from Unia Nevidiacich a Slaborzrakych Slovenska (UNSS), the Slovak National Union of Blinds, organized the workshops with end users and gave advise on Braille aspects.
- M. Omastová and I. Krupa from Polymer Institute of the Slovak Academy of Science in Bratislava provided technical assessment about the material performance.

As a result from this collaboration, several scientific contributions in journals with high impact factor as well as in international conferences have been arisen. A complete list of publications is detailed at the end of this document.

4. "U-SHAPED" ACTUATORS FOR TACTILE APPLICATIONS: NOMS DEVICE FOR VISUALLY IMPAIRED

Part III

Research on alternative photo-sensitive materials

5

Alternative material strategies

Working with LCE materials has a great number of advantages with respect to other materials due to their interesting intrinsic properties, as shown in the first part of this thesis (Chapters 2 and 3). However, when is intended to obtain reversible mechanical actuation, working with LCE is not as simple. As relatively new materials, most part of the chemical compounds required for the preparation of LCE samples should be obtained at lab-scale and in small amounts, using complex synthetic procedures (several days), which increases in time and difficulty when CNTs should be added. In that case, a new preparation step should be introduced prior to the alignment and crosslinking of the material to diminish aggregation and bad-dispersion problems CNTs present (see Chapter 2). Moreover, there is the stretching method (completely manual), which requires certain ability and knowledge to achieve a reasonable degree of LCEs alignment suitable for actuation; process that at the same time, is slightly different for each sample resulting in different contraction and/or expansion movements under actuation.

Although CNTs proved to be an effective and very interesting method for the light-activation of monodomain LCEs, such composites are not ideal to be used for practical applications in which a large number of actuators with geometric restrictions should be activated simultaneously [48]. This is the case of the novel Braille-based tactile device concept introduced in previous chapter, where variations in performance between the different actuators in the array were also due to variations in the assembly process (also completely manual); one of the main issues identified. In addition, and in spite the adjustments, still relatively high power consumption was required to ensure an

5. ALTERNATIVE MATERIAL STRATEGIES

efficient light-to-heat conversion in the material and thus, a proper operation of the actuators (minimum force and displacement to produce a correct tactile signal, in case of "U-shape"); fact that limited the number of actuators in the array.

It is necessary to add that recently published works warn against dangers in handling nanomaterials, paying special attention to CNTs [208] which can cause breathing problems when inhaled and have been described by different world agencies for safety and health at work, such as the European Commission and OSHAS, as potentially carcinogenic elements [209, 210]. In this sense, the use of CNTs for long-term lab-scale testing should be reconsidered.

With the main goal of addressing some of the issues involving working with LCE-CNT composites, simplifying the process of preparation of samples and making it more affordable (not restricted to specialized chemists), a search for new photo-sensitive nanocomposites started in parallel with the work in this thesis at late stages as alternative to LCE-CNTs, improving the response of the system. Other strategies regarding the integration of such actuators to improve the assembly process will be discussed in the next section. Thus, and considering the above mentioned issues, one can identify two different strategies to be followed. The first and the fastest solution consists in replacing the CNTs for other photo-sensitive elements (i.e., change the LCE nanocomposite). In this manner, it would be possible to maintain the LC structure of the film (known behavior and actuation characteristics) while simplifying the synthesis procedures and increasing the safety, thus avoiding homogeneity problems on the material. In this sense, the main requirements for the new photo-sensitive elements are:

- allow absorption of light within the visible spectrum (safety wavelengths range for the human eye),
- deliver enough thermal gradient to induce the nematic-to-isotropic phase change on the LCE material,
- produce repeated fast and reversible response.

The second and more complex strategy is based on the replacement of the LC material by other elastomeric matrix, completely changing the internal structure of the material and so its main characteristics and properties while maintaining the use of

CNTs; broadening the search to commercially-available materials and thus avoiding long synthetic work while reducing the processing costs. However, in that case the difficulties concerning the use of CNTs are still present. Both strategies have started to be investigated and the first results obtained are detailed in this chapter which is divided in two parts, one dedicated to each strategy.

The first part, and the widest, is dedicated to the selection of suitable photo-active dye molecules as alternative to CNTs for the fabrication of novel photo-sensitive LCE nanocomposites. Thus, details of the chemical conformation of the different dyes selected, their absorption characteristics and working principle are described, together with the main changes on the preparation of dye-doped LCE samples with respect LCE-CNT ones. Some characterization results in terms of mechanical contraction and photo-induced stress of the different dye-doped LCE samples prepared are also given. Finally, the actuation response of the first dye-doped LCE actuators is presented together with a comparison between both types of LCE nanocomposites: LCE-CNT and dye-doped ones. To that end, actuators in "U-shaped" configuration were assembled as described in Chapter 4 and integrated to the developed tactile device.

Finally, in the second part of the chapter, a brief introduction to the first investigations concerning the second strategy is given. In this case, a commercially available ethylene-vinylacetate copolymer, EVA, was selected as alternative to LCE matrix for the fabrication of low-cost photo-actuating polymer composites, PAPC.

Dye-doped LCE nanocomposites

5.1 Dye-doped LCE material conformation

5.1.1 Selection of dyes

Whereas LCE-CNT samples absorb light over a wide range of wavelengths (from visible to IR) causing photo-sensitization by conversion of light into heat, dye-doped materials have an optimal absorption range, which limits their actuation and often do not produce enough heat to raise the local temperature of the material by tens of degrees under illumination. However, some industrial applications (e.g., laser plastic welding and the ablation of printing plates) rely in the so-called laser-welding dyes, which can heat a surrounding matrix due to its very efficient mechanism of converting

5. ALTERNATIVE MATERIAL STRATEGIES

the absorbed IR light into local heat (similar concept than CNTs). In this sense, the selection of proper dyes is not a trivial process, and will be strongly affected by the emitting wavelength and the type of light source. Moreover, to ensure a good selection and get a suitable dyeing process of the samples, the dye must be compatible with the LC matrix and ideally soluble in similar organic solvent, to be easily incorporated into the polymeric mixture without adding extra chemical agents which may increase and difficult the preparation steps.

From the different commercially-available solutions, two types of dye molecules were selected: IR and visible, which are briefly described below.

5.1.1.1 IR dye

Infra-Red 1310 dye, IR1310, (Adam Gates, UK) was firstly obtained. With high absorptivity at 1064 nm ($\lambda_{max} = 990$ nm), IR1310 dye finds use in a broad range of applications where the absorption of IR light and the transmission of visible light is important. Moreover, its solubility in toluene was found to be sufficiently high to achieve high levels of doping in the LCE.

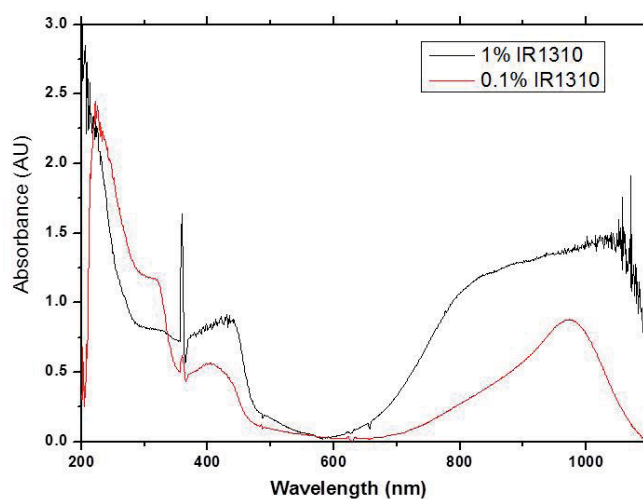


Figure 5.1: Absorption spectra taken from LCE containing 0.1 wt.% and 1 wt.% concentration of added IR1310 dye. Illumination wavelength of 980 nm (100 nm broad) is required to excite it.

Figure 5.1 shows the UV-visible absorption spectra of two LCE samples containing IR1310 dye concentrations of 0.1 % and 1 % (by mass). As expected, the material is

largely transparent to light between 500 nm and 650 nm (which corresponds to the visible range) where the absorbance drops almost to zero and reaches the maximum value with illumination wavelengths in the IR range. Notice that, higher dye content entails greater absorbance, fact that is strongly related to the opacity level of the samples as demonstrated in the case of LCE-CNT composites, which can be clearly distinguished at a glance. A picture of the different types of dye-doped LCE samples used is later presented.

5.1.1.2 Visible dyes

Based on the expectations for the LCE-CNT composites and the safety restrictions imposed from the end users point of view, the NOMS device was designed to work in the visible range using white-light LEDs as light source (see Chapter 4). Therefore, in order to avoid changes on the tablet design, other LCE samples were also created containing two different commercial dyes which absorb in the visible region (both from Sigma-Aldrich): Disperse Red 1 and Disperse Blue 14. This latter was introduced at the end to modify the first one in order to broaden the absorption spectrum.

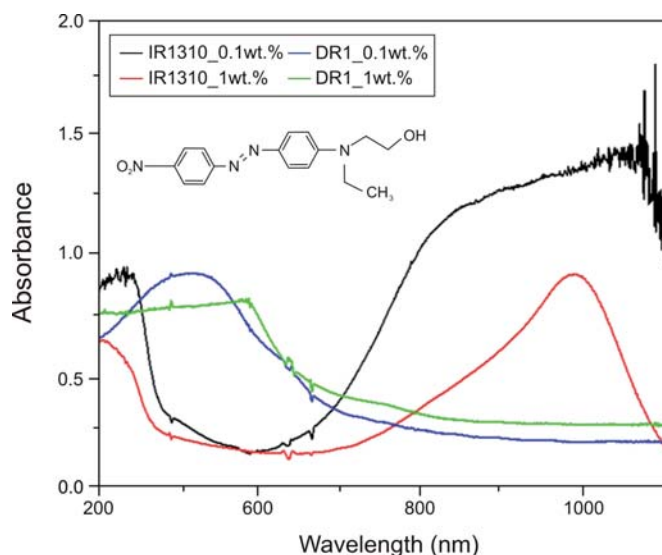


Figure 5.2: Absorption spectra of samples doped with DR1 compared to samples doped with IR1310, with dye contents of 0.1 wt.% and 1.0 wt.%.

5. ALTERNATIVE MATERIAL STRATEGIES

Disperse Red dye

Disperse Red 1 dye, DR1, ($C_{16}H_{18}N_4O_3$) is based on azobenzene molecules which can therefore photo-isomerize under light irradiation [211, 212].

As described in Chapter 2, azobenzene chemical groups can undergo light-induced trans-to-cis isomerization under UV irradiation, leading to the nematic-to-isotropic phase transition in the LCE matrix and thus producing its contraction [150, 155]. In this particular case, however, the azobenzene-based dye molecules were previously functionalized by suitable donor-acceptor groups in order to sensitize them to light in the visible range [213], allowing actuation by white light ($\lambda_{max} = 502$ nm). In this manner, the dye molecules can emit absorbed light as heat, thus changing the LC order in the material [151].

Figure 5.2 depicts the absorption spectra from two LCE nematic samples doped using DR1 in a similar concentrations (0.1 wt.% and 1 wt.% content) in comparison with the ones containing IR1310 dye. Notice that the absorption peak shifted towards the left, leading to a maximum around 500 nm. In contrast to IR1310 dye, similar absorbance level was obtained with both concentrations. In the inset, the correspondent chemical structure of the DR1 dye is presented.

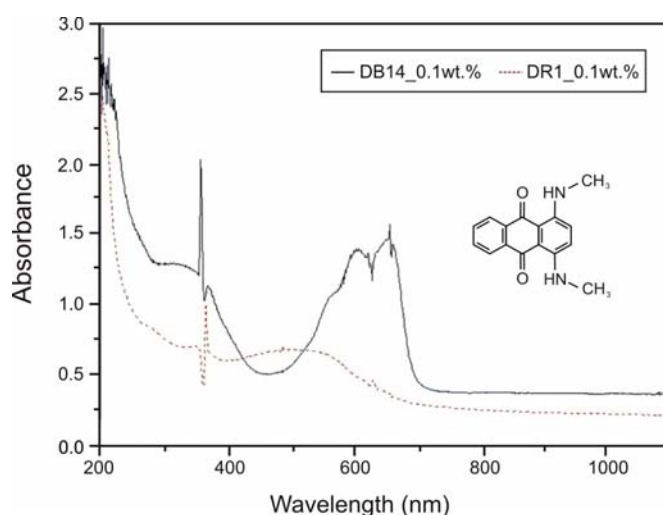


Figure 5.3: Absorption spectra of samples containing 0.1 wt.% of DB14 and DR1 dyes respectively.

Disperse Blue dye

Finally, Disperse Blue 14, DB14, ($C_{16}H_{14}N_2O_2$) was chosen. DB14 is an aromatic organic-based dye derived from anthraquinone that have two different absorption peaks ($\lambda_{max_1} = 595 \text{ nm}$ and $\lambda_{max_2} = 644 \text{ nm}$), which let composite actuation in the whole visible range.

A comparison between the absorption spectra of DB14 and DR1 samples is depicted in Figure 5.3, where the chemical structure of DB14 dye is also given. Note that DB14 seems to have a much stronger absorption cross-section (with a broad peak from 600-650 nm), compared to DR1.

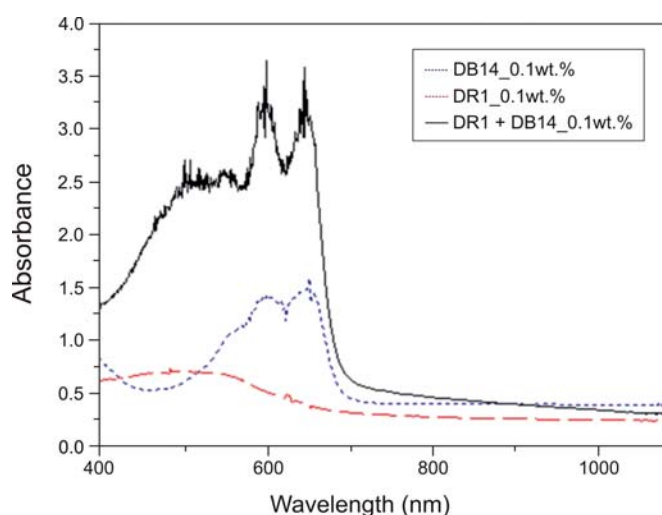


Figure 5.4: Comparison of the absorption spectra of DB14, DR1 and its mixture. In all cases, the dye concentration was 0.1 wt.%.

Combination of dyes

In contrast to CNTs, dye molecules can be combined to create new mixtures as long as the different dyes used have compatible chemical species. In this manner, it is possible to widen the absorption peak, broadening the range of actuation of the final composites. As first attempt, samples containing both DR1 and DB14 visible dye were mixed in a concentration of 0.1 wt.%. The resulting UV-visible absorption spectra is given in Figure 5.4. As was to be expected, there was a significant increase in the region of actuation, thus enabling the use of light sources with wider emission spectrum, as in

5. ALTERNATIVE MATERIAL STRATEGIES

case of the white LEDs chosen for the fabrication of the NOMS tactile device (Chapter 4).

5.2 Dye-doped LCE nanocomposites preparation

The incorporation of organic dyes into the material is synthetically more straightforward than is the case for CNTs, because additional surfactants and complicated ultrasonication procedures are unnecessary for their dispersion in the LCE; simple mixing of the dye with the LC polymer precursors before centrifugation is sufficient.

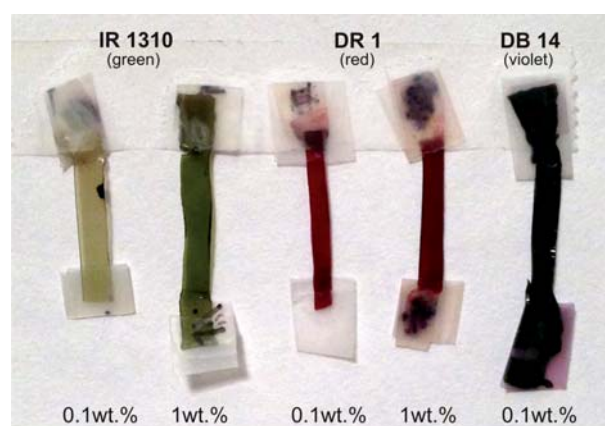


Figure 5.5: Examples of different dye-doped LCE samples fabricated. Each pair of images corresponds to a same dye, which content varies from 0.1 wt.% -left- and 1.0 wt.% -right-.

Monodomain LCE films containing dye molecules were fabricated using the same two-steps crosslinking process above described [85]. Similar to the preparation of LCE-CNT samples, the PMHS backbone polymer, the vinyl-terminated MBB mesogen, and the 11UB divinyl crosslinker were mixed to create the LC matrix. Then, the required amount of dye together with $\text{Pt}(\text{COD})\text{Cl}_2$ catalyst (Sigma-Aldrich) were added and the reaction mixture heated to $80\text{ }^\circ\text{C}$ for approx. 30 minutes under centrifugation. Once formed the weakly cross-linked gel, the samples were aligned by stretching before undergoing a second heating process in order to complete the crosslinking. As a result, samples of uniform thicknesses between 0.2 mm and 0.3 mm were obtained. Extended details of the LC matrix compounds and the preparation procedures can be found at [81, 151].

Examples of the different dye-doped LCE samples obtained using different dye molecules at different concentrations by mass are depicted in Figure 5.5, where it is possible to distinguish differences in color and opacity between them.

5.3 Dye-doped LCE nanocomposites actuation

5.3.1 Thermoelastic characterization

According to the main LCE generalities outlined in previous sections (Chapters 2 and 3), it is clear that the extent to which these films can actuate will depend strongly on the stretching process that they have undergone during preparation. However, leaving behind possible differences on their preparation, one can compare their thermal expansion rate by evaluating changes in length (i.e., contraction movement) upon heating the samples under the same conditions. Figure 5.6 shows the results obtained for different dye-doped samples, each one containing 0.1 wt.% of DR1, DB14 and IR1310 dye respectively. All the samples were previously cut to have the same shape and dimensions (5 mm length, 3 mm width).

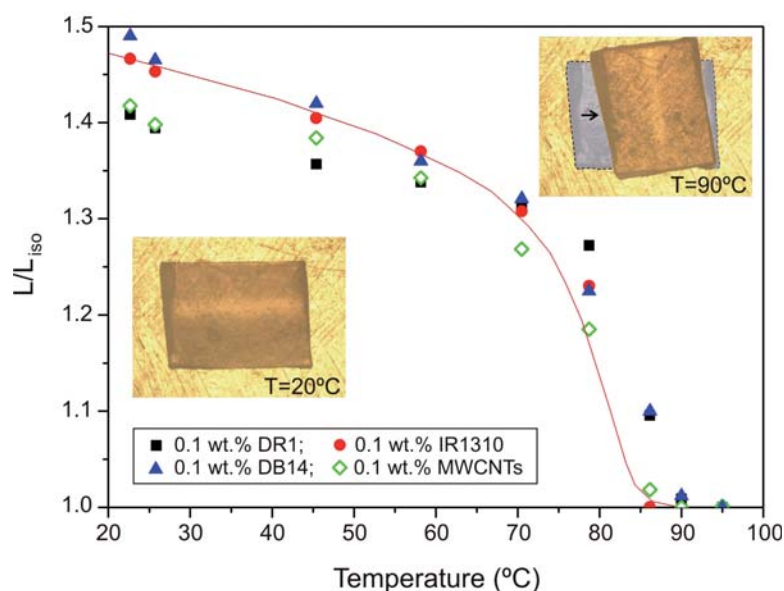


Figure 5.6: Evolution of the contraction of samples as function of temperature for different dye-doped content. In the inset, changes in dimensions of a DR1 sample from $\approx 20^\circ\text{C}$ to 90°C .

5. ALTERNATIVE MATERIAL STRATEGIES

As is usual with this type of LCE films, the length of the samples decreases with temperature up to the transition point, T_{NI} , beyond which the contraction ceases remaining stable, resulting in an overall change in their dimensions as shown in the insets in Figure 5.6. To perform such measurements, the same miniaturized hotplate developed for measuring LCE-CNT samples was employed (see 3.2.1 section in Chapter 3). Again, a CCD camera coupled to a standard optical microscope was used for real-time monitoring of the contraction movement. The heat-activated actuation of these materials was good, with the samples exhibiting similar temperature response to CNT-doped ones under the same measuring conditions. A contraction curve of a sample containing 0.1wt.% of MWCNTs measured under identical conditions also plotted in Figure 5.6 confirms this behavior.

The overall trend is similar for each film, evidencing that adding small amount of dyes (0.1 wt.%) does not alter the natural response of LCE elastomers when changing the order parameter from nematic to isotropic state.

5.3.2 Photo-induced actuation

After analyzing the change in dimensions (i.e., the contraction measurements) of the different samples, their performance under light irradiation was evaluated with the main objective to quantify the maximum force induced by the phase changes in the material. In this manner, it would be possible to compare such values with the ones obtained using LCE-CNT composites. To that end, different types of light sources were used in agreement with the absorption spectra of the dye molecules present in each sample.

The same setup previously developed to perform photo-induced force measurements during LCE-CNT samples characterization was used again (see Figure 3.17 in Chapter 3). Thus, the different dye-doped samples were horizontally placed above the correspondent light source and fixed at both ends using specially designed clamps; one of them coupled to a dynamometer (M5-025, MARK-10) to monitor the data obtained whereas the other one remained fixed. As in prior thermoelastic measurements, all the samples used were cut to have the same dimensions (15 mm length, 3 mm width). To ensure consistent results with uniform illumination, the distance between the samples and the light source was adjusted together with the dynamometer before each test.

5.3.2.1 IR measurements

To perform all the light-excitation tests using samples containing IR1310 dye, a 980 nm wavelength LD (L980P030, Thorlabs) was chosen. Figure 5.7 summarized the main force results obtained for samples with both IR1310 dye content, 0.1 wt.% and 1.0 wt%, under the application of different output powers: 18 mW, 24 mW, 30 mW, 36 mW and 42 mW, for which various quick on-off cycles were recorded.

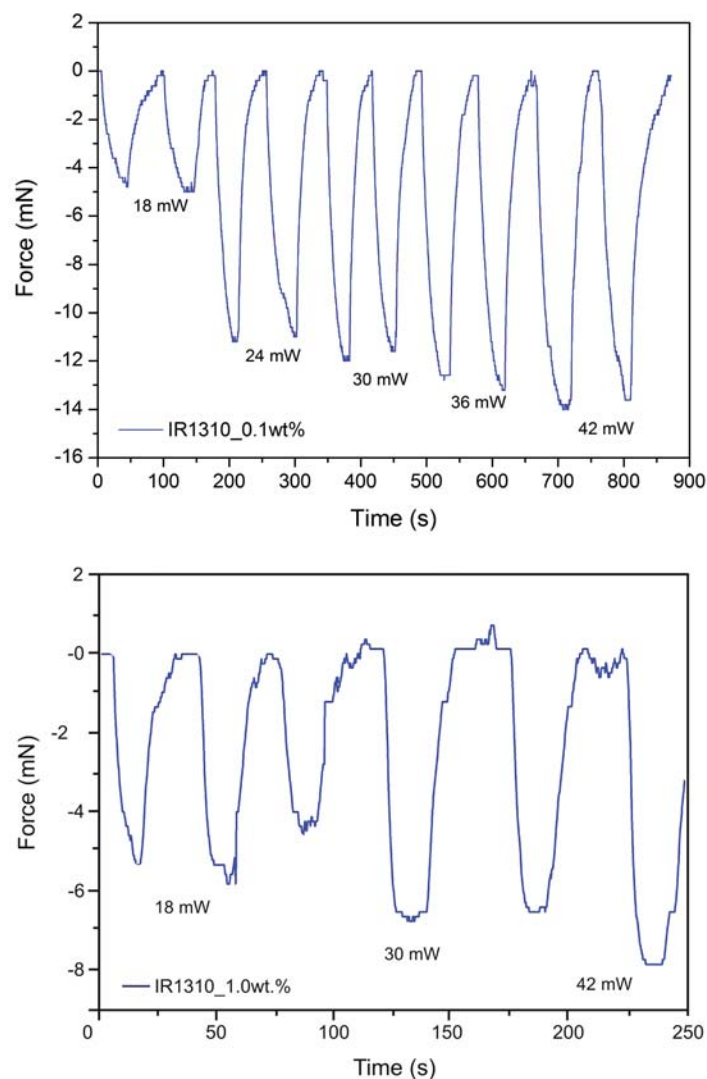


Figure 5.7: Actuation force measurements obtained as function of the power applied for samples containing IR1310 dye at 0.1 wt.% -top- and 1.0 wt.% -bottom-. A 980 nm wavelength LD was used as light source.

5. ALTERNATIVE MATERIAL STRATEGIES

In case of samples containing 0.1 wt.% of IR1310 dye, a peak of 14 mN of maximum force was obtained; value which is significant and comparable to those previously obtained with LCE-CNT composites under same testing conditions (see Ref. [81] and Chapter 3). Moreover, the curves obtained were regular in shape and the 'zero' force value (i.e., the minimum force when the samples are at rest position -in dark-) remained almost constant. However, samples with high dye content, 1.0 wt.%, behaved different. The actuation curves became quite irregular in shape and the force values started oscillating at rest position. In this case, the maximum force reached dropped to 7.98 mN.

From the data obtained, a clear worsening of the force measured by increasing the concentration of dye was observed, fact that can be explained by the increase of rigidity of the LC matrix in similar way when comparable concentrations of solid nanoparticles such as when CNTs were added [81]. Currently, a recent published work by Marshall et al. with similar dye-doped LCE materials demonstrates by calculations of the penetration depth of the light into the material that, even at lower dye concentrations, light does not penetrate far into the film (actuation at surface level); therefore, the actuation response of dye-doped LCE films does not vary linearly with dye concentration [151]. However, the real mechanisms of actuation of such materials have not yet been studied in depth. Further investigations should be performed in that direction.

5.3.2.2 Visible light measurements

Similar photomechanical measurements were performed using the other types of dye-doped samples containing DR1.

Specific wavelength light source

In agreement with the absorption spectrum detailed earlier in this chapter, a green laser with 532 nm of emission wavelength (Newport) was selected as a light source for the characterization of DR1 dye-doped LCE films since its absorption peak lies in the blue-green zone.

Surprisingly, the maximum force values obtained for both dye concentrations were very low compared to the values obtained with the previous samples, even though the

5.3 Dye-doped LCE nanocomposites actuation

emission band of the laser and the absorption peak of DR1 samples were sufficiently close (532 nm and 502 nm, respectively), resulting in only 1.55 mN and 2.9 mN of force for 0.1 wt.% and 1.0 wt.% of dye content. An example of the force curves obtained for a sample containing 0.1 wt.% of DR1 dye is depicted in Figure 5.8 where, in this case, the power irradiation of the laser was about 15 mW.

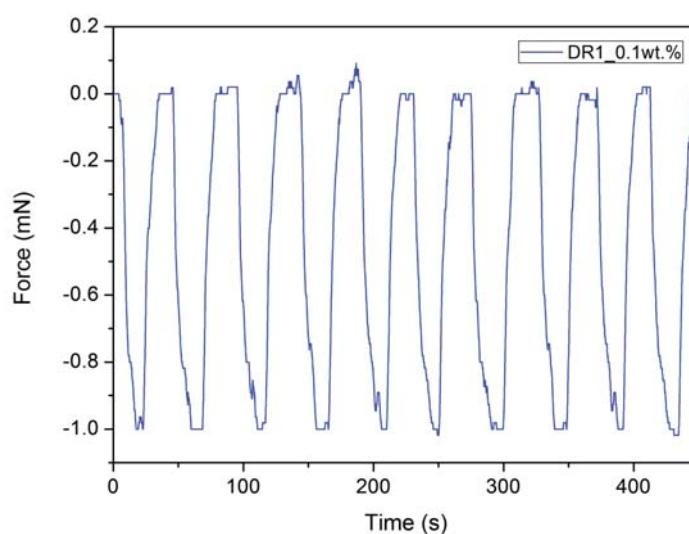


Figure 5.8: Actuation force measurements of a sample containing 0.1 wt.% of DR1 dye using a green laser (532 nm wavelength) as a light source. The irradiation power was about 15 mW.

Such results may be explained by the intrinsic characteristics of the green laser used which has wider angular intensity distribution in comparison to the IR LD previously used and in consequence, lower power density per square unit under the same conditions. Possible defects during the preparation of the samples were discarded because samples from two different batches (same dye content) were measured with the same results.

White light source

After those first tests, and thinking on the integration of such dye-doped materials into the tactile device, a white light source was used to induce a photo-mechanical response to the dye-doped LCE films. Thus, all the samples were again measured under the same conditions and using the same setup, now replacing both the IR LD

5. ALTERNATIVE MATERIAL STRATEGIES

and the green laser by the same white LED (LUXEON-C from Philips) used for the fabrication of the tactile device in Chapter 4.

Similarly, the response of IR1310 and DR1 dye-doped samples were measured as function of different current intensities, in this case ranging from 112 mA to 220 mA, according to the light source specifications [214]. Figure 5.9 shows, as example, the results for IR1310 -bottom left- and DR1 -bottom right- dye-doped samples (0.1 wt.% of dye content), both measured with the LED irradiating at 149.84 mA. A picture of the setup configuration was included (see Figure 5.9-top-) to show the changes on its configuration, since in this particular case, the light source and the different samples should be placed aside.

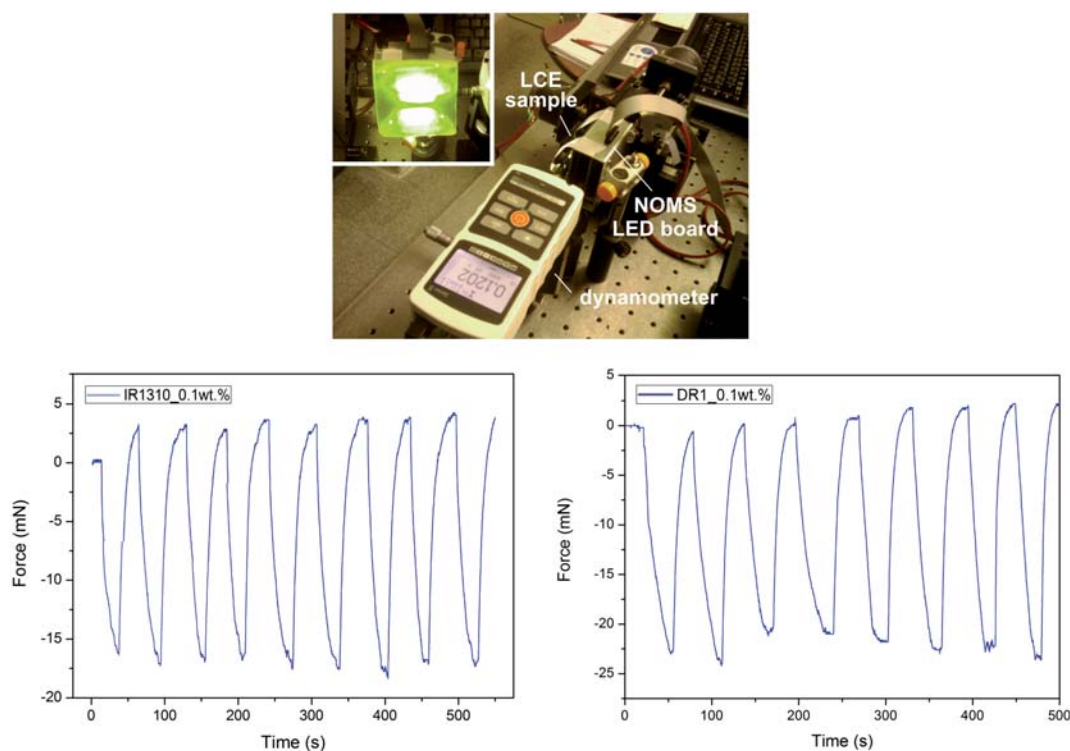


Figure 5.9: Photomechanical response of IR1310 and DR1 dye-doped samples (0.1 wt.%) under LED irradiation. Setup configuration -top- and actuation forces -bottom- measured at 149.84 mA.

Both samples gave rise to regular actuation curves, very similar in shape, proving that dye-doped LCE materials are capable of producing forces comparable to those previously obtained using LCE-CNT films.

5.3 Dye-doped LCE nanocomposites actuation

With regard to samples containing DR1 dye, a good response under LED irradiation was expected in accordance with the spectral power distribution of such light source [214], which presents two emission peaks: a narrower one close to 430 nm and a broader between 520 nm and 580 nm, that coincide with the maximum absorption region of the dye molecules, leading to forces close to 25 mN using an intensity value not so high (149.84 mA).

However, in case of samples containing IR1310 dye, the results were unexpected taking into account the above mentioned characteristics of the light source. An increase in the actuation force was obtained, reaching values of 15 mN; slightly higher than the ones measured with the green laser, probably due to lower power. This fact may indicate that under these same experimental conditions, the principal mechanism for the LCE contraction observed is the dye-mediated heating rather than the isomerization of the molecules, which is in clear agreement with results of early published works [151].

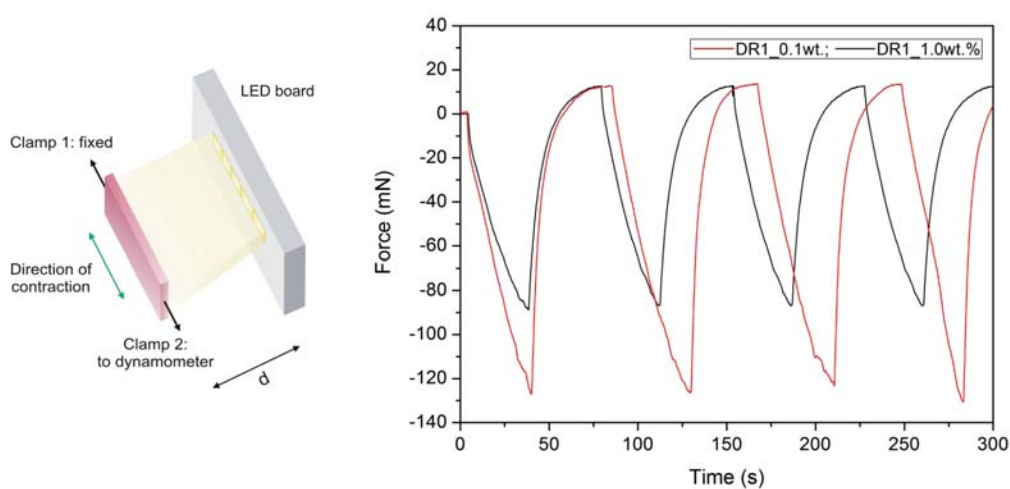


Figure 5.10: Maximum force values obtained under uniform illumination of dye-doped samples using simultaneously an array of 5 LEDs at 172 mA.

It is worth noting, however, that the response times of dye-doped LCE films increase considerably compared to the ones obtained with LCE-CNTs ones, going from few seconds to almost a minute for a complete on-off cycle.

Finally, a last test was performed to check the actuation limit of the nanocomposites before their mechanical fracture, to quantify the maximum force they are able to do.

5. ALTERNATIVE MATERIAL STRATEGIES

Thus, a row with five consecutive LEDs was simultaneously used to illuminate the whole films uniformly, increasing the distance between the light source and the sample, d , to 9 mm. To perform these measurements, samples containing 0.1 wt.% and 1.0 wt.% of DR1 dye were chosen, resulting in actuation forces up to 145 mN in case of lower dye content. The measured force in sample with high DR1 dye content reached 101 mN prior to fracture; a lower value compared to 0.1 wt.% sample but in agreement with previous results. The schematics of the experiment and the first four on-off actuation cycles for both samples are depicted Figure 5.10, where the amplitude of the forces reached can be distinguished. Notice that in both cases, from 75 to 90 seconds were required for a complete on-off cycle.

5.4 Dye-doped LCE actuators

Taking into account the good results obtained in both thermoelastic and photomechanical measurements for the different dye-doped films, their suitability as actuators were tested. Thus, each different LCE dye-doped sample was assembled in "U-shaped" configuration as described in previous chapter to be integrated as actuators to the developed tactile device. Figure 5.11 shows a picture of the actuators layer of the NOMS tactile device where single "U-shape" actuators assembled using different dye-doped films can be distinguished. In this case, samples containing both 0.1 wt.% and 1.0 wt.% of DR1 and IR1310 dyes were used together with a new one containing a mixture of DR1 and DB14 dyes at 0.1 wt.% to check for an increase in the response of DR1 dye as expected from its absorption spectrum (see Figure 5.4 early in this Chapter).

To precede with the performance measurements of the actuators (mainly, actuation force and time) under the application of different power conditions, the testing setup previously developed for this purpose was used together with the rest of the components of the device (see second part of the Chapter 4). Again, the same dynamometer was employed to measure the force induced by the LCE material under illumination through the vertical displacement of the pins. For a picture of the setup see Figure 4.20 in previous chapter).

Similar parameters (i.e., power range and actuation times) were employed to perform dynamic testing of the actuators in order to be comparable to the ones previously obtained for LCE-CNTs.

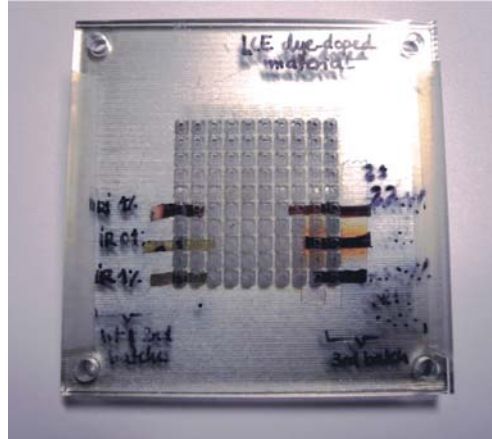


Figure 5.11: Picture of the “U-shape” actuators assembled for testing using the different dye-doped LCE films.

Figure 5.12 shows a sequence of 15 on-off cycles corresponding to three pins assembled using the different LCE dye-doped samples selected (DR1 at 0.1 wt.%, DR1 at 1 wt.% and DB14+DR1 at 0.1 wt.%) at different current intensities. Note that the curves in the graph are upward, describing a stairway. This effect is due to a discrete increase of the current intensity of the light source applied every three on-off cycles. From preliminary measurements and in agreement with the actuation range of the system established using LCE-CNTs samples in previous chapters, the selected LED working intensity values for resting were 142.35 mA, 157.33 mA, 172.32 mA, 187.30 mA and 194.79 mA, respectively.

Table 5.1: Maximum force values obtained as function of the type of dye and its concentration for each “U-shape” actuator.

Photo-sensitive dye	Content by mass [wt.%]	Maximum force [mN]
IR1310	0.1	27.6
	1.0	9.8
DR1	0.1	49.8
	1.0	32.4
DR1+DB14	0.1	14.2
	1.0	n/a
CNTs	0.1	26.1
	1.0	n/a

The results obtained using the different dye-doped LCE samples tested are

5. ALTERNATIVE MATERIAL STRATEGIES

summarized in Table 5.1 where the maximum force values are listed as function of the dye content. For a better comparison, the maximum force values measured using LCE-CNT samples were added.

Although there are significant differences between the maximum force values obtained by the different dye-doped samples when compared by content, all the actuators described actuation curves comparable in shape with pretty similar time responses (see Figure 5.12).

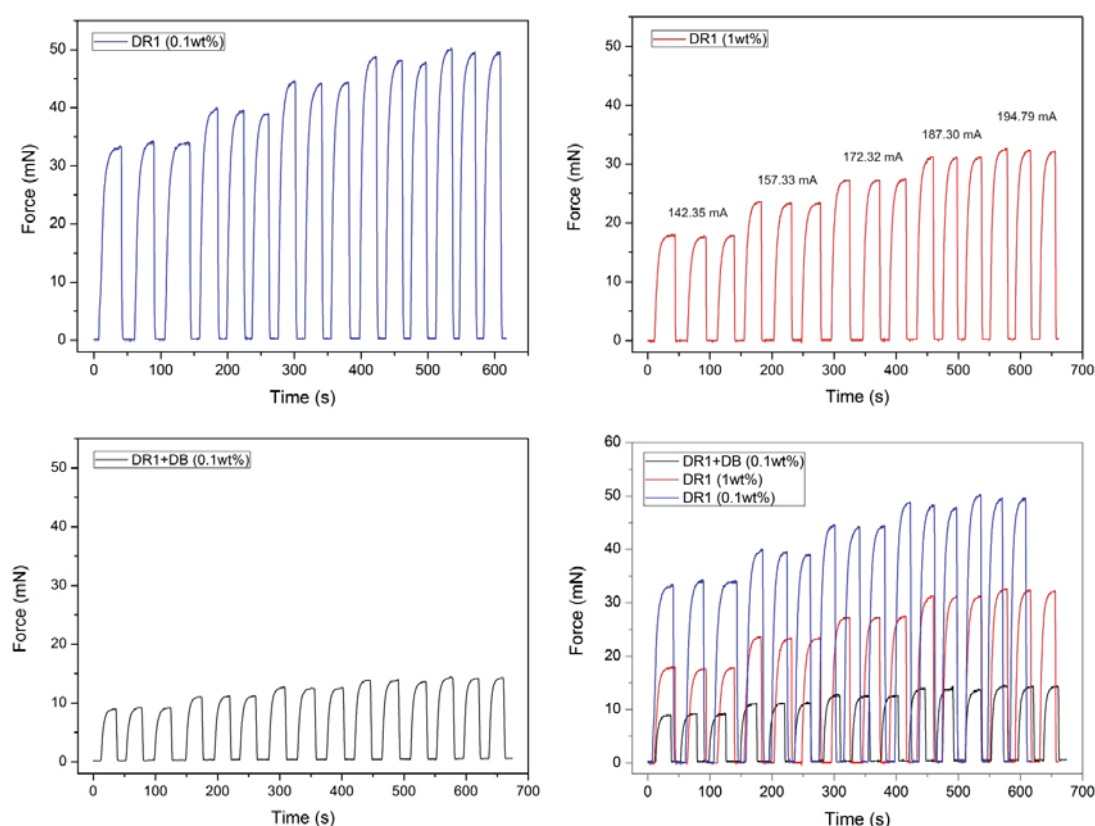


Figure 5.12: On-off actuation force measurements for three pins assembled using different dye-doped LCE samples (DR1 at 0.1 wt.%, DR1 at 1 wt.% and DB14+DR1 at 0.1 wt.%) as function of different current intensities applied.

As in case of LCE-CNT actuators, cyclic measurements using dye-doped LCE samples have been performed and later repeated over different time periods to control their stability and check their viability as tactile actuators. Again, no material degradation was observed remaining both the force and the actuation times constant.

As expected from the good results obtained, with the incorporation of dyes into LC matrices, higher forces can be reached by the pins, allowing a considerable reduction in power consumption (around 32 %) while ensuring the minimum force value of 15 mN required to guarantee a correct tactile perception (see Appendix A). In this manner, it will be possible to increase the efficiency of the system using the same device and with the same material characteristics while maintaining the so-appreciated spring effect of the actuator. Thus, a new actuators layer for the NOMS tactile device containing an array of 10 x 10 actuators using 0.1 wt.% of DR1 dye-doped samples was successfully assembled for future testing (see Figure 5.13).

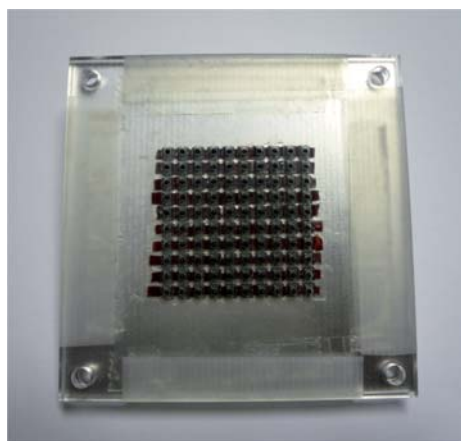


Figure 5.13: Array of 10 x 10 actuators assembled for the tactile device using dye-doped LCE material.

EVA-CNT nanocomposites

5.5 EVA-CNT conformation

Ethylene-vinylacetate copolymer, EVA, is a useful, cheap polymer with a broad range of desirable properties since it approaches elastomeric materials in softness and flexibility but at the same time can be processed like other thermoplastics.

Current applications of EVA are hot melt adhesives, plastic wraps, packaging and foams; it is even used in drug delivery research due to its inertness.

Similar to LCE and other types of polymeric materials, the properties of EVA can

5. ALTERNATIVE MATERIAL STRATEGIES

be influenced by modifying the ethylene/vinyl acetate ratio [215, 216] and modified on demand to obtain different types of composites.

In the field of material science, composites based on EVA are frequently used for the creation of shape-memory materials, such as those stimulated by an electric field [216]. However, this material has not been widely studied as a matrix for elastic photo-actuators since by default, it does not have photo-mechanical response. With the main purpose to provide EVA with photo-sensitive properties, Kzanicová and co-workers have explored different alternatives to determine and optimize the preparation protocols for obtaining proper EVA-CNT composites, which have been conducted in parallel to the work of this thesis. Details concerning the synthesis and preparation of various types of samples containing different CNT surfactants can be found in Ref. [216, 217]. A summary of the final procedure is briefly described in the following section.

In this section, first photo-mechanical characterization results of different EVA-CNT samples are presented as a potential alternative to LCE nanocomposites for the fabrication of new generation of photo-actuators.

5.6 EVA-CNT nanocomposites preparation

The different types of EVA-CNT composites filled with different content of MWCNT and SWCNT were prepared by casting from solution. Similar to the preparation of LCE-CNT, some previous chemical treatment was required in order to guarantee a good dispersion of CNT within the polymeric matrix. In this case, a nanofiller and cholesteryl pyrenecar-boxylate, PyChol, compatibilizer dispersed in chloroform were used [217]. After mixing, such solution was sonicated for 1 h under magnetic stirring (Hielscher 400 S sonicator) at amplitude of 20 % ($\approx 35 \mu\text{m}$, $\approx 60 \text{ Wcm}^2$) and a duty cycle of 100 %. After that, EVA was added and the final solution was stirred for 3 h at 1200 rpm. Then, the solution was poured into a Teflon-coated Petri dish and dried at room temperature for 12 h (similar to the first crosslinking process in case of LCE materials) to obtain a weakly cross-linked composite. The sample was then placed in an oven and gradually heated to 40 °C, 60 °C, and 70 °C for several hours for a complete curing. Additional drying was performed in a vacuum oven for 6 h at 70 °C to assure the complete evaporation of solvents. The composite foil was prepared by

5.7 EVA-CNT nanocomposites actuation

compression molding in a laboratory press (Fontijne SRA-100, The Netherlands) for 15 minutes under a pressure of 2.4 MPa with an applied temperature of 80 °C. Finally, the different EVA-CNT samples were stretched at different rates (20%, 50%, 100% and 150%) at 50 °C for 20 min using a custom-made stretching apparatus to provide them with thermo-mechanical response. After that, the samples were cooled down in ice water to fix the orientation of the CNTs and the polymeric matrix. Using this approach, samples with 40 mm length, 5 mm width and thickness ranging from 0.45 mm to 0.70 mm are obtained.

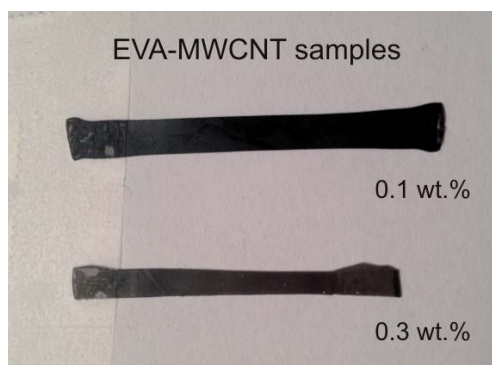


Figure 5.14: Examples of two different EVA-CNT samples fabricated containing 0.1 wt.% and 0.3 wt.% of MWCNTs.

Figure 5.14 shows two different EVA-CNT samples containing 0.1 wt.% and 0.3 wt.% of MWCNT prepared using the above described methodology. Notice that for 0.3 wt.% of CNT the sample is totally black, whereas the sample containing less amount of CNT is still a bit transparent (not so appreciated in the image).

5.7 EVA-CNT nanocomposites actuation

5.7.1 Mechanical strength measurements

To have an estimation of the mechanical behavior of these novel nanocomposites, preliminary measurements of the Young's Modulus were performed in dark (no illumination applied). To that end, the same procedure described for the characterization of LCE-CNT samples (see Chapter 3) was used, as well as the same setup. In this case, however, various EVA-CNT samples containing the same amount of MWCNTs (0.3 wt.%) prepared using different pre-stretching conditions. The total

5. ALTERNATIVE MATERIAL STRATEGIES

elongation of the films per test was limited to $500\ \mu\text{m}$ ($10\ \text{times} \times 50\ \mu\text{m}$) and controlled by means of motorized stages to avoid fracture of the material. Time diagram of the mechanically induced force is presented in Figure 5.15, resulting in a Young's Modulus in the range of 0.7 MPa to 0.9 MPa, calculated using experimental data.

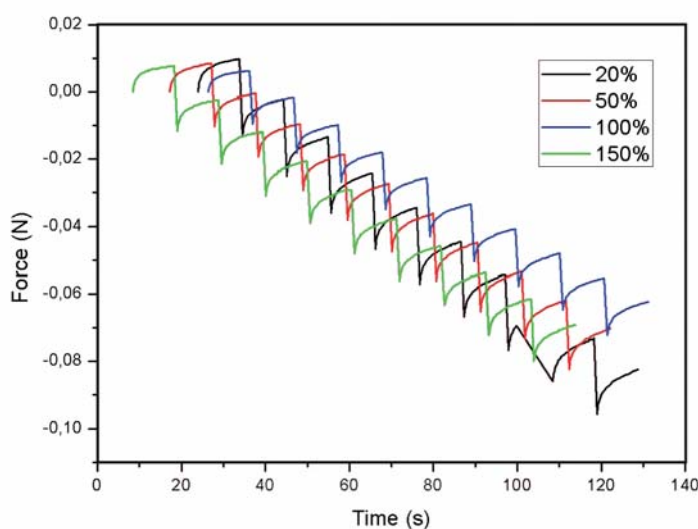


Figure 5.15: Time diagram of the force induced by mechanical stretching of different EVA-CNT samples containing 0.3 wt.% of MWCNTs as function of their pre-stretching rate.

From the data in the graph, it was not possible to obtain a clear relationship between the pre-stretching rate of the samples during their preparation and the Young's modulus values measured. Further and more precise experiments will be necessary to study in depth the possible effect between those two parameters.

5.7.2 Photomechanical actuation

The change in the length of the samples containing different wt.% content of both MWCNTs and SWCNTs was evaluated in a similar way than previous LCE nanocomposites. However, in this case, due to the low range of working temperatures of the material (only from room temperature up to $40\ ^\circ\text{C}$), the thermal actuation was replaced by photo-actuation. Thus, instead of using the miniaturized hotplate (peltier element), a red LD of 670 nm of wavelength was chosen and placed underneath.

Samples of following dimensions 1.5 mm length and 0.8 mm width were placed on a glass substrate previously treated with PTFE to avoid undesirable sticking effects. Same glass/PMMA chamber was used to cover the samples to avoid thermal gradients. Again the same CCD camera coupled to a standard optical microscope was used to record the contraction of the samples. Figure 5.16 shows the results obtained. Although the samples contracted upon illumination the resulting contraction coefficients, λ_i , ranged between 0.95 to 0.98, values significantly lower than the ones obtained using LCE-CNT even dye-doped LCE samples, which were in the range of 0.5 to 0.6.

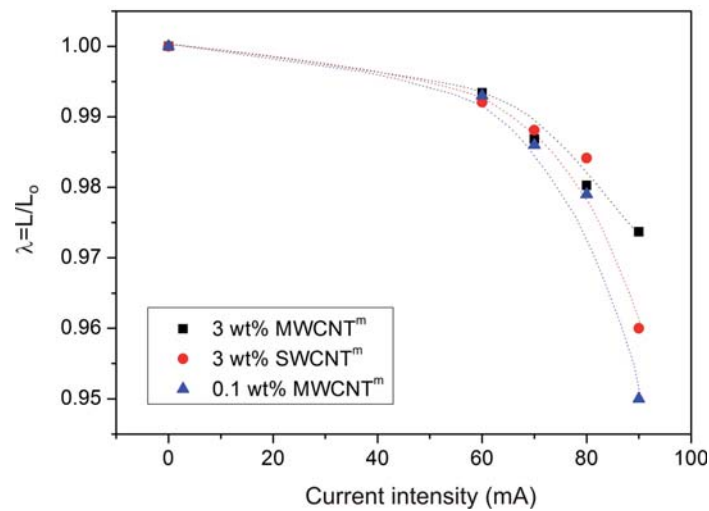


Figure 5.16: Evolution of the contraction along the stretched direction of different EVA-CNTs samples as function of various current intensities applied [218].

No significant differences were obtained between samples containing SWCNT or MWCTN. However, taking into account the knowledge acquired working with LCE-CNT composites and previous studies about the photo-electrical properties of different types of CNT [219, 220, 221], MWCNT were selected to be the most suitable option.

5.7.3 Photo-induced actuation

Photo-induced force measurements of EVA-CNT samples were performed using two different types of light sources, similar to LCE-CNT sample: a red LD (670 nm wavelength) and the LUXEON C white LED from Philips used for the assembly of the NOMS device. Although no spectral dependence by CNTs was expected, different

5. ALTERNATIVE MATERIAL STRATEGIES

characteristics of the light sources (aperture angle, power density, etc.) may cause differences in the material response.

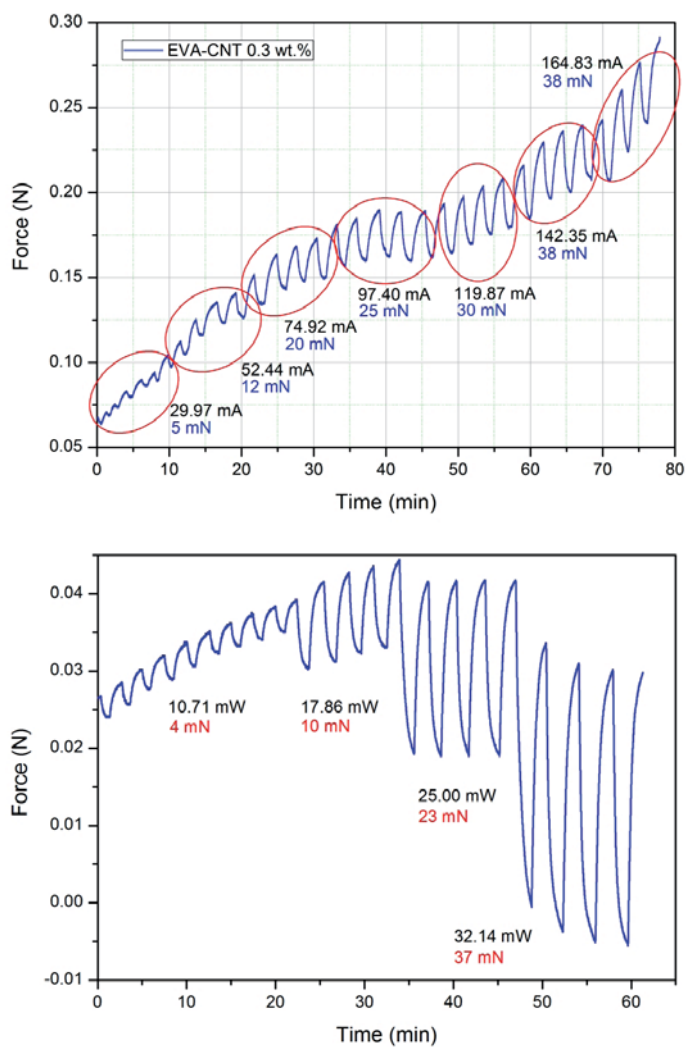


Figure 5.17: Photo-induced force measurements of EVA-CNT film containing 0.3 wt.% of MWCNTs as function of the current intensity applied, using LUXEON C white LED -top- and a 670 nm LD -bottom-.

Again, the same setup developed to perform previous photo-induced force measurements within this thesis was used. Thus, the different EVA-CNT samples containing 0.3 wt.% of MWCNT were cut into small ribbons of 10 mm long and 1.2 mm width and horizontally placed 7 mm above the correspondent light source and fixed at both ends. Due to the temperature limitations of the EVA material, the current

intensity working range for both light sources were previously adjusted to avoid material damage. Table 5.2 details the testing values selected for each type of light source.

Table 5.2: Current intensity working ranges selected for testing as function of the light source.

Light source	Current intensity range [mA]
670 nm LD	60 - 100
LUXEON C LED	7.49 - 164.83

An example of the measurements of the maximum force induced by both types of light sources is depicted in Figure 5.17.

As is easily understood from the graphs shown in figure 5.17, the maximum effective force values reached (difference between the minimum and maximum force values) was in the order of previous LCE-based nanocomposites measured. However, the response of the material under illumination using both types of light sources was very uneven, resulting in a significant drift in the actuation force minimum (rest position, in dark) and maximum (excited, under illumination) values.

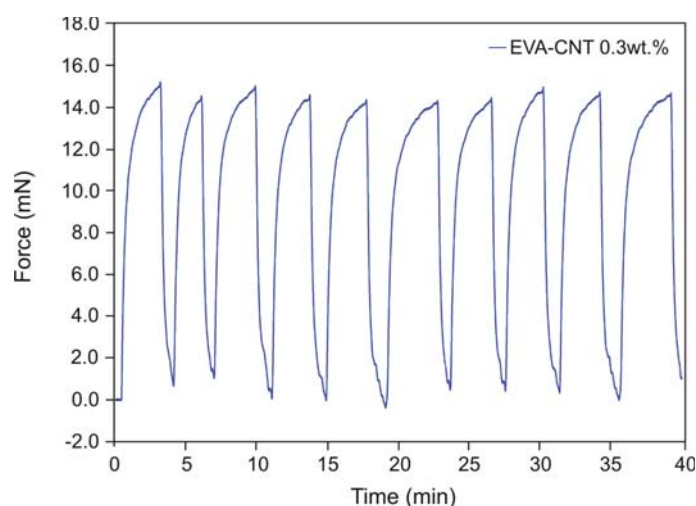


Figure 5.18: On-off actuation force measurements of the same EVA-CNT film under LED illumination after conditioning. The maximum force achieved was around 15 mN under the application of 74.92 mA.

This phenomenon can be explained by the intrinsic nature of the material, which partially retracts the heat supplied by the light source, resulting in a residual amount

5. ALTERNATIVE MATERIAL STRATEGIES

of heat remaining on the sample after each on-off cycle. This phenomenon can be at the same time responsible of the increased actuation times of this type of composites with respect the LCE ones, which increased from few seconds to minutes.

To assess the effect of adding CNT into the matrix, neat EVA samples were also characterized under the same conditions resulting in a practically null response to photo-induced actuation, fact that demonstrated their influence on the material performance. A detailed study of the mechanism involving actuation of these new composites is part of the ongoing work.

Some preliminary measurements adjusting the testing parameters were conducted with the main purpose of improving the response to light of these composites trying to minimize the drift, since the current protocols used for testing was the one developed for LCE samples. To that end, some previous conditioning of the material was conducted, keeping the light source on at the corresponding current intensity selected for testing for several minutes prior to starting with the on-off actuation. In this manner, several consecutive on-off actuation cycles could be performed and both the minimum and the maximum force values obtained resulted more stable (see Figure 5.18). However, some drift still remained. Future Work involving sample conditioning will be addressed in future to minimize such effects and provide a steadier response.

5.8 EVA-CNT actuators

Finally, to check the viability of EVA-CNT samples to be integrated on the NOMS tactile device, a single "U-shaped" actuator was assembled. To this purpose, similar EVA samples containing 0.3 wt.% of MWCNTs was used.

Figure 5.19 shows a picture of the "U-shaped" actuator assembled on the actuators layer of the NOMS tactile device.

Similar to the previous tested "U-shaped" actuators, the setup using the dynamometer was employed to measure the pushing force produced by the pin under illumination. In this case, however, testing parameters such as the current intensity should be adjusted in order to feed the power requirements of the material that, as detailed in the section above, were significantly lower compared to LCE nanocomposites.

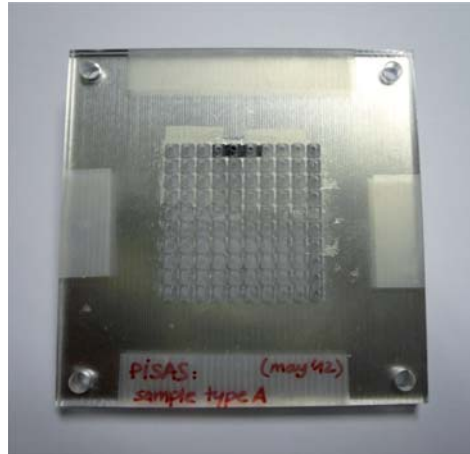


Figure 5.19: Picture of a single “U-shape” actuator assembled for testing using EVA-CNT film containing 0.3 wt.% of MWCNTs.

In contrast with the results obtained using LCE-based nanocomposites on “U-shaped” configuration, the material response in time resulted very irregular but consistent with the results obtained during the characterization of the films in previous section, as depicts the graph in Figure 5.20, where the effective force values of each cycle are given as function of the current intensity applied. After each on-off cycle the pin was supposed to go back to rest position; however, a significant drift of this position was obtained.

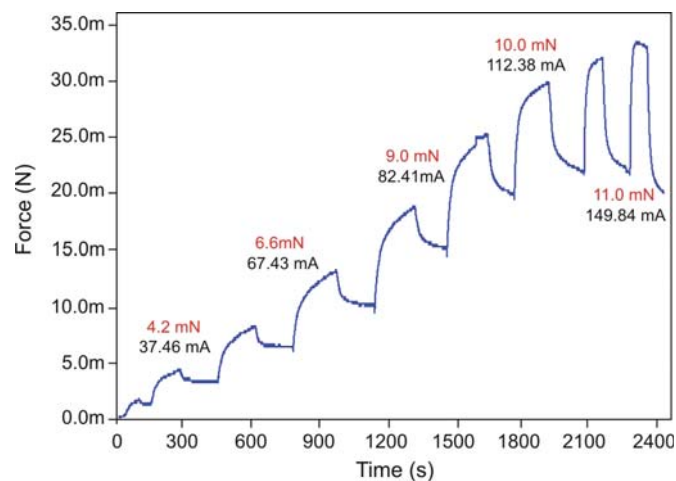


Figure 5.20: On-off measurements of an EVA-CNT actuator containing 0.3 wt.% of MWCNTs. Actuation curves -left- and the maximum force exerted by the pin -right- as function of the current intensity applied.

5. ALTERNATIVE MATERIAL STRATEGIES

To improve the results obtained, again some previous conditioning of the material was performed, keeping the LED on for several minutes until the force started to stabilize. Then, the on-off measurements were repeated resulting in more stable force values, in similar way than in case of EVA-CNT films (see Figure 5.18). However, both the force peak (maximum force value achieved) and the rest position still drifted. Plot in Figure 5.21 evidence such behavior.

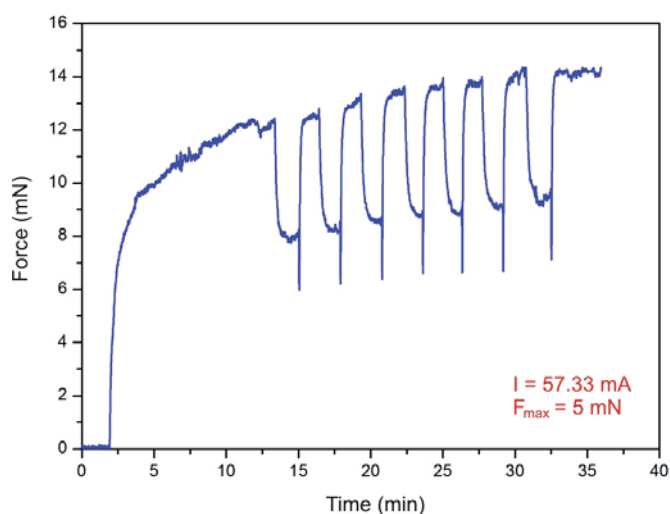


Figure 5.21: On-off actuation force measurements of an EVA-CNT “U-shape” actuator after material conditioning where a noticeable improvement on the measurements is evidenced. The maximum force achieved was 5 mN under the application of 57.33 mA.

5.9 Discussion and summary

In this chapter, a first strategy for the improvement of the “U-shape” actuators performance and thus, the developed NOMS device, has been introduced by means of two different alternatives for the amendment of photo-active LCE-CNT nanocomposites. The first one consists in replacing CNTs by light-absorbing dye molecules while maintaining the LC matrix, whereas the the second one, changes the LC matrix by a commercially-available polymer preserving the embedded CNTs. Both strategies have been exposed and the first characterization results given.

In the first part of the chapter, different dye-doped LCE films have been compared, proving that by the selection of suitable dyes, the sensitization of LCEs to visible-IR

light range can also be achieved in similar way as CNTs, without loss of performance. As first attempt, two types of dye molecules, IR1310 and DR1, with different optimal absorption ranges (IR and visible respectively) have been chosen for the fabrication of testing samples. In all cases, samples with 0.1 wt.% and 1.0 wt.% of dye content were prepared to investigate the possible effects due to increased dye content into the LC matrix, in the same way as previously done with CNTs. In each case, absorption spectrum measurements have been performed together with the evaluation of the force produced under different types of light irradiation.

With the main purpose to evaluate the integration of such materials into the NOMS tactile device, the same white LED used for its fabrication (LUXEON-C, Philips) has later been used for testing, resulting in a significant increase of the actuation force. Taking into account these results, various actuators have been finally assembled in a "U-shape" configuration as described in Chapter 4 and tested following the same actuation parameters as LCE-CNTs ones. The results obtained were good, with actuation curves similar in shape to the ones obtained using CNT. However, the forces reached by dye-doped LCE samples were considerably high, leading to a notable reduction in power consumption (around 32 %) while producing minimum force values to assure correct tactile signal; value which can be optimized in future.

The fabrication of dyed LCE material is a promising way forward, due to the flexibility of the method for tailoring the absorption properties of the LCE material. As demonstrated, photo-active dye molecules are capable of thermally triggering a phase change in the elastomer when subjected to light irradiation without changing the material response when small concentrations are added. In addition, the use of a dye rather than the CNT-surfactant system simplifies the samples fabrication process to some degree, allowing for greater consistency, resulting in great candidates to replace LCE-CNTs for the fabrication of novel opto-mechanical actuators.

In the second part of the chapter, a different strategy was proposed, replacing the LCE matrix by a commercially-available thermopolymer, EVA, while maintaining the CNTs, in order to reduce both synthetic procedures and costs. A brief introduction to the main EVA characteristics has been presented as well as some details about the preparation of EVA-CNT nanocomposites, process which resulted to be not as simple as expected. First testing samples prepared under different conditions have been characterized and some photo-induced force measurements using different light

5. ALTERNATIVE MATERIAL STRATEGIES

sources (LD and white LED) have been presented. The values obtained resulted to be lower but in the order of the ones obtained using LCE materials; however an important drift in the maximum and minimum force values was obtained which reflects the need of changes in the samples measurement protocols. A significant improvement has been achieved by means of conditioning of the samples prior to start the tests. Similar to dye-doped samples described early in this chapter, a "U-shape" actuator has also been assembled using EVA-CNT samples containing 0.3 wt.% of CNTs and the actuation results analyzed. Although proving the possibility to achieve photo-actuation, a significant increase on the actuation times was obtained compared to LCE nanocomposites (from seconds to minutes) together with a non-regular behavior material, losing stability. Future work involves mainly deep characterization of the samples improving the measurement protocols to find the optimum actuation parameters to deeply study the suitability of this new type of photo-sensitive nanocomposites as real candidates for the fabrication of actuators.

The work described in this chapter result as part of the last experiments of NOMS project. The first part of this chapter (study of dye-doped LCE materials) has been done in collaboration to Prof. Eugene M. Terentjev and Dr. Jean E. Marshal from Cavendish Laboratory at University of Cambridge, whereas the second part (study of EVA-CNT materials) has been done in collaboration to Dr. Mária Omastová, Dr. Igor Krupa and Dr. Klaudia Czaniková from Polymer Institute of the Slovak Academy of Science in Bratislava, PISAS. The idea of combining photo-active dyes with LCEs was conceived at IMB-CNM whereas the one involving EVA-CNT materials resulted from the collaboration between both UCAM and PISAS research groups.

All the characterization experiments of both types of nanocomposites were performed at IMB-CNM facilities, together with "U-shape" actuators assembly and the force measurements using the tactile device. Similar to previous chapters, the preparation of dye-doped LCE composites and the absorption spectra measurements were carried out at Cavendish Laboratory which also gave advice about material's behavior, whereas the synthesis and preparation of the samples containing EVA-CNT were in charge of PISAS team.

As a result from this collaboration, a scientific journal article with high impact factor has been published and one more is under preparation.

Part IV

Novel technologies for the fabrication of actuators in an array

6

Punch and die molded actuators

In the field of engineering, silicon-based technologies are the most commonly used for the fabrication of MEMS and NEMS. These well-known techniques are very robust and well-controlled, and allow a batch processing large-scale fabrication of devices combining large number of varied physico-chemical processes [132, 133]. Furthermore, these processes enable the use of several types of materials ranging from silicon and its derivatives to polymers, ceramics, metals and oxides [136]. In this manner, it is possible to fabricate various types of devices such as simple resistors, micro-heaters and transistors for circuitry [222], accelerometers for ITC technologies and automotive field [223], radiation detectors [224], bio-devices [225] and solar cells for energy harvesting [226], among others.

As introduced previous chapters, it is possible to integrate LCE-CNT materials for the fabrication of light-driven pushing actuators for Braille applications resulting in large forces and displacements. However, the existing limitations on shape and direction of movement of the material make necessary the use of other elements (e.g., pins, supports, etc.) to obtain the desired actuation response, which at the same time, create some added difficulties for the later integration of such actuators in a final device.

Taking advantage of the previous knowledge in MEMS design and processing, a new step through the integration of LCE materials with MEMS technology is presented with the main purpose of improving the response of the previous actuators while reducing their variability in actuation due to their individual assembly on the device. Thus, three different approaches based on molding techniques have been explored

6. PUNCH AND DIE MOLDED ACTUATORS

in this section to provide easier manners to fabricate elastomeric actuators in batch using partially cross-linked LCE films (2nd strategy described above, in Chapter 4), leading to arrays of actuators in single LCE matrices combining material shaping and mesogens ordering on the same processing step.

In this chapter, the first approach is presented. The actuators herein described were fabricated by molding through the application of mechanical stretching (stamping procedure) and thermal crosslinking, thus demonstrating the possibility to create sufficiently well-aligned liquid crystal units to produce localized actuation on the millimeter scale.

The chapter is divided in 4 sections. In the first one, the concept and the processing principles of the proposed method are presented. The second and third sections describe the design and fabrication process of the molds used as well as the preparation of the actuators. Additionally, a 3D finite element analysis of the molding process developed as a tool to predict the mechanical limits of the LCE-CNT film under molding performance is presented. Finally, the last section presents the characterization of the developed actuators under different operation conditions.

6.1 Concept

The aim of the present development was to obtain a simple methodology capable to align the LC units and locally shape the LCE films in one single step before the final crosslinking of the material, to fabricate arrays of actuators.

In this first approach, instead of using the standard stretching method through which a uniform and unidirectional alignment of the LCE-CNT material along its length is forced reaching an overall contraction movement, the actuation of the film was forced in another direction, normal to the surface of the film, by shaping the material. Thus, a localized actuation can be reached, creating aligned LC monodomains in a polydomain (non-aligned) LCE film. For this purpose, a stamping process based on molding was proposed from which actuators in a dot-like configuration can be obtained.

The molding system proposed consists in two different parts, named punch and die. The first one, the die part, contains a pattern of holes; whereas the punch part consists of an array of pillars distributed in agreement with the die's holes. Mainly,

the stamping process starts placing a film of LCE-CNT composite gel (very lightly cross-linked) which has been previously formed over the punch mold. Then, the gel is pressed on to the die part containing the appropriate holes with a controlled force, producing mechanical stretching in the gel around the pillars. These regions form the walls of the actuator which will be the actuating regions containing the aligned LC domains. The stretched gel is then held in that conformation during a second crosslinking stage, so that the topology of the LC network becomes fixed (composite completely cured). After the crosslinking is completed, the required actuator geometry is formed and fixed; resulting actuation of the stretched parts of the film whereas the other regions remain unaltered in a polydomain configuration.

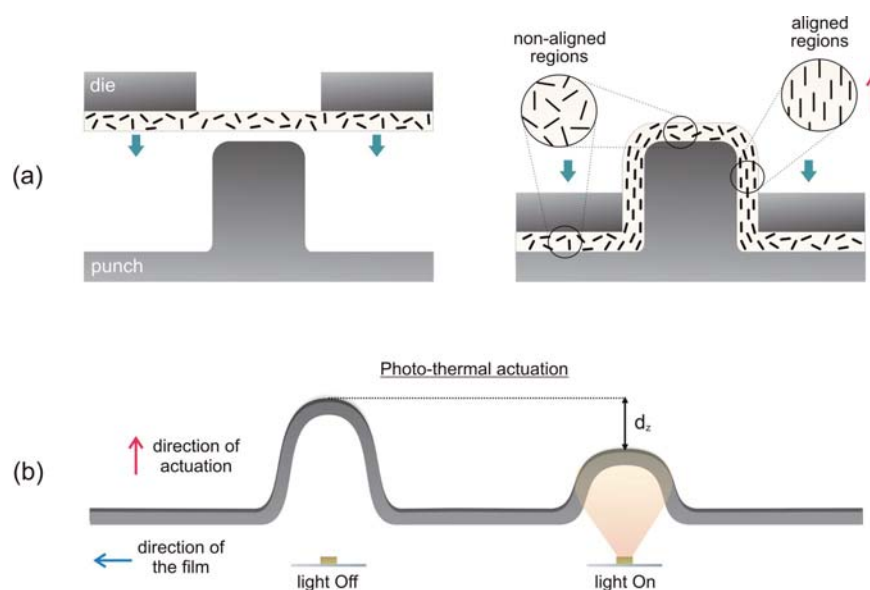


Figure 6.1: Scheme of the molding procedure and the working principle of the actuators obtained.

Figure 6.1 shows schematic views of the concept of the mechanical stretching method proposed to create the array of “punch-and-die” actuators. The design of the molds and their fabrication process, as well as the preparation of the actuators is described in detail in the following sections.

6.2 Molds design and fabrication

Punch and die parts used were specifically designed to fabricate individual and in a six-dot array 1.0-mm-diameter actuators (also referred as dots) according to the Braille standards. However slightly wider 1.5-mm-diameter actuators were also fabricated as testing structures. Hence, on one hand, there are the die molds containing a pattern of holes, and on the other hand, the punch ones which are provided with 200- μm -height pillars.

Both punch and die molds used to obtain the shaped "punch-and-die" actuators were fabricated using the well-known silicon processing and micromachining techniques. The main steps of the microfabrication process of the above mentioned molds have been summarized in Figure 6.2.

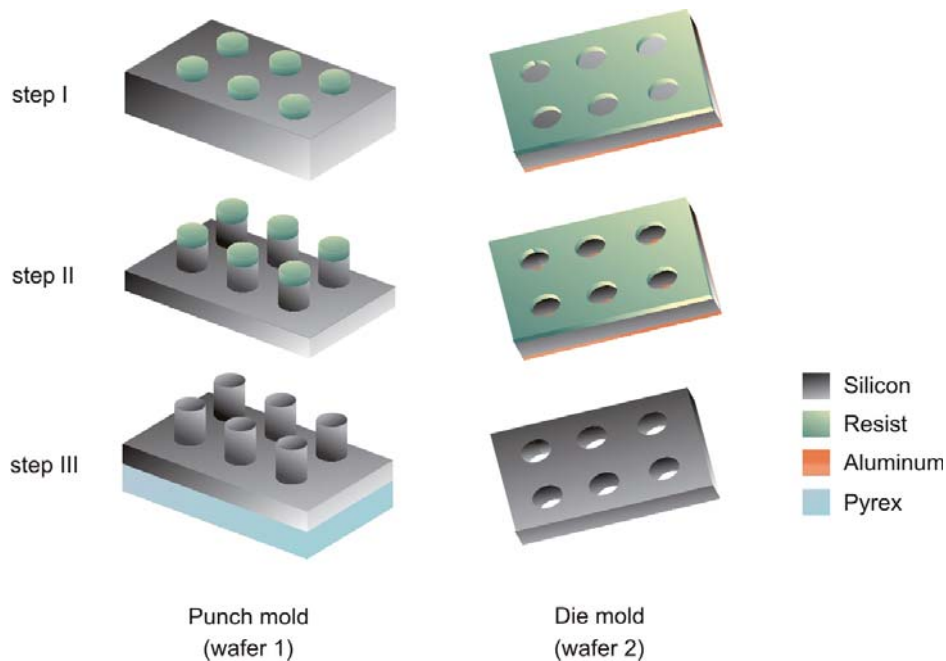


Figure 6.2: Simplified microfabrication process of the punch and die molds.

The process for the fabrication of the punch and die molds started with two silicon wafers of 100 mm in diameter and 500 μm thick, each one for the fabrication of each part of the molds. A double-sided optical contact photolithography was done followed by an anisotropic Deep Reactive Ion Etching, DRIE, of the silicon in the wafers to define the pattern of both the pillars and the holes. Figure 6.2 summarizes the process sequence

used to create the punch mold in wafer 1 (figure 6.2 -left-) and the corresponding die one in wafer 2 (figure 6.2 -right-). In both cases, a 1.0 μm -thick aluminum, Al, layer was deposited and used as etching mask since allows ion penetration to the substrate to remove the non-protected silicon surfaces. DRIE uses a SF_6 plasma gas as etching species for deep, anisotropic silicon etching. Die molds require the full thickness of the wafer to be etched through, so the bottom surface of wafer 2 was protected with resist to avoid damage due to pressure differences once etching reaches this surface completely opening the wafer (step II, figure 6.2 -right-). For the punch molds, 200 μm -high pillars remain after etching the non-protected surface of the wafer 1 (step II, figure 6.2 -left-). This process reduces the volume of silicon in the wafer and can cause fractures in the mold since the wafer becomes mechanically fragile. To improve its robustness, a 1.0-mm-thick Pyrex wafer (7740, Corning) was added below the wafer 1 as new substrate and fixed through anodic bonding to the silicon punch mold (step III, figure 6.2 -left-). The resist and Al layers were removed once both etching processes are completed leading to the final micromachined silicon molds (step III, figure 6.2). Finally, both wafers were cut into individual chips using saw-based cutting to create several sets of punch and die molds for testing purposes.

Figure 6.3 shows tilted views of the two microfabricated wafers containing punch and die patterns as well as an individual set of molds after the cutting process. In order to provide an accurate alignment between the punch and die mold pieces during the stamping process, triangular patterns were added on the four corners of the silicon chips as alignment marks in both sides of each wafer. A size tolerance of 100 μm between both mold pieces allows the punch features to fit properly into the holes in the die.

The pillars in the punch device had diameters of less than 1.0 mm, whereas the die holes had diameters of 1.0 and 1.5 mm. These dimensions allow the 400 μm -thick LCE-CNT composite film to be molded between the two silicon layers.

6. PUNCH AND DIE MOLDED ACTUATORS

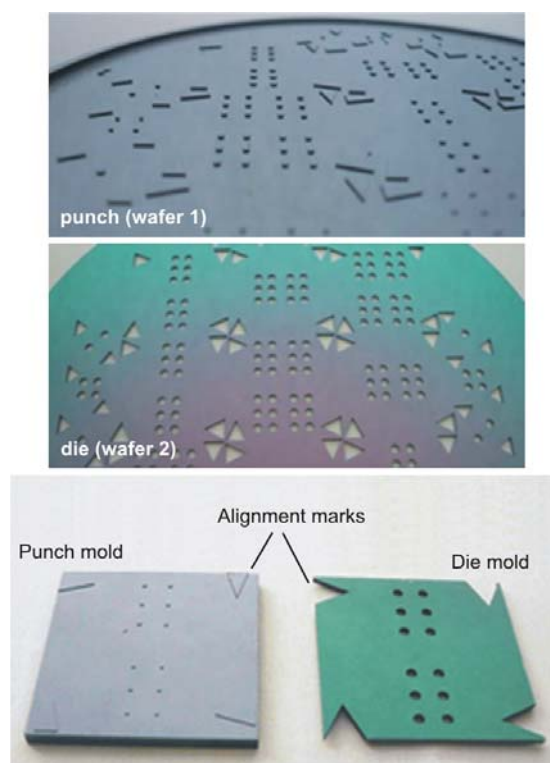


Figure 6.3: Micromachined silicon wafers after the fabrication process -top- and a set of punch and die molds after cutting, ready for testing -bottom-.

6.3 Fabrication and optimization of actuators

6.3.1 Actuators fabrication: stamping process

The “punch-and-die” actuators were fabricated using the LCE-CNT composites presented in previous chapters (see Chapters 2 and 3 for details), using same synthetic route and procedures but only until the first crosslinking was reached, moment when the molding process started.

In order to shape the LCE-CNT film while ensuring a proper alignment of the liquid crystal units in it (similar to the stretching process), the material should be placed inside the molds just when the crosslinking process begins to reach higher contraction. However the composite mixture is rather liquid (contains lot of solvents); then a compromise between the curing degree of the composite and its ease of manipulation should be adopted. In this manner, the molding process starts with a weak gel with few cross-linked polymer chains.



Figure 6.4: Stretching and crosslinking steps for the fabrication of the actuators.

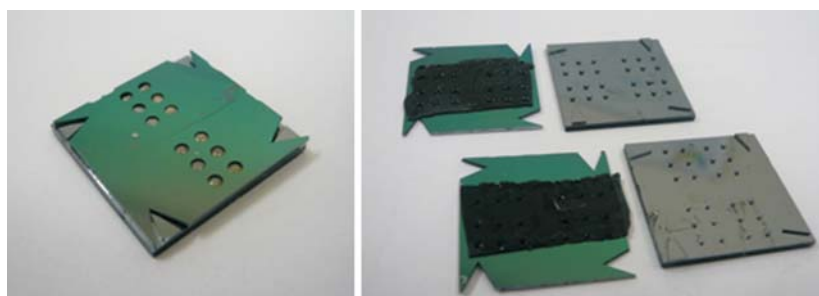


Figure 6.5: Stretched LCE-CNT film after the molding process.

After its extraction from the centrifuge, the LCE-CNT film was placed over the silicon die mold which contains the array of holes. The punch and die molds with the gel were then aligned using the alignment marks designed. Then, the gel was pressed against to the punch mold which has the micromachined pillars, thus producing mechanical stretching in the gel around the pillars (so that these parts of the gel will later form the aligned walls of the actuator). The stretched gel was then held in that conformation for several days to complete the crosslinking process while keeping a constant curing temperature of 100 °C. A Bronze plate of 100 g weight was used to guarantee a uniform pressure all over the surface of the molds. Hence, the topology of the LC network became fixed creating polydomains within a monodomain sample. Figure 6.4 shows pictures of the stretching and crosslinking procedures of the samples. After the crosslinking process was completed, the required feature geometry was formed and the punch mold could be released, as shown in Figure 6.5. In order to minimize the adhesion between the polymer film and the silicon, the surfaces of the molds were silanized at wafer level before cutting. Thus, the LCE-CNT films could be later peeled away and transferred to another rigid support for operational purposes.

6. PUNCH AND DIE MOLDED ACTUATORS

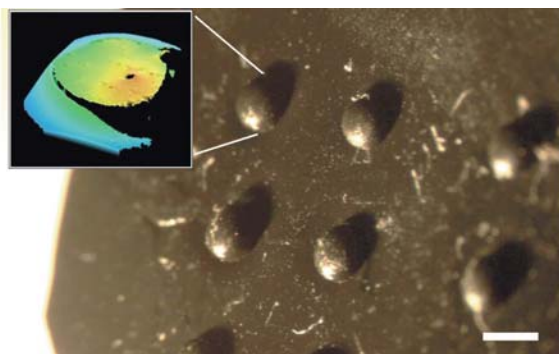


Figure 6.6: "Punch-and-die" actuator pattern of molded LCE-CNT composite. Scale bar = 1 mm.

Figure 6.6 shows an optical stereoscopic image of the shaped LCE-CNT film after releasing the punch mold keeping the permanent actuator pattern in close agreement with the mold sizes. A confocal image detailing the 3D topography of a single "punch-and-die" actuator is shown in the inset.

6.3.2 Actuators optimization: mechanical response limit

In order to assess the correct performance of the molding process and to optimize the mechanical properties of the stretched, blistered film, a new version of the FE model using ANSYS® Multiphysics software was built from the previous approximation in Chapter 3 to study the mechanical limits of the film, especially in those regions that are critical to the stretching procedure: the vertical walls of the actuators and the contact points between the molds and the LCE-CNT film. The 2D model takes advantage on the radial symmetry of the system and employs PLANE183 elements for the composite and silicon materials. This element type is suitable for modeling deformations in nearly incompressible elastoplastic materials and fully incompressible hyperelastic materials like the LCE-CNT composite [227]. Figure 6.7 shows an axonometric partial view of the finite element model used.

To perform this simulations, some of the material parameters measured in previous sections (Chapters 2 and 3) were used, resulting a Young's modulus of the composite in its pre-cured state (the weakly cross-linked gel) in the 25 kPa to 30 kPa range with a rupture stress around 12 kPa. Figure 6.8a displays compressive stress localized in those regions where the material is in contact with the mold edges. The magnitude of

this stress is much higher than the stress in the rest of the film. This issue is crucial for an optimal fabrication of the actuators. If the stress difference is too large between these regions, the film can break before that the rest of the film is sufficiently stretched in the lateral wall zones. In that case, the later actuation of the film would be negligible or not observed at all because of poor LC alignment. For the $300\text{ }\mu\text{m}$ -high punch molds, the break point and overall performance will depend on the pillar diameter.

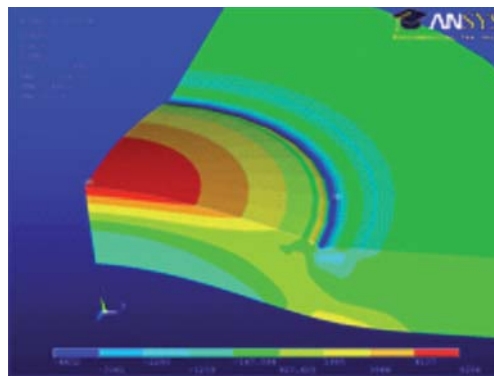


Figure 6.7: Partial view of the FE model used for the simulations.

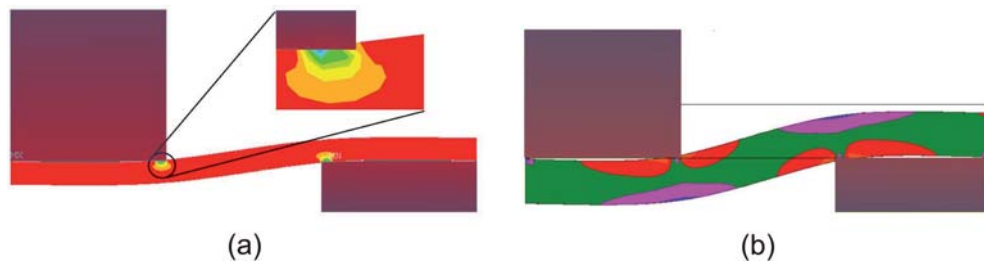


Figure 6.8: Finite Element Analysis of the stretching process. Blister pattern of molded LCE-CNT composite.

To guarantee an optimal actuation of the “punch-and-die” actuators, the strain along the film -mainly in the lateral walls of the actuator- should be uniform and keep constant along all the curing process. The model in Figure 6.8b shows that the main strain variations experienced by the LCE-CNT film are focused on the regions of interest. However, the magnitude of this strain seems to vary along the material thickness, fact that could produce, therefore, a non-uniform actuation.

6.4 Characterization

The actuators fabricated using this punch and die stamping process were mainly characterized by measuring its performance under photothermal excitation. Thus, the degree of contraction achieved was calculated by measuring the change in height of the actuators at different conditions. Moreover, the stability of the actuators response was evaluated from the long-term actuation measurements through cyclic testing, similarly to the previous presented "U-shape" actuators (Chapter 4). The setup configuration and the measurements obtained, together with a discussion of the results are presented in the following sections.

However, a DSC analysis was first carried out to determine the range of temperatures of actuation resulting in $T_g = 15\text{ }^\circ\text{C}$ and $T_{NI} = 85\text{ }^\circ\text{C}$.

6.4.1 Setup configuration

In order to quantify the photothermal actuation a LD emitting at wavelength of 658 nm (HL6512MG, Thorlabs) was selected, switching different driving currents by means of a power controller (ITC 510, Thorlabs). Figure 6.9 schematically shows the setup configuration used. A specially designed support was fabricated to fix a certain distance, z , between the sample and the LD to guarantee uniform illumination of the whole sample, so as to obtain the maximum possible actuation. The sample was illuminated from the underside and the observation carried out from the top side.

Driving currents between 60 mA and 130 mA were used for actuation, which were related to the total power transmitted by the laser beam. For these measurements, the upper power range was determined by considering the maximum input power for the LD which was 63 mW. However, 60 mW were considered for safety reasons.

The optical power incident to the surface of the actuators was calculated considering that the HL6512 LD has a conical radiation pattern with beam divergences $\theta_{\perp} = 8.5^\circ$ and $\theta_{\parallel} = 21^\circ$, and that the bottom surface of the actuators is placed at a distance z from the spot of the light. Thus, the optical power can be calculated as:

$$P(r, z) = P_0 \left[1 - e^{-\frac{2r^2}{w^2(z)}} \right]$$

where $P(r, z)$ is the optical power in milliwatts passing through a circle of radius r in the transverse plane at a distance z , P_0 is the laser's output power, and $W(z)$ is the Gaussian beam width of the laser at such distance. $W(z)$ size depends on z , the beam waist W_0 and the wavelength λ of the light source, and is given by:

$$W(z) = W_0 \sqrt{1 + \left(\frac{z\lambda}{\pi W_0^2} \right)^2}$$

To determine the power incident to the actuator, it has to be noted that the actuator surface intersects the spot at the distance $z = 1.5$ mm. $W(z)$ thus forming an ellipse with major and minor semi-axes given by the divergence angles of the beam. In the case of the 1.5 mm actuator, the area exposed to light is a circle with effective top radius of $450 \mu\text{m}$. According to the expression above, at the actuator-to-laser distance $z = 1.5$ mm, the major and minor semi-axes of $W(z)$ have a length of $550 \mu\text{m}$ and $223 \mu\text{m}$, respectively. Then, by using the optical power expression and considering the size of the intersection between the actuator and beam area, the contributions to $P(z)$ in the directions of the ellipse semi-axes can be calculated. The result was that 86 % of the total power supplied by the laser arrives to the actuator.

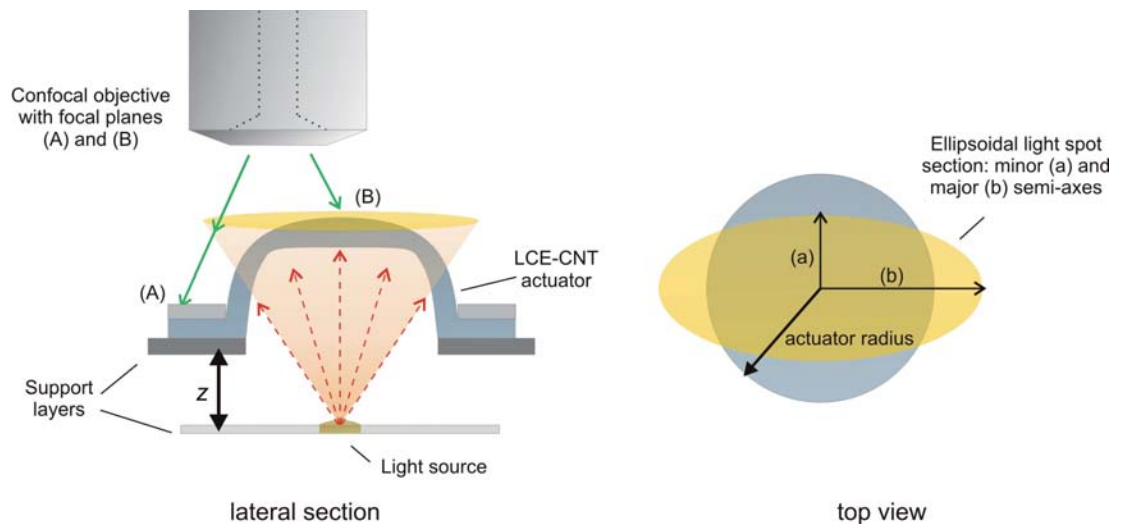


Figure 6.9: Experimental setup for measuring the "punch-and-die" actuators deformation upon illumination.

The transmission losses were neglected due to the low attenuation constant of air and the low traveled distance z . Similarly, the incident power at the 1.0 mm actuator

6. PUNCH AND DIE MOLDED ACTUATORS

surface was calculated adjusting the $W(z)$ value due to the smaller dimensions of the actuators while maintaining z . In that case, the amount of power incident to the sample decreased, resulting 66 % of the total electrical power supplied.

6.4.2 Photomechanical actuation

The photomechanical response of the present actuators was obtained measuring their deformation under LD irradiation. PL μ 3D optical imaging profiler (Sensofar-tech, Spain) located at clean room facilities from IMB-CNM (CSIC) was used to capture the surface profiles of the actuators before and under illumination by means of interference planes analysis. The contraction movement and thus, the degree of deformation of the samples achieved by using this novel stamping technique were calculated from the changes in height of the actuators. The electrical power range used was between 10 mW and 60 mW.

Figure 6.10 plots the actuation curves of three different samples of 1.0-mm and 1.5-mm-diameter actuators as function of the power incident to them. The shape of the actuation curves is in agreement with the ones obtained when measuring the non-shaped LCE-CNT films, proving that the material maintains the same contraction behavior. The lower range of contraction at the left side of the curves (few microns) evidenced, again, the influence of the power applied in the material response. Low power means lower temperature gradient and thus, lower actuation.

From the curves it can be observed that bigger-diameter actuators (1.5 mm) have higher power dynamic and actuation ranges, resulting in a more uniform contraction behavior with a mean maximum deformation around 38 μm . However, in the case of 1.0-mm-diameter actuators, the actuation curves are less uniform and the dispersion in measurements was higher, resulting in a mean maximum deformation around 26 μm under the same power conditions. These differences might be caused by the larger light-exposition surface of 1.5 mm actuators compared with the smaller ones. Higher stretching levels reached during the fabrication of the actuators due to the punch mold design may also explain these variations.

Assuming a homogeneous alignment along the thickness of the samples, the real change in dimensions of the actuators and in consequence, the contraction degree achieved upon illumination can be analyzed in depth. Considering the geometry

of the actuator as a spherical dome and taking into account its height variations under illumination (see scheme plotted in Figure 6.11) the arc length of the circular segment determined by the cavity (central plane), L , can be obtained by the following expressions

$$R = (d^2 + 4h^2)/(8h)$$

$$L = (d^2 + 4h^2)/(4h) \sin^{-1}[(4dh)/(d^2 + 4h^2)]$$

where d is the diameter of the cavity ($d = 2r$) and h is the corresponding sagitta.

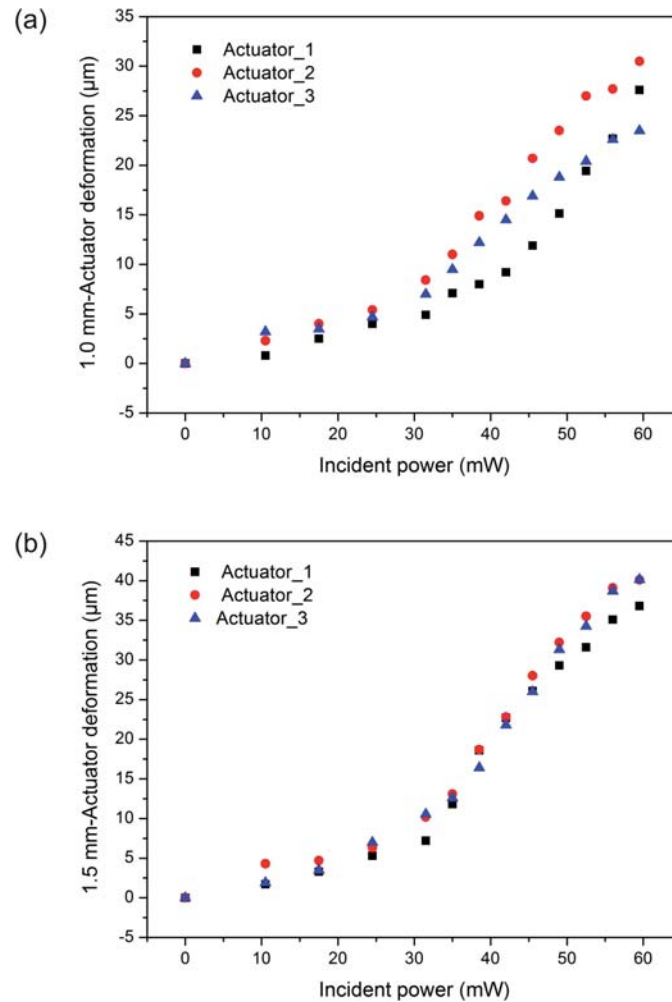


Figure 6.10: Photomechanical response of 1.0-mm and 1.5-mm-diameter "punch-and-die" actuators as function of the incident optical power.

6. PUNCH AND DIE MOLDED ACTUATORS

Performing the corresponding calculations in dark and under illumination the uniaxial thermal expansion resulted to be $\lambda_{chord} = L_{dark}/L_{light} \approx 1.06$, which corresponds to a contraction in length of $\varepsilon_{chord} = 6.00\%$ in case of 1.0-mm-diameter actuators and $\lambda_{chord} \approx 1.07$ and a contraction of $\varepsilon_{chord} = 6.46\%$ in case of 1.5-mm-diameter ones. Considering the composite as a nearly incompressible material (Poisson's ratio of $\nu \approx 0.5$) in agreement with the experiments performed during the LCE-CNT composites characterization (see Chapter 3), the uniaxial thermal expansion in the direction of the thickness (normal surface plane) can be similarly obtained, resulting $\lambda_{thickness} = 1/\lambda_{chord}^2 \approx 0.88$, which corresponds to an expansion of $\varepsilon_{thickness} = 13.17\%$ in case of 1.0-mm-diameter actuators and $\lambda_{thickness} = 0.88$ and an expansion of $\varepsilon_{thickness} = 14.28\%$ in case of 1.5-mm-diameter ones.

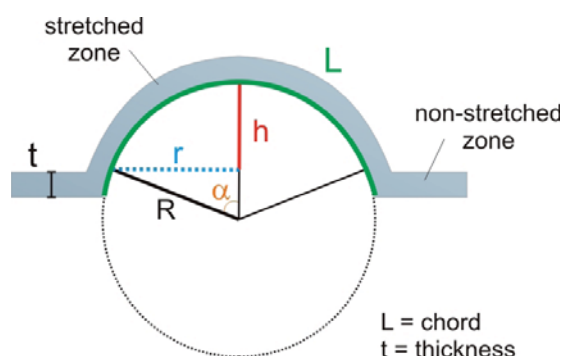


Figure 6.11: Geometric approximation of a punch and die actuator for calculations.

To analyze the repeatability in the short-term actuation of the “punch-and-die” actuators and the reliability of the material, over 60 on-off actuation cycles on both types of samples were carried out. In this case, the incident optical power was set to 48.5 mW in order to ensure no degradation of the material. Moreover, switching times between ‘on’ and ‘off’ states were established taken into account the activation (when heating) and relaxation (when cooling) cycle of the material (see details of LCE-CNT composites characterization in Chapter 3).

Figure 6.12a shows as example, the heights of a 1.5-mm-diameter actuator before and during its light-induced activation measured using the confocal microscope, where a decrease in height, Δh , (i.e., contraction) can be observed due to the changes in the material conformation when T_{NI} is reached. Figure 6.12b plots the contraction values obtained for both actuator sizes with their corresponding mean values, resulting

$\Delta h_{1.0} = 20.91 \mu\text{m}$ and $\Delta h_{1.5} = 33.26 \mu\text{m}$ respectively, values which represent around 10 % of the actuators height at ambient state. No short-term degradation of the material occurred as reflect the standard deviations of the absolute heights measured for both sizes of "punch-and-die" (0.817 and 0.807 in each case). However, from Braille and, in general, tactile applications point of view, the contraction values reached using these type of actuators are still far from the minimum values to be acceptable for correct tactile perception (starting at $200 \mu\text{m}$).

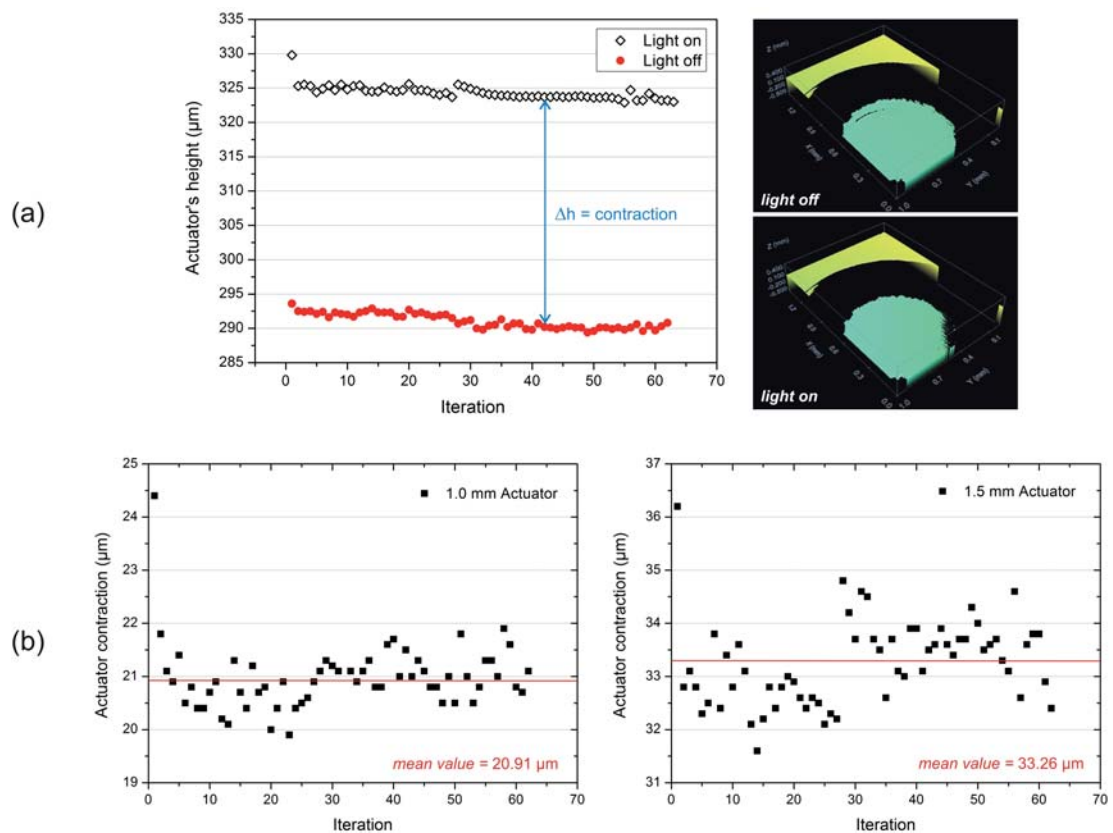


Figure 6.12: Repeatability measurements analysis of on-off switching of both actuators size with their corresponding contraction values.

6.5 Discussion and summary

This chapter reported for the first time a novel and simple approach to the development of arrays of LCE actuators. The method proposed consists in the use of a stamping

6. PUNCH AND DIE MOLDED ACTUATORS

technique to simultaneously shape and align the LCE-CNT material in a single step. In this manner it is possible to obtain arrays of identical actuators using a molding technique while minimizing differences in their performance when integrated on a same tactile device.

The resulting actuators have proved their operation as photo-active elements after being individually characterized, which validates this approach as a proof-of-concept towards i) the fabrication of LCE actuator in batch, and ii) their future integration in microsystems and devices. However, the magnitude of the contraction movement (decrease in height) obtained is rather low mainly due to the non-optimal degree of alignment achieved during the material stretching. This can be attributed to the size and geometry of the punch and die elements due to the restrictions in design imposed for the Braille standards (too small dimensions to reach enough material deformation -stretching- to produce 200 μm of variation in height). The amount of LCE-CNT material also may affects, as well as its degree of precuring (crosslinking of the polymer chains) before starting the stretching process. Nevertheless, the results obtained are encouraging and open new possibilities to combine material processing and technology to obtain alternative approaches.

Further work will be directed to optimize both the dimensions of the molds and the molding system through the combination of different techniques and materials rather than silicon, as well as the improvement of the setup for testing, to be able to measure the force produced by the actuators during their contraction.

The work presented in this chapter has been done in collaboration to Prof. Eugene M. Terentjev and Dr. Jean E. Marshal from Cavendish Laboratory at University of Cambridge as part of the NOMS project experiments, which led two scientific journal papers (see publication lists). The idea was conceived at IMB-CNM where the design of the experiments, the fabrication of the punch and die molds as well as the actuators testing were performed. The composite preparation and the stretching process were carried out at UCAM facilities.

7

Gas-pressure molded actuators

In this chapter, an alternative methodology to simultaneously shape and align LCE-CNT samples for the fabrication of arrays of actuators is proposed following the same concept in the previous chapter, chapter 6. Essentially, this second approach is quite similar to the previous one; however the way to exert force to align the material (i.e., stretching) is modified, replacing the stamping procedure using punch and die molds by a gas-pressure molding process. In particular, this new approach is based on the use of pressure gradients between both opposite sides of the nematic film placed in a mold to produce the desired deformation. In this manner, by controlling the pressure level applied on the system and keeping it constant during the whole crosslinking process it is possible to permanently shape the material in a local way, creating rounded-shaped features [184]. Thus, higher and more controlled local deformation of the LCE-CNT film can be achieved, reaching large actuation.

This chapter describes the concept, the design, fabrication and the optimization of the molds, the fabrication of the samples and their characterization upon thermal and photothermal actuation. SEM and TEM microscopy techniques were used to evaluate the quality of alignment and dispersion of the CNTs in the LCE matrix once the actuators were fabricated using this new approach, in similar way than the film-like samples in Chapter 3. A comparison between different regions of the sample is presented as first results. Additionally, some FE analysis was performed to optimize the response of the actuators as function of the pressure load applied during molding.

7.1 Concept

Similar to the previously presented punch and die method, this new approach enables the fabrication of oriented LC monodomains within a polydomain sample which can be individually actuated producing movement in the perpendicular direction of the film [184]. The main difference between both techniques is the way to exert the force to produce material stretching. In the present approach, is a gas flow which presses the weak cross-linked LCE-CNT film against the actuators pattern replacing the punch mold. In this way, it is possible to gently shape the material controlling the pressure level delivered, thus avoiding the initial drastic deformation produced using punch and die procedure. Then, keeping a constant pressure load throughout the whole crosslinking process it is possible to maintain the degree of deformation achieved fixing the geometry of the actuator. Figure 7.1 schematically shows the concept of the gas-pressure molding technique proposed where the regions with different CNT alignment are distinguished. As in previous approach, only the stretched zones of the film (with both CNT and LC mesogens alignment) can be actuated whereas the other regions, the ones with non-aligned LC domains, remain unaffected.

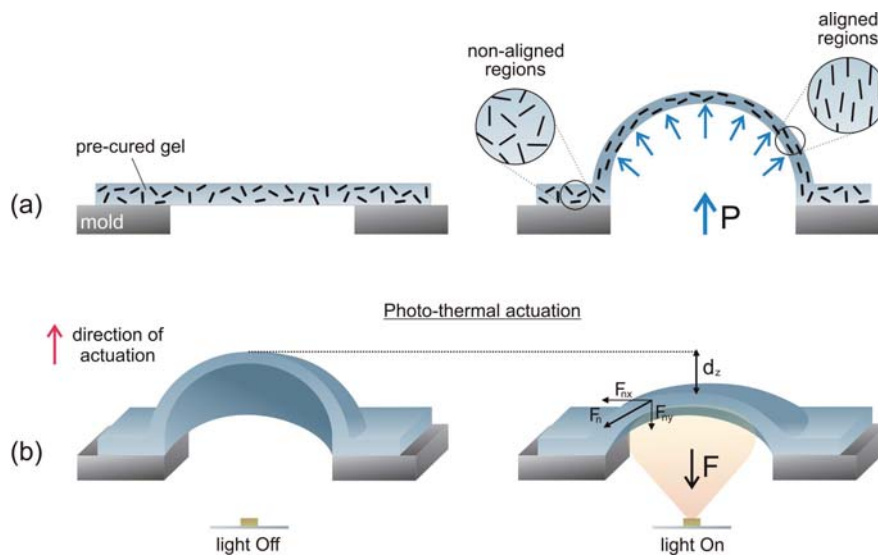


Figure 7.1: Scheme of the molding procedure and the working principle of the actuators obtained.

The main advantages of this new method over the punch and die approach

discussed in Chapter 6, are: i) the possibility of obtaining an alignment of the LCE-CNT composite in a radial distribution, parallel to the plane of the sample (2D orientation); ii) a more accurate final shape of the actuators with completely rounded-edges, similar to a spherical dome, from both inner and outer surfaces, with a reduced thickness; and iii) a material deformation not restricted by the shape and height of the mold but by the pressure applied (in previous approach, the maximum deformation achieved by the film was related with the height of the pillars in the punch piece) .

7.2 Molds design and fabrication

The set of molds used to fabricate the rounded-shaped features by gas-pressure molding had, at least, two parts:

- A first part containing a cavity with regular geometry which acts as a pressure chamber, to uniformly distribute the force exerted by the gas along the whole LCE sample. This piece also contains a rounded channel to deliver the pressure inside the cavity.
- A second part with the pattern for the actuators. This piece was placed on top of the precured sample, in a similar way to the die mold piece used in previous approach.

Figure 7.2 shows a schematic view of the two mold parts required.

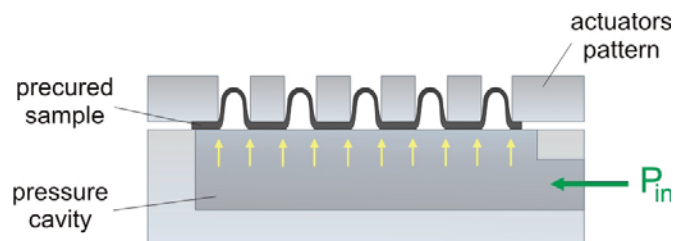


Figure 7.2: Schematic view of the main parts of the molds.

An accurate design of the whole system was required due to the use of gas pressure. For that reason, different sealing and fastening elements were integrated into the design. In this manner, it was possible to maintain the pressure gradient required to properly shape and align the LCE-CNT samples.

7. GAS-PRESSURE MOLDED ACTUATORS

A very important aspect to consider before the fabrication of the molds is the material. According to the LCE characteristics presented in Chapter 3, factors such as the crosslinking level of the polymer chains, the presence of solvents, and the curing temperature applied strongly affect the deformation achieved. When the molding process (i.e., stretching) starts, the material is a lightly cross-linked gel which has certain porosity and thus, certain permeability to gases.

Taking these aspects into account, three different designs of the molds were proposed, fabricated and tested to explore the influence of its geometries on the proper fabrication of the actuators and thus, to determine the best option.

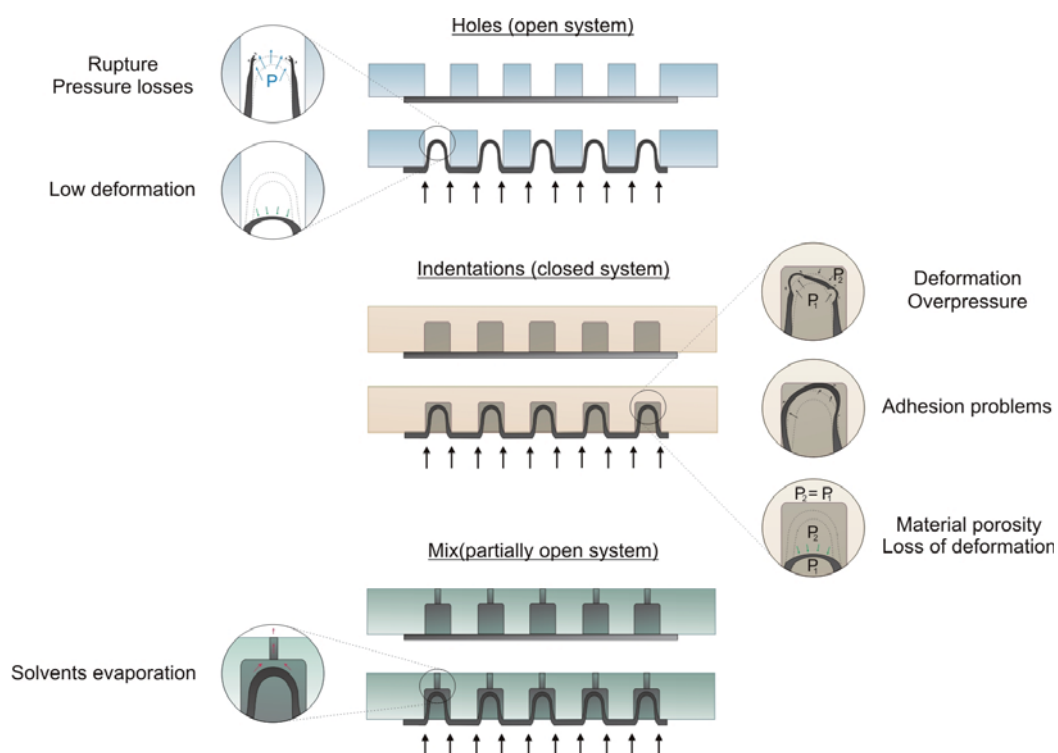


Figure 7.3: Different types of fabricated molds with their main issues observed.

The first design explored named "open system" contains an array of holes as a pattern mold in a single piece, similar to the die mold used in the previous approach. Using this system a pressure gradient between both sides of the sample was successfully achieved resulting on the formation of the actuators at low pressure levels (in the order of tens of millibars). However, the biggest problem proved to be rupture of the LCE-CNT film during the curing process. If the film breaks at any point,

then the pressure gradient achieved decreases immediately disrupting the stretching, so that none of the actuators is formed.

In order to solve this problem, a second design of molds referred as "closed system" was explored. This new design also consists of a single piece but now patterned with an array of indentations instead of holes. By using this approach, the likelihood of film rupture greatly decreases and the pressure load to be applied can be increased. Moreover, if rupture does occur in one actuator, the rest of actuators can still be held under pressure. However, deformities on the shape of the actuators may occur during the evaporation of solvents forming undesired bubbles due to the porosity of the LCE-CNT film in gel phase. This porosity, at the same time, causes a decrease in pressure gradient between both sides of the film, which may result in loss of deformation achieved by the sample if both values (P_1 and P_2 in Figure 7.3) become equal.

Table 7.1: Advantages and issues of the different designs of molds proposed.

Molds design	Advantages	Issues
Open system (holes)	<ul style="list-style-type: none"> • Visual control of the features formation. 	<ul style="list-style-type: none"> • Low pressure level applied (i.e. low deformation achieved). With higher pressure values, rupture of the film may be produced resulting in pressure losses.
Closed system (indentations)	<ul style="list-style-type: none"> • High pressure level applied. 	<ul style="list-style-type: none"> • Undesired deformation of the actuators due to non-proper evaporation of solvents in the film. • Limitation of the degree of deformation achieved due to the geometry and depth of the indentations. • Loss of deformation due to the porosity of the LCE-CNT film in gel phase. • Adhesion problems.
Mix (partially open: indentations + holes)	<ul style="list-style-type: none"> • High pressure level with visual control of the features formation. • Solvents evaporation. 	<ul style="list-style-type: none"> • More complex design and fabrication of the molds. • More control during the crosslinking process.

7. GAS-PRESSURE MOLDED ACTUATORS

Finally, the third design of molds explored is a combination of the both previous ones named "partially-open" system. It consists of an array of indentations which simultaneously contain small holes that can be covered at any time during the crosslinking process by a second non-patterned piece. In this manner, the products from the evaporation of solvents can escape without producing deformities on the material. Further, the rupture of the film can be avoided by applying a pressure ramp through which the pressure load can be gradually increased until reaching the desired value.

The main advantages and issues of these three systems proposed are summarized in Table 7.1 and graphically depicted in Figure 7.3. Besides all the mentioned aspects, added difficulties in handling of LCE-CNT material due to its consistency (gel-like material) are common in all cases.

As can be concluded from the table above, Table 7.1, in order to ensure proper formation of the actuators, a compromise between the pressure level applied and the deformation achieved by the material has to be found. Thus, the third system proposed with a partially-open system resulted to be the best option.

Another but not less important aspect to take into account is the material from which the different parts of the molds are made. Thus, further problems affecting the formation of the round-shaped actuators can also appear depending on which material is selected. The most common ones are listed below:

- Degradation of the molds surface due to the high presence of solvents in the sample, especially methylbenzene, commonly known as Toluene.
- Adhesion of the LCE-CNT sample to the contact surfaces of the molds, mainly to the bottom surface, but also to the lateral walls of indentations or holes which define the pattern of the actuators.
- Deformation of the pieces of the molds during the molding process due to pressure and temperature. As mentioned above, the fabrication process of the actuating LCE-CNT materials requires a crosslinking step in which the samples are held on high temperatures for several hours. This, together with the application of pressure to shape and align the material may cause undesired deformations of the molds and even gas leakages.

7.2 Molds design and fabrication

- Gas leakages between different parts of the molds during the crosslinking process due to bad sealing. Elements such as O-rings, silicone vacuum grease, screws and PTFE tape may help filling joints and gaps to improve the sealing.
- The hardness of the selected material and its difficulty to be mechanized together with the size and geometry of the patterns in the mold, make complicated the formation of rounded edges. Sharped geometries should be avoided to provide better contact between both the mold and the sample avoiding undesired breaks.

Taking into account the above described aspects, four different materials were selected as candidates for the fabrication of the molds: silicon, aluminum, PTFE, and PMMA. Other aspects such as the availability, the expertise in handling, and the price were also considered. A comparison of the issues presented using these materials is summarized in Table 7.2.

Table 7.2: Comparison of the issues presented for the different materials selected for the fabrication of the molds.

Material	Issues				
	Degradation	Adhesion	Deformation	Gas Leakage	Ease to be machined
Silicon	○	●	○	○	●
PMMA	○	◐	●	●	○
PTFE	○	○	◐	◐	○
Aluminum	○	●	○	●	●

● means existing issue while ○ means no significant issue. ◐ refers to some non-critical issues.

In agreement with the results obtained using the three systems of molds proposed together with the considerations about the materials in Table 7.2 and the previous experience acquired working with LCE-CNT materials, it was found that the best option for the fabrication of the molds was combining different materials, thus avoiding the worst aspects of each one. In this manner, sets of molds using different materials combinations can be used, as for example PMMA and silicon, PMMA and aluminum, and PTFE and aluminum among others. Figure 7.4a shows the molds used for the fabrication of the first actuators made in PMMA and silicon, whereas examples of various types of fabricated molds with their main parts are shown in Figure 7.4b. In all cases, the piece containing the actuators pattern was exchangeable while the other parts (e.g. the piece containing the pressure cavity, the fasteners and sealing elements

7. GAS-PRESSURE MOLDED ACTUATORS

and the cover) were reusable. Thus, the piece with the patterns can be replaced after each experiment if damaged.

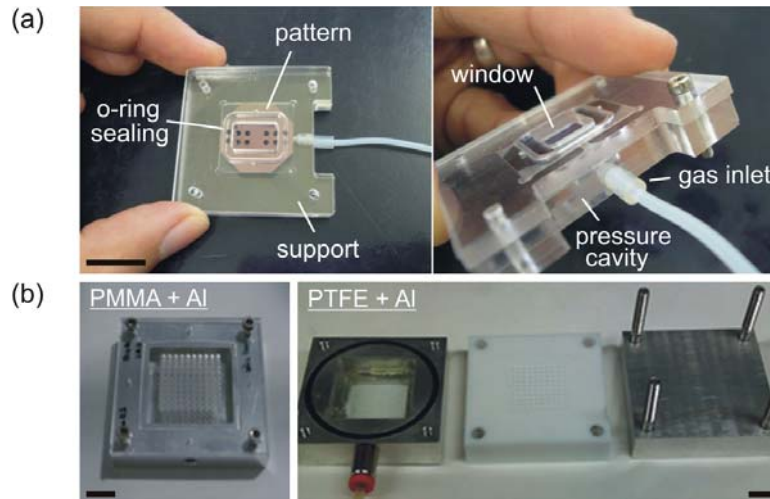


Figure 7.4: Different sets of molds fabricated using different materials combination with their main parts. Scale bar = 10 mm.

7.3 Fabrication and optimization of the actuators

7.3.1 Optimization of the molding process

Previous to the fabrication of the actuators, a finite element analysis, FEA, was carried out in order to anticipate the mechanical behavior of film during molding, predict the loading limits prior fracturing and determine how the tensile forces influence on the actuator performance seeking its optimization. For this purpose, variations on the stress distribution during pressure loading were analyzed thoroughly until material failure.

Again, ANSYS ® software was used to model the LCE-CNT film under pressure loading conditions as function of its composition, geometry and main mechanical properties, emulating the molding method to optimize parameters such as stress and strain. To this purpose, the FE model presented in Chapters 3 and 6 were adapted. In this case, the structural 20-nodes element SOLID186, which supports plasticity and large strains, was chosen to build the 3D model. Vertical restrictions, $u(z) = 0$, on top of LCE-CNT surface, and radial and angular restrictions, $u(r, \theta) = 0$, at the

7.3 Fabrication and optimization of the actuators

external surface of the actuator were imposed as translational degrees of freedom, DOF. Associated composite properties, as Young's modulus, Y , and the thickness of the film, t_F , were considered partially variable due to the material changes during the crosslinking process. Figure 7.5 shows two snapshots taken during the simulation process where the model used and the boundary conditions applied are depicted, whereas Figure 7.6 details the results obtained.

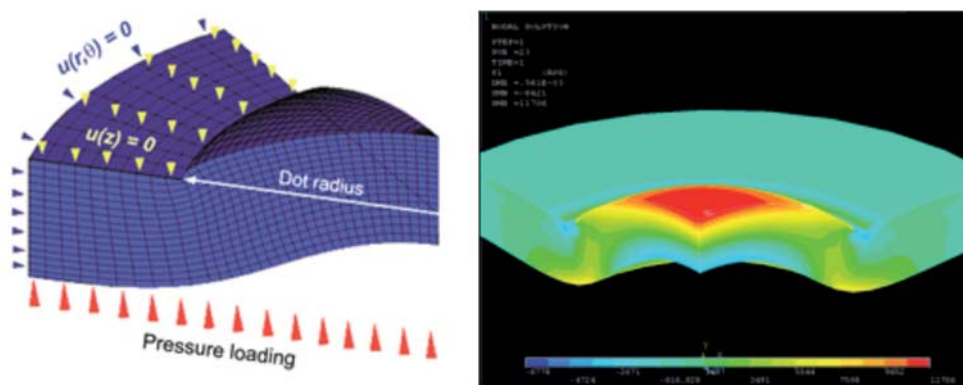


Figure 7.5: Geometry of the finite element model used to perform the simulations with the boundary conditions applied.

Special attention was given to the regions near the perimeter of the actuators where the mold edges and the loaded composite have critical contact and the largest strain ratios were detected (Figure 7.6a). Thus, a rounded-shape pattern was chosen to fabricate the actuators avoiding sharp edges and corners. Unlike the results obtained with the previous punch and die molding approach [227], the failure stress reached using this technique was near 50 % higher under same conditions, and its distribution was considerably more homogenous along the film, resulting on a clear actuation improvement. The maximum load-pressure endured by the film was estimated as function of t_F and Y . Figure 7.6b depicts the linear behavior of the maximum pressure load borne by the composite as function of both variables (standard error < 5 %); revealing higher dependence on Y than t_F . The correlation between the height of the actuator, the pressure load, and the maximum strain values obtained was also analyzed in several regions along the film (see Figure 7.6c-d). Although the height of actuators is highly dependent on the pressure load, the latter is better correlated with the strain reached in the top surface of the actuators. Similar behavior was observed

7. GAS-PRESSURE MOLDED ACTUATORS

for the mean strain in bulk. Both of these two strain regions are directly related to the actuator performance since they include more than 70 % of whole actuator structure. Consequently, the linear ratio between pressure load and actuation can be assured. Finally, Figure 7.6d delimits the 'safe' pressure load region which corresponds to the 90 % of failure pressure value. Higher load implies a trade-off between the actuator performance and the reliability.

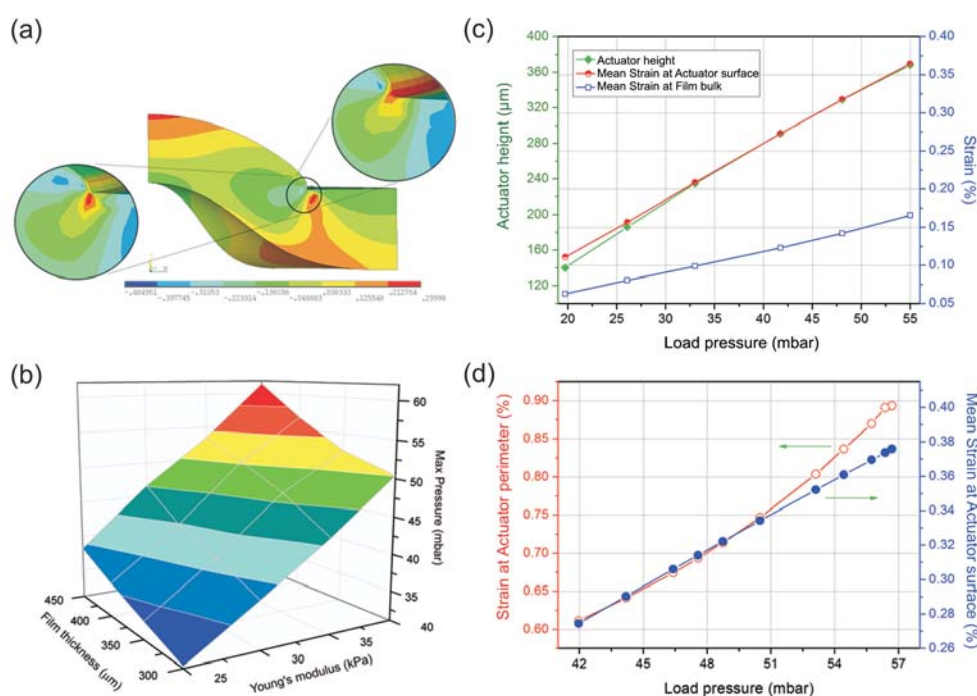


Figure 7.6: Results obtained by FE analysis for the optimization of the actuator response.

7.3.2 Actuators fabrication: gas-pressure molding-based process

The fabrication process of the actuators described in this chapter started with a lightly cross-linked LCE matrix containing 0.3 wt.% ratio of multiwalled CNTs. The synthesis procedure of the LCE-CNT as well as the preparation process of the lightly cross-linked gel is the same detailed in Chapter 2; thus are herein not described.

Immediately after its extraction from the centrifuge, the weak gel was placed on top of the piece containing the patterns. 1.0 mm and 1.5 mm diameter circles with separations of 2.5 mm and 3.0 mm between centers grouped by size were used as

7.3 Fabrication and optimization of the actuators

pattern to produce an array of twelve actuators in a single sample. In this manner, it was possible to study the homogeneity of the method and investigate possible cross-actuation effects between neighboring actuators. Then, this piece was turned and placed on top of a second one which contains the pressure cavity, and both pieces were carefully fastened. Custom-made PDMS O-rings (Sylgard 184, Dow Corning) were added between the different contact surfaces to seal the system. In agreement with the results obtained from FEA simulations as well as the different preliminary tests performed using dummy LCE-CNT samples stretched under different pressures, a nitrogen flow was gradually applied from atmospheric pressure to 40 mbar to successfully form the features on the film and then kept constant and left overnight. Small defects induced during this crosslinking process due to overpressure could produce pores in the film, causing pressure losses even breaks.

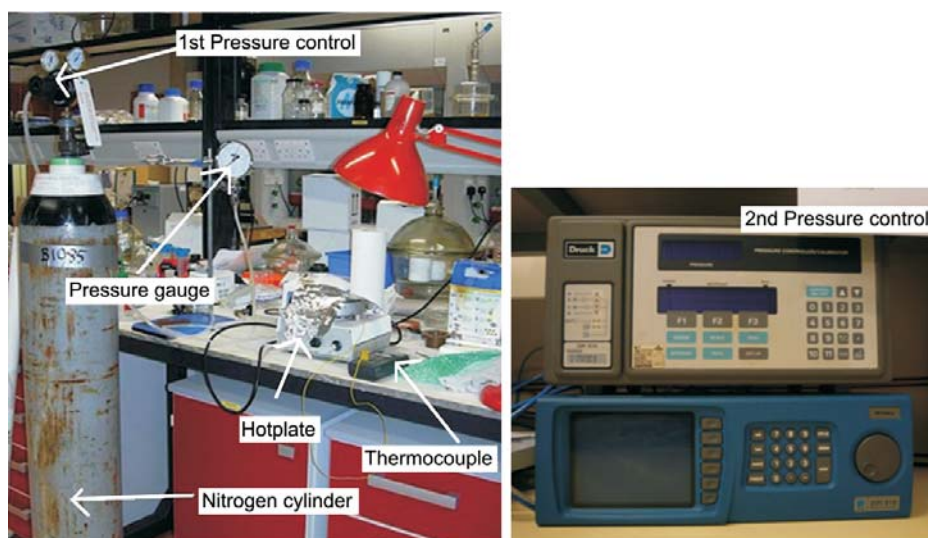


Figure 7.7: Setup configuration for the formation of actuators.

To guarantee a continuous and well-controlled pressure flow during the whole stretching process, two different elements were used (see Figure 7.7). First, a pressure gage was placed on the outlet of the nitrogen cylinder tank (Figure 7.7 -left-). Then, a Druck DPI-515 pressure controller (Figure 7.7 -right-) was coupled to the setup for a more accurate control. Finally, the system was heated at 90 °C whilst maintaining the pressure, to end the crosslinking and fix the shape of the actuators. A hotplate and a thermocouple were added to monitor the temperature during the final crosslinking

7. GAS-PRESSURE MOLDED ACTUATORS

step. After completing the whole curing process, the molds were carefully opened and the sample was left at room temperature. Figure 7.8 graphically summarizes the fabrication process, where it is possible to distinguish the formation of both sizes of features at naked eye (Figure 7.8a-b). Notice that the actuators retrained the deformation acquired during stretching once the molds were removed, maintaining their rounded shape (Figure 7.8c). A picture of a completely cross-linked sample containing an array of 12 actuators can be observed in Figure 7.8d.

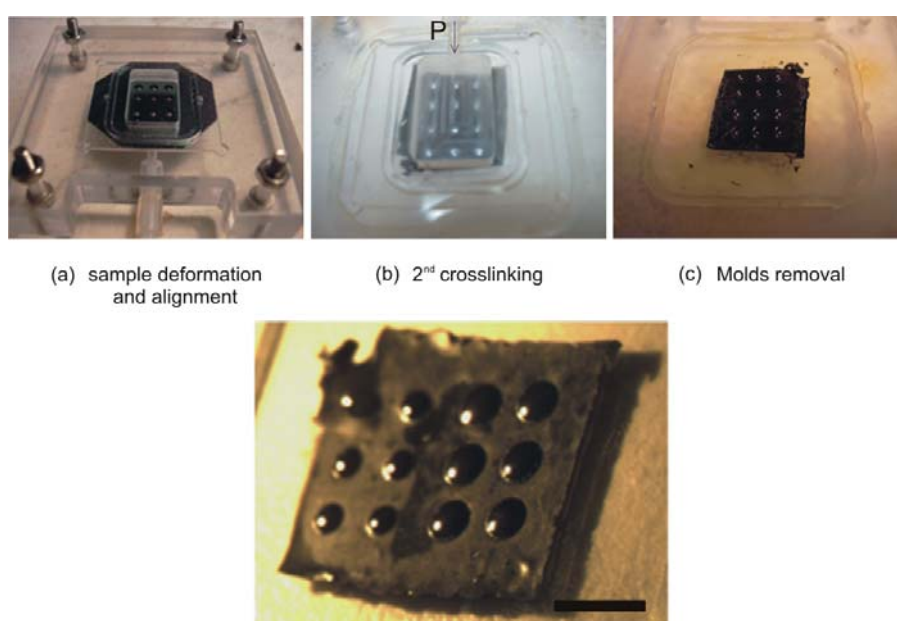


Figure 7.8: Fabrication process of the stretched actuators. Scale bar = 4 mm.

In agreement with the previously exposed and confirmed by FE simulations, the deformation acquired for the LCE-CNT sample during the stretching is strongly dependent on the geometry and the pressure level applied. However, aspects such as the amount of material and the solvents content, the crosslinking level and the curing temperature should also be taken into account. Adjusting those parameters, together with an accurate design of the molds and a proper selection of the materials from which they are made, it is possible to generate a controlled pressure-gradient between both sides of the sample in spite of the existing gas-permeability through the film. In this manner, a desired deformation level can be reached and maintained to fix the final shape of actuators without damage.

7.4 Characterization

7.4.1 Material conformation: microscopy analysis

Prior starting with the characterization of the mechanical performance of the actuators, some microscopy analysis were carried out to evaluate the conformation of the LCE-CNT material and thus, check the degree of alignment reached by CNTs using such method. To that purpose, same SEM and TEM microscopy techniques used for the characterization of film-like LCE-CNT samples in Chapter 3 were used. In this case, however, two different samples were prepared: one from the stretched regions of the sample (i.e., aligned monodomain) and the other one from the non-stretched regions (i.e., non-aligned polydomain). An example of the first results obtained are depicted in Figure 7.9 where some SEM and TEM micrographs corresponding to both regions of the actuators together with a schematics of the sample are given. Similar to previous inspections, both SEM and TEM analysis were carried out at microscopy service facilities from UAB.

As expected, it was not possible to identify clear differences in the alignment patterns between both regions of the actuator, named zone A and B, using SEM microscopy (see Figure 7.9b) because of the material characteristics and the limitations in resolution. However, it was possible to distinguish the presence of CNT in the sample (small bright elements in the micrographs) due to the higher contrast of the tubes with respect the nematic matrix.

Despite the low concentration of CNTs in the sample (0.3 wt.%), some more information could be obtained using TEM analysis. By comparing the TEM micrographs obtained from both zones (see Figure 7.9c), a tendency of the CNTs to be oriented in the direction of the applied pressure (black arrow in the micrograph) could be appreciated in zone A, resulting in a relatively homogeneous distribution in agreement with the results obtained in previous microscopy analysis (see material characterization section in Chapter 3). Conversely, the alignment seem to disappear in samples from the non-stretched zone, zone B, where some aggregates of CNTs were also observed.

These results suggest that this new alignment method proposed works at the nanoscale. However, a detailed study using samples with high density of tubes would be required to verify the tendency.

7. GAS-PRESSURE MOLDED ACTUATORS

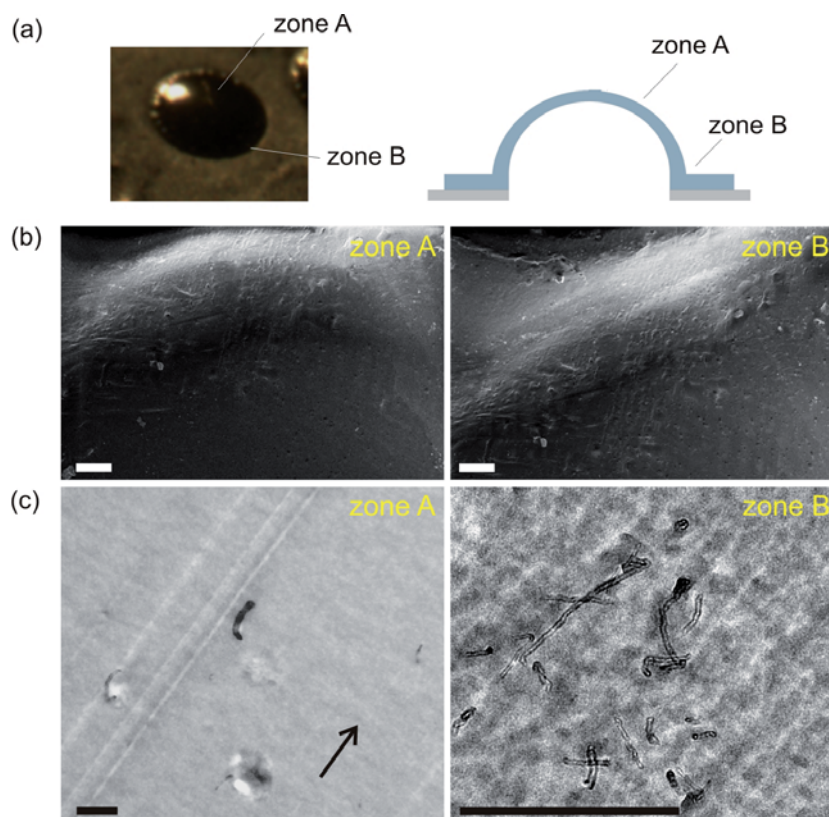


Figure 7.9: Microscopy analysis of the gas-pressure molded LCE-CNT actuators. (a) Top view and cross-section scheme of an actuator where both studied regions can be distinguished: zone A (stretched) and zone B (non-stretched). (b) SEM and (c) TEM micrographs corresponding to both A and B zones. Scale bars are 100 μm and 500 nm, respectively.

7.4.2 Thermal actuation

The performance of the gas-pressure molded actuators was measured through photothermal excitation. However, the change in dimensions of the actuators was first evaluated by optical microscopy to check the efficacy of the stretching method. Thus, the actuators were thermally excited on a range from room temperature to the isotropic state, T_{NI} , for several cycles. Prior to those tests, a DSC analysis was carried out to determine the conformation characteristics of the material, resulting in $T_g = 10^\circ\text{C}$ and $T_{NI} = 90^\circ\text{C}$.

Figure 7.10 depicts two different examples where the decrease in height (i.e., actuation) of the features is evidenced in agreement with results obtained in prior

works, where the photo-thermomechanical properties and the actuation mechanisms of LCE-CNT composites were evaluated [81, 170, 171, 179]. The first example corresponds to a sequence of stereoscopic images showing a complete heating-cooling cycle. The second one shows through the top view of a single actuator at room temperature and at T_{NI} respectively, where the difference in transparency between images evidenced the material phase transition. All the pictures were recorded with a Moticam 2300 3.0 MPixels digital camera mounted on a Leica DM LM upright optical microscope at microsystems laboratory in clean room facilities from IMB-CNM (CSIC).

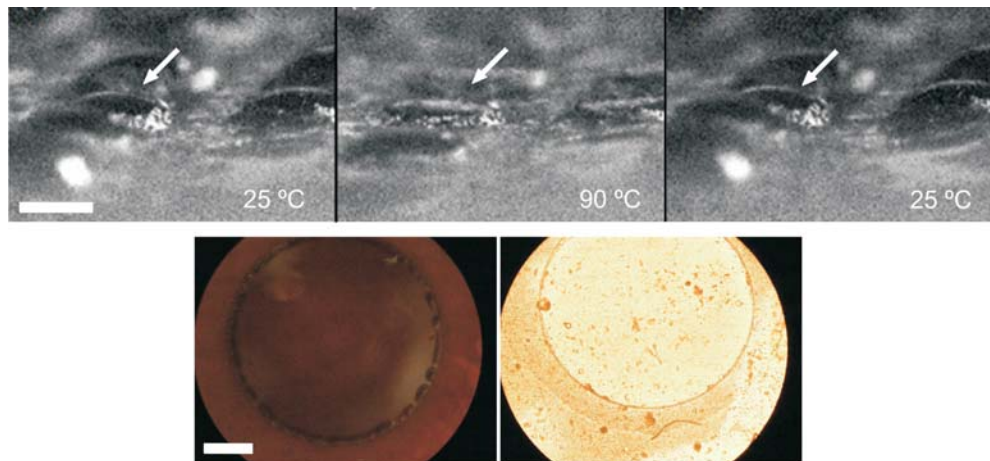


Figure 7.10: Thermal characterization of the stretched actuators. Scale bars are 10 mm and $300\mu\text{m}$, respectively.

7.4.3 Photomechanical actuation

In order to analyze the photomechanical response of the present actuators a setup analogous to the one designed for measuring the previous actuators (see Figure 6.9 in Chapter 6) was used by means of 3D optical imaging profiler (Sensofar-tech, Spain) while irradiating the entire actuator from the underside using the same 660 nm wavelength LD in similar conditions. It is very important to achieve uniform illumination of the whole sample to get regular and symmetric movement, increasing the effective area and maximizing the actuation range. The setup used with a close view of the measuring zone is shown in Figure 7.11 whereas plots reflecting the behavior of the actuators are presented in Figure 7.12.

7. GAS-PRESSURE MOLDED ACTUATORS

Under illumination, the stretched zones of the actuator (the monodomain regions) contracted producing a negative vertical displacement of its center (i.e., flattening the actuator) while the non-stretched zones remained unchanged. Surface profiles of the actuators obtained by means of interference planes analysis are plotted in Figure 7.12a. This contraction effect was measured for all the fabricated actuators in the array with power variations ranging from 25 mW to 50 mW; values previously selected for being in the safety range to avoid material degradation or damage. Similar behavior was obtained for both actuator sizes. However, 1.5 mm diameter actuators exhibited better contraction results, achieving a maximum height variation of $120\ \mu\text{m}$ for 50 mW of power applied (Figure 7.12b), value which represents over 40 % of change in height of the molded shape. Conversely, the maximum height variation measured under same conditions for 1.0 mm diameter actuators was only about 25 %.

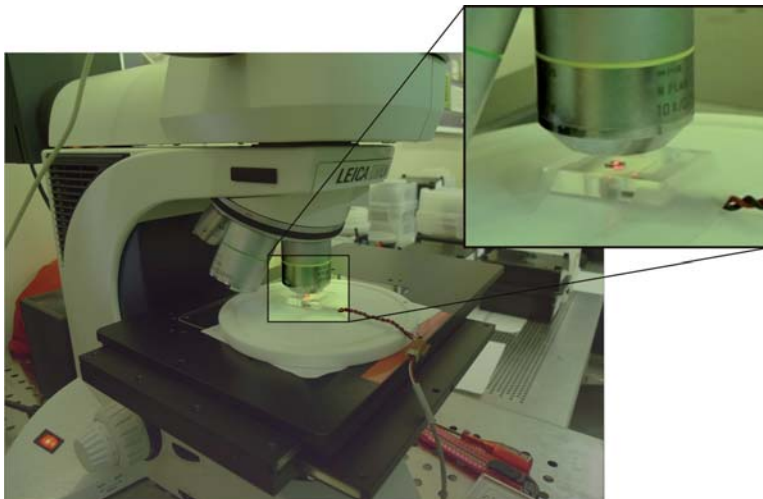


Figure 7.11: Setup for the evaluation of the optomechanical actuation using confocal microscopy.

The real change in dimensions of the actuators and, in consequence, the contraction degree achieved upon illumination was also analyzed. Similar to the calculations performed in Chapter 6 and taking into account the geometry of the actuators and their height variations under illumination, the uniaxial thermal expansion and contraction of the stretched material was calculated resulting in $\lambda_{chord} = 1.148$, which corresponds to a contraction in length of $\varepsilon_{chord} = 12.89\%$. Considering the composite as nearly incompressible (Poisson's ratio of $\nu = 0.5$), the uniaxial thermal expansion in the

direction of the thickness (perpendicular plane) can be similarly obtained, leading to $\lambda_{thickness} = 1/\lambda_{chord}^2 \approx 0.758$, which corresponds to an expansion of $\varepsilon_{thickness} = 31.93\%$.

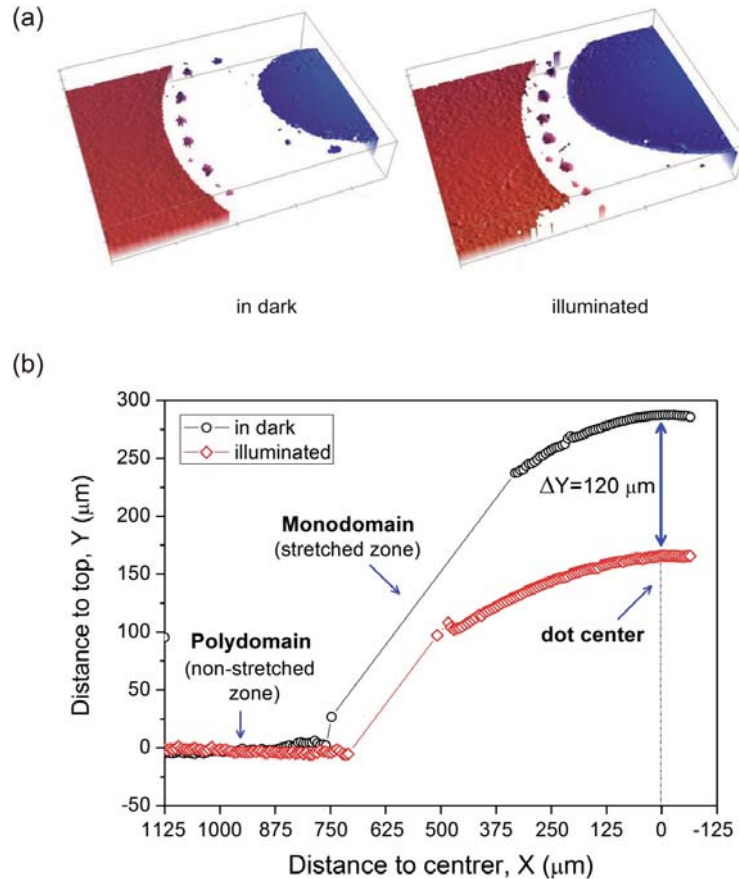


Figure 7.12: Photothermal actuation of gas-pressure molded LCE-CNT actuators.

The mean displacements for 1.5 mm diameter actuators plotted in Figure 7.13 as function of the power applied revealed low dispersion ($\sim 10\%$) and high repeatability. Displacements for the 1.0 mm diameter actuators were likewise measured obtaining higher dispersion ($\sim 21\%$), probably due to some defects in the sample induced during its fabrication. Same measurements were repeated showing reproducibility in short-term actuation with no performance or material degradation, key facets for the application of this type of actuators in future tactile devices. Moreover, no crossactuation between neighboring actuators were observed while testing, thus evidencing the possibility of proper localized contraction of a single actuator in an array.

7. GAS-PRESSURE MOLDED ACTUATORS

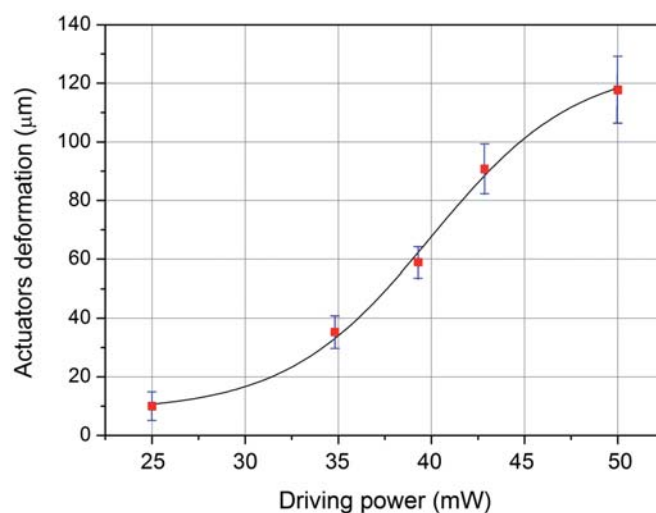


Figure 7.13: Maximum deformation of 1.5 mm diameter pressure-molded actuators with their corresponding error bars measured at different driving powers.

7.5 Discussion and summary

In this chapter a novel approach to the fabrication of an array of LCE actuators has been presented. The concept around this method is similar to the technique described in previous Chapter 6. Meanwhile, the technique herein proposed is based on the application of gas-pressure loads during the LCE-CNT material crosslinking to shape and align it in a single step. Thanks to the design of specific sets of molds it is possible to exert and maintain a well-controlled pressure gradient between both sides of the sample, and thus obtain arrays of actuators in batch within the same sample.

Using the previous knowledge acquired about LCE-CNT material performance, studies for the optimization of the molds (e.g., design and geometry, and composition) were firstly performed to evaluate potential issues prior to the fabrication of the actuators. A FE model was also developed to optimize the actuators formation by adjusting their dimensions and demarcating the safe pressure load.

Once the actuators were successfully obtained, both SEM and TEM inspections were carried out to check the degree of alignment of the CNTs in the LCE matrix at the nanoscale. Thus, samples from both stretched and non-stretched zones, named zone A and B respectively, were analyzed and compared. A tendency of CNTs to be aligned in one direction (i.e., alignment direction) was observed in samples from

zone A whereas the CNTs in samples from zone B seemed to lose alignment and homogeneity in dispersion; results which are in agreement with the ones predicted during the design and optimization of this approach. However, further study with samples containing higher CNT content would be required to confirm these results.

The performance of the fabricated actuators has been first thermally evaluated to prove their operation and then individually characterized under LD excitation to demonstrate their photoactuation. The contraction ratio achieved represents a clear improvement compared with the previous reported methods (Chapter 6, and [227, 228]). However, the values obtained are still far from the vertical displacements obtained using "U-shape" actuators (Chapter 4 and [48]), and the ones required for haptic and Braille-based devices. It has to be noted that the displacements obtained are directly related to the geometry and dimensions of the pattern. In that sense, it can be possible to improve the results increasing the size of the actuators. However, the actuators obtained could not be useful for Braille applications due to the restrictions involving the size and shape of the elements. Other aspects as the amount of material used and the pressure gradient applied have also a strong effect.

Nevertheless, the results presented demonstrate the feasibility of this approach to obtain shaped nematic-based actuators, providing proper photo and thermomechanical responses. Moreover, this technology offers additional opportunities for the integration of such actuators in future devices and systems with applications ranging from valves and membranes in microfluidic systems and lab-on-a-chip devices to movable elements in robotics.

Similar to the approach presented in previous chapter, this has been done in collaboration to Prof. Eugene M. Terentjev and Dr. Jean E. Marshal from Cavendish Laboratory at University of Cambridge as part of the NOMS project experiments, which led a scientific journal paper (see publication list at the end of this thesis). The idea was conceived at IMB-CNM were the design of the experiments, the studies for the design and fabrication of molds as well as the FEA simulations and all the actuators characterization and testing were performed. The composite preparation and the stretching process were carried out at Cavendish Laboratory at UCAM.

7. GAS-PRESSURE MOLDED ACTUATORS

8

Micropillar array

For a direct integration in haptic systems and refreshable Braille devices, actuators producing positive tactile signals are required [46]. Successful approaches in previous chapters (Chapters 6 and 7) demonstrate the possibility of shaping and aligning nematic elastomers in one step to fabricate movable actuators based on the reversible shrinkage phenomenon of LCE materials. However, both methods are focused on producing actuators which contract under the application of temperature gradients, whether by direct heating (thermomechanical effect) or by light irradiation (photomechanical effect), resulting in a decrease in height, and thus a negative tactile signal [105, 112, 229].

Then, to obtain positive tactile signal under actuation using these actuators, two different solutions could be adopted:

- On one hand, additional elements such as pins and supports could be introduced, similar to the ones used in case of "U-shape" approach (see Chapter 4 and Ref. [48]) to reproduce the Braille dots. However, complex systems with several components, an accurate design, and a fine control of the material under actuation are required.
- On the other hand, it is possible to keep permanently the actuation stimulus on and switch it off only when the tactile signal would be required. However, material degradation due to a long time exposure to the stimulus would be produced together with a large increase in power consumption.

8. MICROPILLAR ARRAY

Figure 8.1 summarizes the two above mentioned options.

With the main objective to obtain a direct positive tactile signal under actuation (i.e., application of the stimulus) and at the same time simplify the design of the tactile device and the technology used, a novel methodology for the fabrication of actuators has been developed and presented in this chapter. The approach lies in the direct fabrication of actuators with pushing properties (i.e., expansion movement) using an original two-steps crosslinking process, where a uniaxial compression before the final curing process is applied rather than stretching thanks to the use of molds. This innovative version of the LCE orientation process allows the formation of a two-dimensional prolate polydomain conformation of the material (in the nematic state) which changes to the spherical conformation (in the isotropic state) under actuation. In this manner, it is possible to fabricate arrays of individually oriented actuators with pushing properties which increase their height under the application of an external stimulus (i.e., positive tactile signal) as required for haptic and tactile applications, going a step further for their future integration in MEMS systems.

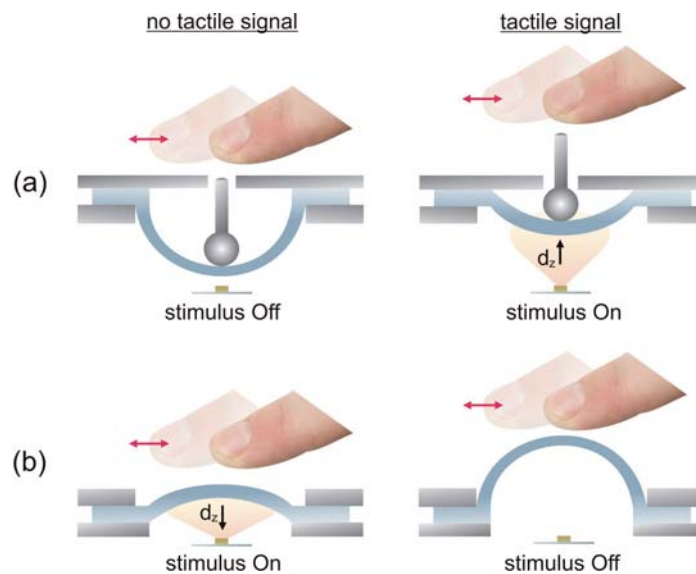


Figure 8.1: Scheme of two possible solutions to adapt the previously described approaches to obtain positive tactile signal for haptic applications.

The following chapter is divided in four sections. In the first one, the concept and the processing principles of the methodology are presented. Both the second and the third sections describe the design and the fabrication process of the actuators as well as

the molds used. Finally, the last section presents the characterization of the fabricated actuators under different operation conditions.

As the material configuration achieved during the fabrication of the actuators is different to the ones obtained in previous designs (same polysiloxane -based LCE matrix but arranged in a different configuration), some material conformation characterization was also performed. Thus, a complete DCS analysis and X-ray diffraction measurements are included.

8.1 Concept and processing principles

The actuators described in this chapter, named hereinafter micropillars due to its final pillar-like shape, are based on the application of a compressive force in the direction of the orientation of the material during the stretching process. In this manner, it is possible to obtain an expansion movement of the whole structure when the isotropic temperature is reached, resulting in a positive increment of the length of the actuator, $L_{iso}/L_{nem} > 1$. Figure 8.1 represents schematically this concept for 2D structures (i.e., strips).

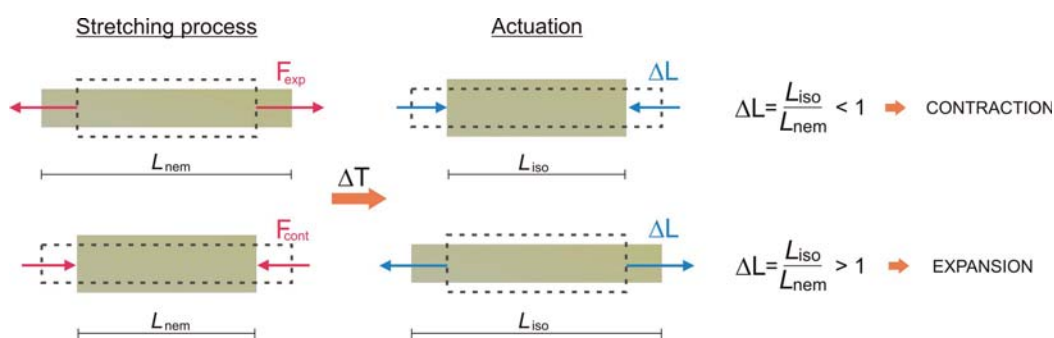


Figure 8.2: Relationship between the type of the stretching force applied and the actuation movement reached.

The approach presented in this chapter aims to transfer this phenomenon in order to create 3D structures out of the LCE film plane, again using molding based techniques: an innovative procedure that allows for the first time the fabrication of microstructured pushing actuators using such LCE materials [230]. The concept around the present approach is similar to the ones discussed in previous Punch and die and gas-pressure molding approaches: the use of a set of molds to shape the material in a more complex

8. MICROPILLAR ARRAY

configuration than a simple film while align it. However, in contrast with them, the actuators obtained are not attached to the same polymer matrix which forms a polydomain (i.e., they do not share the same polymer matrix), rather they are isolated 3D structures with individual oriented domains forming single actuators (see Figure 8.3a). Thanks to a two-steps crosslinking process it is possible to first shape the actuators and then deform them leading to a cylindrical distribution of the two-dimensional prolate polydomain conformation of both the planar oriented mesogens and the polymer backbone (Figure 8.3b) resulting in expansion movement along the macroscopic deformation direction (the cylinder axis, λ_z) and shrinkage in the radial direction, λ_r) as shown in Figure 8.3c). In this manner, arrays of individual pushing micropillars can be obtained.

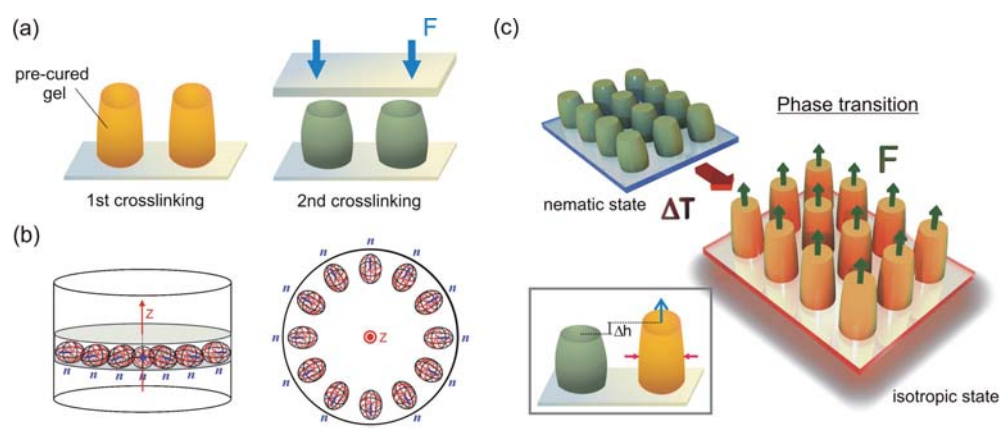


Figure 8.3: Scheme of the orientation concept and the working principle of the array of LCE micropillars as pushing actuators.

8.2 Molds design and fabrication

The molds for the LCE micropillars were micromachined in PTFE to avoid any degradation during the evaporation of solvents and due to high working temperatures throughout the crosslinking process. Pictures in Figure 8.4 show the three parts of the set of molds designed and its main components. The first part (Figure 8.4a) is the base of the mold which acts as support of the rest of the pieces. A squared 30 mm side and 0.5 mm depth cavity was micromachined on its center to allocate the substrates which will contain the array of micropillars. As first attempt Pyrex substrates were chosen to

ensure good heat transfer to the LCE micropillars. The second part contains an array of holes which will define the lateral dimensions and the distribution of the pillars in the array (Figure 8.4b).

The dimensions of the template were calculated taking into account the following aspects:

- the geometry of the pillars, in this particular case, cylinders,
- the volume fraction of volatile components of the LCE material. It is known by experience that LCE material experienced a quasi-isometric contraction during the curing process (expressed by the factor a in Figure 8.5), which in the case of the specific LCE composition used in this experiments is about 75 % of volume reduction.

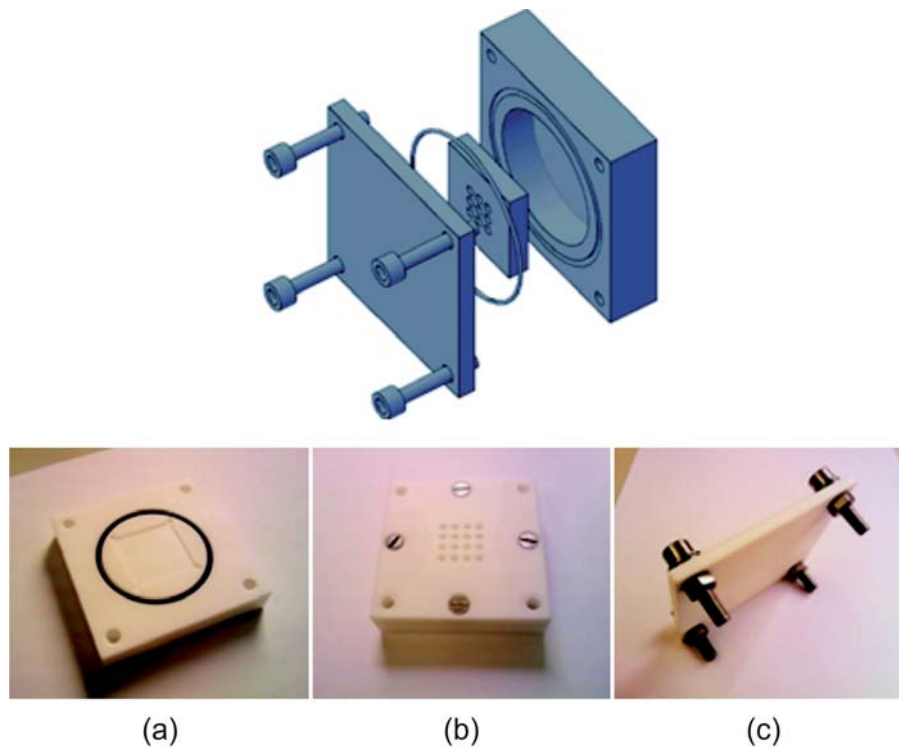


Figure 8.4: Pictures of the fabricated PTFE molds with their different parts.

An O-ring placed between the above mentioned mold parts guarantees a correct union of them avoiding possible material leakage during the micropillars fabrication.

8. MICROPILLAR ARRAY

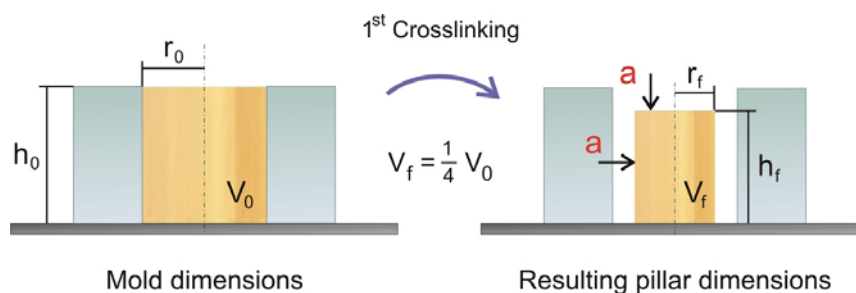


Figure 8.5: Considerations for the design of the molds.

Finally, the third part serves as a molds' cover and also as pressing element for the micropillars deformation during the second crosslinking step (Figure 8.4c). Thanks to the incorporation of a set of screws together with threaded and non-threaded holes, a uniform deformation of the LCE micropillars can be induced by applying a homogeneous uniaxial compression along the vertical axis of the micropillars.

8.3 Fabrication of actuators

8.3.1 Synthesis of nematic side-chain LCE

The orientated nematic LCE micropillar array was prepared using the new orientational process proposed, where both the mesogens and the polymer backbone show a planar orientation. Unlike the previous presented approaches where always the same type of nematic LCE was synthesized and mixed with CNTs to be used for the fabrication of the different proposed actuator, in the present approach a different type of nematic LCE was used. However, the rod-like side-chain mesogen, SCM, and the isotropic side-chain crosslinker, SCC, were synthesized in a similar way as described in [82, 85, 117, 146] and in previous chapters (Chapter 2).

To synthesize the nematic LCE a 20 mol% of crosslinking double bonds or 11.1 mol% of crosslinker was used. In a 5 mL flask, 477 mg (1.60 mmol) of SCM, 4-methoxyphenyl 4-(but-3-en-1-yloxy)benzoate, 83 mg (0.20 mmol) of the isotropic SCC, 1,4-bis(undec-10-en-1-yloxy)benzene, and 120 mg (2.00 mmol SiH) of PMHS (DP = 259) were placed. To this mixture, 2 mL of toluene-free toluene and 40 μ L of 1% Pt cyclooctadieneplatinum(II) chloride, Pt(COD)Cl₂, in dichloromethane were added

were added and carefully stirred for several minutes to guarantee an homogeneous solution of all the components.

At this stage, the mixture is ready to start the crosslinking process to become an actuating SCLCE. Additional elements together with their correspondent surfactants agents such as CNTs, photosensitive dyes and ferro- / ferrimagnetic microparticles can be added to obtain different stimuli-responsive composites. However, a neat sample of nematic LCE was selected to this approach (no additional elements were added) since the main aim was to proof the viability of the proposed novel alignment method. Further composites will be tested in future stages to probe its suitability under other actuation mechanisms, such as visible light.

Figure 8.6 schematically shows the synthetic route to obtain the nematic SCLCE. For this crosslinking composition, the sample has 16 side-chain repeating units between two crosslinkers.

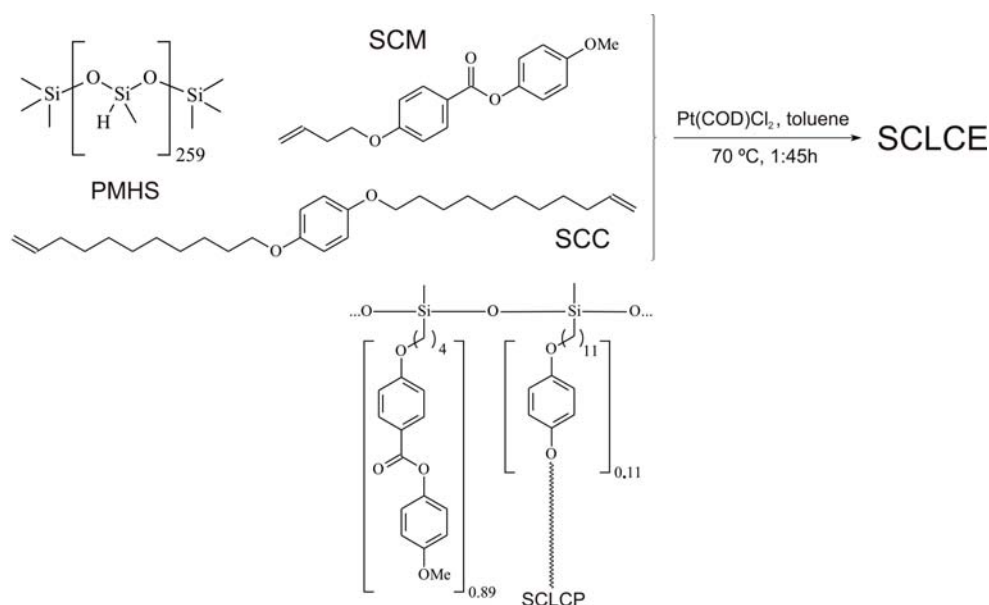


Figure 8.6: Scheme of the synthetic route to the nematic SCLCE used for the fabrication of the micropillars.

8.3.2 LCE Micropillar array preparation

The previously prepared reactive mixture containing the mesogens, the crosslinker, the polymer backbone, and the catalyst all in toluene was placed in the PTFE mold

8. MICROPILLAR ARRAY

filling the holes (see Figure 8.7a) and heated at 70 °C in an oven for 1 h 45 min to start the hydrosilylation reaction (i.e., crosslinking process) [231, 232]. Afterwards, the mold was cooled down until room temperature and removed leading to the elastomer micropillar array (see Figure 8.7b). In this moment, the hydrosilylation process was not completed (the sample was only partially deswollen) so that the elastomer is not totally crosslinked, thus still allowing the possibility to align the material.

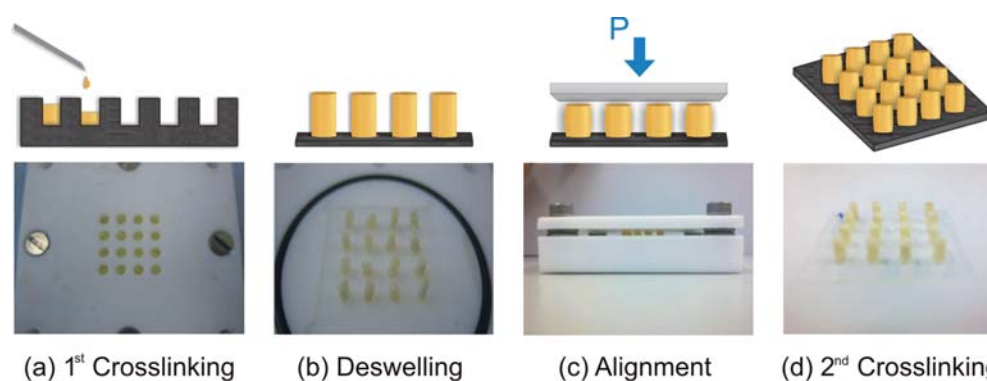


Figure 8.7: Schematic diagram showing the fabrication process to obtain the micropillar array.

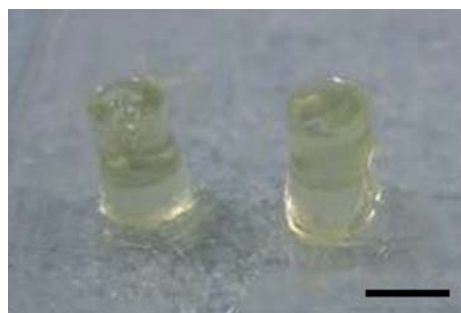


Figure 8.8: Resulting micropillars after the 1st crosslinking stage.

Figure 8.8 shows a detailed picture of two micropillars immediately after the first crosslinking stage, where their cylindrical shape can be clearly distinguished. Then, some pressure was applied by fixing the distance between two of the Teflon-mold plates, the base and the cover ones, in order to align the sample during the deswelling process. In this manner, a uniaxial compression (biaxial deformation) in the direction of the cylindrical axis of the pillars was imposed to fix this orientation (Figure 8.7c). Finally, the crosslinking reaction was completed by leaving the elastomer

in the isotropic phase in an oven under vacuum ($T = 70^\circ\text{C}$) for 2 days. This second step of the curing process allows the completion of the curing reaction, while maintaining the compression of the sample (Figure 8.7d) fixing the final shape of the micropillars at the nematic phase.

Thus, from the original height of 3.63 mm after the first crosslinking stage, the micropillars were uniaxially deformed to 3.00 mm, fixing their height after the second crosslinking process. This uniaxial compression (biaxial deformation) is the key step of the preparation process to guarantee the alignment of the sample, and together with the crosslinking density, will define the final expansion ratio of the LCE micropillars.

A first test to verify changes in the actuators shape was performed, heating the samples from room temperature to the isotropic state temperature ($T \approx 90^\circ\text{C}$). Pictures in Figure 8.9 demonstrate the success of the fabrication process.

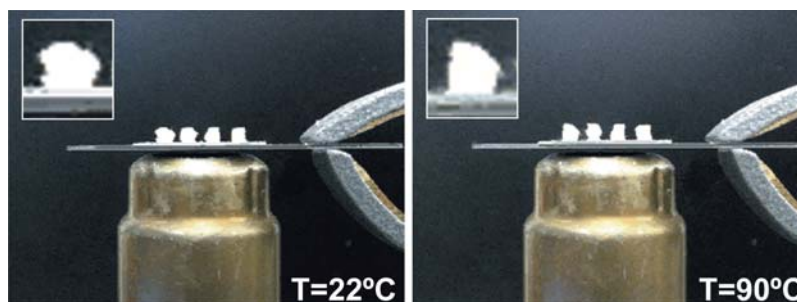


Figure 8.9: In-situ verification of the fabrication process through heating the samples.

All Pyrex substrates used as supports for the fabrication of the micropillars were first treated with allyltrichlorosilane (95 %, ABCR) in order to guarantee a strong chemical adhesion of the LCE micropillars to the substrate, by depositing few drops of the reactive silane on the Pyrex surface under nitrogen atmosphere.

8.4 Characterization

Different characterization procedures were used to check the feasibility of the proposed method for the fabrication of pushing actuators. First of all, some measurements were performed to study the degree and quality of the alignment between the polymer backbone and the mesogens at molecular level, and to demonstrate its novel 2D prolate polydomain conformation. To that end, different techniques such as DSC and X-ray

8. MICROPILLAR ARRAY

diffraction were used. Finally, the performance of the micropillars at macroscale was characterized measuring their length variations in both radial and axial directions as function of temperature. The stress generated during the expansion and contraction movements was also evaluated.

8.4.1 Material conformation characterization

8.4.1.1 DSC measurements

The phase transformation behavior and the thermal properties of the LCE micropillars were evaluated by DSC measurements using a Perkin Elmer DSC8500 differential scanning calorimeter equipped with a liquid nitrogen controller Cryofill at the heating/cooling rates of $dT/dt = 5, 10, \text{ and } 20 \text{ K} \cdot \text{min}^{-1}$. The graphs in Figure 8.10 show the main results obtained. The first order transition temperatures were determined by extrapolating the heating/cooling rate to $0 \text{ K} \cdot \text{min}^{-1}$, resulting in a glass transition temperature of $T_g = -9^\circ\text{C}$ which was determined by the half-vitrification temperature ($1/2 \Delta C_p$). The nematic-to-isotropic phase transformation temperature, T_{NI} , was determined by temperatures of the maxima of the heat flow. The changes in the heat capacity, ΔC_p , and the latent heat, ΔH_{NI} , were calculated from the thermograms, resulting $\Delta C_p = 0.470 \text{ J} \cdot \text{K}^{-1} \text{ g}^{-1}$ characteristic of polysiloxane-based liquid-crystalline elastomers, and a clearing temperature $T_{NI} = 57.2^\circ\text{C}$ with a transition enthalpy $\Delta H_{NI} = 1.23 \text{ J} \cdot \text{g}^{-1}$ common for nematic elastomers.

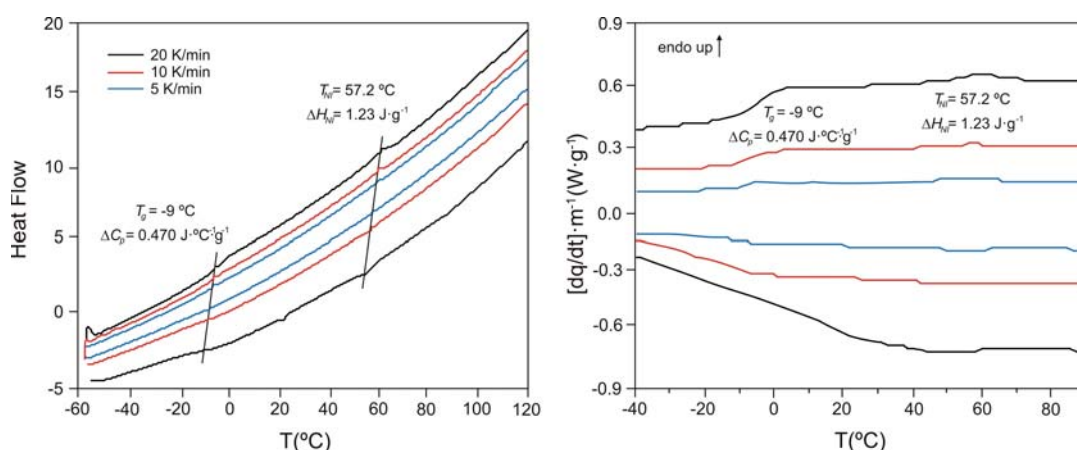


Figure 8.10: DCS curves on a nematic LCE micropillar at the heating/cooling rates $dT/dt = 5, 10, \text{ and } 20 \text{ K} \cdot \text{min}^{-1}$.

These temperature values show that the material is suitable for actuation: it has a soft and flexible polymer backbone, with a relatively low actuation temperature $T_{NI} = 57.2\text{ }^{\circ}\text{C}$ in contrast with similar LCEs, leading to a reduction of the amount of energy required for the actuation of the material. In order to investigate the nematic order in the micropillars, swelling, X-ray, and polarized optical microscopy experiments were performed at room temperature.

8.4.1.2 Swelling measurements

Swelling experiments on the partially crosslinked non-oriented micropillar, P_{pcno} , on the fully crosslinked non-oriented micropillar, P_{cno} , and on the fully crosslinked oriented micropillar, P_{co} , were performed in toluene at $25\text{ }^{\circ}\text{C}$ in order to obtain information about the crosslinking process (effective crosslinking density and network anisotropy) and the orientation of the sample. The dimensions of the LCE micropillars were determined using a Will Strübin-Wetzlar optical microscope.

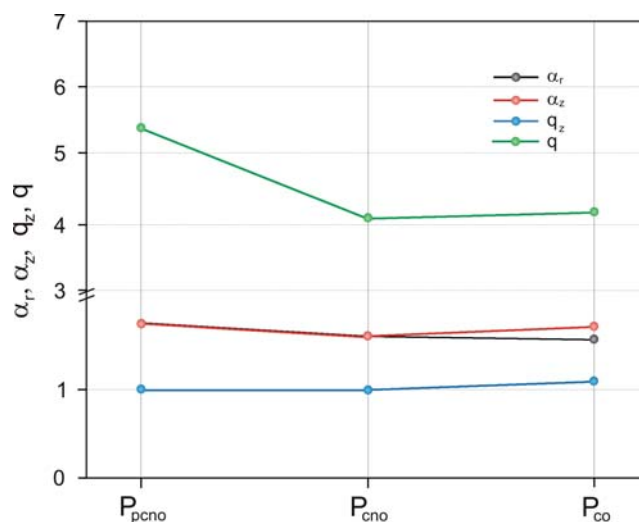


Figure 8.11: Swelling ratios α_r and α_z , swelling anisotropy q_z and swelling parameter q for the partially crosslinked non-oriented micropillar, P_{pcno} , the fully crosslinked non-oriented micropillar, P_{cno} , and the fully crosslinked oriented micropillar, P_{co} , in toluene at $25\text{ }^{\circ}\text{C}$.

The values for the swelling ratio α_z and the radial swelling ratio α_r of 1.56 ± 0.04 and of 1.71 ± 0.05 were obtained, respectively. The higher value for the swelling ratio along the axial cylindrical direction, α_z , already indicates a more compressed state in this direction with respect to the radial one, α_r . Usually, non-oriented samples show

8. MICROPILLAR ARRAY

swelling anisotropy values equal to the unit, and for this radial prolate polydomain sample the swelling anisotropy value $q_z = \alpha_z/\alpha_r$ of 1.10 ± 0.04 indicates that the sample swells more in the z-axis. This anisotropically enhanced swelling capacity manifests as an effect of the applied compression during the alignment of the sample, which leads to an extra expansion when incorporating solvent molecules in the swollen isotropic state. Furthermore, the swelling parameter $q = 4.2 \pm 0.3$ has a value which is close to that for SCLCE samples with a crosslinker content of 10 mol% [145, 233].

The swelling parameter $q = \alpha_r^2 \alpha_z$ for the P_{co} micropillar ($q = 4.2 \pm 0.3$) was similar to the P_{cno} micropillar ($q = 4.1 \pm 0.3$), but lower than for the P_{pcno} micropillar ($q = 5.4 \pm 0.5$). These values confirmed the difference in crosslinking density between the partially crosslinked elastomer, P_{pcno} , with high swelling ratio, and the fully crosslinked elastomers, P_{co} and P_{cno} , with low swelling ratio. Moreover, the anisotropy of the network could be described from the swelling anisotropy, $q = \alpha_z/\alpha_r$, which is the ratio between the axial and the radial swelling ratios. The oriented micropillar P_{co} showed a swelling anisotropy of $q_z = 1.09 \pm 0.04$, which differed from the random distribution of nematic domains in the micropillars P_{pcno} and P_{cno} with swelling anisotropy values of $q_z = 1.00 \pm 0.06$ and $q_z = 1.00 \pm 0.05$, respectively. A summary of these swelling measurements results are plotted in the graph in Figure 8.4.1.2.

8.4.1.3 X-ray Analysis

X-ray diffraction experiments were performed by using a Philips PW 1730 X-ray diffractometer at 4 kW, equipped with a rotating anode in order to obtain direct information on the WAXS reflections in the nematic phase. In all the measurements, which were also performed at room temperature, a Cu K_α radiation of 1.5418 Å filtered by a graphite monochromator and collimated by a 0.8 mm collimator was used with an incident beam normal to the surface of the LCE film. The scattered X-ray intensity was detected by a Schneider image plate system (700 x 700) pixels with 250 μm of resolution. From the WAXS intensities, the mesogen and polymer distances (d_m and d_p) and the mesogen and polymer angle distributions (ϕ) were calculated using a Gaussian distribution

$$f(x) = a \exp \left(- \frac{(x - b)^2}{2c^2} \right) + d$$

where a , b and c are parameters related to curve's peak height, curve's peak central position and curve's width, respectively.

The order parameter ($S = S_d \cdot S_N$) was determined according to Lovell and Mitchell approach [234, 235], where S_d is the director order parameter and S_N is the order parameter that refers to the local orientational order parameter. For the present approach, in which the sample has a macroscopically uniform alignment of the director $S_d \approx 1$ is assumed.

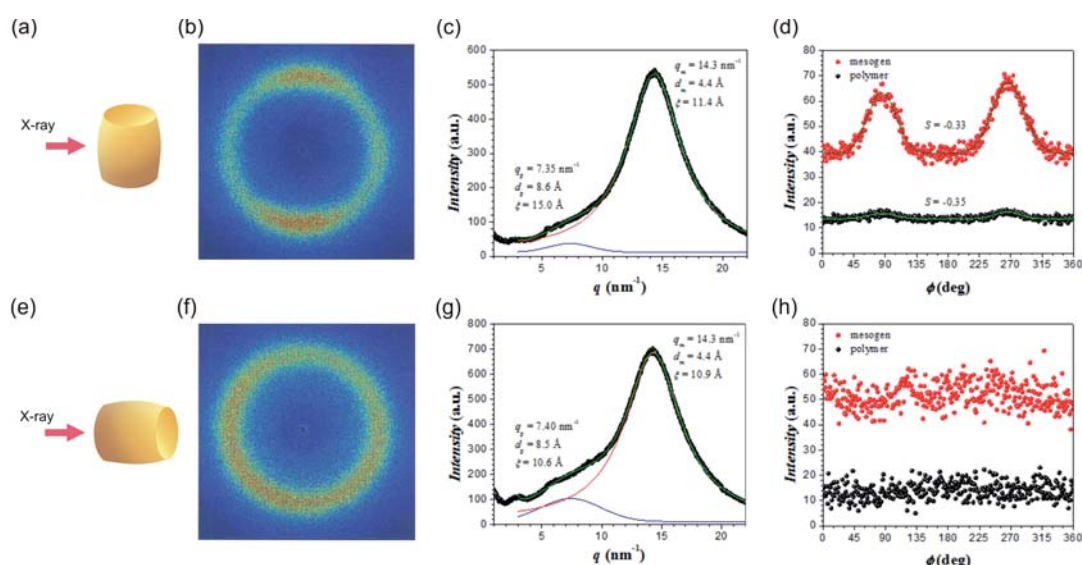


Figure 8.12: Confirmation of the nematic planar orientation of the LCE micropillars by XRD experiments.

X-ray measurements in the two directions (axial and radial) of the micropillars were analyzed by placing the beam perpendicular to each of them. A summary of the main results obtained is depicted in Figure 8.12. The analysis of the sample when the X-ray beam was perpendicular to the cylindrical axial direction (Figure 8.12a) showed a 2D X-ray pattern with two maxima in the meridian (Figure 8.12b), which corresponds to a distribution of mesogens in the plane parallel to the circular cross section of the micropillars. Deeper insight into the orientation of the material was obtained by means of XRD, where the 1D X-ray pattern (Figure 8.12c) shows two maxima at distances $d_p = 8.6 \text{ \AA}$ ($q_p = 7.35 \text{ nm}^{-1}$) and $d_m = 4.4 \text{ \AA}$ ($q_m = 14.3 \text{ nm}^{-1}$) corresponding to the polymer and the mesogen distance, respectively. The azimuthal analysis of these two previously indicated distances shows two maxima at 90° and 270° for both

8. MICROPILLAR ARRAY

distributions (Figure 8.12d). Thus, a radial prolate polydomain conformation for both the polymers and the mesogens is present in the oriented micropillars.

The calculated order parameters for both distributions were negative, with values of $S_p = -0.35$ and $S_m = -0.33$ in agreement with ordered radial distribution of domains in the cylindrical plane of both the polymer and the nematogen (i.e., nematic mesogens). The measurement performed when the X-ray beam was parallel to cylinder-axis direction, as indicated in Figure 8.12e, showed a random distribution of the nematic domains, with no maxima in the 2D X-ray pattern (Figure 8.12f), and no maxima in the azimuthal distribution of both the mesogen and the polysiloxane polymer backbone (Figure 8.12h). The 1D X-ray pattern in Figure 8.12g, in contrast, showed features similar to those of the measurement done with the X-ray beam perpendicular to the z-axis.

8.4.1.4 Polarized light analysis

Polarized optical microscopy experiments were performed on a micropillar section perpendicular to its cylindrical axis in order to investigate the nature of the planar orientation of the mesogens as observed previously by X-ray experiments. To that purpose, a Nikon Eclipse ME600 polarized light optical microscope, equipped with a Nikon DXM 1200F digital camera was used.

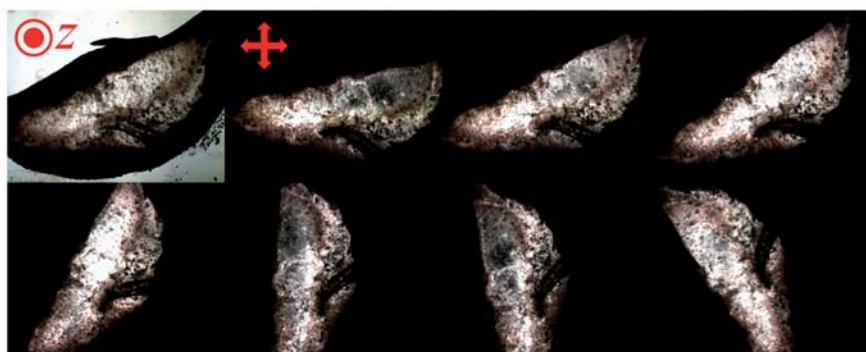


Figure 8.13: Micropillar cross section images using both non-polarized (top-left) and polarized light respectively, at different rotating angles.

The results confirmed the two-dimensional prolate polydomain conformation where birefringence was always present in the sample when measuring it at different rotating angles (see Figure 8.13). Thus, the polydomain was structurally proven due

to the scattering of the sample and the presence of microdomains distributed radially in the plane of the cylinder.

8.4.2 Micropillar actuators characterization

8.4.2.1 Thermoelastic experiments

The change in the dimensions of the micropillars was optically evaluated on a temperature range from room temperature to the isotropic state in order to investigate the mechanism of actuation, from the 2D prolate polydomain conformation of the polymer chains and mesogens to the spherical one. To guarantee uniform heating and cooling rates of the whole sample, the especially designed miniaturized hotplate previously detailed in section 3.2.1 from Chapter 3 was again used. Pictures for measuring the length and diameter of a LCE micropillars under thermal actuation were recorded using a Moticam 2300 3.0 MPixels digital camera mounted on a Leica DM LM upright optical microscope. The change in radius, $\lambda_r = d/d_{iso}$, and height, $\lambda_z = h/h_{iso}$, of the micropillars was calculated by evaluation of the optical pictures with the image processing software ImageJ 1.47.

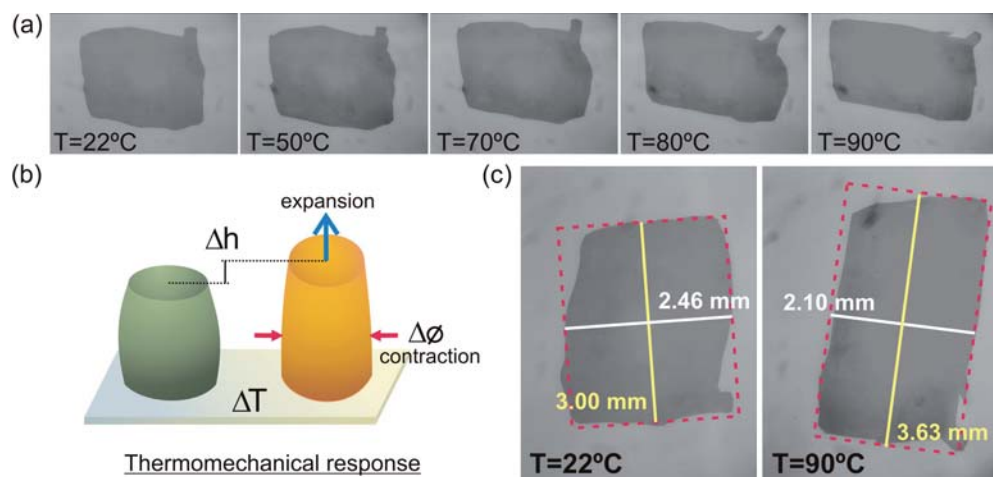


Figure 8.14: Evaluation of the change in dimensions of the micropillars through optical microscopy analysis (thermomechanical response).

In the nematic state, the LCE micropillars have average dimensions of 3.00 mm in height and 2.46 mm in diameter. After heating the LCE array to the isotropic phase, the average dimensions of the micropillars changed to 3.63 mm in height and 2.10 mm

8. MICROPILLAR ARRAY

in diameter. Figure 8.14 reflects these changes in dimensions through the comparison of optical microscopy pictures taken at different temperatures.

These results are also summarized in the thermoelastic plot in Figure 8.4.2.1, where the change in length in the axial, λ_z , and radial, λ_r , directions is shown as a function of temperature. A clear change in both directions is observed, with values at room temperature of $\lambda_r(22^\circ\text{C}) = 1.17$ and $\lambda_z(22^\circ\text{C}) = 0.83$, which correspond to a contraction of $\varepsilon_r(22^\circ\text{C}) = 15\%$ and to an expansion of $\varepsilon_z(22^\circ\text{C}) = 21\%$. Shapes of both contraction and expansion curves in the thermoelastic plot are common for nematic LCEs with an inflexion point at $T_{NI} = 57.5^\circ\text{C}$ related to the clearing temperature of the material, and with no discontinuity when approaching the isotropic state due to the presence of a paranematic phase induced by the crosslinking process.

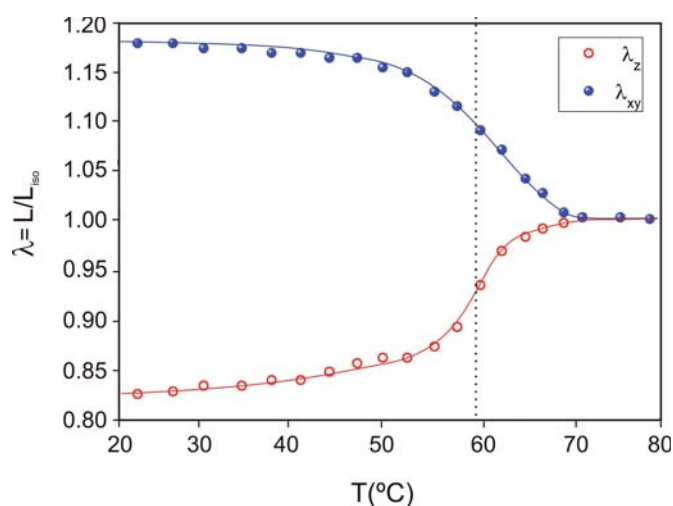


Figure 8.15: Thermoelastic experiment on an oriented nematic LCE micropillar showing the expansion along the axial direction, λ_z , and the contraction along the radial direction, λ_{xy} .

8.4.2.2 Thermomechanical experiments

Finally, the mechanical actuation was analyzed, by measuring the forces exerted by the micropillar during expansion upon heating and contraction upon cooling.

The LCE micropillar array was heated from room temperature to 90°C using the previous described miniaturized hotplate. However, this time the atmospheric chamber was removed to allow free access to the sample. The force (stress) generated

during the expansion of the LCE micropillars when heated was measured as a function of time using a dynamometer which was in contact to the top surface of one single LCE micropillar. Similar to previous setups, the use of microtranslational stages allowed the correct relative positioning between these elements. The dynamometer was coupled to a computer where all relevant data such as temperature, time and the measured force were acquired by a self-developed data acquisition software in LabVIEW interface (National Instruments), similar to the one used for measuring the other LCEs samples in previous chapters 3 and 4. Pictures in Figure 8.16 show the setup used for the evaluation of the mechanical response of the micropillars as well as detail the interaction between the dynamometer tip and the micropillars top surface.

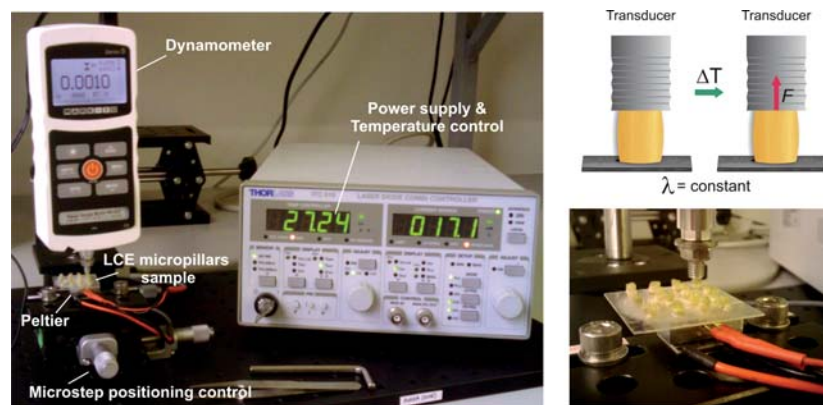


Figure 8.16: Setup for evaluation of the mechanical actuation of the micropillars.

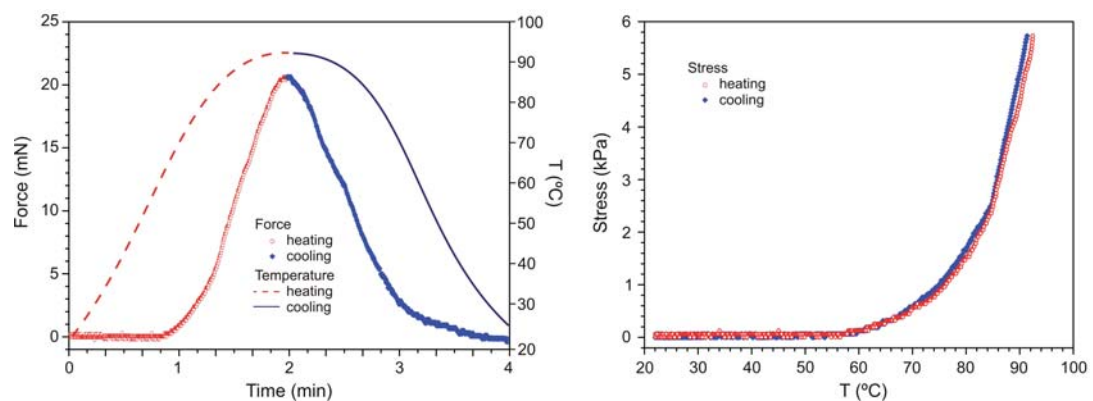


Figure 8.17: Mean force and stress measurements as function of temperature and time during the heating and cooling processes.

8. MICROPILLAR ARRAY

Three complete heating and cooling cycles were recorded and analyzed for each LCE micropillar in the array showing good repeatability and low dispersion. The maximum measured force was $F = 20 \text{ mN}$ at the set temperature of $T_{set} = 90 \text{ }^\circ\text{C}$. The time needed to reach this maximum force was around $t = 2 \text{ min}$, and showed full reversibility and repeatability upon cooling of the LCE micropillar array. In parallel, the true stress was evaluated as a function of the micropillar temperature, taking into account its cross section, its dimensional change as function of the temperature, as well as the measured force. The results show a fast growing stress behavior upon reaching the isotropic phase, with a value of $\sigma_t = 5.6 \text{ kPa}$, and a hysteresis factor of 1.1 between the heating and cooling curves, as plotted in Figure 8.17.

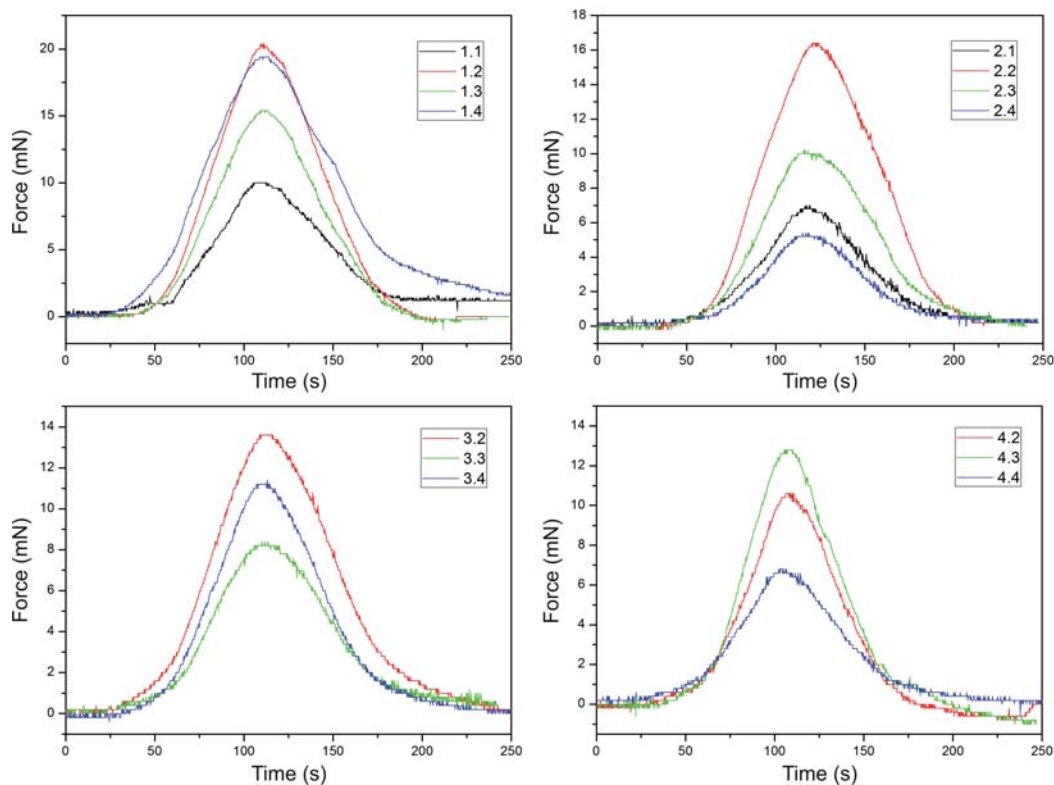


Figure 8.18: Force as function of time measurements of different micropillars under same conditions.

It is worth noting that a significant variation in the actuation force, i.e., the expansion rate, was obtained when comparing the measured values for each single micropillar. Plots in Figure 8.18 evidence this variation. A mapping on the micropillars

array in Figure 8.19 evidenced a non-uniform distribution of the force, where the higher values are mainly concentrated in a lateral side of the array (red zones), thus confirming an irregular deformation of the pillars during their fabrication process, probably due to a poor fixation of the cover during the final crosslinking step. A more accurate fastening system would help to reduce this unevenness.

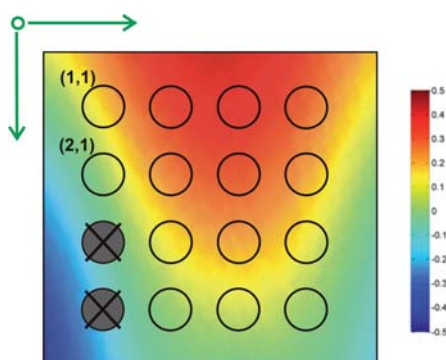


Figure 8.19: Force distribution along the micropillar array.

8.5 Discussion and summary

All nematic LCE samples reported up to now showed a prolate conformation of the polymer backbone together with a nematic orientation which follows the direction of the applied uniaxial stretching (z-axis) resulting in a contraction in the isotropic state which can be used to lift weight or generate retractile forces. The innovative technique presented in this chapter goes a step further leading to nematic LCE actuators able to expand along the z-axis and contract in the other two directions (x- and y-axes). Thanks to a two-dimensional prolate polydomain conformation of the micropillars coming from the uniaxial compression (biaxial deformation), a radial distribution of the polymer backbone and mesogens is reached in plane (xy-plane) resulting in a novel actuation principle allowing LCEs to produce pushing forces upon heating.

In this chapter, a detailed description of the methodology and the processing principles involved has been presented together with a complete characterization of the resulting actuators from both material conformation and actuation points of view. Thus, first some DSC, swelling and X-ray diffraction measurements have been performed to confirm the new configuration of the actuators and obtain their main

8. MICROPILLAR ARRAY

characteristics, such as the transition and glass temperatures, the enthalpy, the swelling ratio and the order parameter. Finally, the parameters involved in their actuation, such as the thermal expansion coefficient and the pushing forces have been analyzed, resulting in very optimistic values taking into account that the system was not yet optimized.

The values for the change in height ($\Delta z = 630 \mu m$), force ($F = 20 mN$), and stress ($\sigma_t = 5.6 kPa$), together with the processability and tunability of the chemistry in terms of mechanical and thermal actuation, and the possibility of obtaining different shapes on demand (besides the common film-like actuators) changing the configuration of the molds make such technique combined with LCE materials, a key enabling technology for the future integration of these materials in microsystems technology, and very suitable for candidates for haptic applications.

The main advantages of this method are the scalability (only limited by the techniques used for the fabrication of molds and the availability of the chemical compounds), its relative simplicity (after an accurate design of the molds the preparation process of the actuators can be easily controlled and require only few steps) and the possibility to obtain arrays of identical actuators with pushing forces, reducing possible variability due to assembly of individual actuators.

As proof of concept, a neat LCE material has been used. Future work will involve the improvement on the deformation process to homogenize the resulting pushing forces, as well as the use of dye-doped LCE composites to allow photo-actuation.

The work described in this chapter has been done in collaboration with Dr. Antoni Sánchez-Ferrer from ETH Zürich, Department of Health Sciences & Technology, Institute of Food, Nutrition & Health, Food & Soft Materials Science Group, who was in charge of the synthesis and preparation of LCEs as well as to perform swelling and X-ray experiments. The concept, the molds design and fabrication, as well as the thermoelastic and thermomechanical experiments were performed at IMB-CNM facilities. As a result from this collaboration, a scientific journal article with high impact factor has been published. Moreover, due to the originality and novelty of that work, an invitation for a book chapter contribution which is now under preparation was received.

9

Micropillar array actuators: integration on a device

Once proved the possibility to fabricate different types of actuators and in array based on the mechanical response of LCE materials and their applicability to develop complex tactile systems, it was necessary to go a step forward.

Photo-induced actuation has been demonstrated to be a suitable alternative for the development of LCE-based actuators, since it is a clean and cheap energy source allowing remote control, resulting in strong actuation forces and shorter actuation times (Chapter 2). However, in spite of such great advantages, it is still difficult to implement in the context of tactile applications as it has been demonstrated in Chapter 4, since a large number of actuators producing high forces and displacements with short actuation times are required, all of them in a confined space. The high power required to actuate the material (i.e., to reach T_{NI} temperature) together with the difficulties to find suitable optical light sources delivering sufficient intensity and small enough to fit Braille requirements (high density of actuators per squared decimeter) becomes one of the most important difficulties looking forward to the development of real-size prototypes (scale up the technology), in which a minimum array of 80 by 80 actuators is required to represent several Braille characters. Thus, other potential alternatives have started to be investigated within this thesis.

The initial idea of the NOMS project was to develop a system similar to a film that could be adapted to the self-luminous screens of current devices such as smartphones, tablets, laptops and computers, using the light emitted for each single pixel in the

9. MICROPILLAR ARRAY ACTUATORS: INTEGRATION ON A DEVICE

screen to induce movement into the LCE material without any extra energy source; a very interesting and ambitious idea but not feasible at this moment since the amount of light emitted by the screens is not enough to produce movement.

However, following such concept and considering the results obtained during LCE's characterization (see Chapter 3) and evaluating the different alternatives proposed in this section for the fabrication of actuators in an array (Chapters 6, 6 and 8), a novel approach has been proposed: a hybrid system combining the light emitted by the screens and direct heating of the material to induce actuation. Preliminary studies of the system have been performed and presented in this chapter which is divided in three sections. First the concept and the working principle of the system are described together with a description of its main parts. The design and the fabrication process of the new actuators as well as their different components are then detailed in the second section. Finally, the last part of the chapter presents the first partial characterization results obtained which encourage continuing this research in a near future.

9.1 Concept and working principle of the device

The system proposed and still under study consists of a direct thermal actuation of the elastomer by means of an array of resistors acting as local heaters (Joule heating effect) which, at the same time, run with the light emitted by the pixels on a current screen by means of phototransistors. In this manner, it is possible to use the screens' own-light as energy source to feed the system avoiding extra power supplies and thus reducing the consumption of the system.

Figure 9.1 schematically depicts the concept around this approach, which is also based on multilayer concept for its great advantages previously pointed out (see 4.6 section in Chapter 4). The first layer, named actuators layer, contains an array of LCE actuators and will be in charge of transmitting the tactile signal to the end-user. Among all the designs of actuators developed within this thesis, the micropillars array system in Chapter 8 was selected to be the most suitable one since a positive tactile signal (i.e., a pushing force) can be directly obtained without adding any external element to transmit the tactile signal. Moreover, a robust actuation with relatively high forces can be reached in response to thermal actuation. Below the actuators layer, there are the arrays of thermoresistors and phototransistors together with their corresponding

electronics. Such layer was conceived as a double-side layer to reduce the thickness of the system and provide a more compact design. In this manner, on the top side (the one in contact with the actuators layer) one can find the array of thermoresistors, one for each single micropillar, whereas on the bottom side, there are the phototransistors and the rest of electronic components in charge to convert and transmit the intensity of light received from the screen into electric signal to power the heaters (see inset in Figure 9.1).

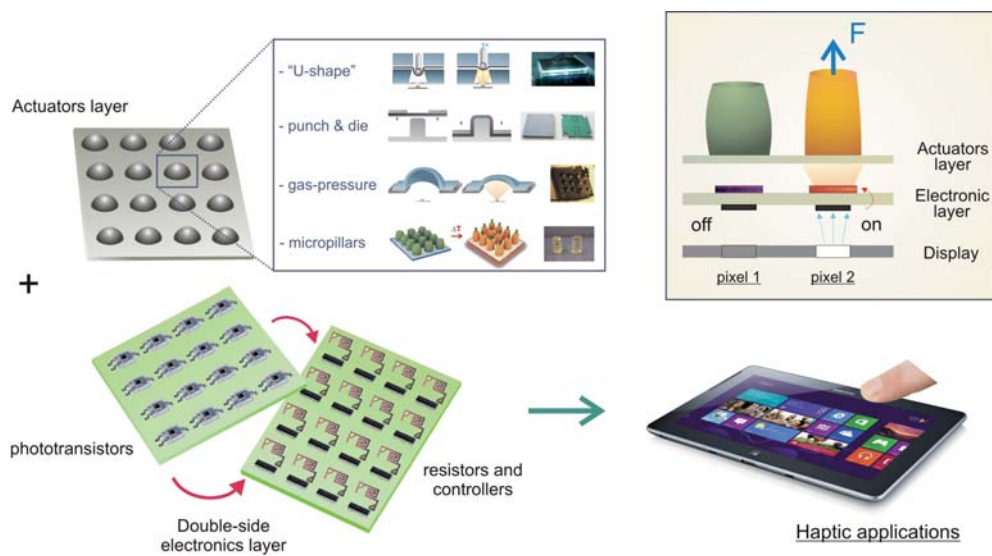


Figure 9.1: Schematic representation of the alternative tactile device approach: a hybrid system combining light and direct heating to actuate the LCE material.

Firstly, several resistances have been fabricated in order to test the power requirements to generate enough heat to properly actuate the material.

9.2 Design and Fabrication of the device

Initially, all the layers forming the devices were conceived to be transparent. In this way, the system could be used by everyone sighted and non-sighted people, providing an added value to the current devices on the market. To this end, printed electronics on flexible polymeric substrates using transparent resistive inks such as Indium Tin oxide, ITO, for the circuitry design would be the best solution. This is a very ambitious objective since technically demanding procedures and the highest requirements of

9. MICROPILLAR ARRAY ACTUATORS: INTEGRATION ON A DEVICE

material development and optimization would be required, which were not the scope of this thesis. Nevertheless, as proof of concept of the proposed technology and with the main objective to validate such approach for future development, a first version of 4 × 4 actuators with its corresponding electronics was fabricated using standard processes and materials in microelectronics [236, 237]. To perform preliminary tests, both sides of the electronic layer were fabricated on two different individual layers. In this manner, it was possible to separately study each part and change the designs without affecting the other components. Once established the best options, the final design will be fabricated together with the other electronic components in a unique layer, as depicted on the scheme in Figure 9.1, and later adapted to be fabricated using printed electronics.

The design criteria and the main steps and processes used for the fabrication of each part of the first testing device are detailed below.

9.2.1 Thermoresistors

9.2.1.1 Design

As mentioned above, this approach is again based on thermal actuation of LCE micropillars. However, in this case the heat is delivered to the micropillars in a local way by the use of thermoresistors: individual heaters placed on the base of each pillar based on the Joule effect, which produce a thermal gradient some electrical current is applied through them [165].

Mathematically, the Joule effect can be expressed such that

$$Q \propto I^2 R t = I \cdot V \cdot t = P \cdot t$$

where the amount of heat released, Q , is proportional to the square of the current, I , which at the same time is proportional to the energy dissipated per charge passing through a resistor per unit time, when Ohm's law is applicable.

Hence, an accurate design of the thermoresistors is required. However, prior to start with their design, some requirements should be taken into account to ensure a correct behavior of the system.

First of all the size of the resistors, which should allow the micropillars completely cover their surface in both nematic and isotropic states to guarantee a correct

transmission of heat between such elements. Thus, the dimensions of the resistors will be fixed as function of the micropillars diameter which, at the same time, will be defined by the size of the molds and the alignment process, as exposed in previous chapter (see section 8.2 in Chapter 8). To conduct these early experiments, the same molds were used for the fabrication of the micropillar array, resulting in micropillar actuators with diameters of 2.46 mm at nematic state and 2.10 mm at isotropic state (see Chapter 8 for details about the molding process).

Moreover, a uniform heat distribution along the surface of the resistors is required in order to guarantee a consistent thermal gradient. Thus, a compact serpentine-like geometry was chosen to increase the electric path. In this manner, the thermal losses in the outer parts of the resistors will be balanced out by the high heat concentration in its center.

Another requisite to consider is the value of the resistors and thus, the material from which they will be made and its thickness. The heaters should provide a thermal gradient high enough to achieve temperatures close to the T_{NI} of the LCE material (at most, 5 °C – 10 °C above) to avoid degradation of the material.

As demonstrated in previous related work [238], an excessive voltage may induce changes on the physical characteristics of the material as well as on its behavior. Figure 9.2 shows permanent damage on a SCLCE sample in which irreversible changes on the color and the shape of the sample were produced by too high voltage, resulting in a later bad actuation.



Figure 9.2: Example of permanent damage on a SCLCE sample due to an excess of voltage. Adapted from [238].

Among the most current materials employed for the fabrication of microheaters, gold, Au, was chosen to be one of the least reactive chemical elements as well as to be good thermal and electric conductor. Typical values of thermal conductivity and electrical resistivity of Au are $318 \text{ Wm}^{-1}\text{K}^{-1}$ and $22.14 \text{ n}\Omega\text{m}$ respectively [239].

9. MICROPILLAR ARRAY ACTUATORS: INTEGRATION ON A DEVICE

Considering the relationship between the resistivity of a material and its geometry, as well as the above mentioned requirements, squared resistors of two different sizes were designed, leading to active surfaces of 1.0 mm x 1.0 mm and 1.5 mm x 1.5 mm respectively. To adjust the value of the resistance (i.e., the final temperature achieved by the resistors) two different Au thicknesses were chosen: 50 nm and 100 nm. Figure 9.3 depicts the final geometry of the resistors. Later, Figure 9.5 shows the array of resistors once fabricated, where both sizes of resistors can be distinguished.

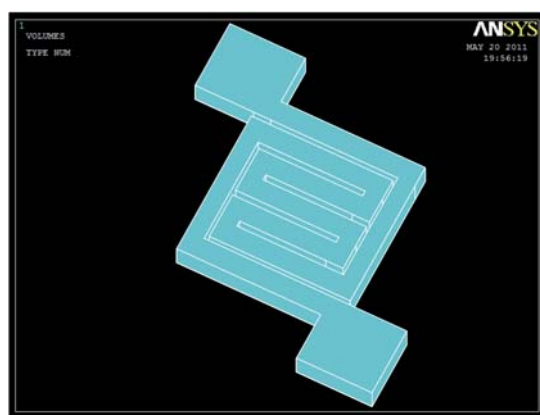


Figure 9.3: Selected geometry for the fabrication of the testing Au thermoresistors.

9.2.1.2 Fabrication

The Au testing thermoresistors were fabricated using one of the standard microfabrication processes known as "lift-off" which is commonly used in microelectronics, especially to pattern metals [240]. Figure 9.4 summarizes the main steps of the microfabrication process used to create the array of Au thermoresistors.

The process starts with a 100 mm Pyrex wafer 500 μ m thick (step I in Figure 9.4). Then, a standard photolithographic process is performed to pattern the designs of the thermoresistors, which were previously transferred to a photomask (steps II to IV) in a sacrificial layer. To that end, a continuous layer of 1.8 μ m thick of positive photoresist is deposited on top of the wafer. After UV exposure, a partial etching of the photoresist is performed, resulting in a non-continuous layer with openings which correspond to the resistors designs. Then, after a surface cleaning, a thin Au layer (50 or 100 nm thick) is deposited on the whole top surface of the wafer covering both the remaining

9.2 Design and Fabrication of the device

photoresist and the apertures. In this case, a 10 nm thick Ti-Ni bilayer was previously deposited to improve the adherence of the Au to the Pyrex substrate (step V). Finally, the rest of the sacrificial material (i.e., the photoresist) is washed out together with the non-desired parts of the Au layer, leading to the final thermoresistors (step VI).

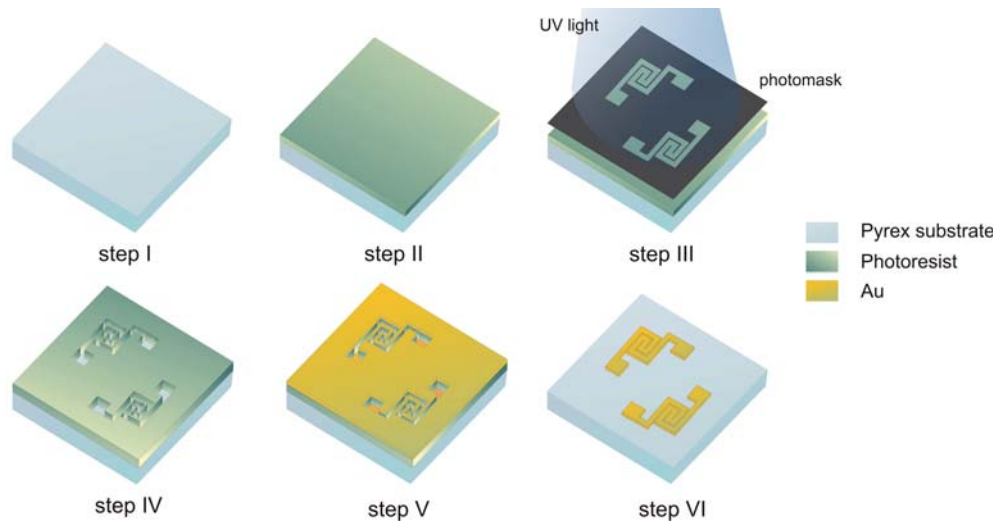


Figure 9.4: Simplified microfabrication process of the Au thermoresistors.

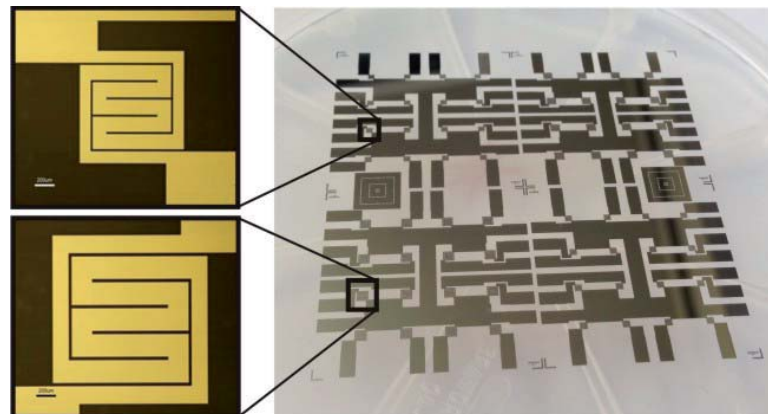


Figure 9.5: Au thermoresistors after the whole fabrication process.

Figure 9.5 shows a Pyrex wafer after the whole fabrication process, where both sizes of thermoresistors with their corresponding tracks and pads can be identified. In each processed wafer, four chips containing 4×4 resistors (each one in a quarter of the wafer) can be obtained, which can be later individualized prior to testing. The total

9. MICROPILLAR ARRAY ACTUATORS: INTEGRATION ON A DEVICE

chip area is 30 mm x 30 mm, with 6 mm spacing between heaters.

9.2.2 Circuitry

9.2.2.1 Design and selection of the main components

Parallel to the design and fabrication of the resistors, some investigations were carried out to propose designs for the rest of elements on the electronic layer. According to the working principle of the system, the circuitry should be able to convert the intensity of light emitted by the pixels on the display into electric signal which, at the same time, should be high enough to produce certain amount of heat once passing through the thermoresistors to induce the desired shape changes in LCE material. The element in charge to perform this function is the phototransistor.

From the different commercially available options on the market, TEMT6200FX01 ambient sensor phototransistor (Vishay Semiconductors, Germany) was selected because of its high photosensitivity and its spectral range, which is similar to the human eye (sensitivity peak at 550 nm) [241], as well as due to its small dimensions (2 mm x 1.25 mm x 0.85 mm) which are in agreement with Braille standards A.2.

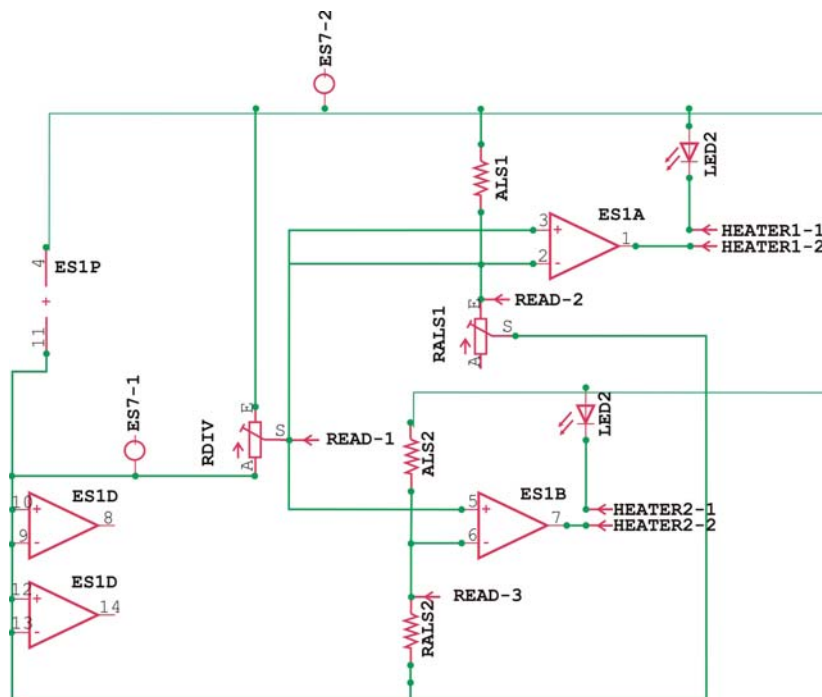


Figure 9.6: Schematic representation of the circuit and its main components.

Besides the phototransistor, other electronic components were required to complete the circuitry among which the operational amplifiers, Op-amps, also known as comparators, play an important role. Such elements will be in charge to transmit the electric signal from the phototransistors to the heaters, allowing only two possible states for the resistors: on and off. In this manner, it would be possible to guarantee a correct operation of the circuit and avoid undesired intermediate states (partially on) and cross reading signals from neighboring actuators, which can induce bad response of the system. MCP6564-E/ST comparators (Microchip Technology Inc., USA) were selected for that purpose. Other elements such as sensitivity regulator resistors and voltage divisors were added to complete the design and set the luminosity threshold for actuation, thus making the circuit sensible to the screen light. A schematic representation of the circuit with its components is shown in Figure 9.6.

Once established the functions and selected the main components, the circuit should be devised, analyzed and optimized to guarantee the correct operation of all the elements avoiding short-circuits [242]. To this end, EAGLE CAD ® electronic design automation, EDA, software (CadSoft, USA) was used.

9.2.2.2 Fabrication

The circuitry was fabricated by photoengraving using a double-sided printed circuit board, PCB, which will mechanically support and electrically connect all the electronic components of the system. In this manner, it is possible to design two different (dependent or independent) circuits on each side of the board. Thus, two different photomasks in a mirror-like disposition were required, each of them with a different design. Figure 9.7 shows the two photomasks used, both of them fabricated on standard cellulose acetate. The first one, (Figure 9.7 -left-) was used to pattern the phototransistors and their corresponding tracks and connection pads, whereas the second one, (Figure 9.7 -right-) to pattern the rest of the components and the soldering unions.

The design of both circuits was replicated on both PCB surfaces by exposing on a photo-sensitive resist coating previously deposited. In this manner, after UV irradiation, the remaining photoresist protected the copper foils while the unwanted copper zones were removed by a subsequent etching process using a home-made

9. MICROPILLAR ARRAY ACTUATORS: INTEGRATION ON A DEVICE

etching solution containing a mixture of hydrochloric acid, HCl, hydrogen peroxide and deionized, H_2O_2 , and deionized, DI, water at 2:1:1 volume ratio.

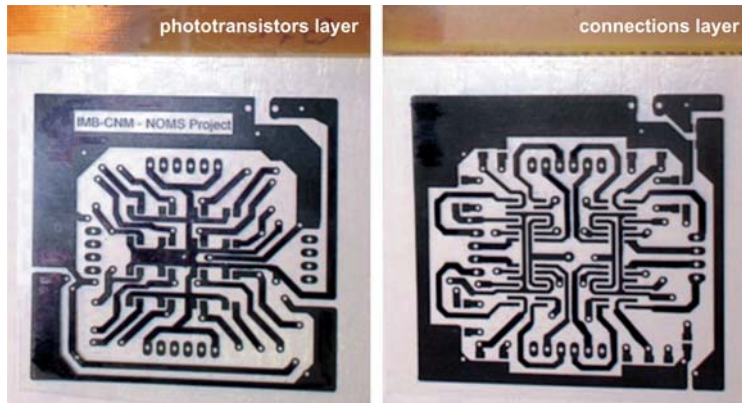


Figure 9.7: Photomask used to pattern the circuitry design to the PCB.

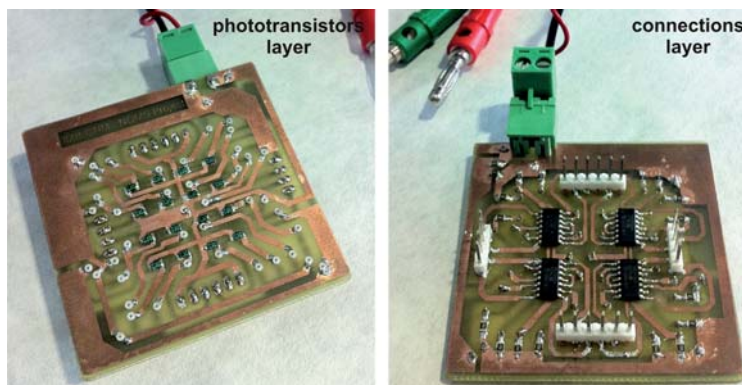


Figure 9.8: Top and bottom layers of the double-side PCB with all the components assembled for a 4 x 4 actuators prototype.

Finally, all the electronic elements such as the phototransistors and comparators, as well as the electric connections on the pads were soldered to their corresponding areas on the board. Figure 9.8 shows pictures of both sides of the PCB after soldering all the electronic components. As it can be observed in Figure 9.8 -right- once soldered, the different elements on the connection layer considerably increase the thickness of the layer, fact that forces the thermoresistors to be placed at certain distance losing compactness. In future designs, advanced PCB techniques in which the different components are embedded in the substrate can be used to reduce the thickness of the layer.

9.3 Micropillar array actuators fabrication

From all the actuators proposed within this thesis, the micropillars array system in Chapter 8 was chosen to be the most suitable one. In this manner, relatively high pushing forces can be directly obtained upon heating without adding external elements such as pins and supports thus simplifying the design. Moreover, the direct thermal actuation mechanism allows the use of pure LCE material instead of LCE-nanocomposites, simplifying the synthetic procedures.



Figure 9.9: Assembled molds and support layer prior to the micropillar array fabrication. Notice that each thermoresistor is centered of a hole.

The synthesis and the preparation of the LCE micropillar array are exactly the same as used in Chapter 8. Hence, the same PTFE molds were used to define the shape and distribution of the pillars to form the array. The only difference lies in the change of the micropillars support layer, which in this case contains the array of Au thermoresistors. As described above, the thermoresistors were uniformly distributed along the support coinciding their centers with the centers of the holes in the mold, resulting in one thermoresistor for each single micropillar. Picture in Figure9.9 shows the system assembled previous to the application of the LCE mixture where such coincidence is evidenced.

Prior to the fabrication of the LCE micropillars, a surface treatment with reactive silane was similarly applied on top surface of the support layer to guarantee good chemical adhesion between both the LCE material and the Pyrex substrate and, at

9. MICROPILLAR ARRAY ACTUATORS: INTEGRATION ON A DEVICE

the same time, protect the Au thermoresistors exposed to the chemicals. Figure 9.10 depicts the array of actuators after the successful fabrication process.

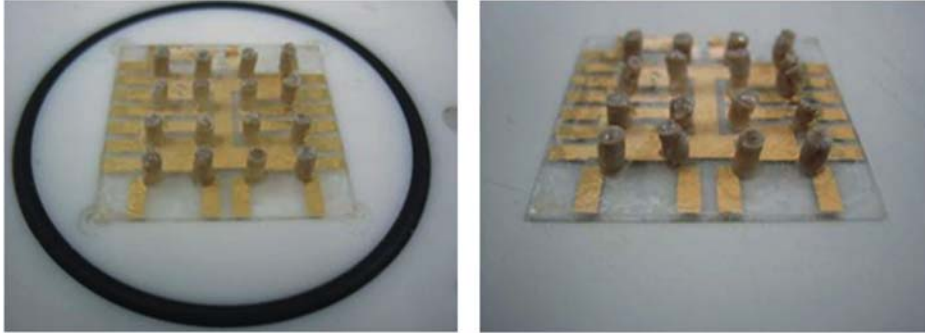


Figure 9.10: Micropillar array actuators after completing the fabrication process. Each single pillar in the array has its independent heater.

9.4 Thermoelectrical micropillars characterization

To evaluate the thermoelectric response of the micropillar actuators, both thermoelastic and thermomechanical measurements were performed in similar way to the ones reported in Chapter 8 but now as function of the electric current applied.

9.4.1 Thermoelastic experiments

First of all the change in dimensions of the micropillars as function of the voltage applied was optically evaluated by means of an optical upright microscope (DM LM from Leica). Movies of the expansion and recovery movements of the micropillars were recorded using a Moticam 2300 3.0 MPixels digital camera and later analyzed using ImageJ 1.47 software.

To better appreciate the shape changes experienced by the pillars as function of the voltage applied and thus be able to compare such results with the ones obtained using a self-constructed miniaturized hotplate (see micropillars characterization experiments in Chapter 8), some pillars were carefully separated from the substrate and horizontally placed on top of the resistors (see Figure 9.11). A sequence of images in Figure 9.11 evidenced those shape changes on a micropillar as function of the voltage applied, from which the corresponding uniaxial thermal expansion coefficients, $\lambda = L/L_{iso}$,

9.4 Thermoelectrical micropillars characterization

could also be evaluated (see graph in Figure 9.11 -bottom-). As expected, from 3.5 V the expansion of the micropillar along the axial direction becomes clearer, reaching the maximum value around 5 V that corresponds to $\lambda_z = 0.87$, which is lightly smaller than the results obtained from previous measurements with the miniaturized hotplate ($\lambda_z = 0.83$, Chapter 8). Such difference may be explained by the power adjustments as well as possible differences during the fabrication of the micropillars. In this case, the use of higher voltages was discarded to avoid irreversible damage on the material as demonstrated in previous works [238], since all the thermal load is applied on the material in a very short time (order of milliseconds).

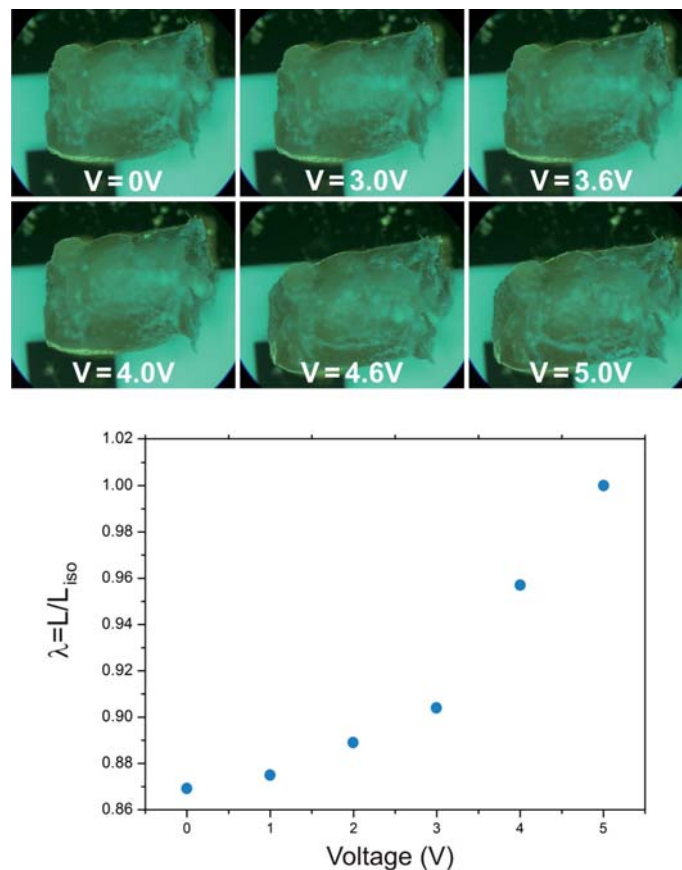


Figure 9.11: Evaluation of the change in dimensions of a micropillar as function of the voltage applied.

9. MICROPILLAR ARRAY ACTUATORS: INTEGRATION ON A DEVICE

9.4.2 Thermomechanical experiments

The mechanical response of the micropillars under actuation was analyzed measuring the force exerted by them during their expansion upon the application of different voltages. To that purpose, voltages from 0 V to 5.5 V were gradually applied to each thermoresistor in order to deliver heat to the micropillars and thus, induce their expansion. The actuation force produced was measured as function of time using the same dynamometer used in previous mechanical characterization experiments, in a pretty similar setup configuration as the one described above in Chapter 8. Again, the same self-developed LabVIEW data acquisition interface was used to collect the signal from the dynamometer as well as the same microstep positioning control to adjust the relative positioning between the dynamometer tip and the top surface of each micropillar in the array. In this case, however, both the heating system and the temperature control sensor were replaced by a DC power supplier (DF1731SB5A, Kaise Corp., Japan) and its corresponding electrical connections. A picture of the setup used to perform such electromechanical experiments is shown in Figure 9.12 where a detail of the contact between the dynamometer tip and the top surface of a micropillar can be observed. A digital multimeter was used to verify the measure.

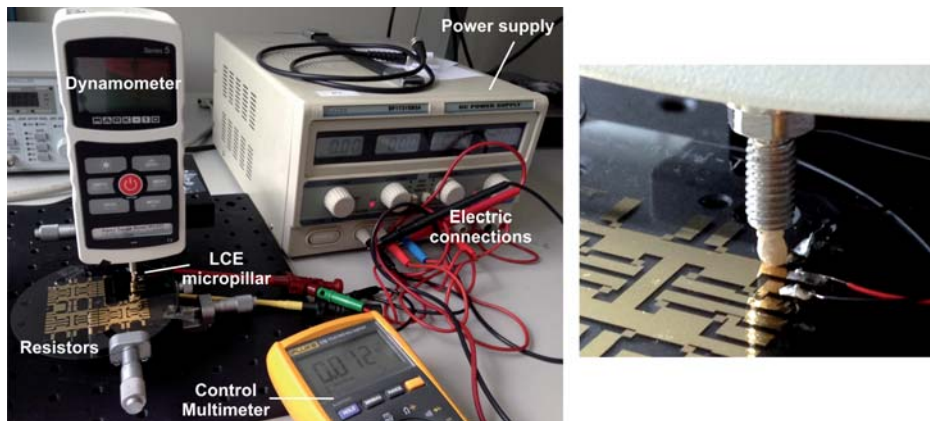


Figure 9.12: Setup used to evaluate the mechanical actuation of the micropillars using Au thermoresistors with a detailed view of the measurements.

Five complete on-off cycles were recorded and analyzed for each micropillar as function of the voltage applied, showing good repeatability and low dispersion in agreement with the results obtained upon direct heating. An example of these cyclic

9.4 Thermoelectrical micropillars characterization

measurements is depicted in Figure 9.13. In this case, the LCE micropillar was actuated by applying a constant voltage of 5.5 V, resulting in a maximum measured force of $F = 19.4$ mN with full reversibility. Again, such value is slightly lower than the force obtained by direct heating in previous measurements (see section 8.4 in Chapter 8) but in agreement with the thermoelastic measurements above.

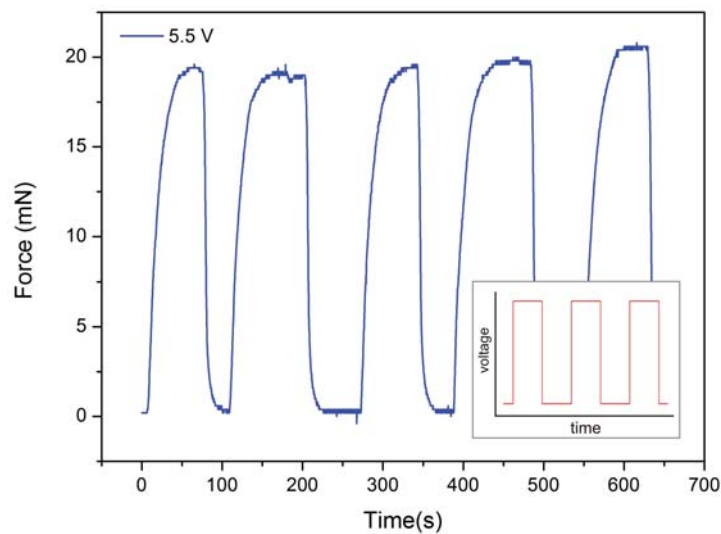


Figure 9.13: Force cyclic measurements as function of the voltage applied and time for one micropillar.

As shown in the graph, the response in time of the material is faster compared with the thermomechanical response measured upon direct heating. The resistors heat up very quickly once the current passes through them reaching temperatures above T_{NI} in few milliseconds, resulting in a nearly instantaneous change between on and off states (see inset in Figure 9.13).

Figure 9.14 shows the evolution of the actuation force as function of the current applied for four different LCE micropillars measured. A significant variation in the actuation force was obtained when comparing the maximum values measured for each single micropillar, evidencing again a non-uniform distribution of the compression force applied during the fabrication of the micropillars in agreement with the results obtained in Chapter 8 and thus, reinforcing the need to optimize such process.

Leaving aside the variability of the measurements obtained, however, the energetic requirements of the system are still too high (≈ 5.5 V) to directly use only the backlight

9. MICROPILLAR ARRAY ACTUATORS: INTEGRATION ON A DEVICE

of a standard screen to feed the resistors and the whole system. In this sense, some adjustments to the design of the thermoresistors should be adopted to reduce the power consumption.

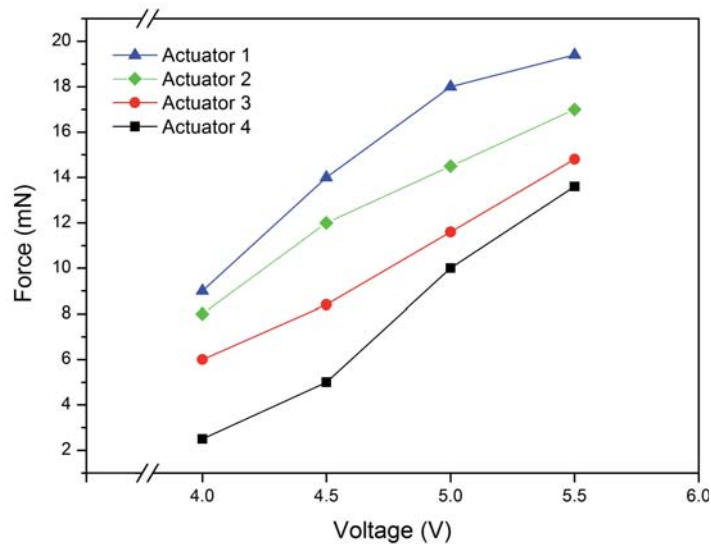


Figure 9.14: Comparison of the actuation force as function of the voltage applied for four different micropillars measured under the same conditions.

9.5 System optimization

As demonstrated in previous chapters, FEM is a very useful tool to predict the response of a system and predict its behavior under different contexts. In this manner, after knowing the real response of the system and analyzing the first characterization results, it is possible to maximize the response of the actuator while reducing the power applied by adjusting different parameters (e.g., the geometry of the thermoresistors, their thickness, the size of the micropillars, etc.) and thus, optimize the system.

To that end, again ANSYS ® multiphysics software was used. In this case, the simulations were focused on the reduction of the thermal load losses through the substrate and not on the LCE material performance itself. As first approach, a 3D thermal solid element, SOLID70, was chosen to perform both steady and transient analysis. Convective heat transfer and thermal radiation of the heaters were considered

as thermal diffusion mechanisms whereas thermal conduction between them and the Pyrex substrate was neglected. To simplify the model, a uniform heat generation along the resistors was assumed.

Figure 9.15 depicts an example of some initial FEA simulations of the heat distribution in the close regions of the thermoresistors when certain amount of power is applied.

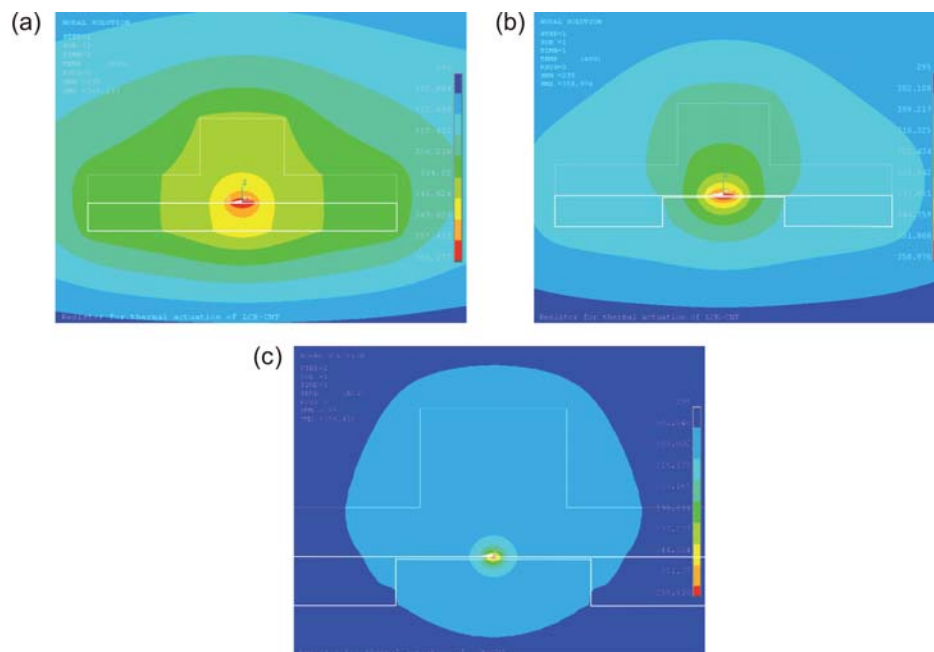


Figure 9.15: Optimization of the power consumption of the system using FEM. Heat distribution of (a) the current system, (b) after substrate micromachining, and (c) after substrate micromachining and reduction of the size of the thermoresistors.

One of the simplest actions to improve the thermal isolation of the system is to consider a reduction of the thickness of the Pyrex substrate just below the thermoresistors (substrate micromachining previous to the preparation of the micropillars). Figure 9.15b shows such effect, where a uniform and more concentrated heat distribution in the regions nearby the resistors was obtained also reducing possible cross talk effects between neighbor resistors. In this manner, the thermal efficiency of the system increases causing a decrease in the power consumption up to 40%, value which varies as function of the final thickness of the substrate as well as the size of the thermoresistor (Figure 9.15c).

9.6 Discussion and summary

In this chapter an innovative and very ambitious technology has been proposed for the development of a new generation of tactile devices based on the use of the own light emitted for each single pixel in a standard display to induce shape changes on LCE material by means of heat provided by an array of thermoresistors. Again a system based on the multilayer approach which allows a parallel development of each part of the system with multiple combinations.

In such early stage of the development of the device, the concept as well as the different parts of the system has been described and the operation principle has also been validated with a first prototype. For the implementation of such approach, the micropillar array system presented in Chapter 8 was used to be the simplest option to obtain pushing forces without including any external element (e.g., pins and supports). However, other actuators as the ones described within this thesis could also be used by adapting the technology (great advantage of the multilayer concept), and thus combining their advantages to compose variations of the device.

Preliminary characterization of the force produced by the actuators as function of the voltage applied was performed together with some FE analysis, demonstrating that the power requirements of the system can be controlled and decreased by technological processes. In this manner, uniform thermal gradients confined nearby the resistors can be obtained allowing the actuation of the LCE material without damage.

Even though the power requirements are not low, the small area they demand (suitable for 80×80 array of actuators), the proven rapid heating (in the order of milliseconds), and the simple controllability, are among the advantages supporting this approach. In addition, no specific software and hardware are required to control the device. Furthermore, innovative fabrication technologies based on printed electronics could be aimed to improve both the thermoresistors and the electronic layers, to achieve a complete system as a fully transparent and flexible polymeric device. A recent publication from Petsch and co-workers [137], in which a LCE micro-actuator with integrated deformable micro-heaters made by combining Au and polyimide were presented, encourage us to continue working with this approach.

In near future, some measurements using an IR camera (similar to the ones presented in Chapter 3) are intended to be performed to study the heat distribution

along the micropillars as function of the voltage applied. This, together with the improvement on the resistors, will help for the general understanding of the system and the improvement its response.

The work described in this chapter emerged after the good results obtained in Chapter 8. All the work, from the design of the circuitry to the assembly and characterization measurements of the system, was performed at IMB-CNM facilities in collaboration with Carlos J. Camargo, who purpose the use of phototransistors to take advantage of the light emitted by standard screens. Dr. Antoni Sánchez-Ferrer from ETH Zürich was again in charge of the synthesis and preparation procedures for the fabrication of the array of LCE micropillars. This work is still ongoing and a journal article summarizing the concept and the main experimental results is currently under preparation.

9. MICROPILLAR ARRAY ACTUATORS: INTEGRATION ON A DEVICE

Conclusions and Future work

Conclusions

The work developed in this thesis presents innovative solutions for the fabrication of actuators for tactile and haptic applications based on the opto-mechanical actuation of liquid crystalline nanocomposites.

This study covers the design, fabrication, characterization and optimization of the different actuator approaches with the ultimate goal of being integrated on a tactile device able to represent both Braille characters and simplified graphical information. An interdisciplinary work which combines a deep understanding of LCE materials, their behavior, processing and characterization, with the photo-actuation phenomenon and MEMS/NEMS technologies to provide novel solutions to the communication problems suffered by people with visual disabilities. In fact, the different actuators presented in this work are likely the first ones using LCE composites with photo-induced properties specifically designed for that application.

In the following, the main conclusions of this work are presented:

- The fundamentals involving the contraction phenomenon in LCE-CNT composites were studied in depth by means of several characterization techniques. Thus, it was possible to better understand their behavior and actuation mechanisms prior to the design and fabrication of the actuators. Standard characterization techniques in material science such as SEM and TEM imaging, X-ray diffraction analysis and DSC, combined with innovative experimental setups were successfully used for the first time "in-situ" observation of the contraction phenomenon of LCE-CNT materials under illumination. All these studies together with preliminary FEM investigations were then used as the basis for the later

Conclusions and Future work

developments of actuators towards an integrated tactile device based on such materials.

- The first actuator approach developed was achieved by using fully-crosslinked LCE-CNT films which, thanks to their configuration in "U-shape", allow the use of the stress gradient induced on them under illumination to exert vertical displacements on movable components. These actuators were characterized and successfully tested at various operation conditions to optimize their geometry, improving the design of their components to reach maximum forces while reducing the power consumption. Thanks to the collaborative work of the different partners of NOMS project, a first prototype of tactile device containing an array of 10 by 10 actuators was assembled, tested and lately evaluated by end users with successful results. The performance of the actuator was good allowing noiseless and wireless actuation, and providing enough forces and displacements to guarantee a correct tactile perception. But some issues were detected especially the variability on the actuation response, mainly due to difficulties on the LCE-CNT samples preparation and the manual assembly process of each actuator on the device. However, this development validated the use of such materials combined with the photo-actuation mechanisms towards a new generation of tactile devices.
- Two different strategies were investigated to simplify and make more affordable the samples preparation process keeping the premise of photo-actuation. Thus, LCE containing photosensitive dye molecules and EVA copolymer with embedded CNT were studied as alternative composites to LCE-CNT. In this way, various samples containing both types of materials were fabricated and characterized and their actuation compared to LCE-CNT. Investigations on EVA-CNT composites are still in preliminary stages but dye-doped LCE materials resulted to be potential candidates to replace LCE-CNT due to their excellent performance.
- Three different innovative and original methodologies were successfully developed with the main purpose of improving the response of previous "U-shape" actuators while reducing their variability in actuation caused by their

individual and manual assembly when integrated on a tactile device. Thus, taking advantage of the previous knowledge in MEMS design and processing and the results obtained during the extensive characterization of LCE-CNT composites, high-density arrays of actuators were obtained. All three approaches lie in the combination of molding techniques and the application of surface forces prior the final crosslinking of the material to shape it and reach sufficient alignment to assure proper actuation under the application of external stimulus.

Using both the first and the second methods, quasi-spherical dome-like actuators were obtained by the application of unidirectional stretching forces using a stamping process or the application of gas-pressure gradients respectively, which resulted in a final contraction of the material under illumination and thus, a decrease in the actuators height. Although strain values achieved by such actuators are still far from the minimum required for a correct tactile perception, these methods are very important as they reported for the first time the possibility of obtaining ordered arrays of LCE actuators within the same elastomeric matrix.

The latter method, also based on molding techniques first introduces the possibility of providing the material with a bidirectional alignment (a novel conformation of LCE materials at molecular level) to which an array of actuators in a pillar-like configuration with expansion movement was achieved, allowing the direct use of these pushing actuators as tactile elements without including additional components. The displacements produced and the magnitude of the force values achieved using this technique lay within the values of interest of tactile displays. However, actuators of a wide variety of shapes and sizes can be obtained by this technique with interests of wide broad of applications far from Braille.

- Finally, a very ambitious and challenging approach for the fabrication of a novel concept of tactile devices was posed based on the micropillar actuators previously developed: an hybrid system combining the light emitted by current displays and the direct heating of LCE material to induce tactile signal by means of phototransistors and arrays of thermoresistors. A first prototype was presented together with the preliminary results proving the viability of the system.

Conclusions and Future work

In summary, the work represent a significant advance towards the integration of smart elastomeric materials into MEMS/NEMS technology for the fabrication of new generation of actuators with varied and very interesting properties and opens new horizons for the development of different technologies based on these materials to be applied in the field of assisting technologies. This research has required the development of innovative fabrication techniques to simultaneously shape and align the LCE materials to provide arrays of microstructured actuators with sufficient photo-mechanical response to be correctly perceived by touching and thus reducing variability in actuation. The technological challenges are great since beside the difficulties in material preparation and handling, a high density of actuators with minimum pushing forces and vertical displacements are some of the requirements imposed by standards to represent Braille characters and ensure their correct tactile information.

Occasionally, the technological processes developed for the fabrication of arrays of actuators resulted in a decrease in the material performance mainly due to a reduction on the degree of alignment achieved, which will have to be addressed in a future optimization of the actuators. Nevertheless, the results obtained are very encouraging for future developments on tactile devices. Furthermore, it must be highlighted that the technology developed is of great interest for a great number of applications especially in microfluidics and biomedical applications and has established the basis for the integration of such materials into micro and nanosystems technology for future development of smart actuators actuated by visible light.

Ongoing and Future work

One of the most important aspects to cover in the near future is to consolidate the proposed technologies for the fabrication of arrays of nematic actuators, especially the micropillars, in order to improve their performance and get a reliable integration in i) the proposed tactile devices and ii) microsystems technology. For that, some research lines have been initiated following the research begun and described in this thesis. Some of them are commented below.

First of all, further research focused on improving the working principle and the whole design and components of the NOMS tactile device is under investigation to

provide an original and optimized prototype, combining the technical achievements with the novel approach introduced in the latter chapter of this thesis maintaining the multilayer concept device. In this sense, next research steps will focus on the search for alternative materials and techniques such as printed electronics, to provide an elegant and long-term solution fully compatible with most of tactile displays, laptops and screens on the market.

Secondly, and with the main objective to continue the research on alternative materials and composites to improve LCE-CNT performance while simplifying the preparation of the samples, other commercially available elastomeric matrices as alternative to EVA and LCE have started to be explored replacing CNTs by photo-sensitive dyes, since they have demonstrated to be suitable mechanisms to induce actuation at lower concentrations.

A third research line will benefit from the knowledge acquired on soft polymer characterization techniques and processing to combine photo-sensitive LCE materials with micro and nanofabrication techniques to develop novel actuators with different attributes at micro and nanoscale, able to be remotely actuated inside living systems. Taking advantage of their reversible contraction and expansion movements it is possible to induce mechanical reactions as well as deliver drugs locally. In this sense, first experiments for the fabrication of such systems have been started. In order to continue this research, a new research project proposal is under preparation.

Finally, the author hoped that this thesis will encourage other students and researchers to continue this research towards the development of innovative actuators to go a step further providing real alternative solutions to improve the communication tasks of blinds.

Conclusions and Future work

Appendix A

Tactile perception and Braille system

The aim of this appendix is to introduce the reader to the basic concepts related to tactile perception mechanisms and Braille code standards in order to better understand the design criteria followed for the design of the actuators introduced within this thesis (single actuators and the arrays), for their later integration as fully-functional Braille and tactile devices.

A.1 Basic tactile perception mechanisms

A.1.1 Mechanoreceptors

Touch or somatosensory, also called tactition or mechanoreception, is a perception resulting from activation of neural receptors, generally in the skin, due to stimuli (changes in internal or external environment) such as touch, cold, heat, pain, and pressure [243]. These mechanoreceptors respond to mechanical energy forces such as touch, pressure, stretching, and movement thanks to tactile perception through the skin, which is the largest organ in the body (it covers almost 2 m^2 in an average adult).

Ranging in complexity from free nerve endings beneath the skin to more complex tactile receptors at the bases of hair, there are different types of skin mechanoreceptors which can be classified following different criteria. Figure A.1 shows a schematic representation of the most representative mechanoreceptors in the skin, whereas Table A.1 summarizes their main characteristics.

A. TACTILE PERCEPTION AND BRAILLE SYSTEM

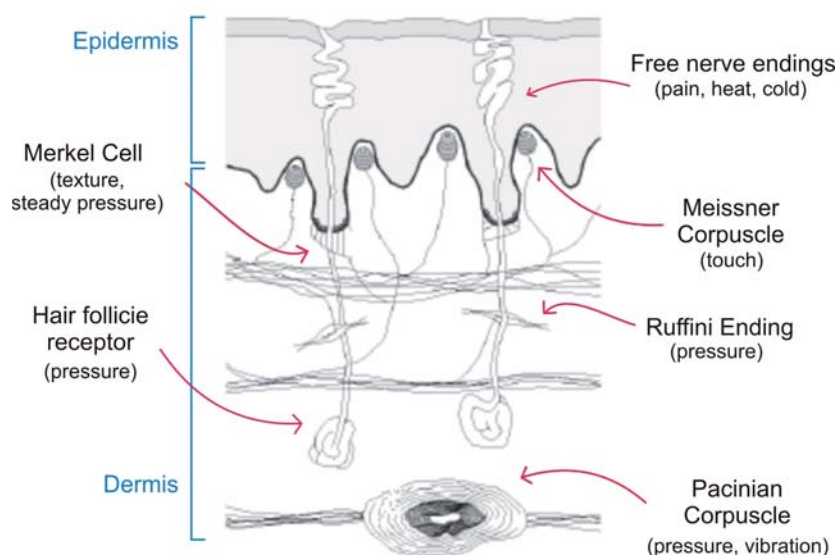


Figure A.1: Mechanoreceptors of glabrous skin. Adapted from [12, 244].

A.1.2 Haptic perception

Haptic perception is the process of recognizing objects through touch by the use of the mechanoreceptors. It involves a combination of somatosensory perception of patterns on the skin surface (e.g., edges, curvature, and texture), and proprioception of hand position and conformation [245]. With previous learning, people can rapidly and accurately identify three-dimensional objects by the use of exploratory procedures, such as moving the fingers over the outer surface of an object or holding the entire object in the hand [246, 247], as well as different types of materials through the information received by touch (comparing shape, roughness, weight, etc.).

From the time the skin is stimulated, a variety of complex mechanical, perceptual, and cognitive phenomena take place so as to perceive the information through touch. Under stimulation skin undergoes deformation which is projected to the different mechanoreceptors underneath its surface. Next, these receptors encode and transmit the stimulus to the central nervous system where it is processed, integrated and relayed to increasingly higher levels of brain processing for interpretation. Thanks to the information previously stored in our memory (from touch and the other senses) it is possible to identify the different elements we perceive. However, psychological factors such as attention and emotion can significantly vary the sensation perceived [12].

Table A.1: Tactile receptors in the Human skin. Table source: [248]

Skin Receptor Type	Receptor Class	Skin Type	Probable Sensory Correlation	Receptive Field, Range (and Median)	Frequency Range (and most sensitive)	# of Fingertip Receptor (and on Palm)
Pacinian corpuscles	PC	G,H	Vibration, tickle	10-1000 mm^2 (100 mm^2)	10-800 Hz (200-300 Hz)	21/ cm^2 (9/ cm^2)
Messiner's corpuscles	RA	G	Touch, tickle, motion, vibration	1-100 mm^2 (13 mm^2)	10-200 Hz (20-40 Hz)	140/ cm^2 (25/ cm^2)
Hair tactile nerve	RA	H	Touch, vibration	$\approx 0.01mm^2$	10-100 Hz (?)	10/ cm^2 200/ cm^2 (scalp)
Ruffins ending	SA II	G,H	Stretch, shear, tension (?)	10-500 mm^2 (60 mm^2)	7 Hz	49/ cm^2 (16/ cm^2)
Merkel's cells	SA I	G	Pressure, edge (?)	2-100 mm^2 (11 mm^2)	0.4-100 Hz (7 Hz)	70/ cm^2 (8/ cm^2)
Tactile disks	SA I	H	Pressure, edge (?)	3-50 mm^2	1-100 Hz (?) (1 n Hz) (?)	70/ cm^2 (?) (8/ cm^2)(?)

PC= Pacinian afferents; RA= rapidly-adapting afferents; SA II = slowly-adapting, large receptive field afferents; SA I = slowly-adapting, small receptive field mechanoreceptive afferents; G= glabrous (hairless) skin; H = hairy skin.

Young blind people, especially the born-blind ones, have the other senses (especially, touch and ear), together with the spatial orientation and representation abilities more developed than people without this disability to compensate them for the lack of visual information. Hence, with an appropriate learning process they can train the fingers (the mechanoreceptors on there) to improve their haptic perception mechanisms. This is the case of Braille [5].

A.2 Braille Standards

Braille code is the worldwide standardized codification system commonly used for blind and visually impaired people for reading, writing and getting access to information.

A. TACTILE PERCEPTION AND BRAILLE SYSTEM

A traditional Braille system consists in a six-dot based cell, two dots wide and three dots high, typically numbered 1, 2, 3 downward on the left and 4, 5, 6 downward on the right. By the combination of those six dots, also named as tactels, in a single cell, 64 different characters including the space can be obtained allowing the representation of not only letters but also numbers as well as specific digraph symbols from the different languages [22]. Figure A.2 summarizes the main dimensions and the geometric distribution of the tactels for a correct Braille representation which were followed in this thesis for the design of the actuators.

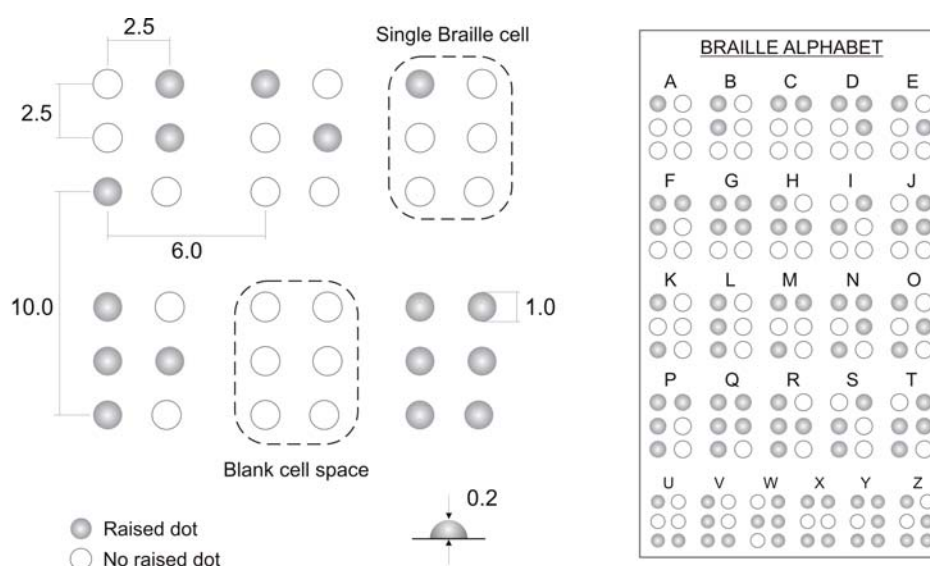


Figure A.2: Geometry and dimensions of Braille characters standards for six-dot Braille cells. All the measurements are in millimeters.

Although having nearly 200 years of existence, dimensions in Braille cells are not fully standardized, especially in tactel diameter and height [46] and the different Braille organisms in different countries have adapted the standards to their own language needs, resulting in significant differences between Braille charts between countries [5]. Figure A.2 -left- show the Spanish version of Braille alphabet chart based on six-dot Braille system as example of the characters formation. Therefore, the six-dot Braille system it not the only code used. Enterprising inventors, teachers and Braille users have sought to expand the possibilities of the Braille cell by increasing the number of tactels from six to eight, providing a more friendly system for specific applications such as music notation and the representation of mathematical equations, as well as to

encode new characters such as "@" [12]. These expansions have resulted in a cell that is two dots wide and four dots high resulting in up to 256 possible combinations.

All these multiple combinations and the parallel existence of different Braille standard codes increase the difficulties of visually impaired people to share and exchange Braille reading material. Moreover, there is a small amount of available Braille reading material (mainly in the field of education) and is very expensive, which is usually edited and provided by the same national associations of blinds.

Besides these language issues, the tactel dimensions and its minimum height needed to be properly perceived (0.2 mm), it is necessary to consider the degree of stiffness of the material in which Braille characters are printed (e.g., paper and plastic). Thus, the materials used for the fabrication of Braille tactels should be resistant to wear and stiff enough to ensure certain stability when users read them, and also have a touch-friendly surface for a more comfortable use. The most common force value produced by the fingers when tightening to ensure correct perception of tactels is in the range from 20 mN to 30 mN. However this value can be reduced up to 15 mN in the case of actuators, where the element in contact with the fingertip exerts a pushing force against it instead of a vibrotactile signal.

A. TACTILE PERCEPTION AND BRAILLE SYSTEM

Appendix B

Protection layer

In contrast with the other actuator approaches presented within this thesis, using the “U-shape” design the active LCE material has no direct contact with the environment, thus avoiding material degradation caused by dust and skin secretions. However, these elements can produce undesired effects during the actuators performance, even blockage of some pins due to a continuous usage. For these reasons, a protection film was introduced on top of the actuation layer at the latest stage of the assembly process.

To that end, preliminary qualitative tests with different flexible materials available on the market were performed resulting in several suitable candidates. However, there is a clearly trade-off between the robustness of any cover layer and the unimpeded functioning of the tactile device. Only the thinnest materials were suitable as protection layer since the thicker ones can reduce drastically the correct tactile perception of the tactile signal. Moreover, aspects such as the roughness and the ease to glide the fingers through them were also considered since it was very important to maintain a pleasant tactile perception to the end users. Thus, the opinion of two blind persons, Dr. Jordi Roig de Zárata and Dr. Branislav Mamojka as members of Organización Nacional de Ciegos Españoles (ONCE) and Únia nevidiacich a slabozrakých Slovenska: Úvodná stránka (UNSS) respectively, and at the same time, partners of the NOMS project, was taken into account.

The results of the evaluation of the most representative materials tested are shown in Table B.1.

In spite of the results, only a small number of very thin materials were pre-selected for further testing since most of them resulted to be too thick and were not available

B. PROTECTION LAYER

in thinner formats, thus reducing the possibilities only to silicone-based films among which Silex25 and Silex50 were the preferred ones. Ideally Silex25 was the best option since the resistance to deformation of a film is proportional to its section. However, it presents some difficulties in handling due to its reduced thickness.

Table B.1: Evaluation of protection films for the tactile display.

Film name	Material	Thickness [μm]	Hardness (HRC)	Tensile	Color	Touch	Comments
HT6240 W/256M	silicone	250	40	800	clear	not bad	too thick
HT6240 TRANS SIL No PSA	silicone	250	40	800	clear	ok	too thick
HT6220 LSR Sheet No PSA	silicone	250	20	800	black	not bad	too thick, need to be glued
HT6135 LSR Sheet No PSA	silicone	250	35	800	off-white	ok	too thick
Super clear sheet	silicone*	250	n/a	n/a	transparent	ok	too thick
COHR9235 W/256M	silicone**	380	30	1150	gray	bad	too thick, too rigid
PDMS200	Poly dimethyl- siloxane	200	n/a	n/a	transparent	not bad	too thick, too sticky
PMMA200	Poly methyl- metacrylate	200	n/a	n/a	transparent	ok	too thick, too rigid
Silex50	silicone	50	n/a	n/a	nearly transparent	ok	ok
Silex25	silicone	25	n/a	n/a	transparent	ok	ok

* Liquid silicone rubber; ** Gum Based Solid Silicone.

In the experimental characterization of the tactile device presented within this thesis (Chapter 4) the effects on the mechanical response of the actuators due to the incorporation of the protection layer were not taken into account since all the tests were carried out without the inclusion of such layer. Further investigation involving the selection and testing of the protection layer will be done as part of future work.

References

- [1] WORLD HEALTH ORGANIZATION WHO. [link]. 1
- [2] PERKINGS SCHOOL FOR THE BLIND. **The Next Generation of Perkins Brailers**. 1
- [3] B.L. MCGINNITY, J. SEYMOUR-FORD, AND K.J. ANDRIES. **Reading and Writing**, 2004. 1, 3
- [4] ONCE ORGANIZACIÓN NACIONAL DE CIEGOS ESPAÑOLES. **Catalog, BrailleDesk: An Eight-Dot Braille Keyboard**. 1
- [5] C. BONET-BORRÁS. **Braille The Pleasure of Reading: We Blind People Want to Continue Reading with Our Fingers**. *Eur. J. Inform. Prof.*, 5:77, 2004. 1, 3, 4, 247, 248
- [6] 33rd Applied Imagery Pattern Recognition Workshop (AIPR'04), Washington DC, USA. *Embedded reading device for blind people: user-centered design*, 2004. 1
- [7] C.A. LINDLEY. *Practical image processing in C: Acquisition, manipulation, storage*. Wiley Professional Computing. John Wiley & Sons, New York, USA, 1991. 1
- [8] SME Winter Annual Meeting, Symposium on Haptic Interfaces for Virtual Environment and Teleoperator System. *The PHANTOM haptic interface: a device for probing virtual objects*, 1994. 1
- [9] J.P. FRITZ AND K.E. BARNER. **Design of a haptic data visualization system for people with visual impairments**. *IEEE Trans. Rehabilitation Engineering*, 7:372, 1999. 1
- [10] P. PIETY. **Audio Description, A Visual Assistive Discourse: An Investigation into Language Used to Provide the Visually Disabled Access to Information in Electronic Texts**, 2003. 1, 2
- [11] ON THE BUS PROJECT. MASS FACTORY. [link]. 2
- [12] J PASQUERO. **Survey on Communication through touch**. Technical report, TR-CIRM, Centre for Intelligent Machines, McGill University, Canada, 2006. 2, 5, 8, 10, 246, 249
- [13] H.T. CHOI, I.M. KOO, K. JUNG, S. ROH, J.C. KOO, ET AL. *A Braille Display System for the Visually Disabled Using Polymer Based Soft Actuator*, Chap. 23 in *Biomedical applications of electroactive polymer actuators*. John Wiley & Sons, Ltd., 2009. 2, 8, 13
- [14] USA AMERICAN FOUNDATION FOR THE BLIND (AFB) NEW YORK. **Celebrating 200 Years of Braille. Monograph**. 3
- [15] J. BLISS, M. KATCHER, C. ROGERS, AND R. SHEPARD. **Optical-to-tactile image conversion for the blind**. *IEEE Transactions on Man-Machine Systems*, 11:58, 1970. 3
- [16] IEEE. *A Direct Translation Reading Aid for the Blind*, 54, 1966. 3
- [17] TIMERIME. [link]. 4
- [18] KG F.H. PAPANMEIER, GMBH & Co. [link]. 4
- [19] G. WEBER. **Braille displays**. *IT&D, e-Journal*, 1, 1994. 5
- [20] K. UCHINO. *Piezoelectric Actuators and Ultrasonic Motors*. Kluwer Academic Publishers, Norwell, MA, USA. John Wiley & Sons, New York, USA, 1997. 5
- [21] S.A. ARABSHAHI AND Z. JIANG. **Development of a tactile sensor for Braille pattern recognition: sensor design and simulation**. *Smart Mater. Struct.*, 14:1569, 2005. 5
- [22] ONCE ORGANIZACIÓN NACIONAL DE CIEGOS ESPAÑOLES. [link]. 5, 248
- [23] ONCE CIDAT. **Eco Plus 80, Users manual**, 2000. 5, 6
- [24] TRIUMPH TECHNOLOGY. [link]. 5, 6
- [25] J. PASQUERO, J. LUK, V. LEVESQUE, W. QI, V. HAYWARD, AND K.E. MACLEAN. **Haptically Enabled Handheld Information Display with Distributed Tactile Transducer**. *IEEE Trans. on Multimedia*, 9:746, 2007. 5, 8, 9
- [26] M. LANG, 2010. [link]. 5, 6
- [27] B. FRICKE AND H. BAEHRING. **Design of a tactile graphic I/O tablet and its integration into a personal computer system for blind users**. *J. Microcomputer Applications*, 16:259, 1993. 7, 8
- [28] NANO OTPO-MECHANICAL SYSTEMS NOMS PROJECT. [link]. 7, 10
- [29] HYPERBRAILLE. METEC AG. [link]. 7
- [30] D.G. CALDWELL, N. TSAGARAKIS, AND C. GIESLER. **An integrated tactile/shear feedback array for stimulation of finger mechanoreceptor**. page 287. OEEE international conference on Robotics and Automation, 1999. 8
- [31] S. INO, S. SHIMIZU, T. ODAGAWA, M. SATO, M. TAKAHASHI, T. IZUMI, AND T. IFUFUBE. **A tactile display for presenting quality of materials by changing the temperature of skin surface**. page 2200. IEEE International workshop on robot and human communication, 1993. 8
- [32] K. DREWING, M. FRITSCHI, R. ZOPF, M.O. ERNST, AND M BUSS. **First evaluation of a novel tactile display exerting shear force via lateral displacement**. *ACM transactions on Applied Perception*, 2:118, 2011. 8
- [33] I. SARAKOGLU, N. TSAGARAKIS, AND D.G. CALDWELL. **A portable fingertip tactile feedback array? Transmission system reliability and modelling**. page 547. First hoin eurohaptics conference and symposium on haptic interfaces for virtual environment and teleoperator systems, WHC'05, 2005. 8
- [34] P. WELLMAN, W. PEINE, G FAVALORA, AND R. HOWE. *Mechanical design and control of a high.bandwidth shape memory alloy tactile display*, 232 of *Lecture Notes in control and information science*. Springer Verlag, 1998. 8
- [35] P.M. TAYLOR, A. HOSSEINI-SIANAKI, AND C.J. VARLEY. **An Electrorheological Fluid-based Tactile Array for Virtual Environments**, 1996. 8
- [36] A. BICCHI, E.P. SCILINGO, N. SGAMBELLURI, AND D. DE ROSSI. **Haptic interfaces based on magnetorheological fluids**. page 6. Eurohaptics, 2002. 8

REFERENCES

- [37] T.H. YANG, H.J. KWON, S.S. LEE, J. AN, J.H. KOO, ET AL. **Development of a miniature tunable stiffness display using MR fluids for haptic application.** *Sens. Actuat. A - Phys*, **163**:180, 2010. 8, 9
- [38] Y. BAR-COHEN. **Dynamic Braille**, 2009. 8, 13
- [39] N. MALUF AND K. WILLIAMS. *An introduction to microelectromechanical systems engineering, 2n edition*. Artech House, 2003. 8
- [40] M. SHINOHARA, Y. SHIMIZU, AND A. MOCHIZUKI. **Three-dimensional tactile display for the blind.** *IEEE Trans. Rehab. Eng.*, **6**, 1998. 8
- [41] M. BENALI-KHOUDJA, M. HAFEZ, AND A. KHEDDAR. **VITAL: An electromagnetic integrated tactile display.** *Displays*, **28**:1333, 2007. 8, 9
- [42] Y. HAGA, W. MAKISHI, K. IWAMI, K. TOTSU, K. NAKAMURA, AND M. WSASHI. **Dynamic Braille display using SMA coil actuator and magnetic latch.** *Sens. Actuat. A - Phys*, **119**:316, 2005. 8
- [43] DCIS. *Thermopneumatic actuator for tactile displays*, 2003. 8
- [44] W. GU, H. CHEN, Y.C. TUNG, ET AL. **Multiplexed hydraulic valve actuation using ionic filled soft channels and Braille displays.** *Appl. Phys. Lett.*, **90**:033505-1, 2007. 8, 12
- [45] J.J. KWON, S.W. LEE, AND S.S. LEE. **Braille dot display module with a PDMS membrane driven by a thermopneumatic actuator.** *Sens. Actuat. A - Phys*, **154**:238, 2009. 8
- [46] J.S. LEE AND S.J. LUCYSZYN. **A Micromachined Refreshable Braille Cell.** *Microelectromechanical Systems*, **14**(4):673, 2005. 8, 199, 248
- [47] Smart Structures and Materials. **Electroactive Polymer Actuators and Devices(EAPAD) SPIE. Braille display device using soft actuator**, **5385**, 2004. 9
- [48] N. TORRAS, K.E. ZINOVIEV, C.J. CAMARGO, E.M. CAMPO, H. CAMPANELLA, J. ESTEVE, ET AL. **Tactile device based on opto-mechanical actuation of liquid crystal elastomers.** *Sensor Actuat. A: Phys*, **208**:104, 2014. 9, 10, 11, 14, 90, 131, 197, 199
- [49] L. YOBAS, T. SEKITANI, M. TAKAMIYA, M. DOI, K. ASAKA, ET AL. **Sheet-type Braille Displays by integrating Organic Field-Effect transistors and polymeric actuators.** *IEEE Trans. Electron Devices*, **54**:202, 2007. 10, 12, 13
- [50] SPIE, EAPAD Conference, Vol. 7287. *Tactile Display with Dielectric Multilayer Elastomer Actuators*, 2009. 10, 12
- [51] M. UBERLE, N. MOCK, AND M. BUSS. **VISHARD10, a novel hyper-redundant haptic interface.** IEEE International symposium on haptic interfaces for virtual environment and Teleoperator systems, HAPTICS'04, 2004. 10
- [52] ASSISTING PERSONAL GUIDANCE SYSTEM FOR PEOPLE WITH VISUAL IMPAIRMENT ARGUS PROJECT. [link]. 10
- [53] AUDIO DESCRIPTION: LIFELONG ACCESS FOR THE BLIND ADLAB PROJECT. [link]. 10
- [54] PERSONAL ASSISTIVE DEVICE FOR BLINDS BLINDPAD PROJECT AND VISUALLY IMPAIRED PEOPLE. [link]. 10
- [55] USA MICROSOFT CORPORATION. REDMON. **Light-induced shape-memory polymer display screen**, 2009. 10
- [56] USA APPLE CORPORATION. CUPERTINO, CA. **Incredible Shape Shifting Device Interface**, 2010. 10
- [57] ANDREW MITCHELL. **SAMSUNG "Touch Messenger" Braille Mobile Phone**, 2006. 11
- [58] SIWEI LIU. **Tactility Toshiba Mobile Phone**, 2009. 11
- [59] ANDREW MITCHELL. **Squibble Portable Braille interface**, 2009. 11
- [60] SUMIT DAGAR. **Touchscreen Braille Phone**, 2011. 11
- [61] J. D' ALESSANDRO. AUBURN UNIVERSITY. **Omnifer case**, 2011. 11
- [62] SHIKUN SUN. SHEFFIELD HALLAM UNIVERSITY. **Drawbraille Mobile Phone**, 2012. 11
- [63] A. LENDLEIN, M. BEHL, S.A. MADBOULY, K. KRATS, M. HEUCHEL, ET AL. *Shape-memory polymers*. Springer-Verlad, Berlin Heidelberg, 2010. 12
- [64] M. WARNER AND E.M. TARENTJEV. *Liquid Crystal Elastomers*. Oxford University Press: Oxford, UK, 2007. 12, 14, 22, 23, 28, 32, 33, 52, 59
- [65] Y. BAR-COHEN. *Electroactive polymer (EAP) actuators as artificial muscles: reality, potential and challenges*. SPIE Press Book, USA (PM136), 2004. 12, 37
- [66] E. SMELA. **Conjugated polymer actuators.** *MRS Bull.*, **33**:197, 2008. 12
- [67] R.H. BAUGHMAN. **Conducting polymer artificial muscles.** *Synthetic Metals*, **78**:339, 1996. 12
- [68] R.H. BAUGHMAN AND T. MIRFAKHRAI. **Polymer artificial muscles.** *Materials today*, **10**:30, 2007. 12
- [69] Electroactive Polymer Actuators and Devices(EAPAD) SPIE. *Refreshable tactile displays based on bistable electroactive polymer*, **7976**, 2011. 12, 14
- [70] Smart Structures and Materials. **Electroactive Polymer Actuators and Devices(EAPAD) SPIE. Novel multilayer electrostatic solid state actuators with elastic dielectric**, **5759**, 2005. 12
- [71] Electroactive Polymer Actuators and Devices(EAPAD) SPIE. *Application of EAP materials toward a refreshable Braille display*, **7287**, 2009. 12
- [72] P. BROCHU AND Q. PEI. **Advances in dielectric elastomers for actuators and artificial muscles.** *Macromol. Rapid. Commun.*, **31**:10, 2010. 12
- [73] Electroactive Polymer Actuators and Devices(EAPAD) SPIE. *PVDF core-free actuator for Braille displays: design, fabrication process, and testing*, **7976**, 2011. 12
- [74] Y. BAR-COHEN. **Active Reading Display for Blind (ARDIB), New Technology Report.** Technical report, 2001. 12
- [75] R. HEYDT AND S. CHHOKAR. **Refreshable Braille display based on electroactive polymers**, 2003. 12, 13
- [76] Y. BAR-COHEN, M.M. TREXLER, R.M. DEACON, K.A. POTTER, D.W. LEE, ET AL. *Biomimetics - Nature-based Innovation*. CRC Press, Boca Raton, FL, 2012. 12, 13
- [77] J.W. GOODYBY. *Handbook of Liquid Crystals Set*. Wiley-VCH, Weinheim, 1998. 14, 29
- [78] H. FINKELMANN. *Thermotropic liquid crystals*. John Wiley & Sons: UK, 1987. 14, 23
- [79] P.G. DE GENNES. **A semi-fast artificial muscle.** *C. R. Acad. Sci. Ser. IIb: Mec.*, **324**:343, 1997. 14, 29, 87

- [80] P.G. DE GENNES, M. HEBERT, AND R. KANT. **Artificial muscles based on nematic gels.** *Macromol. Symp.*, **113**:39, 1997. 14, 29
- [81] J.E. MARSHALL, Y. JI, N. TORRAS, K. ZINOVIEV, AND E.M. TERENTJEV. **Carbon-nanotube sensitized nematic elastomer composites for IR-visible photo-actuation.** *Soft Mater.*, **8**:1570, 2012. 14, 35, 37, 38, 39, 40, 52, 55, 72, 73, 106, 138, 142, 193
- [82] H. FINKELMANN, A. GREVE, AND M. WÄRNER. **The elastic anisotropy of nematic elastomers.** *Eur. Phys. J. E; Soft Matter Biol. Phys.*, **5**:281, 2001. 14, 32, 40, 204
- [83] S.M. KELLY AND M. O'NEILL. **Liquid crystals, displays and laser materials.** In *Handbook of advanced electronic and photonic materials and devices*. Clarendon Press: Oxford, UK, 2000. 14, 29
- [84] T.T. LARSEN, A. BJARKLEV, D.S. HERMANN, AND J. BROENG. **Optical devices based on liquid crystal photonic bandgap fibers.** *Opt. Express*, **11**:2589, 2003. 14, 29
- [85] J. KÜPPER AND H. FINKELMANN. **Nematic liquid single crystal elastomers.** *Makromol. Chem. Rapid Commun.*, **12**:717, 1991. 14, 25, 27, 32, 40, 41, 88, 138, 204
- [86] W.H. DE JEU, C. OHM, M. BREHMER, R. ZENTEL, AND ET AL. **Applications of Liquid Crystalline Elastomers, in Liquid Crystal Elastomers: materials and applications.** **250** of *Advances in polymer science*. Springer Verlag, Berlin Heidelberg, 2012. 14
- [87] C. OHM, M. BREHMER, AND R. ZENTEL. **Liquid Crystalline Elastomers as Actuators and Sensors.** *Adv. Mater.*, **22**:3366, 2010. 22, 24, 29, 87
- [88] F. REINITZER. **Beiträge zur Kenntnis des Cholesterins.** *Wien. Monatsch. Chem.*, **9**:421, 1888. 22
- [89] O. LEHMANN. **Zeitschrift für physikalische Chemie.** *Phys. Chem.*, **4**:462, 1889. 22
- [90] P.G. DE GENNES. **The Physics of Liquid Crystals (2nd edition 1993).** Oxford University Press: Oxford, UK, 1974. 22, 87
- [91] P.G. DE GENNES. **Soft material (Nobel lecture).** *Angew. Chem.*, **104**:856, 1992. 22
- [92] P.G. DE GENNES. **Soft material (Nobel lecture).** *Angew. Chem. Int. Ed. Engl.*, **31**:842, 1992. 22
- [93] H. IWAI, J. FUKASAWA, AND T. SUZUKI. **A liquid crystal application in skin care cosmetics.** *Int. J. Cosmet. Sci.*, **20**(2):87, 1998. 22
- [94] M. SHLENS, M.R. STOLTZ, AND A. BENJAMIN. **Orthopedic applications of liquid crystal thermography.** *West J. Med.*, **122**:367, 1975. 22
- [95] Y. YU AND T. IKEDA. **Photodeformable Polymers: A New Kind of Promising Smart Material for Micro- and Nano-Applications.** *Macromol. Chem. Phys.*, **206**:1705, 2005. 22
- [96] M. SCHATZ. **Voltage-dependent optical activity of a twisted nematic liquid crystal.** *Appl. Phys. Lett.*, **18**:127, 1971. 22
- [97] ANTONI SÁNCHEZ-FERRER. **PhotoActive Liquid-Crystalline Elastomers.** PhD thesis, Universitat de Barcelona, Spain, 2011. 23, 29, 32, 41
- [98] B. MOSSETY-LESZCZAK AND M. WŁODARSKA. **Liquid Crystalline Organic Compounds and Polymers as Materials of the XXI Century: From Synthesis to Applications.** Transworld Research Network: Kerala, India, 2011. 23, 28, 29
- [99] H. FINKELMANN, H. RINGSDORF, AND J.H. WENDORFF. **Liquid-crystalline main-chain elastomers.** *Makromol. Chem.*, **179**:273, 1978. 23
- [100] J. GARCIA-AMORÓS, D. VELASCO, ET AL. **Polysiloxane side-chain azobenzene-containing liquid single crystal elastomers for photo-active artificial muscle-Like actuators.** In *Advanced elastomers - technology, properties and applications*. Intech Publishing group, 2012. 23, 25, 35
- [101] E.K. FLEISCHMANN, H.L. LIANG, N. KAPERNAUM, F. GIESSELMANN, J. LAGERWALL, AND R. ZENTEL. **One-piece micropumps from liquid crystalline core-shell particles.** *Nat. Commun.*, **3**:1178/2193, 2012. 24
- [102] **Nematic liquid crystal elastomers as artificial muscle materials,** 2003. 25
- [103] T. IKEDA, J.I. MAMIYA, AND Y. YU. **Photomechanics of liquid-crystalline elastomers and other polymers.** *Angew. Chem. Int. Ed.*, **46**:506, 2007. 25, 28, 29
- [104] H. YU AND T. IKEDA. **Photocontrollable Liquid-crystalline actuators.** *Adv. Matter.*, **23**:2149, 2011. 25, 65
- [105] H. YANG, G. YE, X. WANG, AND P. KELLER. **Micron-sized liquid crystalline elastomer actuators.** *Soft Matter*, **7**(3):815, 2011. 25, 199
- [106] D.J. BROER, J. LUB, AND G.N. MOL. **Synthesis and photopolymerization of a liquid-crystalline diepoxide.** *Macromolecules*, **26**:1244, 1993. 25
- [107] W. MORMANN, C. KICKERTZ, AND M. BRÖCHER. **Liquid Crystalline Organisation and Reaction Rate in the Formation of Liquid Crystal Thermoset Networks from Diepoxides and Dicyanates.** *Macromol. Symp.*, **90**:70, 2010. 25
- [108] M.A. ESPINOSA, V. CÁDIZ, AND M. GALIÁ. **Cholesteric liquid-crystal epoxy resins derived from 6-hydroxy-2-naphthoic acid.** *J. Polym. Sci. Part A: Plum. Chem.*, **39**(16):2847, 2001. 25
- [109] G.H.F. BERGMANN, H. FINKELMANN, V. PERCEC, AND M. ZHAO. **Liquid-crystalline main-chain elastomers.** *Macromol. Rapid Commun.*, **18**:353, 1997. 25, 52
- [110] A.R. TAJBAKHSH AND E.M. TERENTJEV. **Spontaneous thermal expansion of nematic elastomers.** *Eur. Phys. J. E*, **6**:181, 2001. 25, 32, 33, 40, 52
- [111] E. K. FLEISCHMANN AND R. ZENTEL. **Liquid-Crystalline Ordering as a concept in materials science: from semiconductors to stimuli-responsive devices.** *Angew. Chem. Int. Ed.*, **52**:8810, 2013. 26, 29
- [112] A. BUGUIN, M.H. LI, P. SILBERZAN, B. LADOUX, AND P. KELLER. **Micro-Actuators: When Artificial Muscles Made of Nematic Liquid Crystal Elastomers Meet Soft Lithography.** *Journal of American Chemical Society*, **128**:1088, 2006. 26, 89, 199
- [113] C.L. VAN OOSTEN, C.W.M. BASTIAANSEN, AND D.J. BROER. **Printed artificial cilia from liquid-crystal network actuators modularly driven by light.** *Nat. Mater.*, **8**:677, 2009. 26
- [114] C. OHM, C. SERRA, AND R. ZENTEL. **A continuous flow synthesis of micrometer-sized actuators from liquid crystalline elastomers.** *Adv. Mater.*, **21**:4859, 2009. 26
- [115] C. SERRA, N. BERTON, M. POUQUEY, L. PRAT, AND G. HADZIOANNOU. **Predictive Approach of the Influence of the Operating Parameters on the Size of Polymer Particles Synthesized in a Simplified Microfluidic System.** *Langmuir*, **23**:7745, 2007. 26, 31
- [116] S. KRAUSE, J.H. DERSCH, R. AN WENDORFF, AND H. FINKELMANN. **Photocrosslinkable Liquid Crystal Main-Chain Polymers: Thin Films and Electrospinning.** *Macromol. Rapid Commun.*, **28**:2062, 2007. 27, 88

REFERENCES

- [117] J. KÜPPER AND H. FINKELMANN. **Liquid crystal elastomers: influence of the orientational distribution of the crosslinks on the phase behaviour and reorientation processes.** *Makromol. Chem. Phys.*, **195**:1353, 1994. 28, 204
- [118] P.G. DE GENNES. **Physique Moleculaire.** *C. R. Acad. Sci. Series B*, **281**:101, 1975. 29, 32, 87
- [119] H. FINKELMANN, H.J. HOCK, AND G. REHAGE. **Investigations on liquid crystalline polysiloxanes 3. Liquid crystalline elastomers - a new type of liquid crystalline material.** *Makromol. Chem. Rapid Commun.*, **2**:317, 1981. 29
- [120] A. SÁNCHEZ-FERRER AND H. FINKELMANN. **Uniaxial and shear deformation in liquid-crystalline elastomers.** *Mol. Cryst. Liq. Cryst.*, **508**:348, 2009. 29
- [121] J. ESTEVE, E.M. TERENTJEV, AND E.M. CAMPO, editors. *Light-induced disorder in liquid-crystalline elastomers for actuation*, **8107**. SPIE, NOMS Conference, 2011. 29
- [122] P.J. COLLINGS AND M. HIRD. *Introduction to liquid crystals: chemistry and physics.* Taylor and Francis Ltd.: Bristol, UK, 1997. 29
- [123] P.J. COLLINGS. *Liquid crystals. Nature's delicate phase of matter.* Princeton University Press: New Jersey, USA, 2002. 29
- [124] P. XIE AND R.B. ZHANG. **Liquid crystal elastomers, networks and gels: advanced smart materials.** *J. Mater. Chem.*, **15**(26):2529, 2005. 29
- [125] H. REN, D.W. FOX, B. WU, AND S.T. WU. **Liquid crystal lens with large focal length tunability and low operating voltage.** *Optics express*, **15**(18):11328, 2007. 29
- [126] H. JIANG, C. LI, AND X. HUANG. **Actuators based on liquid crystalline elastomer materials.** *Nanoscale*, **5**:5225, 2013. 29
- [127] F. CHENG, R. YIN, Y. ZHANG, C.C. YEN, AND Y. YU. **Fully plastic microrobots which manipulate objects using only visible light.** *Soft Mater*, **6**:3447, 2010. 29, 30
- [128] A. SÁNCHEZ-FERRER, T. FISCHL, M. STUBENRAUCH, A. ALBRECHT, H. WURMUS, M. HOFFMANN, AND H. FINKELMANN. **Liquid-Crystalline Elastomer microvalve for microfluidics.** *Adv. Mater.*, **23**:4526, 2011. 30, 88, 89
- [129] M. CHEN, X. XING, Z. LIU, Y. ZHU, H. LIU, Y. YU, AND F. CHENG. **Photodeformable polymer material: towards light-driven micropump applications.** *Appl Phys A*, **100**:39, 2010. 30
- [130] A. SÁNCHEZ-FERRER, T. FISCHL, M. STUBENRAUCH, H. WURMUS, M. HOFFMANN, AND H. FINKELMANN. **Photo-crosslinked side-chain liquid-crystalline elastomers for microsystems.** *Macromol. Chem. Phys.*, **210**:1671, 2009. 30, 88, 89
- [131] M. YAMADA, M. KONDO, J. MAMIYA, Y. YU, M. KINOSHITA, C.J. BARRET, AND T. IKEDA. **Photomobile polymer materials: towards light-driven plastic motors.** *Angew. Chem. Int. Ed.*, **47**:4986, 2008. 30, 88, 89
- [132] J.W. JUDY. **Microelectromechanical systems (MEMS): fabrication, design and applications.** *Smart Mater. Struct.*, **10**:1115, 2001. 31, 163
- [133] A. MERLOS, M. ACERO, M.H. BAO, J. BAUSELLS, AND J. ESTEVE. **TMAH/IPA anisotropic etching characteristics.** *Sensors and Actuat. A-Phys*, **37**:737, 1993. 31, 163
- [134] C. OHM, N. HABERKORN, P. THEATO, AND R. ZENTEL. **Template-Based Fabrication of Nanometer-Scaled Actuators from Liquid-Crystalline Elastomers.** *Small*, **7**:194, 2011. 31
- [135] E.K. FLEISCHMANN, H.L. LIANG, N. KAPERNAUM, F. GIESSELMANN, J. LAGERWALL, AND R. ZENTEL. **One-piece micropumps from liquid crystalline core-shell particles.** *Macromol. Rapid. Commun.*, **2**:1178, 2012. 31
- [136] A. SÁNCHEZ-FERRER, N. TORRAS, AND J. ESTEVE. **Integration of Liquid-Crystalline Elastomers in MEMS/MEOMS, in Liquid Crystalline Polymers: Structure and Chemistry.** **31**, 87, 163
- [137] IEEE 27th International Conference on Micro Electro Mechanical Systems (MEMS). *Thermotropic liquid crystal elastomer micro-actuator with integrated deformable micro-heater*, 2014. 31, 236
- [138] C. LI, Y. LIU, X. HUANG, AND JIANG H. **Direct sun-driven artificial heliotropism for solar energy harvesting based on a photo-thermomechanical liquid-crystal elastomer composite.** *Adv. Funct. Mater.*, **22**:5166, 2012. 31, 88, 89
- [139] N. LI, Y. LI, AND X. WANG. **Photoresponsive submicron-sized hollow spheres obtained from amphiphilic azobenzene-containing random copolymer.** *Polymer*, **53**:3975, 2012. 31
- [140] R. WEI, Y. HE, X. WANG, AND P. KELLER. **Nematic Liquid Crystalline Elastomer Grating and Microwire Fabricated by Micro-Molding in Capillaries.** *Macromol. Rapid Commun.*, **34**:330, 2013. 31
- [141] M. STEINHART, S. ZIMMERMANN, P. GÖRING, A.K. SCHAPER, ET AL. **Liquid crystalline nanowires in porous alumina: geometric confinement versus influence of pore walls.** *Nano Lett.*, **5**:429, 2005. 31
- [142] P.G. DE GENNES. **Nematic liquid crystals.** *J. Phys. Colloq.*, **5**:3, 1971. 32, 87
- [143] D.L. THOMSEN, P. KELLER, J. NACIRI, R. PINK, H. JEON, D. SHENOY, AND B.R. RATNA. **Liquid Crystal Elastomers with Mechanical Properties of a Muscle.** *Macromol.*, **34**(17):5868, 2001. 32, 40, 52
- [144] M. CAMACHO-LOPEZ, H. FINKELMANN, P. PALFFY-MUHORAY, AND M. SHELLEY. **Fast liquid-crystal elastomer swims into the dark.** *Nat. Mater. Lett.*, **3**:101038, 2004. 34, 40, 56
- [145] A. SÁNCHEZ-FERRER, A. MEREKALOV, AND FINKELMANN H. **Opto-Mechanical Effect in Photoactive Nematic Side-Chain Liquid-Crystalline Elastomers.** *Macromol. Rapid Commun.*, **32**:672, 2011. 34, 210
- [146] H. FINKELMANN, U. KIECHLE, AND G. RHAGE. **Behavior of Liquid Crystalline Side Chain Polymers in an Electric Field.** *Mol. Cryst. Liq. Cryst.*, **94**:343, 1983. 34, 204
- [147] E. GEBHARD AND R. ZENTEL. **Ferroelectric liquid crystalline elastomers 1. Variation of networks topology and orientation.** *Macromol. Chem. Phys.*, **201**:902, 2000. 34, 38
- [148] M. WINKLER, A. KAISER, S. KRAUSE, H. FINKELMANN, AND A.M. SCHMIDT. **Liquid crystal elastomers with magnetic actuation.** *Macromol. Symp.*, **291-292**:186, 2010. 34, 37, 38
- [149] K.D. HARRIS, C.W.M. BASTIAANSEN, J. LUB, AND D.J. BROER. **Self-assembles polymer films for controlled agent-driven motion.** *Nano Lett.*, **5**:1857, 2005. 34
- [150] H. FINKELMANN, E. NISHIKAWA, G.G. PEREIRA, AND M. WARNER. **A New Opto-Mechanical Effect in Solids.** *Phys. Rev. Lett.*, **87**:134302, 2001. 35, 40, 52, 77, 136

- [151] J.E. MARSHALL AND E.M. TERENTJEV. **Photo-Sensitivity of dye-doped liquid crystal elastomers.** *Soft Matter*, 9:8547, 2013. 35, 37, 136, 138, 142, 145
- [152] Y. YU, M. NAKANO, AND T. IKEDA. **Photomechanics: direct bending of a polymer film by light.** *Nature*, 425:6954, 2003. 35, 40
- [153] S.V. SERAK, N.V. TABIRYAN, T.J. WHITE, AND T.J. BUNNING. **Azobenzene liquid crystal polymer-based membrane and cantilever optical systems.** *Optics Express*, 17:15736, 2009. 35, 56
- [154] C.L.M. HARVEY AND E.M. TERENTJEV. **Role of polarization and alignment in photoactuation of nematic elastomers.** *Eur. Phys. J.E.*, 23:185, 2007. 35
- [155] K.G. YAGER, C.J. BARRETT, Z. YUE, T. IKEDA, ET AL. *Smart light-responsive materials: azobenzene-containing polymers and liquid crystals.* Wiley, 2009. 35, 40, 136
- [156] J. GARCIA-AMORÓS, H. FINKELMANN, AND D. VELASCO. **Role of the local order on the thermal cis-to-trans isomerisation kinetics of azo-dyes in nematic liquid crystals.** *J. Mater. Chem.*, 21:1094, 2011. 35
- [157] C.L. VAN OOSTEN, D. CORBETT, D. DAVIES, M. WARNER, C.W.M. BASTIAANSEN, AND D.J. BROER. **Bending dynamics and directionality reversal in liquid crystal network photoactuators.** *Macromolecules*, 41:8592, 2008. 35, 40
- [158] J. CVIKLINSKI, A.R. TAJBAKHSH, AND E.M. TERENTJEV. **UV-isomerisation in nematic elastomers as a route to photo-mechanical transducer.** *Phys. Rev. E*, 9:427, 2002. 35
- [159] H. RAU. *Photoisomerization of Azobenzenes.* In *Photochemistry and Photophysics*. CRC Press: Boca Raton, FL, USA, 1990. 35
- [160] Y. JI, J.E. MARSHALL, AND E.M. TERENTJEV. **Nanoparticle-liquid crystalline elastomers composites.** *Polymers*, 4:316, 2012. 37, 39
- [161] V. DOMENICI, M. CONRADI, M. REMŠKAR, M. VIRŠEK, B. ZUPANČIČ, ET AL. **New composite films based on MoO_3-x nanowires aligned in single crystal elastomer matrix.** *J. Mater. Sci.*, 46:3639, 2011. 37
- [162] A. KAISER, M. WINKLER, S. KRAUSE, H. FINKELMANN, AND A.M. SCHMIDT. **Magnetoactive liquid crystal elastomer nanocomposites.** *J. Mater. Chem.*, 19:538, 2009. 37
- [163] S. COUNTRY, J. MINE, A.R. TAJBAKHSH, AND E.M. TERENTJEV. **Nematic elastomers with aligned carbon nanotubes; new electromechanical actuators.** *Europhys. Lett.*, 64:654, 2003. 37
- [164] J.M. HABERL, A. SÁNCHEZ-FERRER, A.M. MIHUT, H. DIETSCH, A. HIRT, AND R. MEZZENGA. **Strain-induced macroscopic magnetic anisotropy from Smectic Liquid-crystalline elastomer-maghemite nanoparticle hybrid nanocomposite.** *Adv. Mater.*, 25:1787, 2013. 37
- [165] M. CHAMBERS, H. FINKELMANN, M. REMKAR, A. SÁNCHEZ-FERRER, B. ZALAR, AND S. ZUMER. **Liquid crystal elastomer-nanoparticle systems for actuation.** *J. Mater. Chem.*, 19:1524, 2009. 37, 222
- [166] P.M. AJAYAN, M. TERRONES, A. DE LA GUARDIA, V. HUC, N. GROBERT, ET AL. **nanotubes in a Flash-ignition and reconstruction.** *Science*, 296:705, 2002. 38, 53, 77
- [167] P.M. HOGAN, A.R. TAJBAKHSH, AND E.M. TERENTJEV. **UV manipulation of order and macroscopic shape in nematic elastomers.** *Phys. Rev. E*, 65:041720, 2002. 38, 40, 77
- [168] C. LI, Y. LIU, C. LO, AND H. JIANG. **Reversible white-light actuation of carbon nanotube incorporated liquid crystalline elastomer nanocomposites.** *Soft Mater.*, 22:5166, 2012. 38, 39, 40
- [169] S. CANTOURNET, M.C. BOYCE, AND A.H. TSOU. **Micromechanics and macromechanics of carbon nanotube-enhanced elastomers.** *J. Mech. Phys. Solids*, 55:1321, 2007. 38, 75
- [170] N. TORRAS, K.E. ZINOVIEV, J.E. MARSHALL, E.M. TERENTJEV, AND J. ESTEVE. **Bending kinetics of a photo-actuating nematic elastomer cantilever.** *Appl. Phys. Lett.*, 99:254102, 2011. 38, 39, 40, 80, 111, 193
- [171] J. ESTEVE, E.M. TERENTJEV, AND E.M. CAMPO, editors. *Opto-mechanical parameters of Liquid Crystals elastomers with carbon nanotubes*, 8107. SPIE, NOMS Conference, 2011. 38, 40, 193
- [172] M. MONTHIUX AND V.L. KUZNETSOV. **Who should be given the credit for the discovery of carbon nanotubes?** *Carbon*, 44:1621, 2006. 38
- [173] S. IJIMA. **Helical microtubes of graphitic carbon.** *Nature*, 354:56, 1991. 38
- [174] K.K. HON, D. CORBETT, AND E.M. TERENTJEV. **Thermal diffusion and bending kinetics in nematic elastomer cantilever.** *Eur. Phys. J. E*, 25:83, 2008. 39, 56, 80
- [175] M. WARNER AND L. MAHADEVAN. **Photoinduced deformations of beams, plates and films.** *Phys. Rev. Lett.*, 92:134302, 2004. 39, 56
- [176] A. KIOSHIO, M. YUDASAKA, M. ZHANG, AND S. IJIMA. **A simple way to chemically react single-wall carbon nanotubes with organic materials using ultrasonication.** *Nano Lett.*, 1:361, 2001. 39
- [177] J.I. PAREDES AND M. BURGHARD. **Dispersion of individual single-walled carbon nanotubes of high length.** *Langmuir*, 20:5149, 2004. 39
- [178] Y.Y. HUANG AND E.M. TERENTJEV. **Tailoring electrical properties of carbon nanotube-polymer composites.** *Adv. Funct. Mater.*, 20:4062, 2010. 39
- [179] Y. JI, Y.Y. HUANG, R. RUNGSAWANG, AND E.M. TERENTJEV. **Dispersion and Alignment of Carbon Nanotubes in Liquid Crystalline Polymers and Elastomers.** *Adv. Mater.*, 22:3436, 2010. 39, 42, 47, 193
- [180] Y. JI, Y.Y. HUANG, A.R. TAJBAKHSH, AND E.M. TERENTJEV. **Polysiloxane surfactants for the dispersion of carbon nanotubes in nonpolar organic solvents.** *Langmuir*, 25:12325, 2009. 39
- [181] A.V. AHIR, Y.Y. HUANG, AND E.M. TERENTJEV. **Polymers with aligned carbon nanotubes: active composite materials.** *Polymer*, 49:3841, 2008. 42
- [182] J.J. BOZZOLA AND L.D. RUSSELL. *Electron microscopy, (2nd edition)*. Jones & Bartlett publisher: Massachusetts, USA, 1998. 46
- [183] R.F. EGERTON, P. LI, AND M. MALAC. **Radiation damage in the TEM and SEM.** *Micron*, 35:399, 2004. 46
- [184] M.T. POSTEK, D.E. NEWBURY, S.F. PLATEK, D.C. JOY, AND T.K. MAUGEL, editors. *Study of LCE nanocomposites through electron microscopy*, 8036. SPIE, NOMS Conference, 2011. 47, 179, 180
- [185] L. GIANUZZI, F. STEVIE, B.I. PRENITZER, P.E. RUSSELL, B. HOLDFORD, B.W. KEMPHALL, ET AL. *Introduction to focused ion beams.* Springer: NY, USA, 2005. 48
- [186] K.A. BURKE AND P.T. MATHER. **Soft Shape Memory in Main-Chain Liquid Crystalline Elastomers.** *J. Mater. Chem.*, 20:3449, 2010. 52
- [187] J.H. LIENHARD IV AND J.H. LIENHARD V. *A Heat transfer textbook (4th edition)*. Phlogiston Press: Cambridge, Massachusetts, USA, 2008. 59

REFERENCES

- [188] WANTING REN. *Structure-property relations in siloxane-based main chain liquid crystalline elastomers and related linear polymers*. PhD thesis, Georgia Institute of Technology, 2007. 59
- [189] R.J. YOUNG AND P.A. LOVELL. *Introduction to Polymers (3rd edition)*. CRC Press, Taylor & Francis Group, 2011. 59
- [190] W. REN, P.J. McMULLAN, AND A.C. GRIFFIN. **Poisson's ratio of monodomain liquid crystalline elastomers**. *Macromol. Chem. Phys.*, 209:1896, 2008. 60
- [191] S. DEY, D.M. AGRA-KOOIJMAN, W. REN, P.J. McMULLAN, A.C. GRIFFIN, AND S. KUMAR. **Soft Elasticity in Main Chain Liquid Crystal Elastomers**. *Crystals*, 3:363, 2013. 60
- [192] E.M. TERENTJEV. **Phenomenological theory of non-uniform nematic elastomers: free energy of deformations and electric-field effects**. *Europhys. Lett.*, 23:27, 1993. 75
- [193] M. WARNER AND S. KUTTER. **Uniaxial and biaxial soft deformations of nematic elastomers**. *Phys. Rev. E*, 65:051707, 2002. 75
- [194] J. ADAMS AND M. WARNER. **Elasticity of smectic-a elastomers**. *Phys. Rev. E*, 71:021708, 2005. 75
- [195] L.H. JIN, Z. ZENG, AND Y.Z. HUO. **Thermomechanical modeling of the thermo-order-mechanical coupling behaviors in liquid crystal elastomers**. *J. Mech. Phys. Solids*, 58:1907, 2010. 75
- [196] W. ZHU, M. SHELLEY, AND P. MUHORAY. **Modeling and simulation of liquid-crystal elastomers**. *Phys. Rev. E*, 83:051703, 2011. 75
- [197] S.V. AHIR AND E.M. TERENTJEV. **Photomechanical actuation in polymer-nanotube composites**. *Nature Mat.*, 4:491, 2005. 75
- [198] S.V. AHIR AND E.M. TERENTJEV. **Infrared actuation in aligned polymer-nanotube composites**. *Phys. Rev. B*, 73:085420, 2006. 77
- [199] L.R.G. TRELOAR. *The physics of rubber elasticity (ed. 2005)*. Clarendon Press: Oxford, UK, 1958. 78
- [200] S.J. WOLTMAN, G.D. JAY, AND G.P. CRAWFORD. **Liquid-crystal materials find a new order in biomedical applications**. *Nature Mat.*, 6:929, 2007. 87
- [201] Y. JIANG, D. XU, L. XUESONG, C. LIN, W. LI, Q. AN, C. TAO, H. TANG, AND G. LI. **Electrothermally driven structural color based on liquid crystal elastomers**. *J Mater Chem*, 22:11943, 2012. 89
- [202] D.T.V. PAWLUK AND R.D. HOWE. **Dynamic contact of the human fingerpad against a flat surface**. *J. Biomech. Eng.*, 121:605, 1999. 97
- [203] PAWLUK D.T.V. AND R.D. HOWE. **Dynamic lumped element response of the human fingerpad**. *ASME J. Biomech. Eng.*, 121:178, 1999. 97
- [204] T.C. PATAKY, M.L. LATASH, AND V.M. ZATSORSKY. **Viscoelastic response of the finger pad to incremental tangential displacements**. *J. Biomech.*, 38:141, 2005. 97
- [205] M. WIERTLEWSKI. *Reproduction of tactual textures: Transducers, Mechanics and Signal Encoding*. Clarendon Press: Oxford, UK, 2013. 97
- [206] Q. WANG AND V. HAYWARD. **In vivo biomechanics of the fingerpad skin under local tangential traction**. *J. Biomech.*, 121(4):851, 2007. 99
- [207] Eurohaptics 2003. *Experimental evidence of lateral skin strain during tactile exploration*, 2003. 99
- [208] C.A. POLAND, R. DUFFIN, I. KINLOCH, A. MAYNARD, W.A.H. WALLACE, ET AL. **Carbon nanotubes introduced into the abdominal cavity of mice show asbestos-like pathogenicity in a pilot study**. *Nat. Nano.*, 3:423, 2008. 132
- [209] NATIONAL INDUSTRIAL CHEMICALS NOTIFICATION AND AUSTRALIA ASSESSMENT SCHEME (NICNAS). **Human health hazard assessment and classification of carbon nanotubes**. Technical report, Safe Work Australia, October 2012. 132
- [210] EUROPEAN COMMISSION. **Types and uses of nanomaterials, including safety aspects. Second regulatory review on nanomaterials**. Technical report, Safe Work Australia, October 2012. 132
- [211] J. BAHRENBURG, K. RÖTTGER, R. STEWERTSEN, F. RENTH, AND F. TEMPS. **Sequential photoisomerisation dynamics of the pushpull azobenzene Disperse Red 1**. *Photochem. Photobiol. Sci.*, 11:1210, 2012. 136
- [212] K.M. TAIT, J.A. PARKINSON, S.P. BATES, W.J. EBENEZER, AND A.C. JONES. **The novel use of NMR spectroscopy with in situ laser irradiation to study azo photoisomerisation**. *J. Photochem. Photobiol. A*, 154:179, 2003. 136
- [213] J. GARCIA-AMORÓS, H. FINKELMANN, AND D. VELASCO. **Increasing the isomerisation kinetics of azo dyes by chemical bonding to liquid-crystalline polymers**. *Chem. Eur. J.*, 17:6518, 2011. 136
- [214] PHILIPS LUMILEDS LIGHTING COMPANY. **Luxeon C Datasheet DS41**, 2014. 144, 145
- [215] J.J. GEORGE AND A.K. BHOWMICK. **Influence of matrix polarity on the properties of ethylene vinyl acetate-carbon nanofiller nanocomposites**. *Nanoscale. Res. Lett.*, 4:655, 2009. 150
- [216] K. CZANIKOVÁ, I. KRUPA, M. ILČIKOVÁ, D. JR. CHORVÁT, M. VALENTIN, ET AL. **Photo-actuating materials based on elastomers and modified carbon nanotubes**. *J. of Nanophotonics*, 6:063522-1, 2012. 150
- [217] M. CZANIKOVÁ, K. ILČIKOVÁ, I. KRUPA, M. MICUSIK, P. KASÁK, E. PAVLOVÁ, ET AL. **Elastomeric photo-actuators and their investigation by confocal laser scanning microscopy**. *Smart Mater. Struct.*, 22:104001, 2013. 150
- [218] K. CZANIKOVÁ, N. TORRAS, J. ESTEVE, I. KRUPA, P. KASÁK, E. PAVLOVÁ, ET AL. **Nanocomposite actuators based on ethylene vinyl acetate copolymer filled with carbon nanotubes**. *Sensors Actuat. B-Chem*, 186:701, 2013. 153
- [219] L. LIU AND Y. ZHANG. **Multi-wall carbon nanotube as a new infrared detected material**. *Sensors Actuat. A-Phys*, 116:394, 2004. 153
- [220] National Academy of Sciences of the United States of America. *A black body absorber from vertically aligned single-walled carbon nanotubes*, 106, 2009. 153
- [221] Y. ZHANG AND S. IJIMA. **Elastic response of carbon nanotube bundles to visible light**. *Phys. Rev. Lett.*, 82:3472, 1999. 153
- [222] G.J. SNYDER, J.R. LIM, C.K. JUANG, AND J.P. FLEURIAL. **Thermoelectric microdevice fabricated by a MEMS-like electrochemical process**. *Nature Mater.*, 2:528, 2003. 163
- [223] J.A. PLAZA, A. COLLADO, E. CABRUJA, AND J. ESTEVE. **Piezoresistive accelerometers for MCM package**. *J. Micromech. Syst.*, 11:794, 2002. 163
- [224] G. LUTZ. *Semiconductor Radiation Detectors. Device Physics*. Springer, 1999. 163

- [225] A.C.R. GRAYSON, R.S. SHAWGO, A.M. JOHNSON, N.T. FLYNN, Y.W. LI, ET AL. **A BioMEMS review: MEMS technology for physiologically integrated devices.** *Procc. of the IEEE*, **92:6**, 2004. 163
- [226] K.A. COOK-CHENNAULT, N. THAMBI, AND SASTRY A.M. **Powering MEMs portable devices - a review of non-regenerative and regenerative power supply systems with special emphasis on piezoelectric energy harvesting systems.** *Smart Mater. Struct.*, **3:043001**, 2008. 163
- [227] C.J. CAMARGO, H. CAMPANELLA, J.E. MARSHALL, N. TORRAS, K.E. ZINOVIEV, E.M. TARENTJEV, AND J. ESTEVE. **Batch fabrication of optical actuators using nanotube-elastomer composites towards refreshable Braille displays.** *J. Micromech. Microeng.*, **22:75009**, 2012. 170, 187, 197
- [228] C.J. CAMARGO, H. CAMPANELLA, J.E. MARSHALL, N. TORRAS, K.E. ZINOVIEV, E.M. TARENTJEV, AND J. ESTEVE. **Localised actuation in composites containing carbon nanotubes and liquid crystalline elastomers.** *Macromol. Rapid Commun.*, **32:falta**, 2011. 197
- [229] H. YANG, A. BUGUIN, J.M. TAULEMESSE, K. KANEKO, S. MÉRY, ET AL. **Micron-sized main-chain liquid crystalline elastomer actuators with ultralarge amplitude contractions.** *Journal of the American Chemical Society*, **131(41):15000**, 2009. 199
- [230] N. TORRAS, K.E. ZINOVIEV, J. ESTEVE, AND A. SÁNCHEZ-FERRER. **Liquid-crystalline elastomer micropillar array for haptic actuation.** *Journal of Materials Chemistry C*, **1:1–8**, 2013. 201
- [231] W. CASERI AND P.S. PREGOSIN. **Hydrosilylation chemistry and catalysis with cis-PtCl₂ (PhCH: CH₂)₂.** *Organometallics*, **7:1373**, 1988. 206
- [232] B. MARCINIEC. *Comprehensive Handbook on Hydrosilylation*. Pergamon Press, Oxford, 1992. 206
- [233] S. T. KIM AND H. FINKELMANN. **Cholesteric liquid single-crystal elastomers (LSCe) obtained by the anisotropic deswelling method.** *Macromol. Rapid Commun.*, **22:429**, 2001. 210
- [234] R. LOVELL AND G.R. MITCHELL. **Molecular orientation distribution derived from an arbitrary reflection.** *Acta Crystallogr., Sect. A: Cryst. Phys., Diffraction, Theor. Gen. Crystallogr.*, **37:135**, 1981. 211
- [235] G.R. MITCHELL AND A.H. WINDLE. *Development in Crystalline Polymers-2*. Elsevier Applied Science, London, 1988. 211
- [236] J. BOUSSEY. *Microsystems Technology: Fabrication, Test and Reliability*. Kogan Page Science, London, UK., 2003. 222
- [237] T.R. HSU. *MEMS & Microsystems: Design, Manufacture, and Nanoscale Engineering, 2nd Edition*. John Wiley & Sons, 2008. 222
- [238] SIMONE ZUFFANELLI. **Estudi d'un actuador tèrmic transparent per aplicacions hàptiques**, 2011. 223, 231
- [239] J.G. COOK AND M.P. VAN DER MEER. **The thermal conductivity and electrical resistivity of gold 80 to 340 K.** *Canadian Journal of Physics*, **48:254**, 1970. 223
- [240] M. HATZAKIS, B.J. CANAVELLO, AND J.M. SHAW. **Single-Step Optical Lift-Off process.** *IBM J. Res. Dev.*, **24:452**, 2010. 224
- [241] VISHAY SEMICONDUCTORS. **Ambient Light Sensor in 0805 Package, Doc. Num. = 81317**, 2014. 226
- [242] L. STOK, D. HATHAWAY, K. KEUTSER, ET AL. *Electronic Design Automation for Integrated Circuits Handbook - 2*. CRC Press, imprint of Taylor and Francis Group, Boca Raton, 2006. 227
- [243] Y.G. SUN, Z.Q. ZHAO, X.L. MENG, J. YIN, X.Y. LIU, AND Z.F. CHEN. **Cellular Basis of Itch Sensation.** *Science*, **325(5947):1531**, 2009. 245
- [244] MEDICAL SCHOOL DULUTH UNIVERSITY OF MINNESOTA. [link]. 246
- [245] A. STRERI AND E.S. SPELKE. **Haptic perception of objects in infancy.** *Cognitive Psychology*, **23(1):1–23**, 1988. 246
- [246] R.L. KLATZKY, S.J. LEDERMAN, AND METZGER V.A. **Identifying objects by touch: An 'expert system'.** *Perception & Psychophysics*, **37(4):299**, 1985. 246
- [247] S.J. LEDERMAN AND R.L. KLATZKY. **Hand movements: A window into haptic object recognition.** *Cognitive Psychology*, **19(3):342**, 1987. 246
- [248] R.A. FREITAS JR. *Nanomedicine, Vol. I: Basic Capabilities*. Landes Bioscience, Georgetown, TX, 1999. 247

REFERENCES

Scientific contributions

Book Chapters

- A. Sánchez-Ferrer, **N. Torras**, and J. Esteve *Integration of Liquid-Crystalline Elastomers in MEMS/MEOMS*, in *Liquid Crystalline Polymers: Structure and Chemistry* V. K. Thakur and M. R. Kessler, Springer International Publishing, (submitted)

Journal Articles

1. **N. Torras**, C. J. Camargo, A. Sánchez-Ferrer and J. Esteve *LCE Micropillar Array with thermoresistors as pushing actuators*, (under preparation)
2. **N. Torras**, J. P. Aguil, P. Vázquez, M. Duch, A. M. Hernández-Pintó, J. Samitier, J. Esteve, T. Suárez, M.L. Pérez-García, and J. A. Plaza *Suspended planar-array chips for molecular multiplexing at the microscale*, (under preparation)
3. **N. Torras**, J. E. Marshall, K. E. Zinoviev, C. J. Camargo, H. Campanella, E. M. Campo, E. M. Terentjev and J. Esteve *Gas-pressure moulding fabrication of smart actuators from nematic liquid-crystalline elastomers*, *Macromolecular Materials Engineering*, (2014); 299, pp. 1-7. DOI: 10.1002/mamae.201300462
4. **N. Torras**, K. E. Zinoviev, C. J. Camargo, E. M. Campo, H. Campanella, J. Esteve, J. E. Marshall, E. M. Terentjev, M. Omastová, I. Krupa, B. Mamojka, P. Teplický, B. Roeder, P. Bruns, M. Vallribera, R. Malet, V. Soler, J. Roig, N. Walker, D. Yates, F. Crompvoets *Tactile device based on opto-mechanical actuation of liquid crystal elastomers*, *Sensors and Actuators A: Physical*, (2014); 208, pp. 104-112. DOI:10.1014/j.sna.2014.01012
5. **N. Torras**, K. E. Zinoviev, J. Esteve and A. Sánchez-Ferrer *Liquid-Crystalline Elastomer Micropillar Array for Haptic Applications*, *Journal of Materials Chemistry C*, (2013); 1, pp. 5183-5190. DOI: 10.1039/c3tc31109k
- *Front cover design*.
6. Klaudia Czaniková, **Núria Torras**, Jaume Esteve, Igor Krupa, Peter Kasák, Ewa Pavlová, Ivan Chodák, Mária Omastová *Nanocomposite actuators based on ethylene vinyl acetate*

Scientific contributions

- copolymer filled with carbon nanotubes*, Sensors and Actuators B: Chemical, (2013); 186, pp. 701-710. DOI: 10.1013/j.snb.2013.06054
7. D. Naumenko, V. Snitka, M. Duch, **N. Torras**, J. Esteve *Stress mapping on the porous silicon microcapsules by Raman microscopy*, Microelectronic Engineering, (2012); 98, 488-491 Special issue from 38th International Conference on Micro and Nano Engineering, MNE'11, 19-23 September 2011, Berlin, Germany. DOI: 10.1016/j.mee.2012.07.089
 8. Carlos J. Camargo, Humberto Campanella, Jean E. Marshall, **Núria Torras**, Kirill Zinoviev, Eugene M. Terentjev, Jaume Esteve, *Batch fabrication of optical actuators using nanotube-elastomer composites towards refreshable Braille displays*, Journal of Micromechanics and Microengineering, (2012); 22, 75009, pps. 9. DOI: 10.1088/0960-1317/22/7/075009
- Selected paper for special issue: Highlights 2012.
 9. Jean Marshall, Yan Ji, **Núria Torras**, Kirill Zinoviev, Eugene M. Terentjev, *Carbon-nanotube sensitized nematic elastomers for IR-visible photo-actuation*, Soft Mater, (2012); 8, 5, pp. 1570-1574. DOI: 10.1039/c1sm06656k
 10. **N. Torras**, K.E.Zinoviev, J.E.Marshall, E.M.Terentjev, J.Esteve, *Bending kinetics of photoactuated nematic elastomer cantilever*, Applied Physics Letter, (2011); 99, 254102, pps. 4. DOI: 10.1063/1.3670502
- Selected paper for special issue: Virtual Journal of Nanoscale Science & Technology, January 9, 2012, 25, 2.
 11. Carlos J. Camargo, Humberto Campanella, Jean E. Marshall, **Núria Torras**, Kirill Zinoviev, Eugene M. Terentjev, Jaume Esteve, *Localised Actuation in Composites Containing Carbon Nanotubes and Liquid Crystalline Elastomers*, Macromolecular Rapid Communications, (2011); 32, 24, pp. 1953-1959. DOI: 10.1002/marc.201100578
- Front cover design.

Proceedings

1. K. Czaniková, I. Krupa, P. Kasák, M. Ilcáiková, N. Torras, D. Chorvát, D. Racko, M. Slouf, M. Omastová *Photo-thermal actuation of Ethylene Vinylacetate/Carbon Nanotubes composites*, Proceedings of the 10th Eurofillers International Conference, Eurofillers 2013, 25-29 August 2013, Bratislava, Slovakia, art. no. OP9. ISBN: 978-80-970923-3-7
2. K. Czaniková, I. Krupa, P. Kasák, M. Ilcáiková, J. Mosnáček, M. Micusík, N. Torras, J. Esteve, D. Chorvát, D. Racko, E. Pavlová, M. Omastová *Photo-actuation study of Ethylene Vinylacetate copolymer filled with modified carbon nanotubes*, Proceedings of the 10th Eurofillers International Conference, Eurofillers 2013, 25-29 August 2013, Bratislava, Slovakia, art. no. Po14. ISBN: 978-80-970923-3-7

3. N. Torras, K. E. Zinoviev, C. J. Camargo, E. M. Campo, H. Campanella, J. Esteve, J. E. Marshall, E. M. Terentjev, M. Omastová, I. Krupa, B. Mamojka, P. Teplický, B. Roeder, P. Bruns, M. Vallribera, R. Malet, V. Soler, J. Roig, N. Walker, D. Yates, F. Cromptoets *Nematic opto-mechanical actuators for the fabrication of refreshable tactile systems*, Proceedings of the 17th International Conference on Solid-State Sensors, Actuators and Microsystems, Transducers'2013, 16-20 June 2013, Barcelona, Spain, art. no. W1D.004. IEEE Catalog Number: CFP13SSA-USB. ISBN: 978-1-4673-5981-8
4. C.J. Camargo, N. Torras, H. Campanella, J.E. Comrie, K. Zinoviev, E.M. Campo, E.M. Terentjev, J. Esteve *Mechanical modeling of thermally actuated LCE-CNT composite*, Proceedings of the SPIE Conference on Nano-Opto-Mechanical Systems (NOMS) 8107, 21 August 2011, San Diego, California, USA, art. no. 81070J. DOI: 10.1117/12.897120
5. C.J. Camargo, N. Torras, H. Campanella, J.E. Comrie, K. Zinoviev, E.M. Campo, E.M. Terentjev, J. Esteve *Microstamped opto-mechanical actuator for tactile displays*, Proceedings of the SPIE Conference on Nano-Opto-Mechanical Systems (NOMS) 8107, 21 August 2011, San Diego, California, USA, art. no. 810709. DOI: 10.1117/12.893279
6. N. Torras, C.J. Camargo, K. Zinoviev, H. Campanella, J.E. Comrie, E.M. Campo, E.M. Terentjev, J. Esteve *Opto-Mechanical Characterization of Liquid Crystals Elastomers with Carbon Nanotubes*, Proceedings of the SPIE Conference on Nano-Opto-Mechanical Systems (NOMS) 8107, 21 August 2011, San Diego, California, USA, art. no. 810704. DOI: 10.1117/12.892892
7. N. Torras, J. Llobet, J. Marshall, K. Zinoviev, D. Yates, L. Rotkina, J. Esteve, E.M. Terentjev, E.M. Campo, *Study of LCE nanocomposites through electron microscopy*, Proceedings of the SPIE Scanning Microscopy Conference 8036, 26-28 April 2011, Orlando, Florida, USA, art. no. 80360G. DOI: 10.1117/12.885539
8. E.M. Campo, H. Campanella, Y. Y. Huang, K. Zinoviev, N. Torras, C. Tamargo, D. Yates, L. Rotkina, J. Esteve, E.M. Terentjev, *Electron microscopy of polymer-carbon nanotubes composites*, Proceedings of the SPIE Scanning Microscopy Conference 7729, 7-11 March 2010, San Diego, California, USA, art. no. 772904. DOI: 10.1117/12.867718

Conferences

1. A. Sánchez-Ferrer, N. Torras, K. E. Zinoviev, J. Esteve *Liquid-Crystalline Elastomer Micropillar Array for Haptic Actuation*, 12th Swiss Soft Days, 14th October 2013, Berna, Switzerland (Oral presentation).
2. A. Sánchez-Ferrer, J. M. Haberl, N. Torras, K. E. Zinoviev, J. Esteve *Liquid-Crystalline Elastomer Micropillar Array for Haptic Actuation*, 7th International Liquid Crystalline Elastomer Conference, ILCEC7, 10-12th September 2013, Shanghai, China (Poster session).

Scientific contributions

3. M. Duch, N. Torras, J. A. Plaza, J. Esteve, *Nanosphere lithography on 3D microparticles for nanoplasmonic applications in living cells*, 39th International Conference on Micro and Nano Engineering, MNE 2013, 16-19 September 2013, London, UK (Poster session).
4. K. Czaniková, I. Krupa, P. Kasák, M. Ilčíková, N. Torras, D. Chorvát, D. Racko, M. Slouf, M. Omastová *Photo-thermal actuation of Ethylene Vinylacetate/Carbon Nanotubes composites*, 10th Eurofillers International Conference, Eurofillers 2013, 25-29 August 2013, Bratislava, Slovakia (Oral presentation).
5. K. Czaniková, I. Krupa, P. Kasák, M. Ilčíková, J. Mosnáček, M. Micusík, N. Torras, J. Esteve, D. Chorvát, D. Racko, E. Pavlová, M. Omastová *Photo-actuation study of Ethylene Vinylacetate copolymer filled with modified carbon nanotubes*, 10th Eurofillers International Conference, Eurofillers 2013, 25-29 August 2013, Bratislava, Slovakia (Poster session).
6. N. Torras, K. E. Zinoviev, C. J. Camargo, E. M. Campo, H. Campanella, J. Esteve, J. E. Marshall, E. M. Terentjev, M. Omastová, I. Krupa, B. Mamojka, P. Teplický, B. Roeder, P. Bruns, M. Vallribera, R. Malet, V. Soler, J. Roig, N. Walker, D. Yates, F. Cromptvoets *Nematic opto-mechanical actuators for the fabrication of refreshable tactile systems*, 17th International Conference on Solid-State Sensors, Actuators and Microsystems, Transducers'2013, 16-20 June 2013, Barcelona, Spain (Oral presentation).
7. D. Naumenko, V. Snitka, M. Duch, N. Torras and J. Esteve, *Stress mapping on porous silicon microcapsules by Raman microscopy*, 38th International Conference on Micro and Nano Engineering, MNE'11, 19-23 September 2011, Berlin, Germany (Poster session).
8. C.J. Camargo, N. Torras, H. Campanella, J.E. Comrie, K. Zinoviev, E.M. Campo, E.M. Terentjev, J. Esteve *Mechanical modeling of thermally actuated LCE-CNT composite*, SPIE Conference on Nano-Opto-Mechanical Systems (NOMS) 8107, 21 August 2011, San Diego, California, USA (Oral presentation).
9. C.J. Camargo, N. Torras, H. Campanella, J.E. Comrie, K. Zinoviev, E.M. Campo, E.M. Terentjev, J. Esteve *Microstamped opto-mechanical actuator for tactile displays*, SPIE Conference on Nano-Opto-Mechanical Systems (NOMS) 8107, 21 August 2011, San Diego, California, USA (Oral presentation).
10. N. Torras, C.J. Camargo, K. Zinoviev, H. Campanella, J.E. Comrie, E.M. Campo, E.M. Terentjev, J. Esteve *Opto-Mechanical Characterization of Liquid Crystals Elastomers with Carbon Nanotubes*, SPIE Conference on Nano-Opto-Mechanical Systems (NOMS) 8107, 21 August 2011, San Diego, California, USA (Oral presentation).
11. C.J. Camargo, N. Torras, H. Campanella, J.E. Comrie, K. Zinoviev, E.M. Campo, E.M. Terentjev, J. Esteve, *Electron microscopy of polymer-carbon nanotubes composites*, 16th International Conference on Solid-State Sensors, Actuators and Microsystems, Transducers'11, 5-9 June 2011, Beijing, china (Poster session).

12. N. Torras, J. Llobet, J. Marshall, K. Zinoviev, D. Yates, L. Rotkina, J. Esteve, E.M. Terentjev, E.M. Campo, *Light-Actuated CNT-doped elastomer blisters towards Braille dots*, SPIE Conference 8036, 26-28 April 2011, Orlando, Florida, USA (Oral presentation)
13. N. Torras, M. Duch, R. Gómez, J.A. Plaza y J. Esteve *Development of 3D porous polysilicon devices*, 8th Spanish Conference on Electron Devices, CDE'11, 8-11 February 2011, Palma de Mallorca, Spain (Poster session).
14. N. Torras, C.J. Camargo, J. Marshall, K. Zinoviev, H. Campanella, E.M. Campo, E.M. Terentjev, J. Esteve *Opto-Mechanical characterization of Liquid Crystals Elastomer*, 8th Spanish Conference on Electron Devices, CDE'11, 8-11 February 2011, Palma de Mallorca, Spain (Oral presentation).
- *Awarded with Best Session's Talk.*
15. N. Torras, M. Duch, R. Gómez-Martínez, N. Torres, J.A. Plaza, J. Esteve, *3D Porous polysilicon devices for biomolecular recognition*, 36th International Conference on Micro and Nano Engineering, MNE'10, 19-22 September 2010, Genoa, Italy (Poster session).
16. N. Torras, K. Zinoviev, J. Esteve, J.A. Plaza, H. Campanella, C.J. Camargo, E.M. Campo, E.M. Terentjev, Y. Ji, *Characterization of Liquid Crystals Elastomer actuated by visible light*, 8th International Conference on Nanoscience & Nanotechnology, NN10, 14-16 July 2010, Ouranopolis, Halkidiki, Greece (Poster session).
17. E.M. Campo, H. Campanella, Y. Y. Huang, K. Zinoviev, N. Torras, C. Tamargo, D. Yates, L. Rotkina, J. Esteve, E.M. Terentjev, *Electron microscopy of polymer-carbon nanotubes composites*, SPIE Conference on Scanning Microscopy 7729, 7-11 March 2010, San Diego, California, USA (Oral presentation).

Patents

Método de obtención de un array de micropartículas planares con multiplexado molecular superficial, array obtenido y su uso. J. Esteve, J.A. Plaza, M. Duch, N. Torras, M.L. Pérez-García, J.P. Aguil. P201430864 (may 2014).

Participation in Projects

NEMSPUN: Integration of electrospun nanofibers to MEMS/NEMS technologies for development of zero-power devices. Ministerio de Ciencia e Innovación. i-LINK+ program for International Scientific collaborations (i-LINK0616). Jaume Esteve Tintó (IMB-CNM, CSIC).

Scientific contributions

MINAHE4: Micro y Nano Herramientas 4. Ministerio de Ciencia e Innovación (TEC2011-29140-C03-01). Jose Antonio Plaza Plaza (IMB-CNM, CSIC).

NOMS: Nano-Opto Mechanical Systems. European Commission, 7th Framework Programm for Research (NMP-228916). Jaume Esteve Tintó (IMB-CNM, CSIC).

CSIC-COLCIENCIAS: Detectores de campo de partículas (carbón) en suspensión basados en MEMS y WSN. Instituto Colombiano para el Desarrollo de la Ciencia y la Tecnología (COLCIENCIAS). Humberto Campanella (IME) and Maria Gabriela Calle Torres (UNI Norte).

MINAHE3: Micro y Nano Herramientas 3. Ministerio de Ciencia e Innovación (TEC2008-06883-C03-01). Jose Antonio Plaza Plaza (IMB-CNM, CSIC).

CALCAT1: A novel Micromechanical Test Frame for characterization of small-scale materials and devices. Generalitat Catalunya's Engineering Innovation Program (CALCAT09). Jasmina Casals Terré (UPC) and Lorenzo Valdevit (UCI).

-1.5 months stay at University of California, Irvine, (UCI) with Prof. Valdevit's group (July-August 2010)

List of abbreviations

- ε_i : Expansion/contraction expressed in percentage
- F_i : Actuation Force
- I_i : Current Intensity
- λ_i : Uniaxial thermal expansion/contraction
- L_i : Sample length
- L_{iso} : Sample length in isotropic phase (during the application of an external stimulus)
- L_{nem} : Sample length in nematic state (no stimulus applied)
- ν : Poisson's ratio
- T_g : Glass transition temperature
- T_{NI} : Transition temperature from nematic to isotropic phase, also known as clearing temperature
- 11UB**: 1,4 alkeneoxybenzene, cross-linking unit
- AD**: Audio Description
- ANSYS**: Finite Element Analysis software
- Au**: Gold, chemical element
- CCD**: Charge-Coupled Device
- CSIC**: Consejo Superior de Investigaciones Cientificas
- DI water**: Deionized water
- DOF**: Degrees of Freedom. Referred to Finite element modeling
- DSC**: Differential Scanning Calorimetry
- EAP**: Electro Active Polymer
- EDA**: Electronic Design Automation
- EVA**: Ethylene-Vinylacetate copolymer
- FE**: Finite Element
- FEA**: Finite Element Analysis
- FEM**: Finite Element Modeling
- FIB**: Focused Ion Beam
- FWHM**: Full Width Half Maximum

HCl: Hydrochloric acid

H_2O_2 : Hydrogen peroxide

IMB-CNM: Institut de Microelectrònica de Barcelona, Centre Nacional de Microelectrònica

IPMC: Ionic Polymer-Metal Composite

IR: Infra-Red light

ITO: Indium Tin Oxide

LC: Liquid Crystal

LCD: Liquid Crystal Display

LCE: Liquid-Crystalline Elastomer

LD: Laser Diode

LED: Light Emitting Diodes

MBB: 4-methoxyphenyl-4-(1-buteneoxy) benzoate, Rigid-rod LC mesogen

MCLCE: Main-Chain Liquid-Crystalline Elastomer

MEMS: Micro-electro Mechanical Systems

MWCNT: Multi-Walled Carbon Nanotube

NEMS: Nano-Electro Mechanical Systems

Ni: Niquel, chemical element

NOMS: Nano-Opto-Mechanical Systems. Acronym of a EU-FP7 project

Op-am: Operation Amplifier

PC: Personal computer

PCB: Printed Circuit Board

PAPC: Photo-Actuating Polymer Composite

PDMS: Polydimethylsiloxane

PET: Polyethylene terephthalate

PMHS: Polymethylhydrosiloxane

PMMA: Polymethylmetacrylate

POM: Polyoxymethylene

PTFE: Polytetrafluoroethylene

PVDF: Polyvinylidene fluoride

PyMC: End-capping pyrene group for improving the CNT dispersion into LCE matrix

SCC: Side-Chain Crosslinker

SCLCE: Side-Chain Liquid-Crystalline Elastomer

SCM: Side-Chain Mesogen

SEM: Scanning Electron Microscopy

SMA: Shape Memory Alloy

SWCNT: Single-Walled Carbon Nanotube

TEM: Transmission Electron Microscopy

Ti: Titanium, chemical element

UCAM: University of Cambridge, UK

UV: Ultra Violet light

VCSEL: Vertical Cavity Surface Emitting Laser

WAXS: Wide Angle X-ray Scattering

WHO: World Health Organization

XRD: X-ray Diffraction

